NASA TECHNICAL NOTE

NASA TN D-4688

NASA TN, D-4688

AERODYNAMIC STABILITY CHARACTERISTICS OF THE APOLLO COMMAND MODULE

by William C. Moseley, Jr., Ralph E. Graham, and Jack E. Hughes

Manned Spacecraft Center
Houston, Texas

NATIONAL AERONAUTICS AND SPACE ADMINISTRATION • WASHINGTON, D. C. • AUGUST 1968

NASA TN D-4688

AERODYNAMIC STABILITY CHARACTERISTICS OF THE APOLLO COMMAND MODULE

By William C. Moseley, Jr.,
Ralph E. Graham, and Jack E. Hughes

Manned Spacecraft Center
Houston, Texas

NATIONAL AERONAUTICS AND SPACE ADMINISTRATION

For sale by the Clearinghouse for Federal Scientific and Technical Information
Springfield, Virginia 22151 – CFSTI price $3.00

ABSTRACT

Results from wind-tunnel tests conducted during the design and development of the Apollo command module are presented. Investigations were made to develop static and dynamic stability data for the basic configuration of the command module. Parametric studies were conducted to determine the effects of varying certain geometric dimensions of the basic command module configuration. Studies of modifications designed to provide an increased lift-to-drag ratio were also conducted. Representative samples, from an extensive series of tests of alterations designed to eliminate an apex-forward trim condition, are included.

CONTENTS

TABLES

FIGURES

AERODYNAMIC STABILITY CHARACTERISTICS OF THE APOLLO COMMAND MODULE

By William C. Moseley, Jr.,
Ralph E. Graham, and Jack E. Hughes*
Manned Spacecraft Center

SUMMARY

Wind-tunnel tests were conducted to obtain static- and dynamic-stability data for the basic Apollo command module configuration at Mach numbers from 0.4 to 9.0 and angles of attack of -25° to 198°. Similar studies were made to determine the effects which variations in certain geometric dimensions of the basic configuration would have on the aerodynamic characteristics. Varying the corner radius and the afterbody angle provided limited control of the trimmed angle of attack, while varying the heat-shield radius had little effect.

It was discovered that the center-of-gravity restrictions to provide the nominal lift-to-drag ratio requirement of 0.5 would be difficult to maintain. Several modifications were studied in an attempt to provide an increase in the lift-to-drag ratio without major alteration of the trimmed angle of attack and the center-of-gravity location. These modifications included a fixed flap on one side of the heat shield, corner modifications, and canted heat shields. All of the modifications reduced the trimmed angle of attack by 8° or more, but no substantial improvement was indicated when the center of gravity was adjusted to regain the design angle of attack of 147°.

The basic and modified basic configurations of the Apollo command module were found to have an undesirable trim point (apex forward) near angles of attack of 40° to 80°. This trim point was especially prominent at subsonic velocities.

A series of investigations was conducted on modifications designed to eliminate this condition. These alterations included apex modifications such as blunted noses and extended cylindrical noses, as well as fixed and deflectable apex flaps. The effects of the addition of a series of strakes to the command module were also studied.

The extended cylindrical nose section reduced the strength of the trim point, while a half-cylindrical nose section eliminated the trim point completely. However, such modifications required redesign of the spacecraft and, therefore, were not considered further. Design considerations also precluded the use of apex flaps, some of

---

*ITT/Federal Electric Corporation.

which did eliminate the undesirable trim point. Several strake or spoiler configurations were effective, but made the vehicle dynamically unstable.

A proposal was studied which required resequencing the abort so that the launch escape tower would be retained and used to provide the necessary moment to orient the command module to the heat-shield-forward attitude. An intensive series of tests was performed on configurations in which plates, known as the tower flap, were added to the escape tower. Certain of the tower-flap configurations were effective in reducing or eliminating the undesirable trim condition, but their effectiveness was reduced by the impingement of the shock wave on the command module at velocities of Mach 6.0 and greater. Negative damping, resulting in tumbling, was exhibited at angles of attack from 100° to 180° at velocities from 0.3 to 0.8; therefore, tower flaps were eliminated from further study.

INTRODUCTION

The Apollo Spacecraft Program, with the ultimate goal of a manned lunar landing, was inaugurated by the National Aeronautics and Space Administration (NASA) as part of the continuing program of space exploration following Project Mercury and the Gemini Program. Initial study contracts, NASA Space Task Group studies, and other studies established the design requirements and specifications for the Apollo spacecraft. Some of the early wind-tunnel studies, used to support and to verify the selection of a configuration for development, are reported in references 1 to 4. The Apollo wind-tunnel program was established as part of the design-and-development program initiated to support the Apollo Spacecraft Program. The entire Apollo wind-tunnel program is discussed in reference 5. The stability characteristics of the production Apollo command module (CM) are presented in reference 6, while similar data for the Apollo launch escape vehicle (LEV) are found in reference 7. Stability characteristics of the Apollo LEV, with canard surfaces deployed, are reported in reference 8.

The wind-tunnel program was necessary to verify the theoretical estimates of the stability characteristics of the basic entry vehicle. Parametric studies were made to determine what effects on the aerodynamic characteristics would be induced by variations in certain geometric dimensions of the vehicle such as corner radius, afterbody angle, heat-shield radius, and nose radius. Tests were made of modifications to the heat-shield corner, of the use of heat-shield flaps, and of canting of the heat shield in an attempt to establish simple means of supplementing the center-of-gravity (c.g.) method of lift-to-drag ratio (L/D) control by passive modifications. Investigations were made to determine the effectiveness of adding strakes and flaps to the Apollo CM to eliminate an undesirable trim condition. Additional studies concerning this problem were made of the CM and escape-tower configuration and the effects of adding a plate or plates to the forward portion of the tower.

The purpose of this paper is to present the static- and dynamic-stability characteristics of the configurations tested in the process of selecting a configuration which meets the CM design requirements. Because of the large number of configurations tested, only a select group are presented. Static-stability data are presented for a Mach-number range from 0.3 to 10.0 and for a large angle-of-attack range. Dynamic-stability data for Mach numbers from 1.5 to 6.0 are also presented for the Apollo CM

and variations. Static-stability data, for determining the effectiveness of adding flaps to the escape-tower structure, are presented for Mach numbers from 0.3 to 10.0 at angles of attack from -118° to 360°. Dynamic-stability data for a tower-flap configuration at Mach numbers from 0.3 to 0.8 are presented at angles of attack from 0° to 360°.

The positive direction of forces and moments and the body system of axes are illustrated in figure 1. The data presented in this paper are referenced to both the body and the stability systems of axes.

SYMBOLS

C_A axial-force coefficient, $\frac{\text{axial force}}{q_\infty S}$

C_D drag coefficient, $C_N \sin \alpha + C_A \cos \alpha$

C_L lift coefficient, $C_N \cos \alpha - C_A \sin \alpha$

C_m pitching-moment coefficient, $\frac{\text{pitching moment}}{q_\infty Sd}$

$C_{m,a}$ pitching-moment coefficient about theoretical apex

$C_{m,c.g.}$ pitching-moment coefficient about nominal c.g.

$C_{m_q} + C_{m_{\dot{\alpha}}}$ damping-in-pitch parameter $\frac{\partial C_m}{\partial \frac{qd}{2V}} + \frac{\partial C_m}{\partial \frac{\dot{\alpha} d}{2V}}$, per rad

$\overline{C_{m_q}} + \overline{C_{m_{\dot{\alpha}}}}$ average damping-in-pitch parameter over one full oscillation

C_{m_α} pitching-moment curve slope parameter (measured at trim angle of attack), $\frac{\partial C_m}{\partial \alpha}$, per rad

C_N normal-force coefficient, $\frac{\text{normal force}}{q_\infty S}$

C_n yaw-moment coefficient, $\frac{\text{yawing moment}}{q_\infty Sd}$

C_Y	side-force coefficient, $\frac{\text{lateral force}}{q_\infty S}$
C_l	rolling-moment coefficient, $\frac{\text{rolling moment}}{q_\infty Sd}$
d	maximum body diameter (full scale), 154 in.
I	moment of inertia, ft-lb/sec^2
k	reduced frequency parameter, $\frac{\omega d}{2V}$
M	free-stream Mach number
q	pitching angular velocity, rad/sec
q_∞	free-stream dynamic pressure, lb/ft^2
R	Reynolds number (based on maximum model diameter)
S	maximum cross-sectional area perpendicular to body X-axis, ft^2
V	free-stream velocity, ft/sec
X, Y, Z	body reference axes
$\frac{x}{d}$	longitudinal location ratio of c.g. measured from theoretical CM apex
$\frac{z}{d}$	vertical location ratio of c.g. measured from CM centerline
α	angle of attack (of model centerline), deg
$\dot{\alpha}$	rate of change of angle of attack, rad/sec
α_t	trim angle of attack, deg
β	angle of sideslip, deg
θ	angular displacement, rad
$\dot{\theta}$	angular velocity, rad/sec
$\ddot{\theta}$	angular acceleration, rad/sec^2

Φ	cylindrical polar-coordinate angle measured about the X-axis
ω	circular frequency of oscillation, rad/sec

Subscripts:

a	theoretical CM apex
c.g.	center of gravity
m	model

Operators:

$(\dot{})$	time derivative
$(\ddot{})$	second derivative (time)

Because of the number and variety of configurations tested, some means for ready identification were required. Letters are used to denote a basic configuration, and numbered subscripts identify modifications or additions to the basic configuration.

C	basic Apollo CM configuration
F	basic flap configurations
L	basic strake configuration
T	basic escape-tower structure configurations
V	vent

FACILITIES AND MODELS

Test Facilities

The broad scope of expected flight conditions (extremes of Mach number, Reynolds number, and angle of attack) required the use of a variety of wind-tunnel facilities. All such facilities employed to acquire the data contained in this report are listed in table I conjointly with tunnel size and capability. Models and the ranges over which they were tested are presented in table II. No attempt is made in this paper to present data by facility, to compare data, or to define any Reynolds number, model support, or other facility effects.

Models

Test models used in the test regimen varied in size from 0.02- to 0.105-scale of the Apollo CM and from 0.045- to 0.105-scale of the escape-tower structure. Sketches of models for which data are presented appear in figure 2, and photographs of typical test models are presented in figure 3.

The initial wind-tunnel tests were conducted to verify the theoretical studies which established the basic configuration. The basic configuration used in these investigations is shown in figure 2(a). The table included in this figure shows the alterations made in some of the geometric dimensions of the model to determine the effects of such variations on the aerodynamic characteristics. For configurations C to C_5, the afterbody angle and the heat-shield radius were held constant while variations were introduced in the corner radius and the apex radius. Surface modifications to the CM models used in some of the tests are shown in figures 2(b) and 2(c).

Models used in the investigations into means of improving the L/D are depicted in figure 2(d). Each heat shield incorporated different modifications designed for L/D improvement. These modifications included a fixed flap on the edge of the heat shield (configuration C_{25}) or changes in corner radii (C_{26} and C_{27}). Several models with canted heat shields are shown as configurations C_{28} to C_{32}.

The models, which were used in the initial tests directed toward the elimination of an apex-forward static-trim point (fig. 2(e)), included apex modifications such as blunted noses (C_{22} and C_{23}) and extended cylindrical and half-cylindrical noses (C_{34} and C_{35}). Tests also were made of models of the basic CM (designated F, F_2, F_4, F_5, F_6, and F_7) to which a series of fixed and deflectable apex flaps were added as shown in figure 2(f). Several heat-shield-flap modifications were tested, and two of these configurations (F_8 and F_{11}) are shown in figure 2(g).

Other modifications to the basic CM consisted of the addition of various strakes. The first model (C_{15}) tested in this series utilized four strakes (fig. 2(g)). Configurations L, L_2, and L_3 (fig. 2(h)) show some of the variations in length and location of the strakes. Other configurations (figs. 2(i) to 2(k)) included tapered strakes and some which wrapped completely around the apex. Some of the apex-cover or paddle-strake configurations investigated are shown in figure 2(l).

Investigations were also conducted on the use of the CM and escape-tower combination and the addition of various plates at different locations on the escape-tower structure. A representative sampling of the configurations tested is shown in figures 2(m) to 2(o).

Model size was predicated on tunnel size and capability of simulating desired flight conditions with minimum tunnel interference. Tunnel angle-of-attack sectors are usually designed for small angle-of-attack ranges and for specified loading conditions; however, selective model-mounting techniques permitted testing throughout

the entire angle-of-attack range (0° to 360°), as required. Aerodynamic force-and-moment data were measured by internally mounted strain-gage balance systems. Since balances were not readily adaptable to the large angle ranges required, the balances were selected for gross overall loading in many cases.

TEST TECHNIQUES AND ACCURACY

Test Techniques

Static-stability tests. - Static force-and-moment tests were conducted using sting-mounted models attached to a strain-gage balance which measured the force-and-moment data. The rolling moments were on the order of magnitude of the sensitivity of the balance and, therefore, were difficult to measure.

A series of models, identical except for the location of the balance cavities, was used to allow testing over the desired angle-of-attack ranges. The balance cavities were positioned to allow different installations in order to obtain variations in the angle between the axis of symmetry of the model and the balance axis. The basic angle range of the support systems was also adjustable and, with the various model-offset angles, permitted testing over the entire angle-of-attack range (0° to 360°) as required.

Dynamic-stability tests. - Dynamic-stability data were acquired by using the limited-free-oscillation and the free-to-tumble test techniques. The limited-free-oscillation technique involved testing statically balanced models about the vehicle c.g. Test data were obtained by deflecting the models to the desired attitude, then releasing them suddenly and recording the time histories of the resulting oscillations. Use of this technique required limiting the oscillation amplitude to ±25°.

The free-to-tumble technique allowed statically balanced models (mounted on a transverse rod through the c.g.) to tumble freely through an angle-of-attack range from 0° to 360°. A typical model installation is shown in figure 3(e). Some problems were encountered in designing a method of mounting the model on a system in which friction and interference had to be minimal. A gas bearing support, similar to one used successfully at supersonic Mach numbers in the limited-free-oscillation tests, failed because of galling under the buffeting subsonic-loading conditions. A precision ball bearing mount was designed and proved to be satisfactory. Friction or tare damping generally contributed a fractional part of the aerodynamic damping of the system. Bench tests were made to determine the friction damping under load, and tare corrections were applied to the data.

Input data for calculating the damping-moment coefficient are acquired by using the θ time history. This is accomplished by applying the single-degree-of-freedom equation of motion.

$$I\ddot{\theta} + \left(C_{m_q} + C_{m_{\dot{\alpha}}}\right)\left(\frac{q_\infty S d^2 \dot{\theta}}{2V}\right) + C_{m_\alpha} q_\infty S d\theta = 0$$

If C_m were available from static tests and if I were measured in advance, then $C_{m_q} + C_{m_{\dot{\alpha}}}$ would be the only variable. The equation of motion could be solved by integration with assumed values for $C_{m_q} + C_{m_{\dot{\alpha}}}$ until the θ time histories were simulated. A more thorough discussion of this technique is found in reference 9.

Accuracy of Data

Accuracy tolerances of the force-and-moment coefficients were derived from balance calibration data and from data repeatability (table III).

PRESENTATION OF RESULTS

Table IV presents a summary of aerodynamic test data included in the designated figures. These data were acquired from studies made on the basic configuration of the Apollo CM and from parametric studies designed to show the effects of variations of certain geometric dimensions on the aerodynamic characteristics of the Apollo CM. These investigations were followed by a brief study of several modifications of the heat-shield radius and of the corner radius to determine if such variations would provide an increased L/D. An extensive series of investigations were made of modifications designed to eliminate an undesirable trim condition (apex forward) of the Apollo CM. These investigations involved geometric modifications or additions to the apex of the Apollo CM, a series of apex flaps (fixed and deflectable), and several heat-shield flap modifications. The effects of the addition of strakes to the CM and the use of apex-cover strakes were also studied as possible means of eliminating the apex-forward trim condition. Finally, a series of tests was made of a configuration which consisted of the CM and escape tower. Modifications, known as tower flaps, were made to this configuration by adding one or more plates of various shapes and sizes to the tower structure.

DISCUSSION OF RESULTS

In the system of axes about which the data are reduced, the apex-forward attitude of the CM is defined as $\alpha = 0°$. Generally, the pitching-moment data are referenced about both the theoretical apex of the model (fig. 1) and a nominal c.g. Data referenced about the nominal c.g. are used to provide a more realistic representation of the moment data.

Basic Configuration and Parametric Studies

The basic configuration C was defined in mid-1961 and was submitted to the prime contractor as the configuration for development. The configuration was defined by theoretical studies and by estimates of the aerodynamic characteristics. Preliminary wind-tunnel results, obtained at Langley Research Center in 1961 (refs. 1 and 2), confirmed the theoretical study results. The initial data studies in the Apollo

wind-tunnel program were made to provide additional data on the basic configuration. These test results for Mach numbers 0.4 to 9.0 are presented in figures 4, 5, and 6.

The pitching-moment coefficient data of figures 4, 5, and 6 indicate that the hypersonic trim point for the nominal c.g. $\left(\frac{x}{d} = -0.685,\ \frac{z}{d} = 0.059\right)$ is approximately $\alpha = 147°$. The data also indicate that the nominal hypersonic $L/D \approx 0.5$ could be attained, but that probability of maintaining the desired trim angle of attack is marginal because of the location of the c.g. An undesirable (apex forward) trim point (near $\alpha = 50°$ to $60°$) is also indicated by the test results, and is prominent at Mach numbers from 0.4 to 3.27. Buffeting of the model occurred at subsonic speeds and was associated with the undesirable trim point. The buffeting resulted in a severe data scattering and limited the acquisition of data in the $\alpha = 40°$ to $80°$ range. The data scattering can also be seen in the other coefficient data presented.

A parametric study to show the effects of variations in the corner radius, afterbody angle, and heat-shield radius was conducted at the Jet Propulsion Laboratory 20-inch Supersonic Wind Tunnel and 21-inch Hypersonic Wind Tunnel. Preliminary studies had indicated that additional volume was required in the apex region of the CM. The basic configuration C was modified by reducing the nose or apex radius from 0.10d to 0.059d. This modified configuration, designated C_2, has aerodynamic characteristics similar to configuration C and is also used in this discussion for purposes of comparison. Some aerodynamic effects of varying the corner radius at the juncture of the heat shield and the afterbody are presented in figure 7. Corner radii of 0.0d (sharp), 0.05d, 0.10d, and 0.15d were investigated. The data indicate a systematic variation of the force-and-moment coefficients as the corner radius is increased from 0.0d to 0.15d. Pitching-moment coefficient data show that the trim angle of attack reduces with an increase in corner radius. At a constant $\alpha > 140°$, lift and drag coefficients decrease as the corner radius is increased (figs. 7(e) and 7(f)). It may be seen from figure 7(g) that the L/D for a constant $\alpha > 140°$ also decreases as the corner radius is increased. Since the corner radius of 0.0 had to be excluded from further consideration because of heat-protection problems, the modified basic configuration C_2 was selected as the shape giving the highest trimmed L/D of the remaining configurations.

Using the C_2 dimensions, tests were made with the afterbody angle as the only variable. The aerodynamic effects of varying the afterbody angle from $30°$ to $40°$ are given in figure 8. The pitching-moment data, referenced about the apex of the CM and about the nominal c.g., are presented in figures 8(a), 8(b), and 8(c). The data for configurations C_2 and C_8 indicate that either can fulfill the basic entry requirements; however, the trim angle of attack ($\alpha \approx 147°$), which is required for $L/D \approx 0.5$, exposes the afterbody more on the C_8 configuration than on the C_2 configuration. Volumetric requirements precluded the use of C_9 and C_{10}; therefore, the C_2 configuration was retained for further evaluation.

Using the C_2 dimensions, tests were made to determine some effects of varying the heat-shield radius from 1.0d to 1.4d (fig. 9). For the range of heat-shield radii

tested, the data indicate that, within limits, the heat-shield radius has only a small effect on the aerodynamic characteristics. Thus, C_2 remained the prime configuration for further development.

L/D Improvement Studies

During the early test phases of the design and development of the Apollo CM, it became evident that the Z center-of-gravity restrictions, necessary to maintain the nominal L/D requirement of 0.5, would be difficult to satisfy. A brief study of several heat-shield modifications was made to determine if a reduced Z offset could be used to obtain an L/D of 0.5 with a minimum trim angle of attack of 147°. (The modification could have provided a solution to the problem if it had resulted in higher values of L/D versus angle of attack or in lower values of C_m versus angle of attack.) Typical of the configurations which were selected were a fixed flap on one side of the heat shield (C_{25}), corner modifications (C_{26} and C_{27}), and canted heat shields (C_{28} to C_{32}). As indicated by figure 10(a), all modifications reduced the trim angle of attack by 8° or more; however, the L/D values versus angle of attack were also reduced for all configurations except C_{25} and C_{27} (fig. 10(b)). Although C_{25} and C_{27} required smaller Z offsets to trim at $\alpha \leq 147°$, the improvement was considered minor compared to the structural, heat-protection, and other associated design requirements imposed by the modification. These considerations precluded further study of heat-shield modifications to improve the c.g. requirements.

Undesirable Trim Condition

As noted previously, the basic and the modified basic configurations (C and C_2) have an undesirable trim point (apex forward) near $\alpha = 40°$ to 80°. If the vehicle were to trim in this attitude at entry, portions of the CM would be subjected to heating conditions beyond the design capabilities of the heat protection provided. At subsonic velocities and low altitudes, probability of successful deployment of the earth-landing system would be compromised. A series of tests were made involving geometric modifications or additions to the basic CM in an attempt to eliminate the undesirable trim condition. These tests involved apex modifications such as blunted noses, an extended cylindrical nose, and a series of fixed and deflectable apex flaps. Heat-shield flap modifications were also tested. The addition of strakes to the CM was investigated, as was the use of apex-cover strakes. Finally, combinations of the CM and the escape tower were tested. Modifications, known as tower flaps, consisted of the addition of a plate or plates to the tower structure.

Some aerodynamic effects of modifying the apex of the CM are given in figure 11. The blunted apex configurations (C_{22} and C_{23}) did not materially affect the aerodynamic characteristics in the critical angle-of-attack range of undesirable trim. The extended cylindrical nose (C_{34}) did reduce the strength of the trim point while a half-cylindrical nose (C_{35}) eliminated the undesirable trim point completely. Since the

addition of the half-cylindrical nose would have involved redesign of the spacecraft, other possible modifications were studied.

Some effects of adding flaps at or near the apex of the CM are given in figures 12, 13, and 14. As previously noted, some of the flap configurations were deflectable while others were fixed additions or modifications to the basic CM configuration (fig. 2(e)). The only apex flaps that were effective in eliminating the undesirable trim point were CF_2 and C_2F_7 (figs. 12 and 14). (The reference c.g. for these data remains $\frac{x}{d} = -0.685$, $\frac{z}{d} = 0.059$.) The configuration CF_2 (fig. 2(e)) used a large deflectable surface. Design considerations of the support and deflecting mechanism of the CF_2 were a major problem, particularly in the nose area where the earth-landing system must be housed. The configuration C_2F_7 was considered a possible choice because it did eliminate the undesirable trim point.

Two heat-shield modifications (F_8 and F_{11}) were investigated (figs. 13, 14, and 15). The data obtained at $M = 0.7$, $M = 1.65$, and $M = 5.0$ indicate that neither of the two heat-shield flap configurations eliminated the undesirable trim point.

A preliminary test of the CM with strakes added was made at Mach numbers from 2.6 to 3.4 (fig. 16), although the subsonic Mach-number region was the most critical. The data of figure 16(b) indicate that the strake configuration (C_{15}) provides a destabilizing increment in pitching moment in the region of undesirable trim ($\alpha = 40°$ to $80°$). Additional tests were then initiated to determine an optimum strake configuration based on the preliminary results with C_{15}. Some of the configurations studied are given in figures 2(h) to 2(k), and results showing some aerodynamic effects may be found in figure 15 and figures 17 to 30. The data of figure 17, determined at $M = 0.7$, indicate that strakes are effective in providing a destabilizing increment in pitching moment in the critical angle-of-attack range of $40°$ to $80°$. The degree of effectiveness is dependent upon the configuration as indicated by figure 17(a). The data of figures 18 to 21 show some results for selected strake configurations at Mach numbers of 1.65 and 5.0, and the data indicate that the strakes eliminate the undesirable trim point at these Mach numbers. The pitching-moment coefficient provided by the strakes is indicated as being dependent upon the configuration. Note that the trim angle of attack with the heat shield forward ($\alpha \approx 147°$) is essentially unaffected by the addition of the strakes. The strake configurations studied indicated that a single strake in the yaw plane ($\phi = 90°$ to $270°$) would provide the required destabilizing pitching-moment coefficient; therefore, further studies were limited to modification features in the yaw plane.

Results of additional strake-configuration tests are given in figures 15 and 21. The pitching-moment coefficient data referenced to the c.g. indicate that the configurations provide a destabilizing pitching moment in the critical angle-of-attack range of $40°$ to $80°$, and that configuration L_{16} eliminates the undesirable trim condition.

The data for the strake configurations indicated that a tapered strake, located in the yaw plane and having a 12-inch span at the apex end and tapering to zero near the heat-shield corner, would provide the destabilizing increment in pitching-moment

coefficient throughout the flight Mach-number range. A detailed evaluation of the aerodynamic characteristics of the selected configurations $C_{38}L_{28}$ and $C_{29}L_{28}$ was then begun. These two configurations differed slightly in tower-leg wells. Static aerodynamic characteristics for this configuration are given in figures 23 to 26. The data presented in figures 23(a) and 24(a) indicate that the $C_{38}L_{28}$ configuration eliminates the undesirable trim point at all Mach numbers tested except the lowest subsonic Mach number ($M = 0.7$). Other studies indicate that data similar to the $M = 0.7$ data would exist at Mach numbers below $M = 0.7$.

In figures 25 and 26, the lateral-stability characteristics of the configuration are defined at selected Mach numbers and angles of attack. These data were needed to evaluate the fuel requirements of the attitude-control system and/or the c.g. adjustments necessary to maintain attitude during flight. The data were obtained under extremely adverse conditions in that the measured rolling-moment coefficients were, in some cases, of the same order of magnitude as the quoted balance accuracies. Analysis of the data indicated that fuel requirements would be significant if proper management of the c.g. was not maintained.

The oscillatory-stability characteristics of several early Apollo configurations are given in references 10 to 15. The only test data of this nature, available for the strake configuration, are presented in figure 27. These data were obtained by using limited-free-oscillation test techniques and are for supersonic Mach numbers only. The data show the configuration to have positive damping at supersonic Mach numbers for the conditions tested (angle of attack, k, R, and c.g.). Some preliminary studies indicated, however, that the CM with strakes would have negative damping at subsonic Mach numbers. Tests of the clean CM and of several strake configurations in the Langley Spin Tunnel (ref. 16) indicated that the CM would trim at an angle of attack of approximately 40° (apex forward). The tests also indicated that the CM was dynamically unstable with the heat shield forward, which resulted in large oscillation, tumbling, and spinning motions. The strake modifications in most cases eliminated the apex-forward trim condition but resulted in a tumbling condition when the model diverged from the apex-forward trim condition.

An apex-end or paddle strake was investigated. Preliminary static-stability studies at $M = 0.4$ indicated that both C_2L_{37} and C_2L_{38} were effective (fig. 28). Further evaluations of the C_2L_{37} configuration were then made at $M = 0.7$ and $M = 1.2$ (figs. 29 and 30). The data indicate that the paddle strake was effective in eliminating the undesirable trim point; however, preliminary dynamic-stability tests showed that the paddle strake was dynamically unstable and tumbled at subsonic speeds.

Another proposed solution to the apex-forward trim condition involved resequencing of the abort. Originally, in the event of an atmospheric abort, the tower-rocket combination would be jettisoned; the vehicle would stabilize with the heat shield forward; the apex cover would be jettisoned; and the earth-landing system would be deployed. The proposed resequencing involved the retention of the tower structure (after burnout, the escape rocket would be jettisoned). It was expected that the CM-tower combination would be statically unstable in the tower-forward attitude and that flow in and around the tower structure would provide the pitching moment to rotate the vehicle to a heat-shield-forward attitude. The tower structure was expected to provide positive damping to

reduce the ensuing oscillation. The tower and the apex cover would then be jettisoned, and the earth-landing system would be deployed. Tests were made of tower modifications (tower flaps) designed to provide additional pitching moment. Figures 31 and 32 show data for typical tower-flap configurations at $M = 0.4$ to $M = 3.5$ and indicate that the tower flap eliminates the undesirable trim condition in the $\alpha = 40°$ to $\alpha = 80°$ range. Results of tests at higher Mach numbers are given in figures 33 and 34. The configurations presented were chosen to give an indication of the range of variation available from the modifications investigated.

The CM-tower configuration alone is stable in the apex-forward attitude at $M = 6.0$ as indicated in figure 33. This reduced effectiveness of the CM-tower combination in overcoming the apex-forward trim condition is caused by a shock-interaction pattern which results in a shock impingement on the lower surface of the CM (fig. 3(f)). Some of the tower-flap configurations eliminate the undesirable trim condition. The data at $M = 10.0$ (fig. 34) indicate that the configuration $C_{38}T_{62}$ is effective in eliminating the undesirable trim condition, although the effectiveness is greatly reduced at the higher Mach numbers.

Tests were then initiated to define the oscillatory-stability characteristics of the tower-flap configuration, using the transverse-rod (free-to-tumble) test technique. Static pitching-moment coefficient data were measured to determine the support-interference effects. Results of these tests are given in figure 35. The data for subsonic Mach numbers ($M = 0.3$ to $M = 0.8$) are given in figure 36. The data indicate that the configuration has negative damping in the 100° to 240° angle-of-attack range. The configuration tumbled at all the Mach numbers tested.

CONCLUDING REMARKS

Investigations were made to provide data on the stability characteristics of the Apollo command module basic configuration. Subsequent studies were made to determine the effects which varying certain geometric dimensions (such as corner radius, afterbody angle, heat-shield radius, and nose radius) would have on the aerodynamic characteristics of the Apollo command module. An abbreviated study was made of several modifications of the Apollo command module which were designed to increase the trimmed lift-to-drag ratio without materially affecting the trimmed angle of attack or the center-of-gravity location. An extensive series of investigations was conducted on modifications designed to eliminate an undesirable trim condition (apex forward) of the Apollo command module.

Limited control of the trimmed angle of attack was obtained by varying the corner radius and the afterbody angle of the Apollo command module. Variations in the radius of the heat shield had little effect on the aerodynamic characteristics. Modifications designed to increase the lift-to-drag ratio, without materially affecting the center-of-gravity location and the trimmed angle of attack, were shown to be essentially ineffective.

The basic and modified basic configurations have an undesirable apex-forward trim point at angles of attack between 40° and 80°. This trim point was especially

prominent at subsonic speeds. The addition of selected strakes to the command module was effective in eliminating this undesirable trim condition, but the vehicle proved to be dynamically unstable with such additions. The Apollo command module and tower configuration without modifications did not eliminate the undesirable trim point. The addition of a plate or plates to the tower structure did result in eliminating the undesirable trim condition, but the configuration was not dynamically stable.

Manned Spacecraft Center
National Aeronautics and Space Administration
Houston, Texas, April 5, 1968
914-50-89-00-72

REFERENCES

1. Morgan, James R.; and Fournier, Roger H.: Static Longitudinal Aerodynamic Characteristics of a 0.07-Scale Model of a Proposed Apollo Spacecraft at Numbers of 1.57 to 4.65 (U). NASA TM X-603, 1961.

2. Pearson, Albin O.: Wind-Tunnel Investigation of the Static and Longitudinal Aerodynamic Characteristics of Models of Reentry and Atmospheric-Abort Configurations of a Proposed Apollo Spacecraft at Mach Numbers from 0.30 to 1.20 (U). NASA TM X-604, 1961.

3. Pearson, Albin O.: Wind-Tunnel Investigation of the Static Longitudinal Aerodynamic Characteristics of a Modified Model of a Proposed Apollo Atmospheric-Abort Configuration at Mach Numbers from 0.30 to 1.20 (U). NASA TM X-686, 1962.

4. Fournier, Roger H.; and Corlett, William A.: Aerodynamic Characteristics in Pitch of Several Models of the Apollo Abort System from Mach 1.57 to 2.16 (U). NASA TM X-910, 1964.

5. Moseley, William C., Jr.; and Martino, Joseph C.: Apollo Wind Tunnel Testing Program — Historical Development of General Configurations. NASA TN D-3748, 1966.

6. Moseley, William C., Jr.; Moore, Robert H., Jr.; and Hughes, Jack E: Stability Characteristics of the Apollo Command Module. NASA TN D-3890, 1967.

7. Moseley, William C., Jr.; and Hondros, James G.: Aerodynamic Stability Characteristics of the Apollo Launch Escape Vehicle. NASA TN D-3964, 1967.

8. Moseley, William C., Jr.; and Redd, Bass: Aerodynamic Stability Characteristics of the Apollo Launch Escape Vehicle (LEV) with Canard Surfaces Deployed. NASA TN D-4280, 1967.

9. Redd, Bass; Olsen, Dennis M.; and Barton, Richard L.: Relationship Between the Aerodynamic Damping Derivatives Measured as a Function of Instantaneous Angular Displacement and the Aerodynamic Damping Derivatives Measured as a Function of Oscillation Amplitude. NASA TN D-2855, 1965.

10. Boisseau, Peter C.: Low-Speed Static and Oscillatory Stability Characteristics of a Model of the Apollo Launch-Escape Vehicle and Command Module (U). NASA TM X-894, 1963.

11. Kilgore, Robert A.; and Averett, Benjamin T.: Wind-Tunnel Measurements of Some Dynamic Stability Characteristics of 0.055-Scale Models of Proposed Apollo Command Module and Launch-Escape Configurations at Mach Numbers from 2.40 to 4.65 (U). NASA TM X-769, 1963.

12. Averett, Benjamin T.; and Kilgore, Robert A.: Dynamic-Stability Characteristics of Models of Proposed Apollo Configurations at Mach Numbers from 0.30 to 1.20 (U). NASA TM X-912, 1964.

13. Averett, Benjamin T.; and Wright, Bruce R.: Some Dynamic Stability Characteristics of Models of Proposed Apollo Configurations at Mach Numbers from 1.60 to 2.75 (U). NASA TM X-971, 1964.

14. Averett, Benjamin T.: Dynamic-Stability Characteristics in Pitch of Models of Proposed Apollo Configurations at Mach Numbers from 0.30 to 4.63 (U). NASA TM X-1127, 1965.

15. Hodapp, A. E., Jr.; and Uselton, B. L.: Dynamic Stability Tests of a 0.045-Scale Apollo Command Module at Mach Numbers 2.5 through 6 and Mach Number 10 (U). AEDC-TDR-63-52, March 1963.

16. Lee, Henry A.; and Burk, Sanger M., Jr.: Low-Speed Dynamic-Model Investigation of Apollo Command Module Configurations in the Langley Spin Tunnel. NASA TN D-3888, 1967.

TABLE I. - TEST FACILITIES AND CAPABILITIES

(a) Continuous tunnels

Test facility	Size of test section	Mach number	Reynolds number range/ft
Ames Unitary Plan Wind Tunnel (Ames-U PWT)	11 by 11 ft 9 by 7 ft 8 by 7 ft	0.7 to 1.4 1.5 to 2.6 2.4 to 3.5	10^6 to 10^7 10^6 to 7×10^6 0.5×10^6 to 5×10^6
Ames 2-foot Transonic Wind Tunnel	2 by 2 ft	0 to 1.4	2.0×10^6 to 8.4×10^6
Arnold Engineering Development Center: Tunnel A (AEDC-A)	40 by 40 in.	1.5 to 6.0	0.3×10^6 to 9×10^6
Tunnel C (AEDC-C)	50 in. (diameter)	10.0	0.29×10^6 to 2.5×10^6
Jet Propulsion Laboratory 20-inch Supersonic Wind Tunnel (JPL-20 SWT)	18 by 20 in.	1.3 to 5.0	0.4×10^6 to 6×10^6
Twenty-one-inch Hypersonic Wind Tunnel (JPL-21 HWT)	21 by 15-to-28 in.	5.0 to 9.5	0.25×10^6 to 3.6×10^6
Langley Unitary Plan Wind Tunnel (2 test section)	4 by 4 ft	1.47 to 4.65	0.56×10^6 to 7.83×10^6
Langley 8-foot Transonic Pressure Tunnel	7.1 by 7.1 ft	0.2 to 1.3	2.5×10^6 to 5.05×10^6

TABLE I. - TEST FACILITIES AND CAPABILITIES - Concluded

(b) Intermittent tunnels

Test facility	Size of test section	Mach number	Reynolds number range/ft
North American Aviation Trisonic Wind Tunnel (NAA-TWT)	7 by 7 ft	0.2 to 3.5	5×10^6 to 14×10^6
North American Aviation Supersonic Aerophysics Laboratory (NAA-SAL)	16 by 16 in.	0.7, and 1.56 to 3.75	5×10^6 to 14×10^6

TABLE II. - MODELS AND TEST RANGES

Model	Scale	Facility	Mach number range	Reynolds number range $\times 10^{-6}$ (a)	Angle of attack range, deg	Dynamic pressure, lb/ft^2
FS-1	0.02	Ames 2 × 2 TWT	0.4 to 1.35	0.92 to 2.12	-2 to 184	--
		JPL-20 SWT	1.65 to 5.01	.724 to 1.17	-25 to 184	300 to 574
		JPL-21 HWT	5.0 to 9.0	.290 to .884	-20 to 200	440
		NAA-SAL	1.575 to 3.27	.539 to 1.16	-10 to 190	270 to 984
FS-2	0.105	Ames-UPWT	0.5 to 3.5	3.4 to 7.14	-15 to 195	--
		NAA-TWT	.4 to .7	11.0 and 13.2	40 to 80	661 to 1880
FS-3	0.045	AEDC-A and C	4.0 to 10.0	1.31 to 2.43	-15 to 205	49.75 to 1850
FD-2	0.055	Langley-UPWT	2.4 to 4.65	1.05 to 3.39	134 to 158	175 to 556
FD-5	0.045	AEDC-A	1.5 to 6.0	0.31 to 3.26	15 oscillation amplitude	54 to 646
FD-6	0.10	Ames 12-ft	0.3 to 0.8	1.14 to 5.28	Free-to-tumble	129 to 366

[a]Based on model diameter.

TABLE III. - ACCURACY OF WIND-TUNNEL-FACILITY DATA

Reynolds number	Mach number	Coefficient							
		C_m	C_N	C_A	C_L	C_D	C_Y	C_n	C_l
AEDC-A									
2.43×10^{-6}	4	±0.0075	±0.021	±0.028	±0.018	±0.031	±0.008	±0.002	±0.003
2.13	5	±.0086	±.027	±.034	±.029	±.038	--	--	--
2.01	6	±.0085	±.030	±.079	±.043	±.078	±.032	±.003	±.020
.58	6	±.008	±.014	±.022	--	--	--	--	--
1.63	6	±.006	±.010	±.014	--	--	--	--	--
AEDC-C									
1.31×10^{-6}	10	±0.0049	±0.014	±0.015	±0.015	±0.014	±0.011	±0.008	±0.004
.18	10	±.020	±.056	±.037	--	--	--	--	--
.69	10	±.004	±.013	±.023	--	--	--	--	--
AMES-UPWT									
--	--	±0.006	±0.008	±0.008	±0.008	±0.008	±0.0099	±0.0035	±0.0035
JPL-20 SWT and 21 HWT									
--	--	±0.0001	±0.006	±0.005	±0.005	±0.010	--	--	--
NAA-TWT									
5.0×10^{-6}	0.4	±0.0033	±0.0037	±0.0054	±0.0054	±0.0041	--	--	--
6.6	.4	±.005	±.007	±.008	±.007	±.010	--	--	--
11.3	.4	±.002	±.0025	±.0029	±.0027	±.0029	--	--	--
8.1	.7	±.004	±.005	±.004	±.003	±.005	--	--	--
13.0	.7	±.0015	±.0019	±.0022	±.0019	±.0022	--	--	--
9.6	1.2	±.002	±.003	±.002	±.002	±.004	--	--	--
14.2	1.2	±.0011	±.0014	±.0016	±.0017	±.0017	--	--	--

TABLE IV. - SUMMARY OF TEST DATA

Figure number	Mach number range	Angle-of-attack range, deg	Nature of investigation
4	0.4 to 1.35	-10 to 185	Static — basic configuration
5	1.575 to 3.27	-25 to 190	Static — basic configuration
6	3.99 to 9.0	-20 to 198	Static — basic configuration
7	1.65 to 9.0	124 to 180	Static — parametric
8	1.65 to 9.0	124 to 180	Static — parametric
9	1.65 to 9.0	124 to 180	Static — parametric
10	7.3	123 to 178	Static — L/D improvement
11	.7	-8 to 88	Static — trim problem apex modifications
12	.7	-8 to 88	Static — trim problem flap configurations
13	.7	0 to 165	Static — trim problem flap configurations
14	1.65 and 5.0	0 to 168	Static — trim problem flap configurations
15	2.6 to 3.4	46 to 175	Static — trim problem strake configurations
16	.7	-8 to 88	Static — trim problem strake configurations
17	1.65 and 5.0	0 to 168	Static — trim problem strake configurations
18	5.0	40 to 168	Static — trim problem strake configurations
19	1.65 and 5.0	0 to 168	Static — trim problem strake configurations
20	1.65 and 5.0	0 to 168	Static — trim problem strake configurations
21	.4	39 to 94	Static — trim problem strake configurations
22	.7	35 to 120	Static — trim problem flap and strake configurations
23	.7 to 3.4	-15 to 194	Static — trim problem strake configurations
24	4.0 to 10.0	-20 to 205	Static — trim problem strake configurations

TABLE IV. - SUMMARY OF TEST DATA - Concluded

Figure number	Mach number range	Angle-of-attack range, deg	Nature of investigation
25	0.7 to 3.0	0 to 150	Lateral stability strake configurations
26	4.0 to 10.0	0 to 155	Lateral stability strake configurations
27	1.5 to 6.0	138 to 148	Dynamic — strake configurations
28	.4	-15 to 180	Static — apex strake configurations
29	.7	-10 to 182	Static — apex strake configurations
30	1.2	-15 to 176	Static — apex strake configurations
31	.4 to 3.5	-3 to 158	Static — tower flap configurations
32	.5 to 3.0	-15 to 360	Static — tower flap configurations
33	6.0	-5 to 25	Static — tower flap configurations
34	10.0	-118 to 118	Static — tower flap configurations
35	.3 to .8	0 to 360	Static — tower flap support interference effects
36	.3 to .8	0 to 360	Dynamic — tower flap, free to tumble

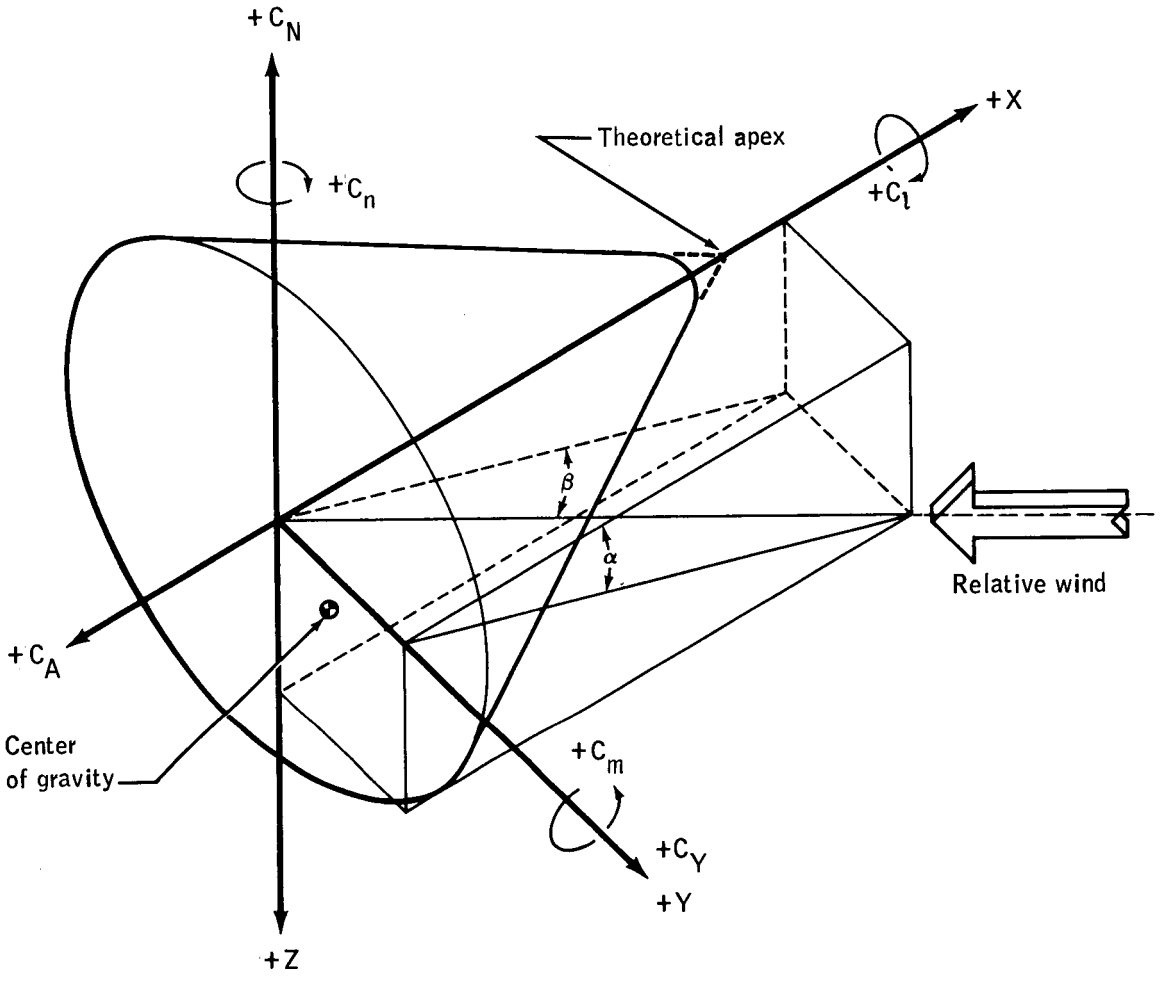

Figure 1.- Sketch showing body system of axes.

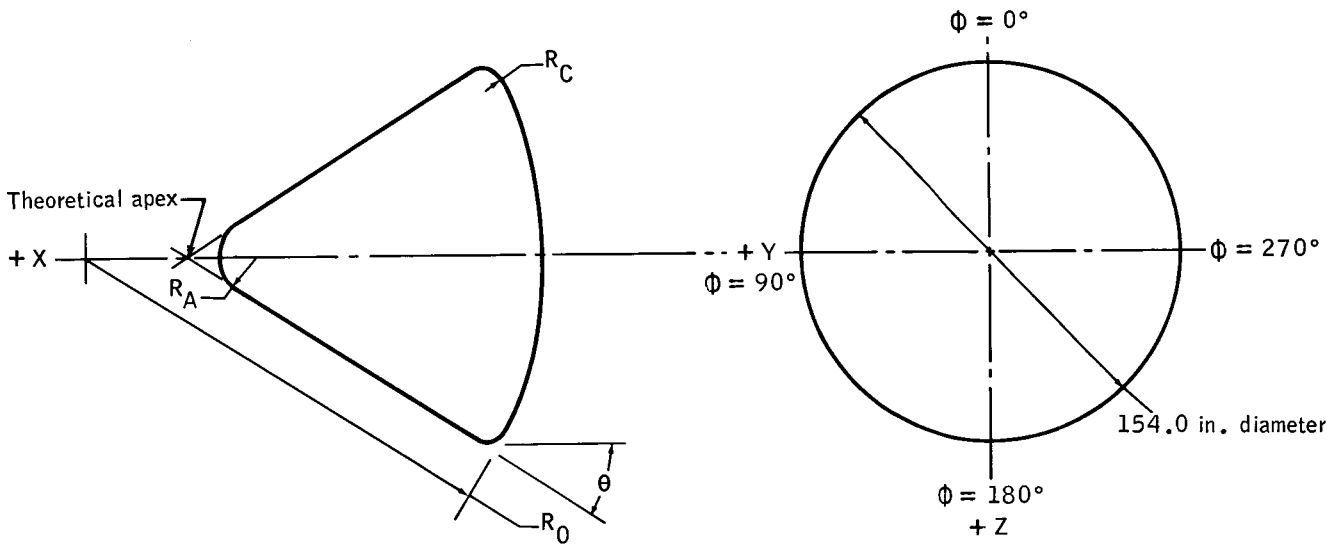

Command module	θ, deg	R_A, in.	R_C, in.	R_0, in.
C	33	15.4	7.7	184.8
C_2		9.152	7.7	
C_3			0.0	
C_4			15.4	
C_5			23.1	184.8
C_6			7.7	154.0
C_7	33			215.6
C_8	30			184.8
C_9	36			184.8
C_{10}	40	9.152	7.7	184.8

(a) Basic configuration with geometric modifications.

Figure 2.- Command module test-model configurations. (Full scale dimensions are in inches.)

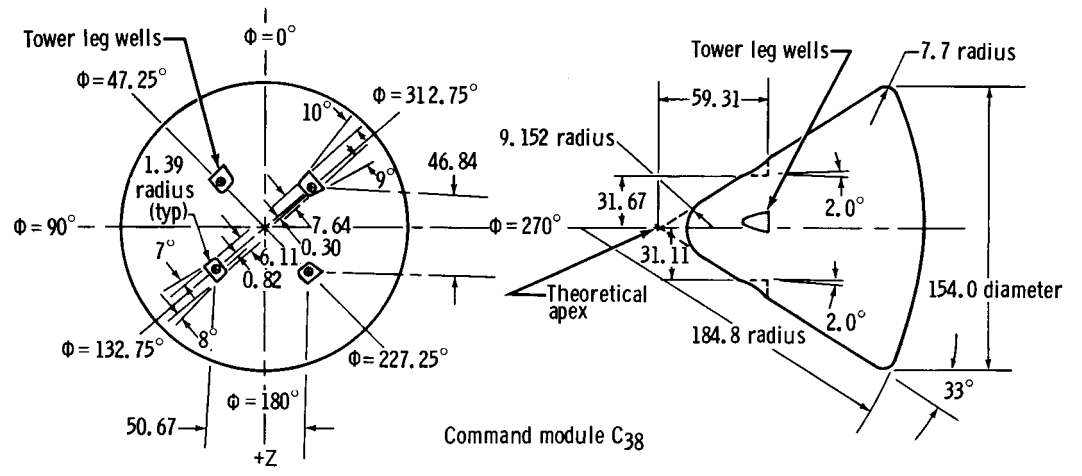

Command module C_{38}

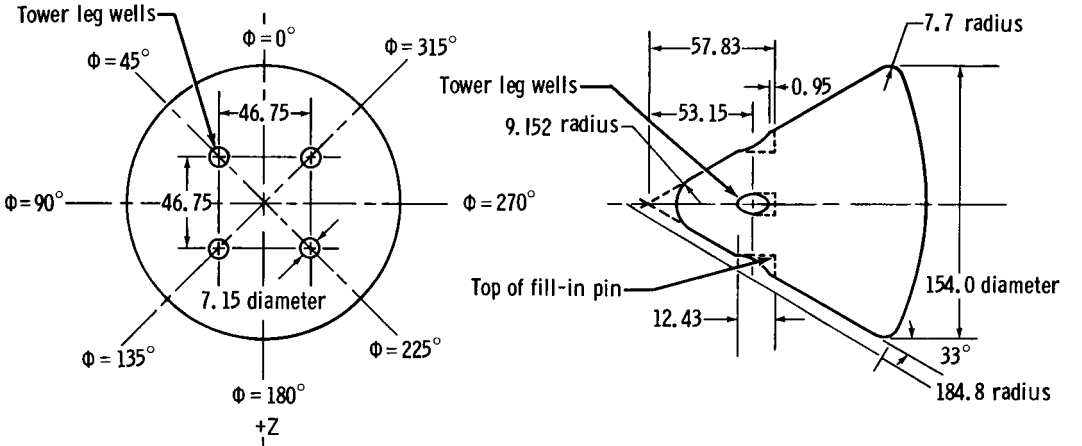

Command module C_{39}

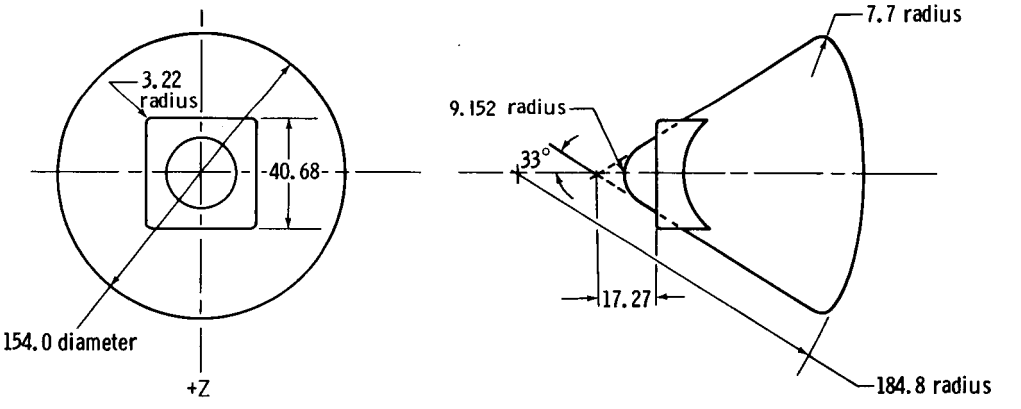

Command module C_{41}

(b) Surface modifications (C_{38}, C_{39}, and C_{41}).

Figure 2. - Continued.

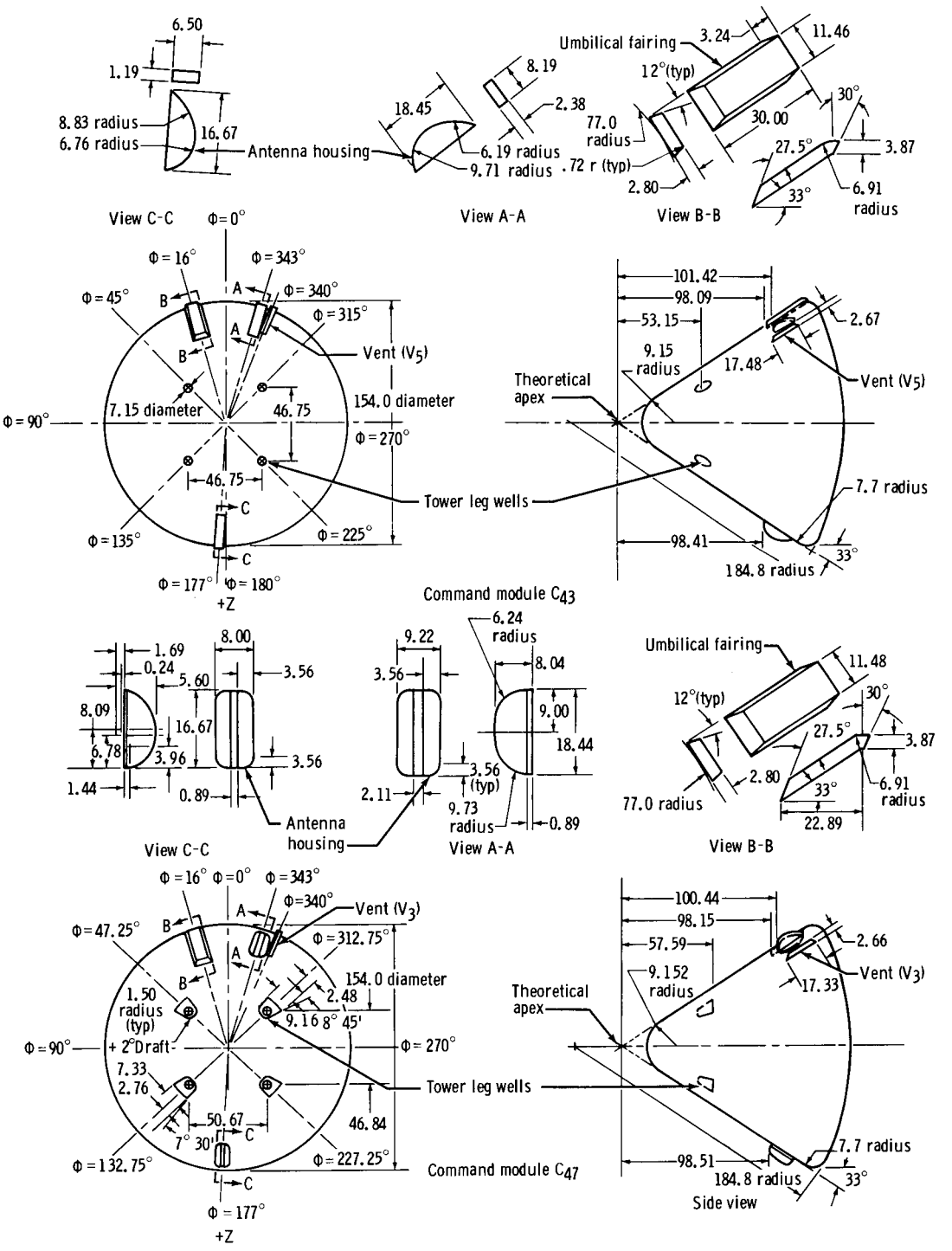

(c) Surface modifications (C_{43} and C_{47}).

Figure 2. - Continued.

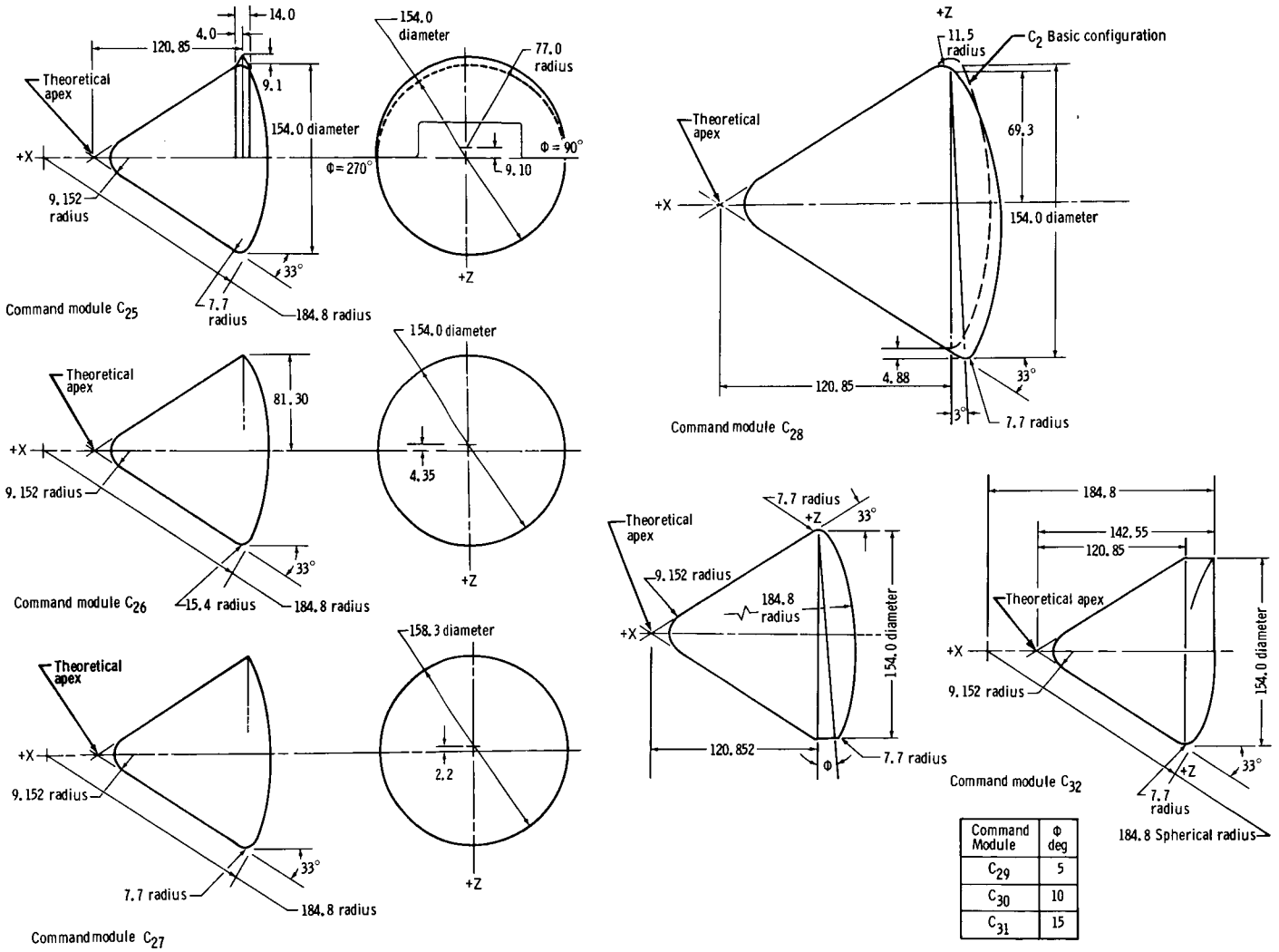

Command Module	Φ deg
C_{29}	5
C_{30}	10
C_{31}	15

(d) Canted heat shields and other modifications tested in L/D investigations.

Figure 2. - Continued.

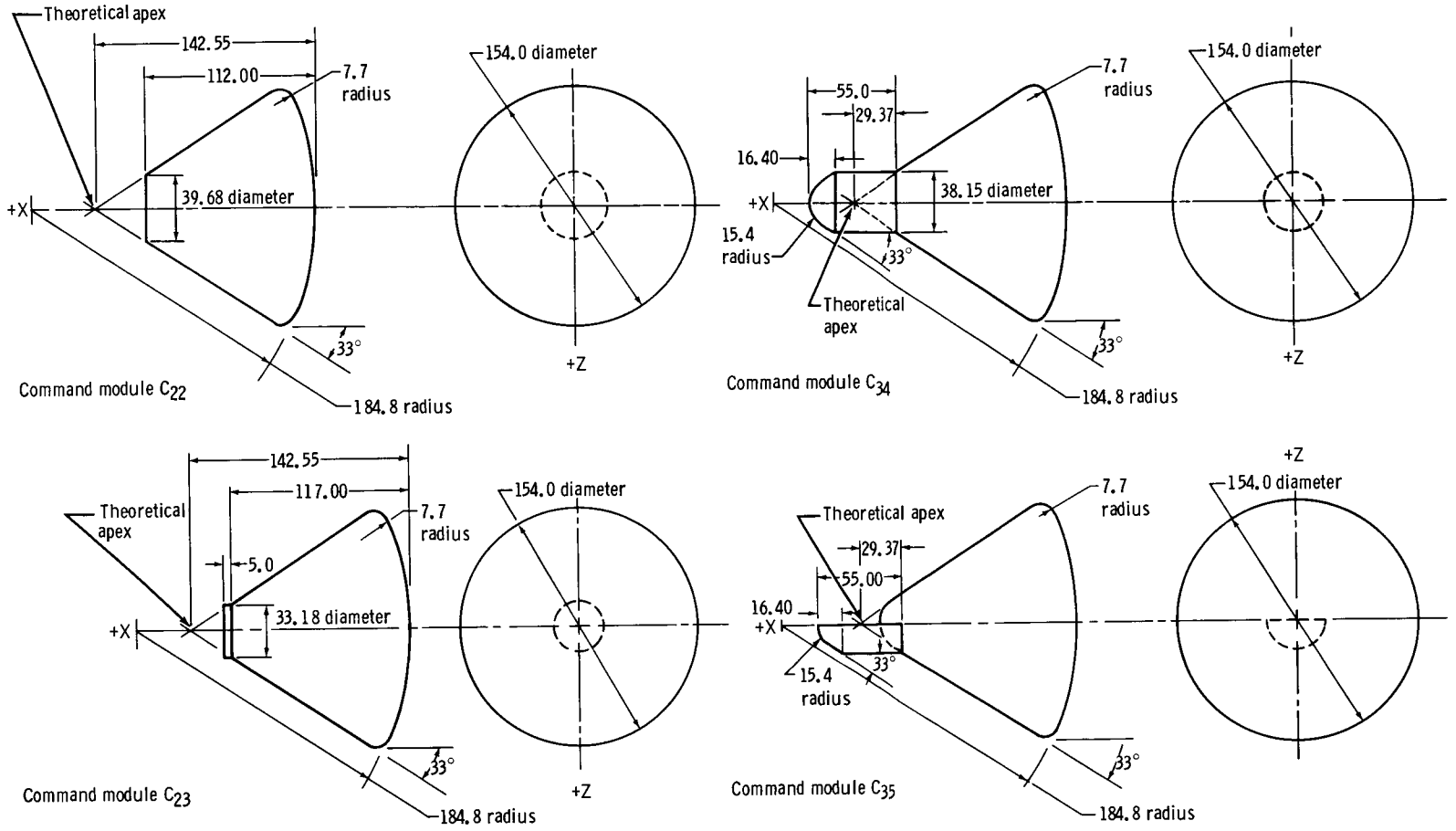

(e) Apex modifications used in trim-point investigations.

Figure 2. - Continued.

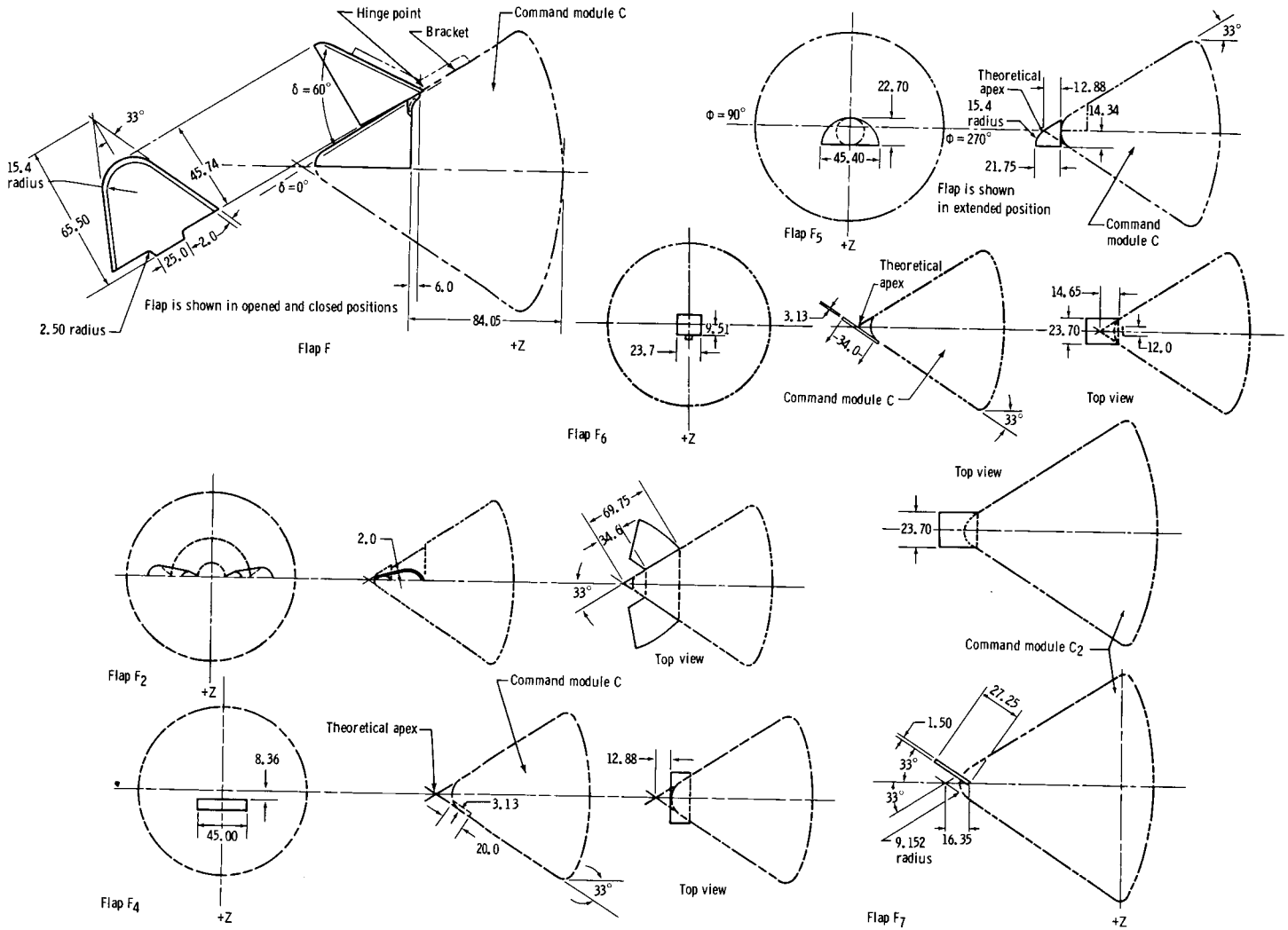

(f) Flap configurations (F to F_7).

Figure 2. - Continued.

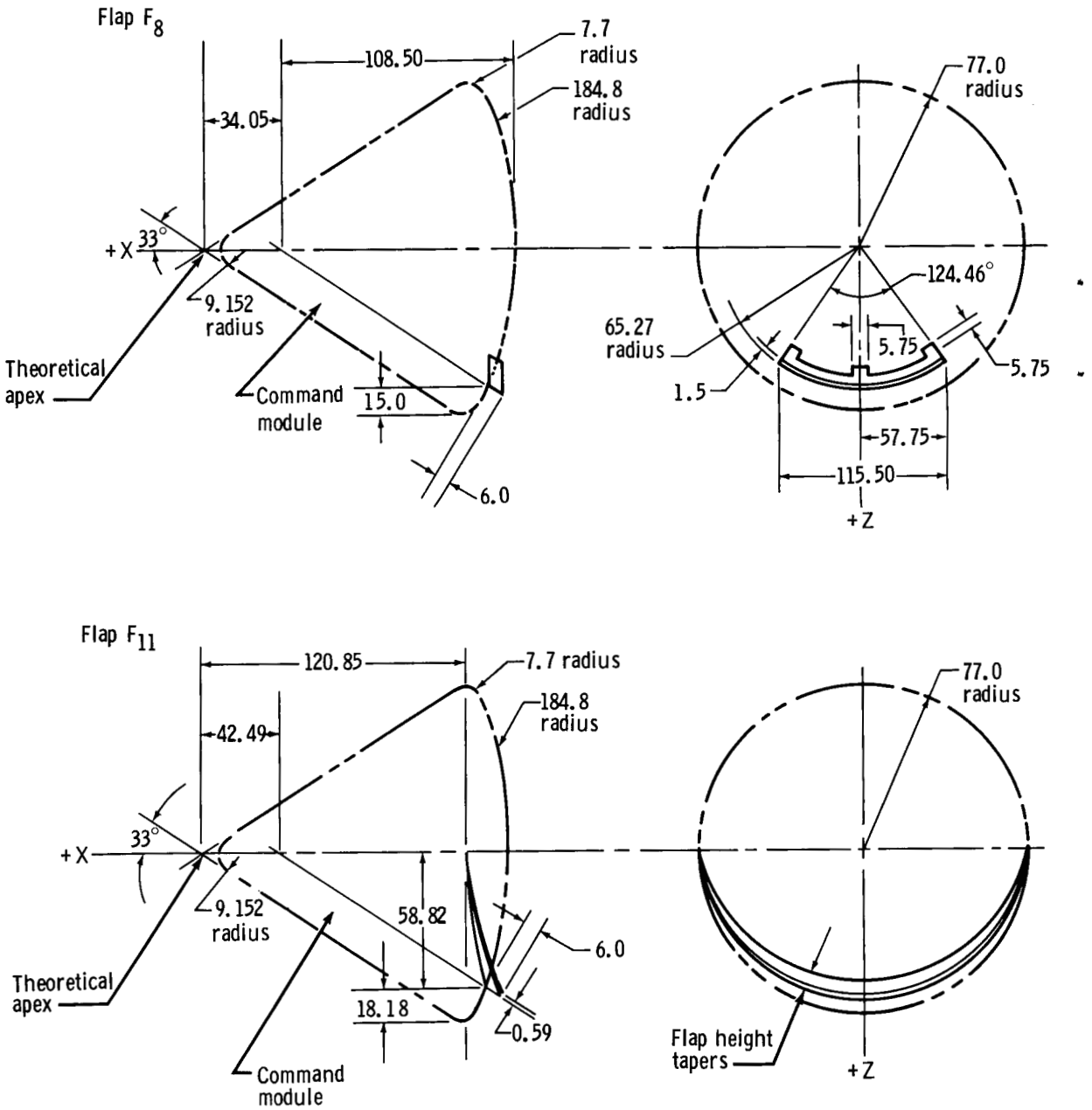

(g) Flap configurations (F_8 and F_{11}).

Figure 2. - Continued.

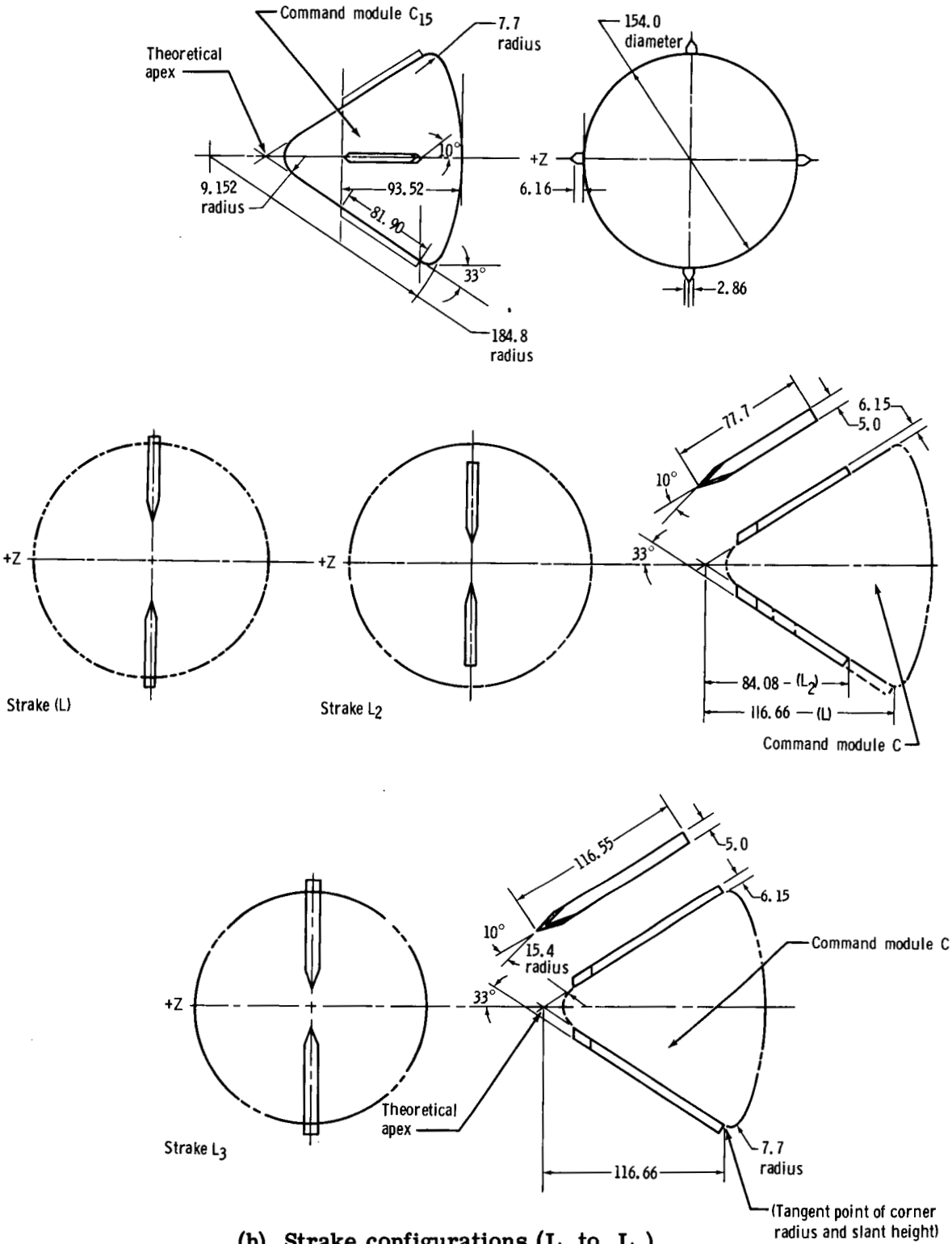

(h) Strake configurations (L to L_3).

Figure 2. - Continued.

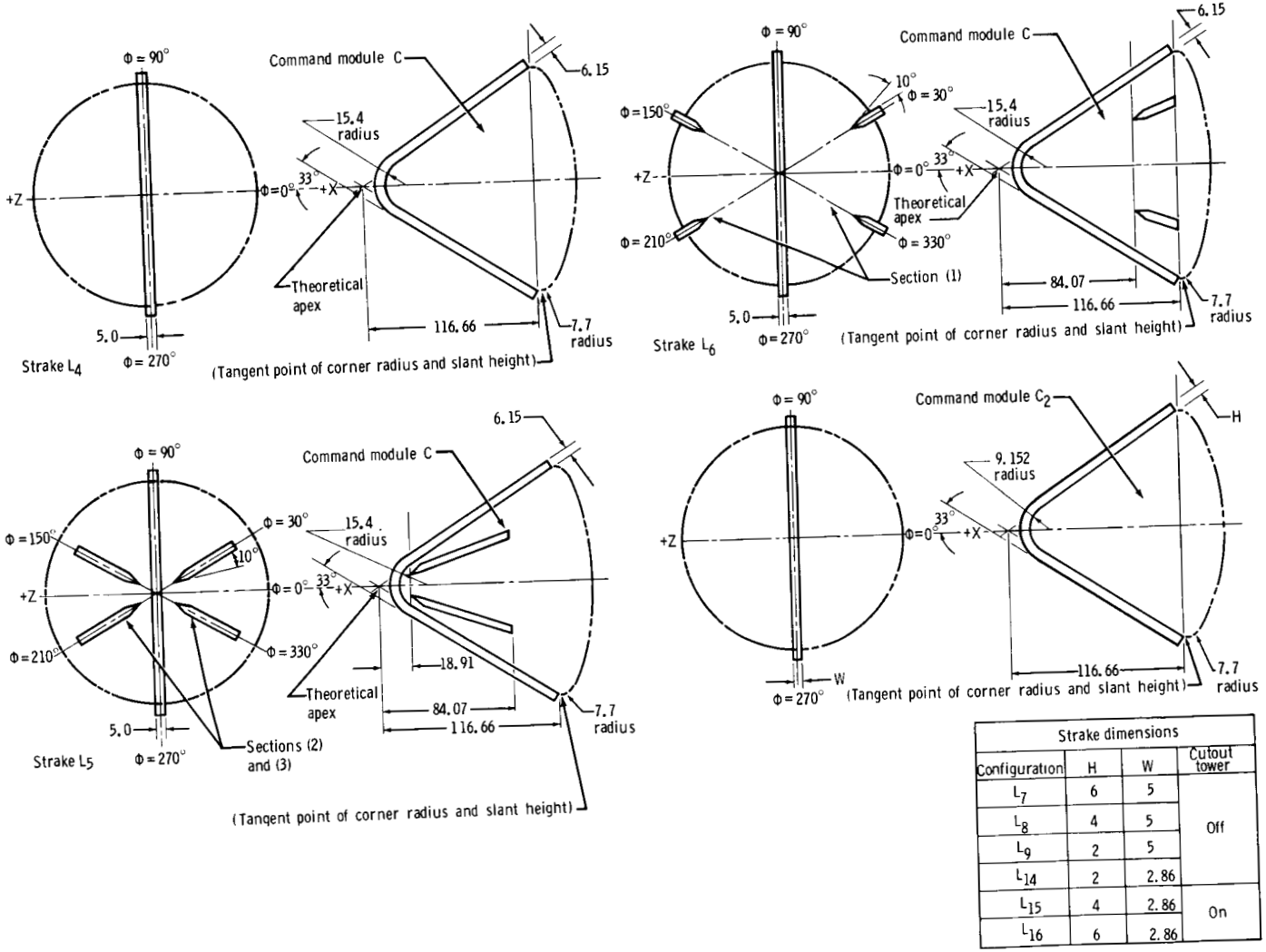

Strake dimensions			
Configuration	H	W	Cutout tower
L_7	6	5	Off
L_8	4	5	
L_9	2	5	
L_{14}	2	2.86	
L_{15}	4	2.86	On
L_{16}	6	2.86	

(i) Strake configurations (L_4 to L_9 and L_{14} to L_{16}).

Figure 2.- Continued.

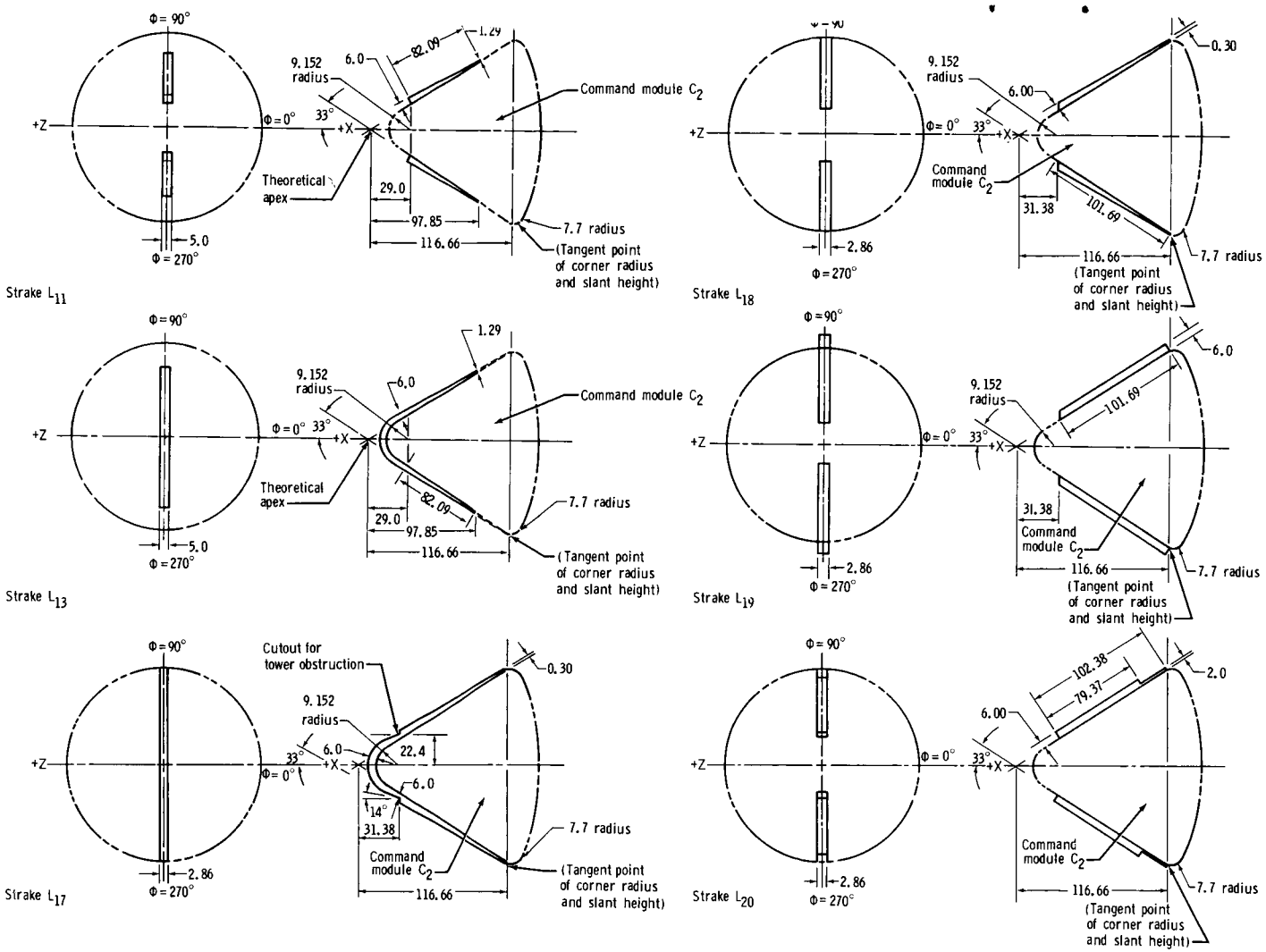

(j) Strake configurations (L_{11}, L_{13}, and L_{17} to L_{20}).

Figure 2. - Continued.

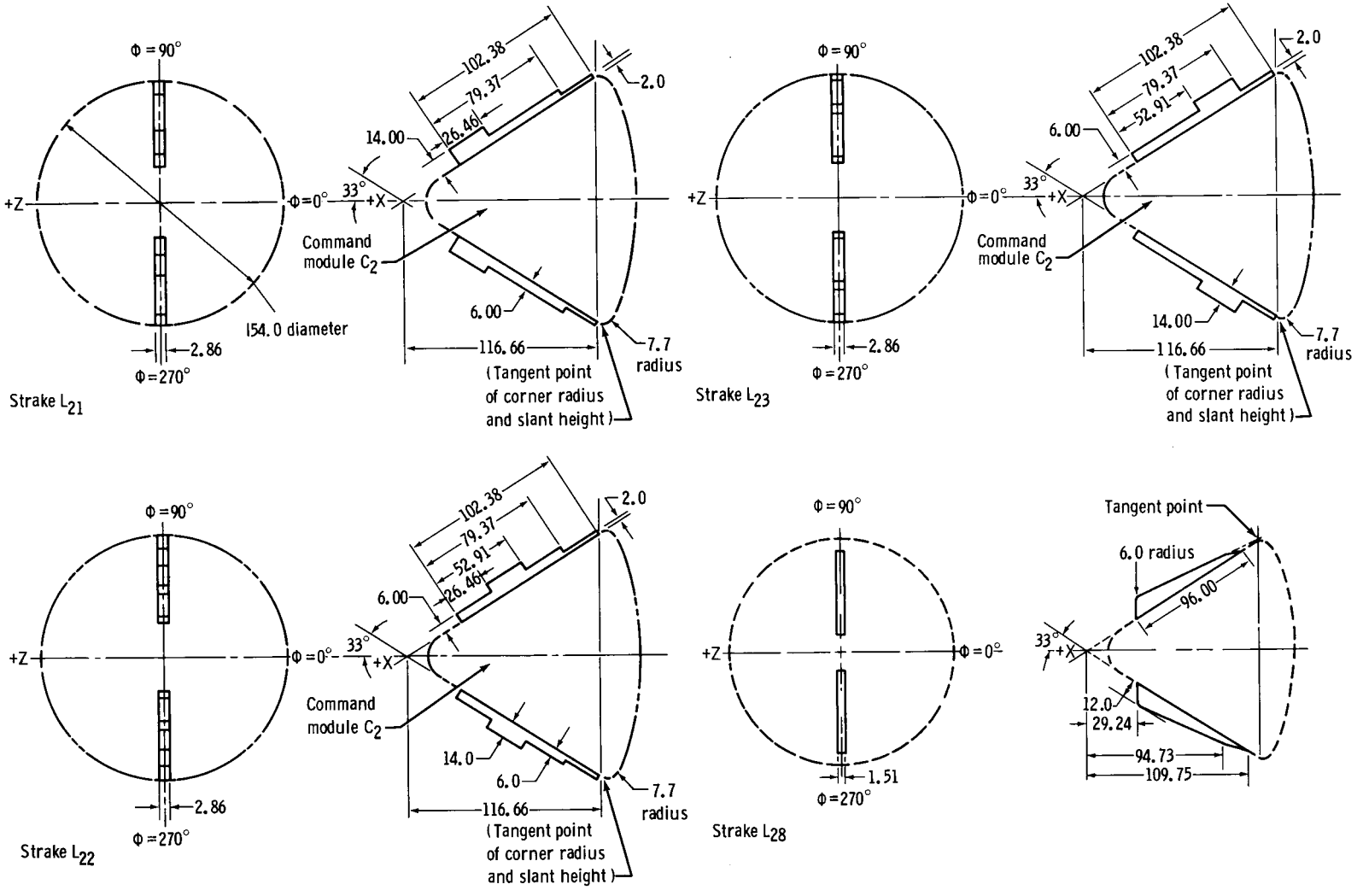

(k) Strake configurations (L_{21} to L_{23}, and L_{28}).

Figure 2. - Continued.

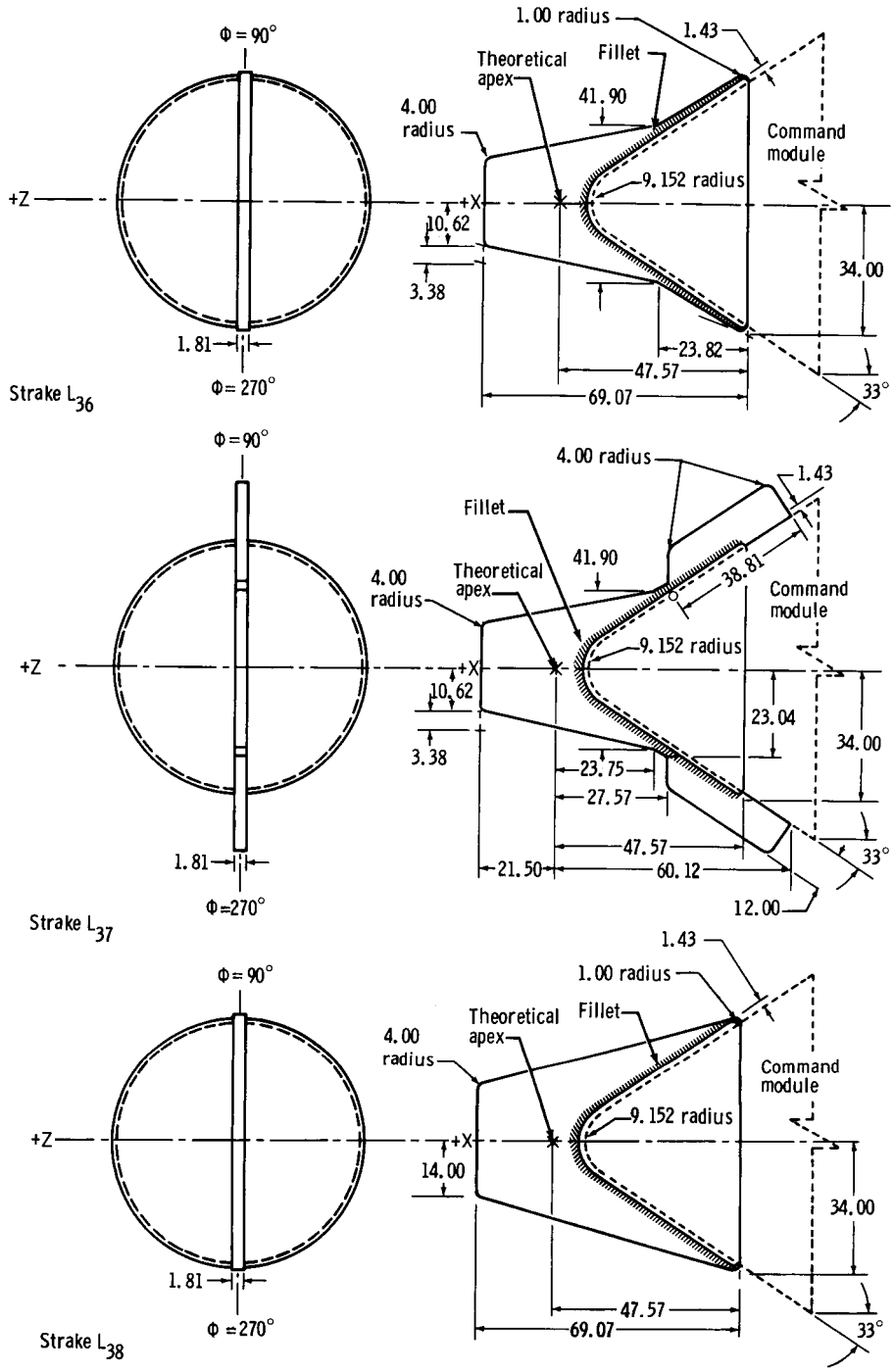

(l) Strake configurations (L_{36} to L_{38}).

Figure 2. - Continued.

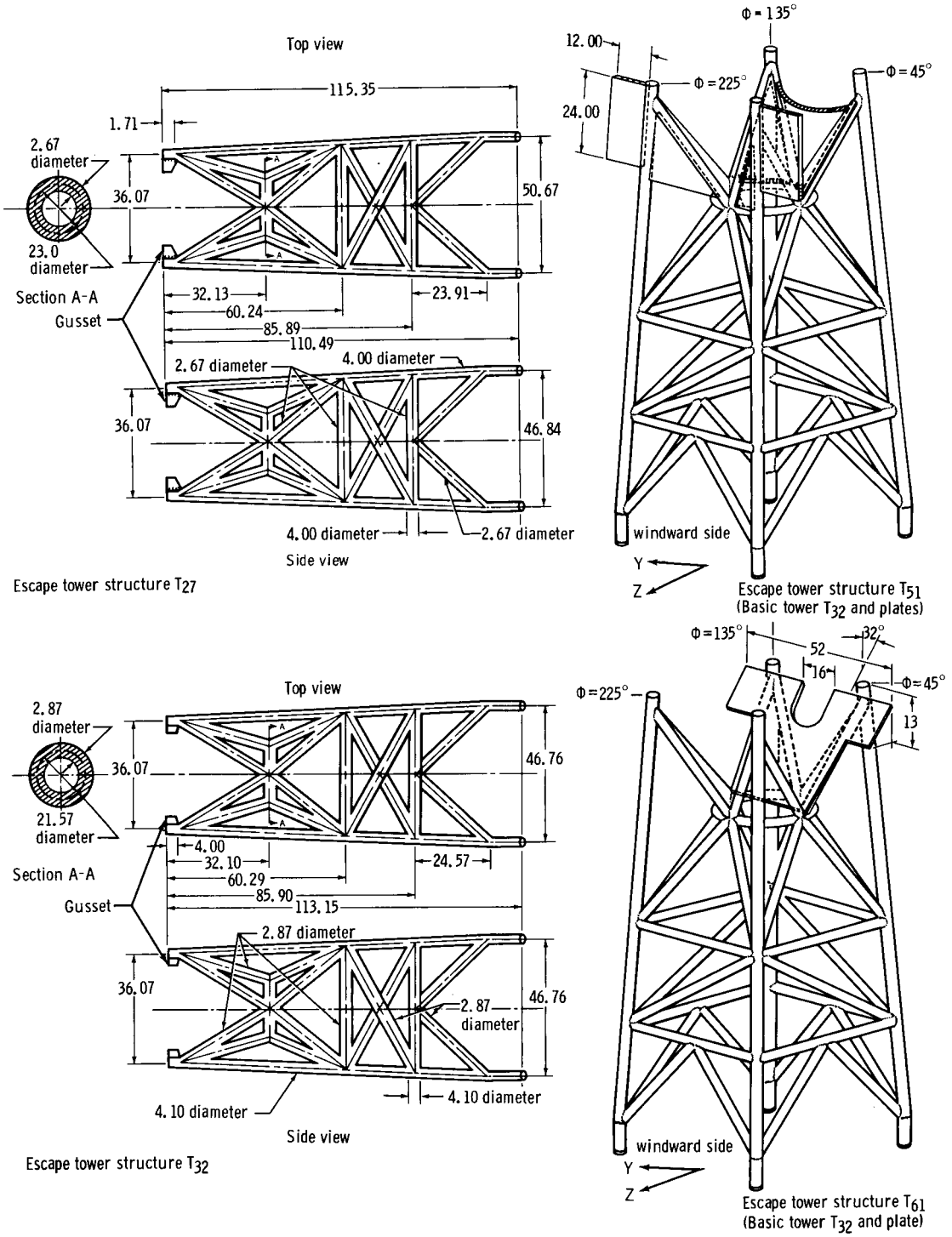

(m) Escape-tower structures (T_{27}, T_{32}, T_{51}, and T_{61}).

Figure 2. - Continued.

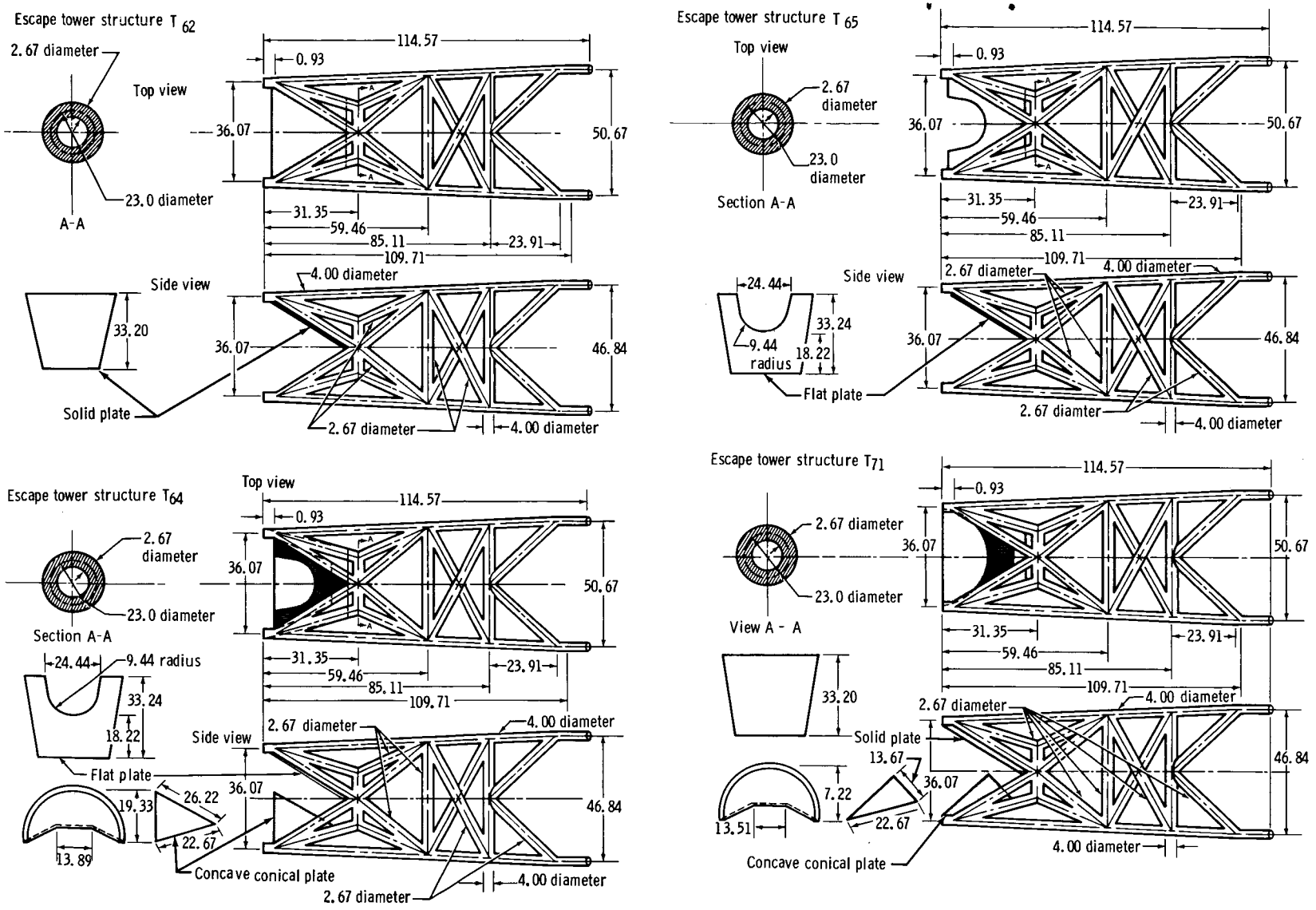

(n) Escape-tower structures (T_{62}, T_{64}, T_{65}, and T_{71}).

Figure 2. - Continued.

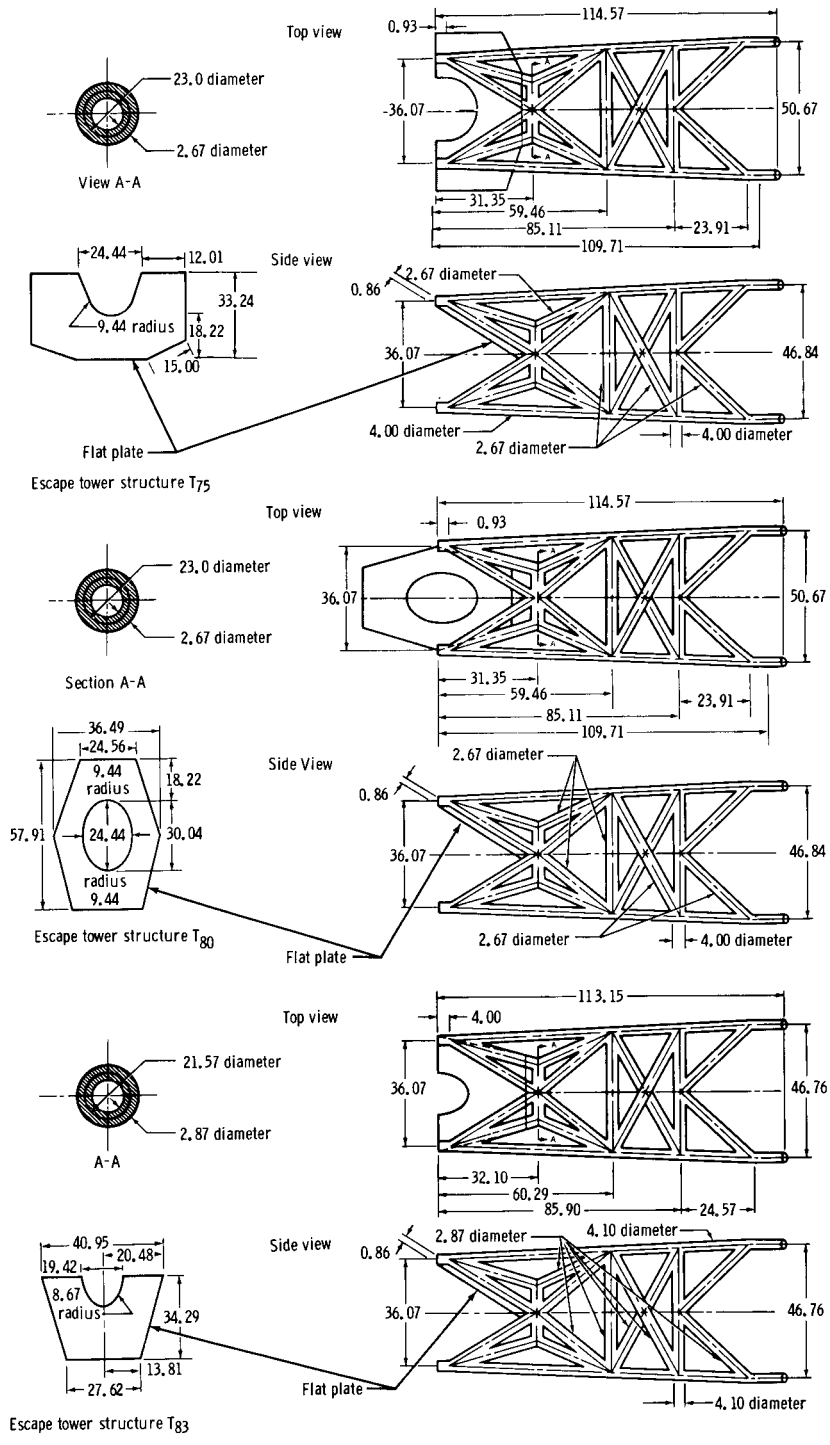

(o) Escape-tower structures (T_{75}, T_{80}, and T_{83}).

Figure 2. - Concluded.

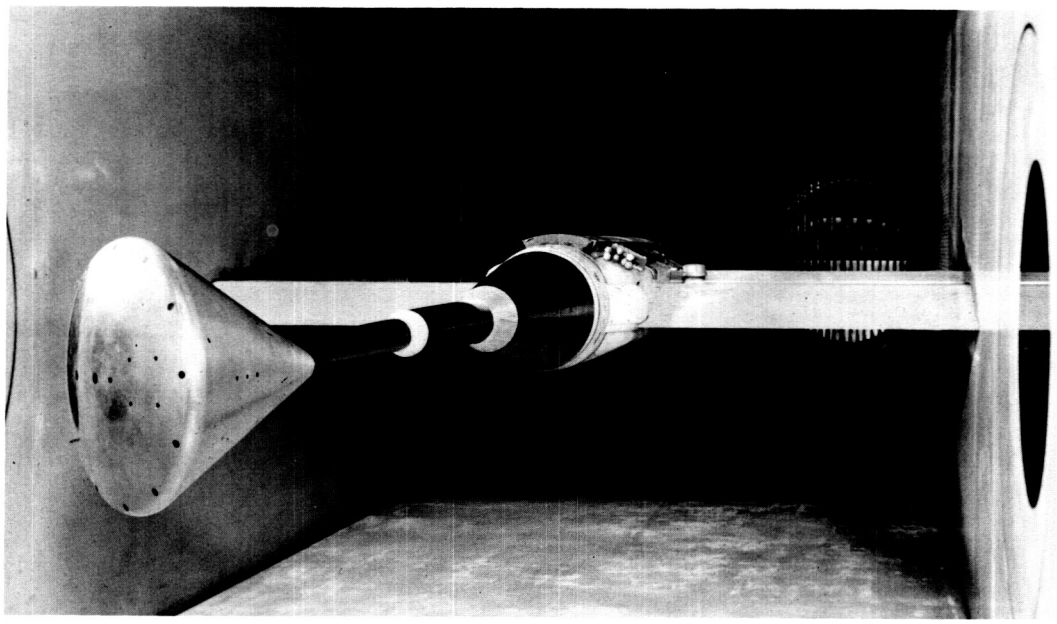

(a) Photograph of 0.105-scale model in the 9- by 7-foot test section of the Ames-UPWT (configuration C_2).

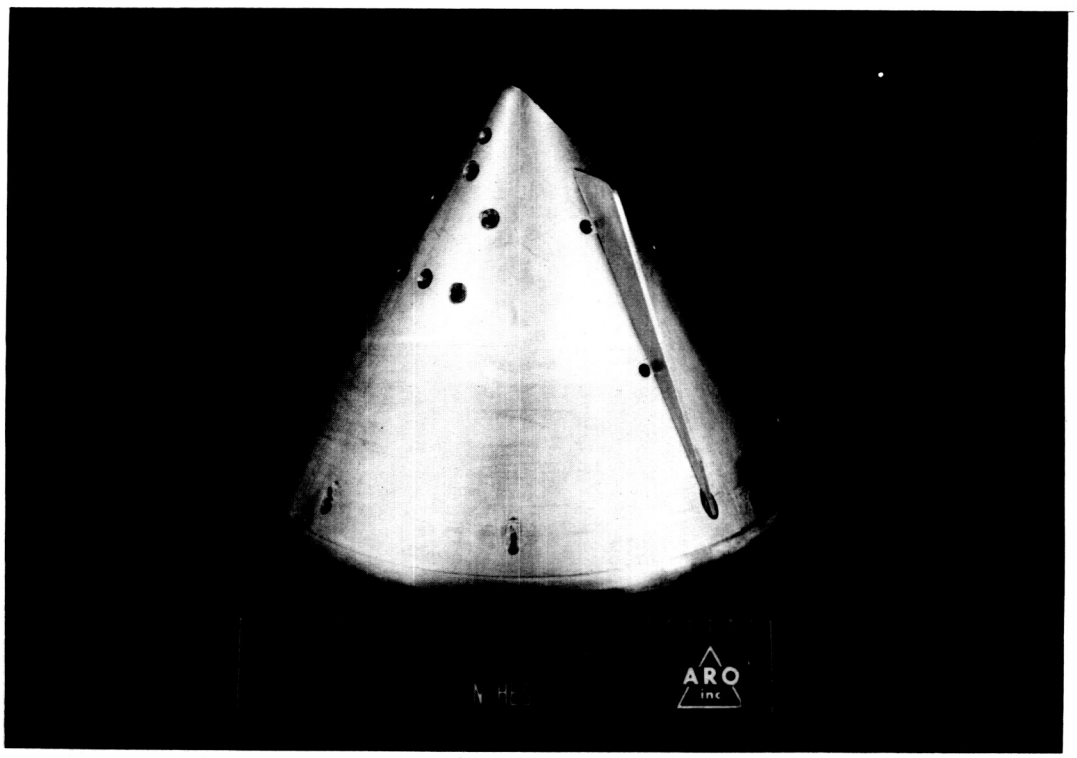

(b) Photograph of 0.045-scale model with strakes (configuration $C_{38}L_{28}$).

Figure 3. - Typical wind-tunnel test models of the Apollo command module.

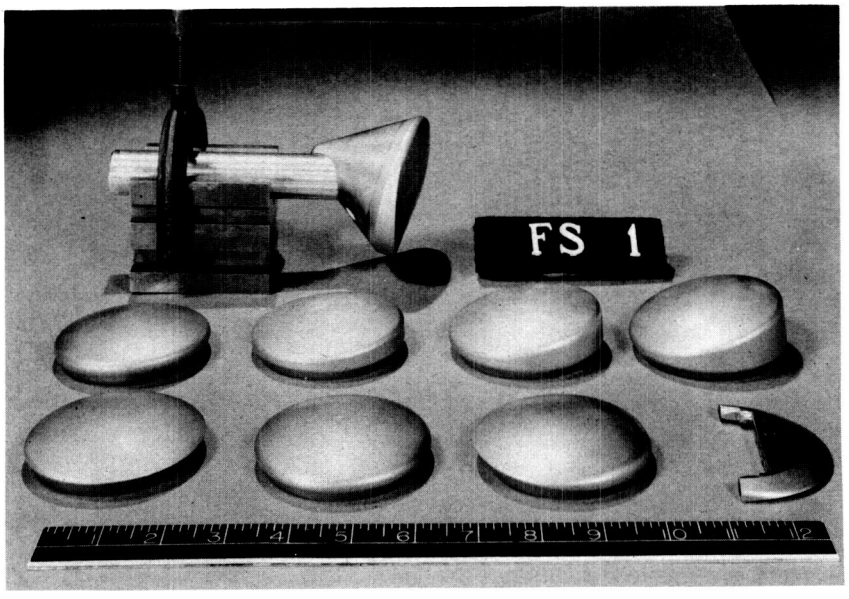

(c) Photograph of 0.02-scale model, showing various modifications tested for lift-to-drag ratio improvement.

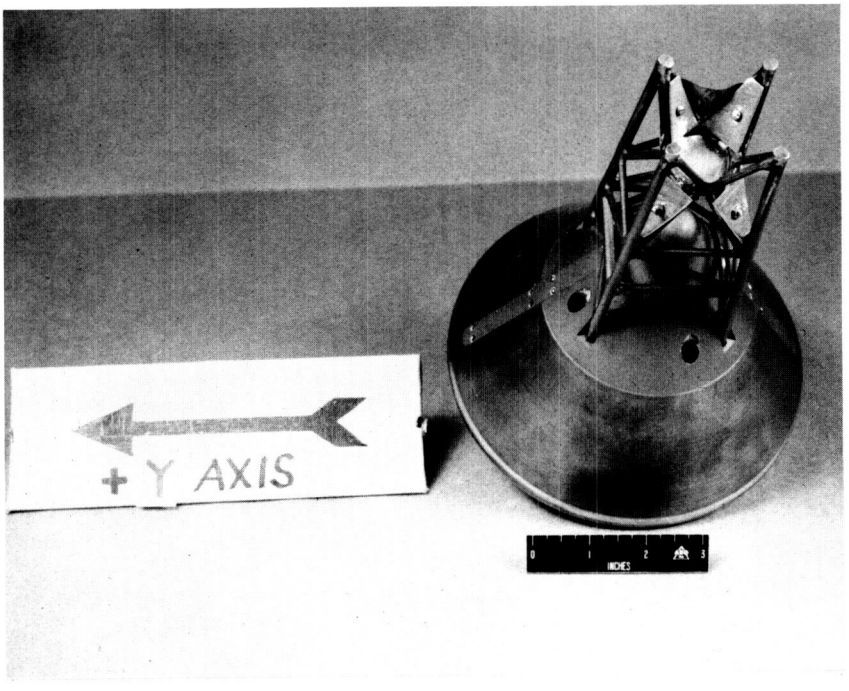

(d) Photograph of 0.045-scale model of Apollo command module and escape-tower structure (configuration $C_{38}T_{62}$).

Figure 3. - Continued.

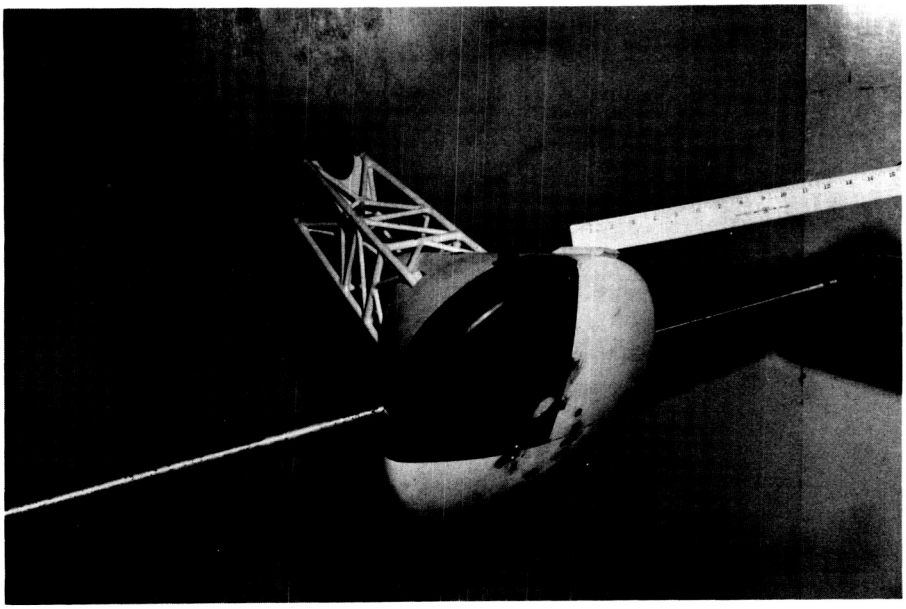

(e) Photograph of 0.10-scale model of the command module and escape-tower structure (configuration $C_{47}V_3T_{65}$) mounted on transverse rod in the Ames 12-foot facility.

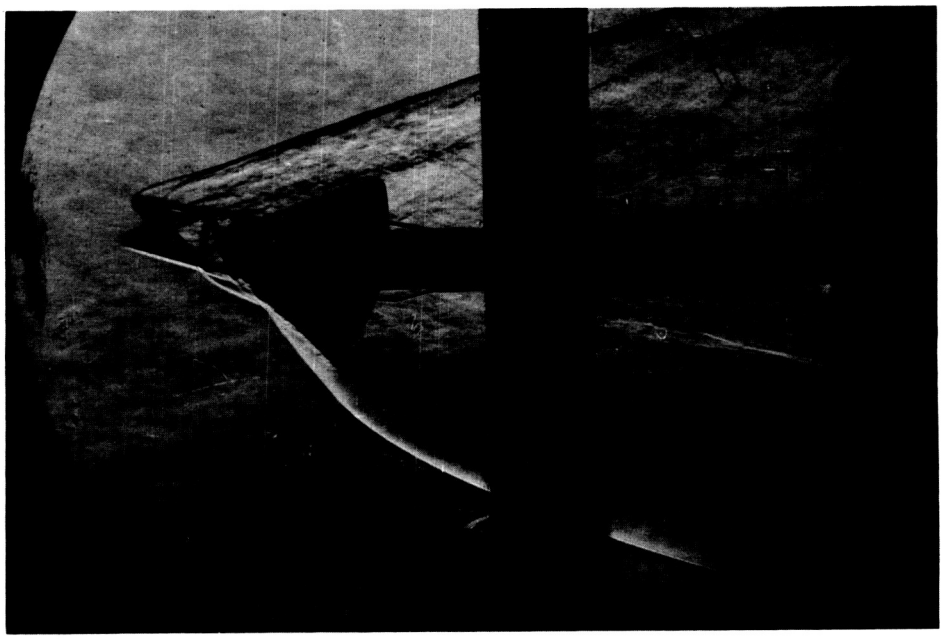

(f) Schlieren photograph of 0.045-scale model of the command module and escape-tower structure (configuration $C_{38}T_{64}$) in the AEDA-A facility at $\alpha = 15°$, $M = 6.0$.

Figure 3. - Concluded.

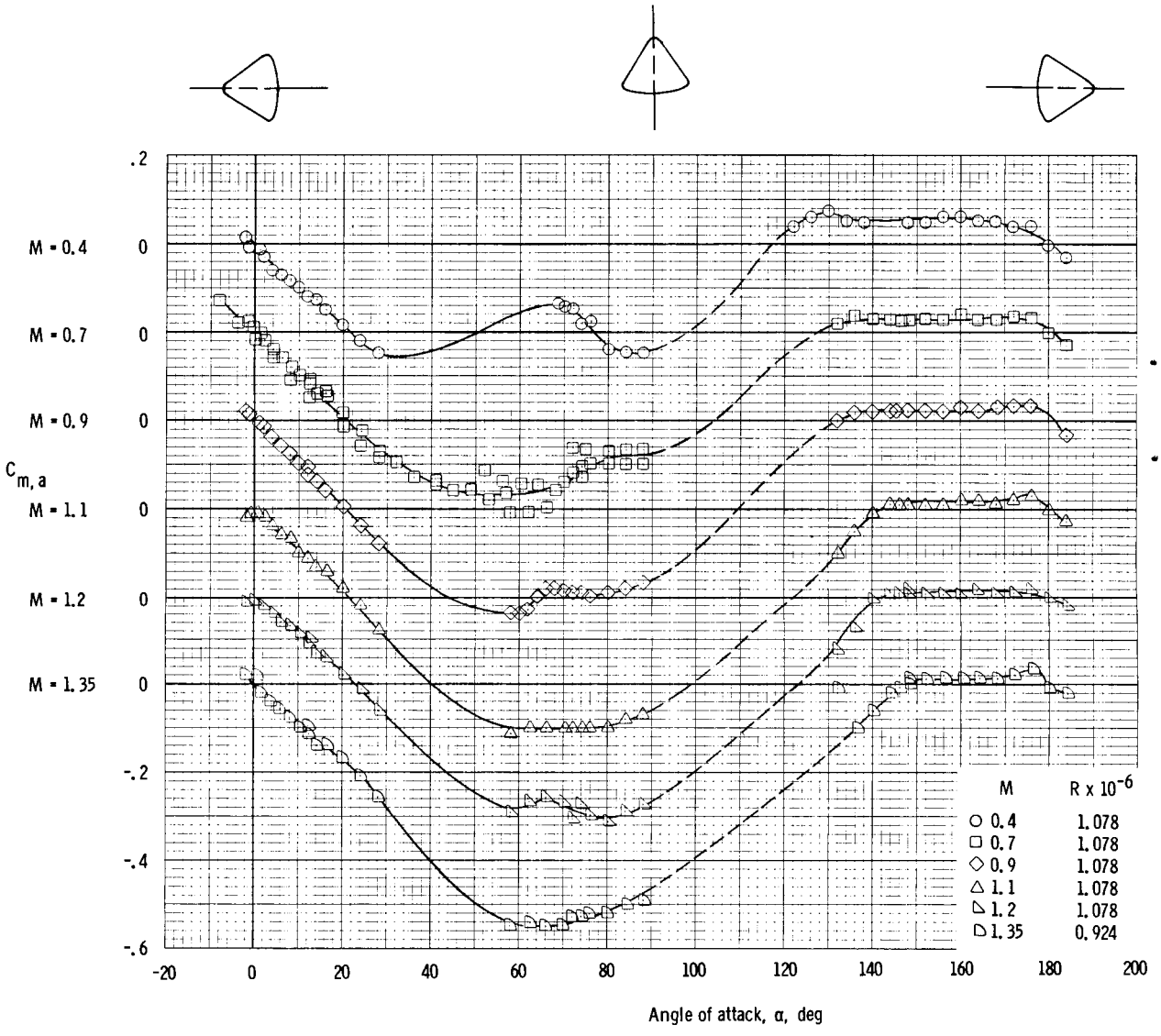

(a) Pitching-moment coefficient (apex).

Figure 4. - Aerodynamic characteristics of the Apollo command module (configuration C) obtained at Ames 2- by 2-foot TWT facility at M = 0.4 to M = 1.35 (c.g. = x/d = -0.685, z/d = 0.059).

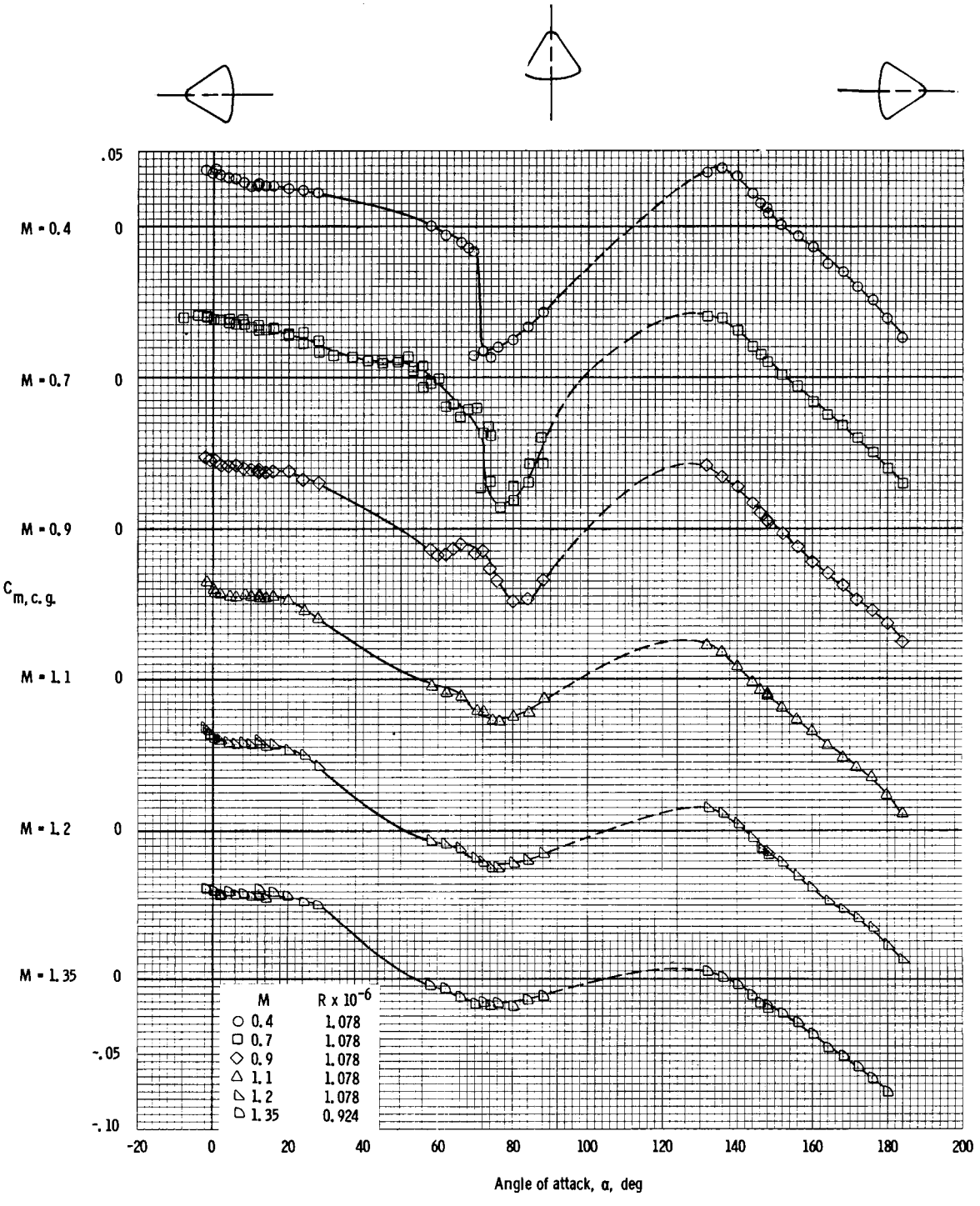

(b) Pitching-moment coefficient (c.g.).

Figure 4. - Continued.

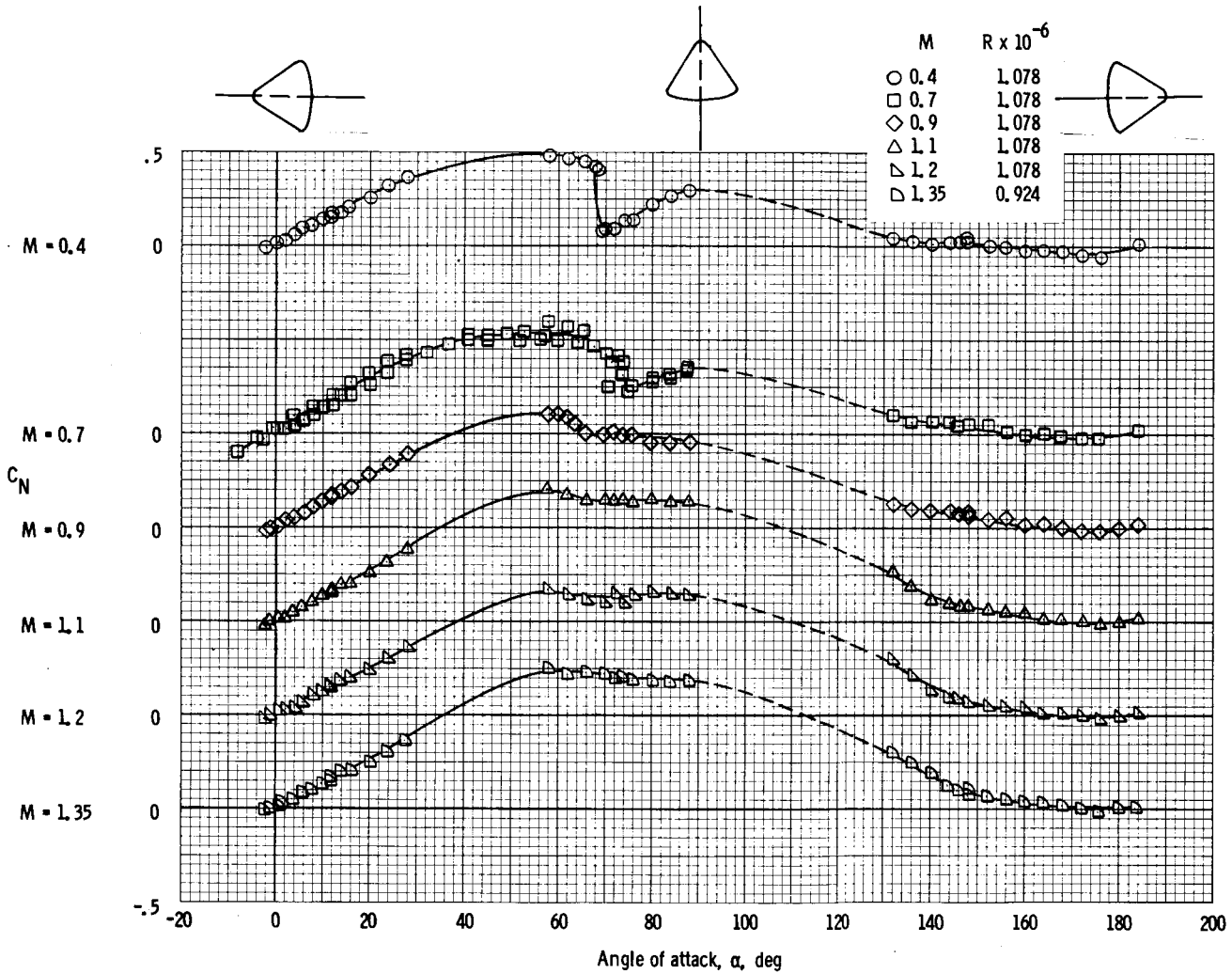

(c) Normal-force coefficient.

Figure 4. - Continued.

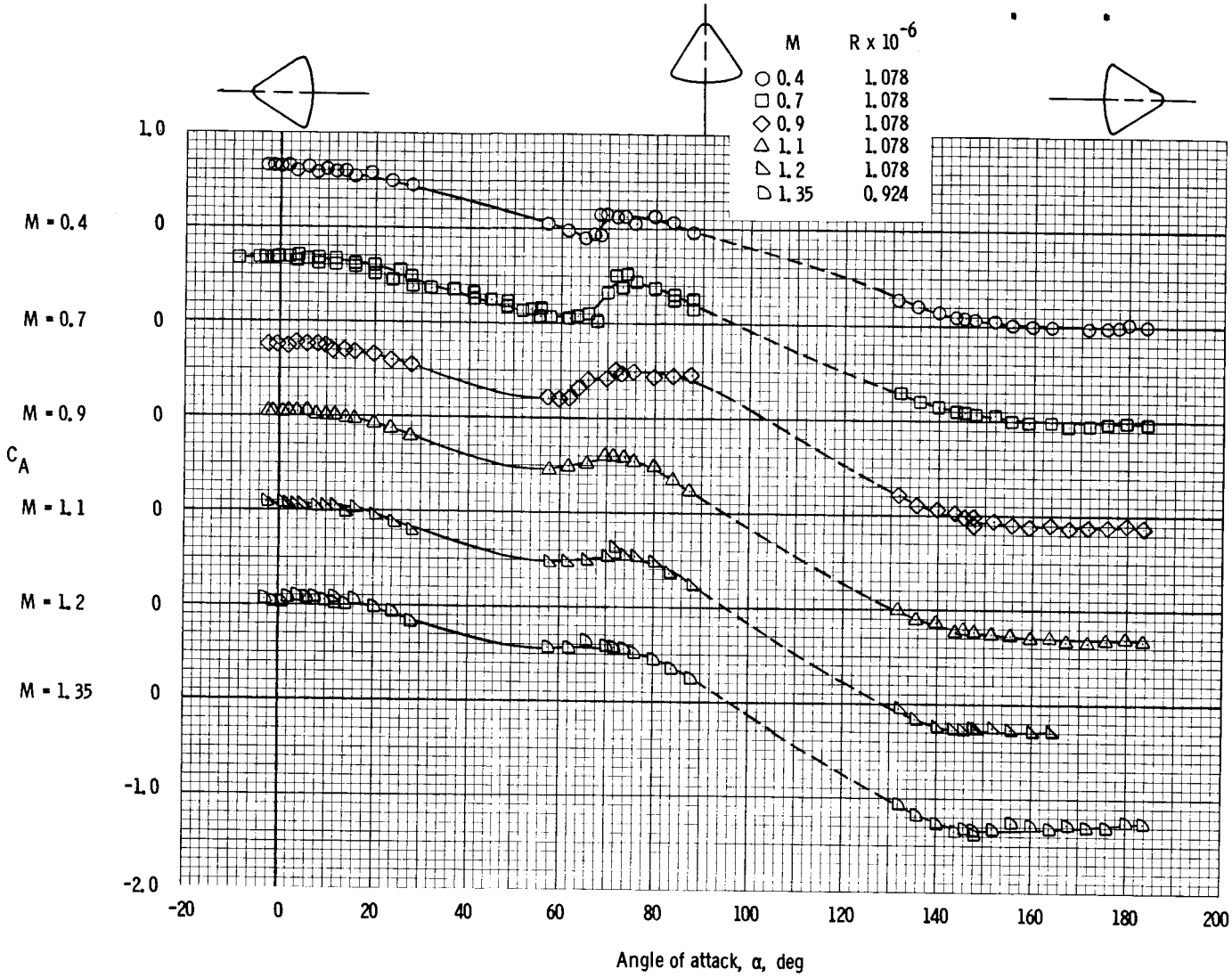

(d) Axial-force coefficient.

Figure 4. - Continued.

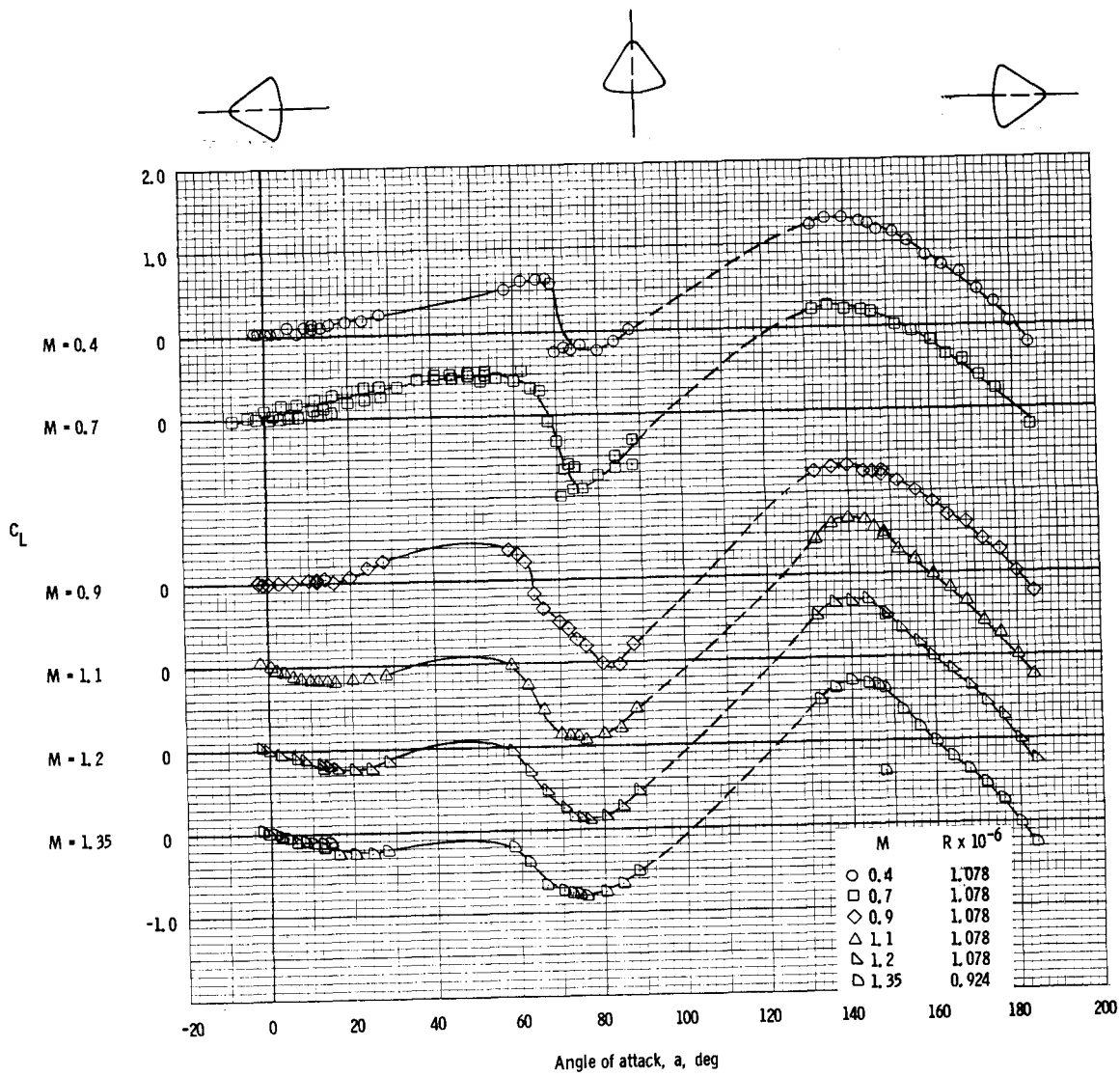

(e) Lift coefficient.

Figure 4.- Continued.

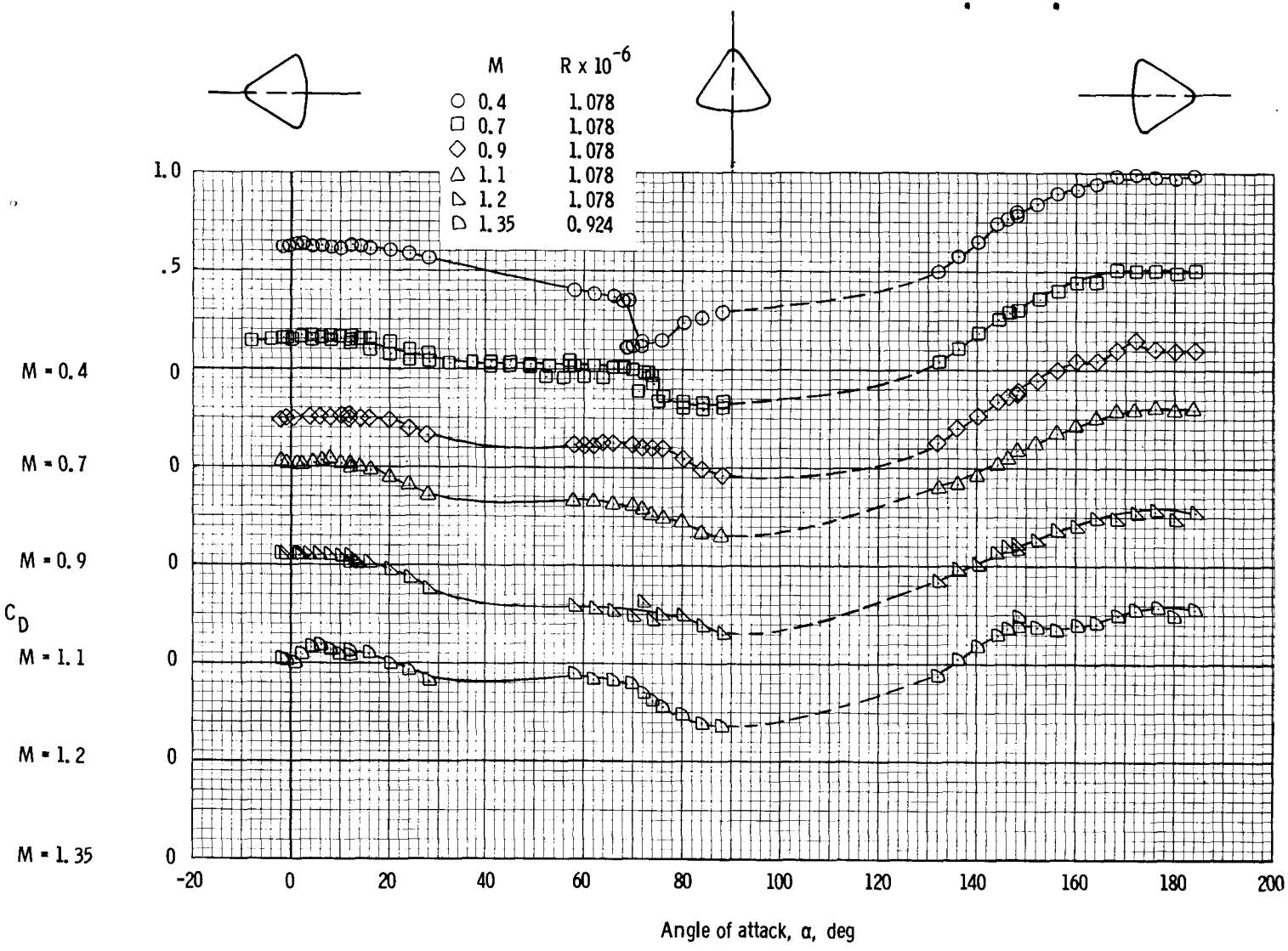

(f) Drag coefficient.

Figure 4. - Concluded.

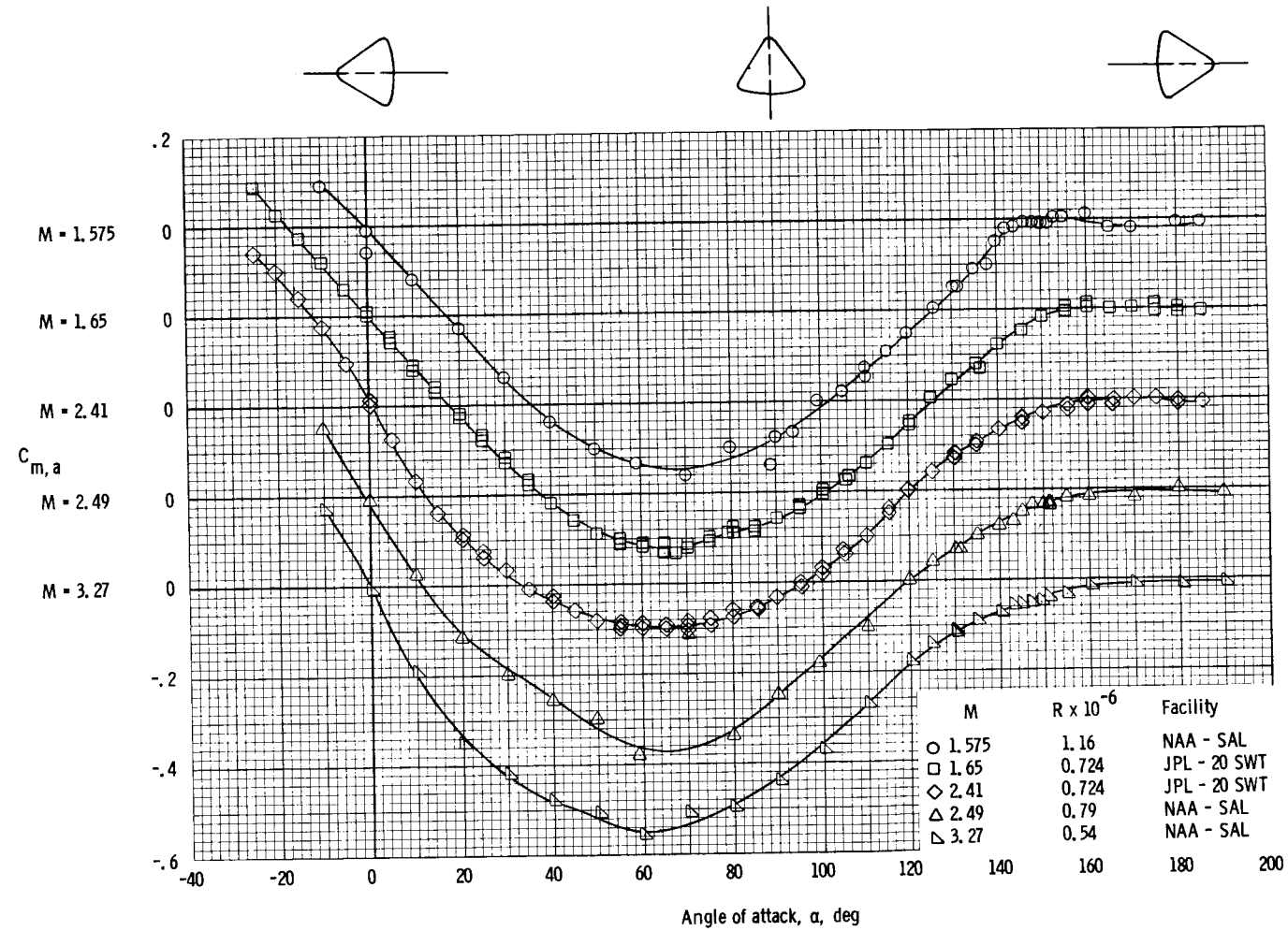

(a) Pitching-moment coefficient (apex).

Figure 5. - Aerodynamic characteristics of the Apollo command module (configuration C) at M = 1.575 to 3.27 (c.g. = x/d = -0.685, z/d = 0.059).

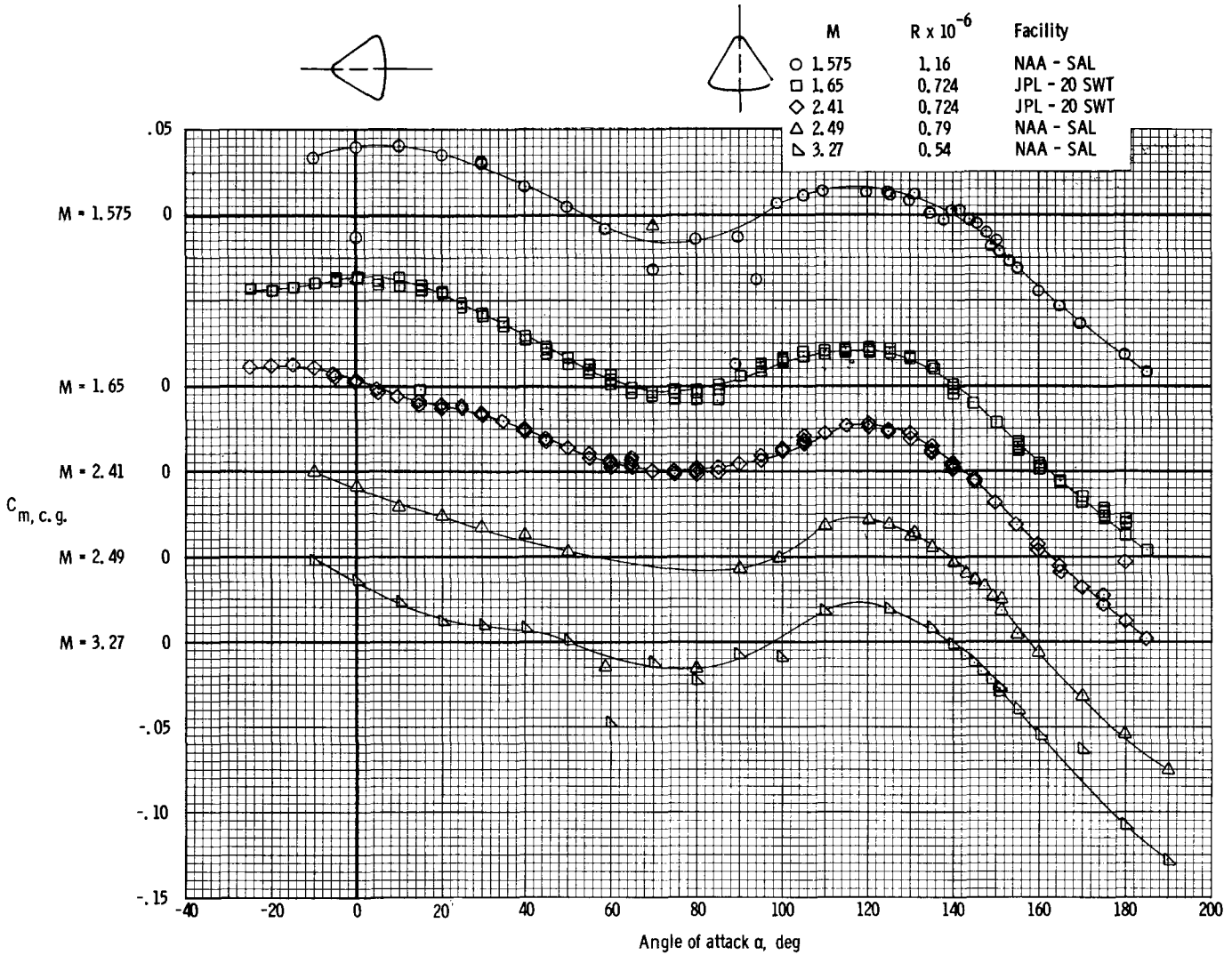

(b) Pitching-moment coefficient (c. g.).

Figure 5. - Continued.

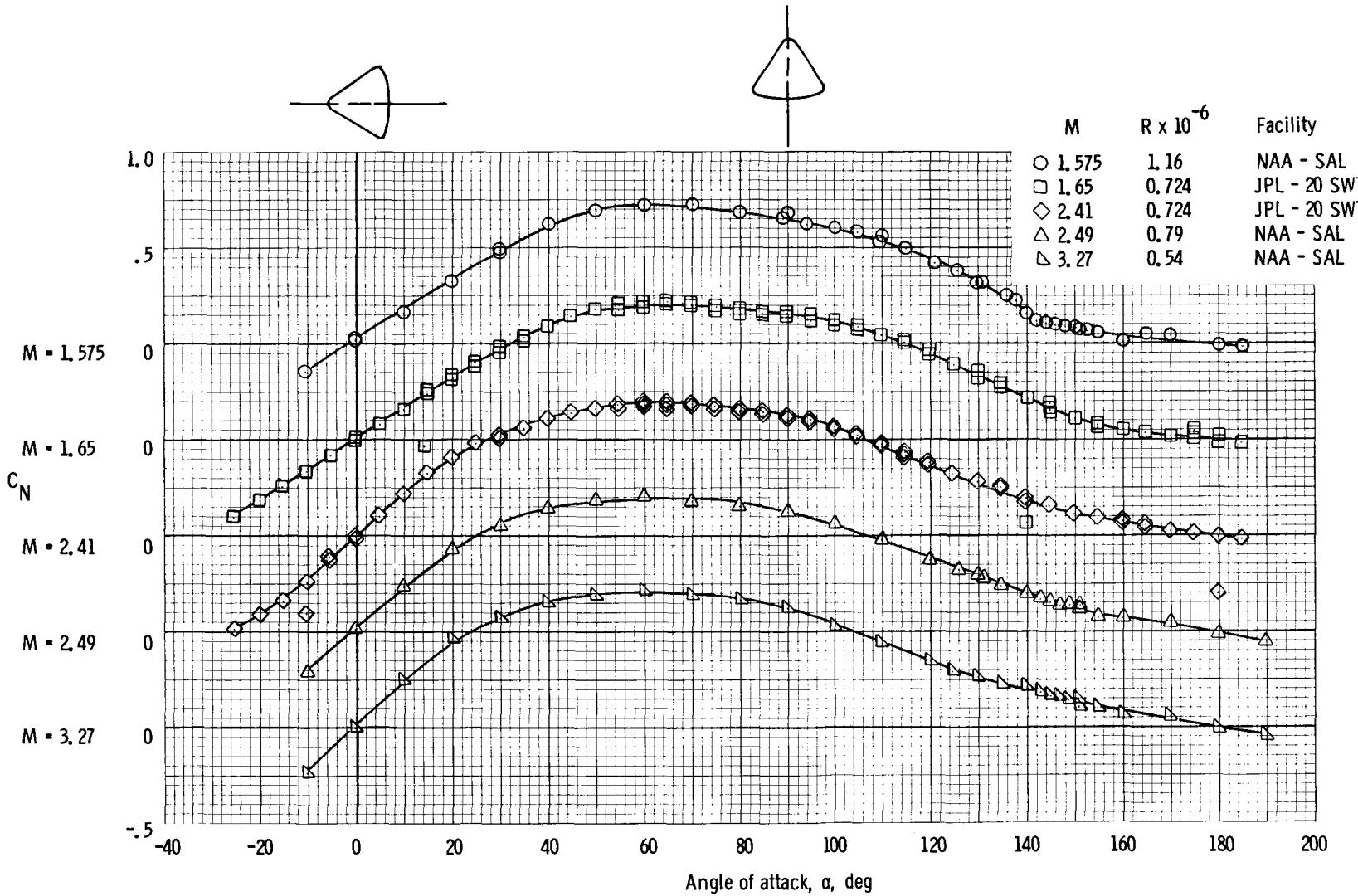

(c) Normal-force coefficient.

Figure 5. - Continued.

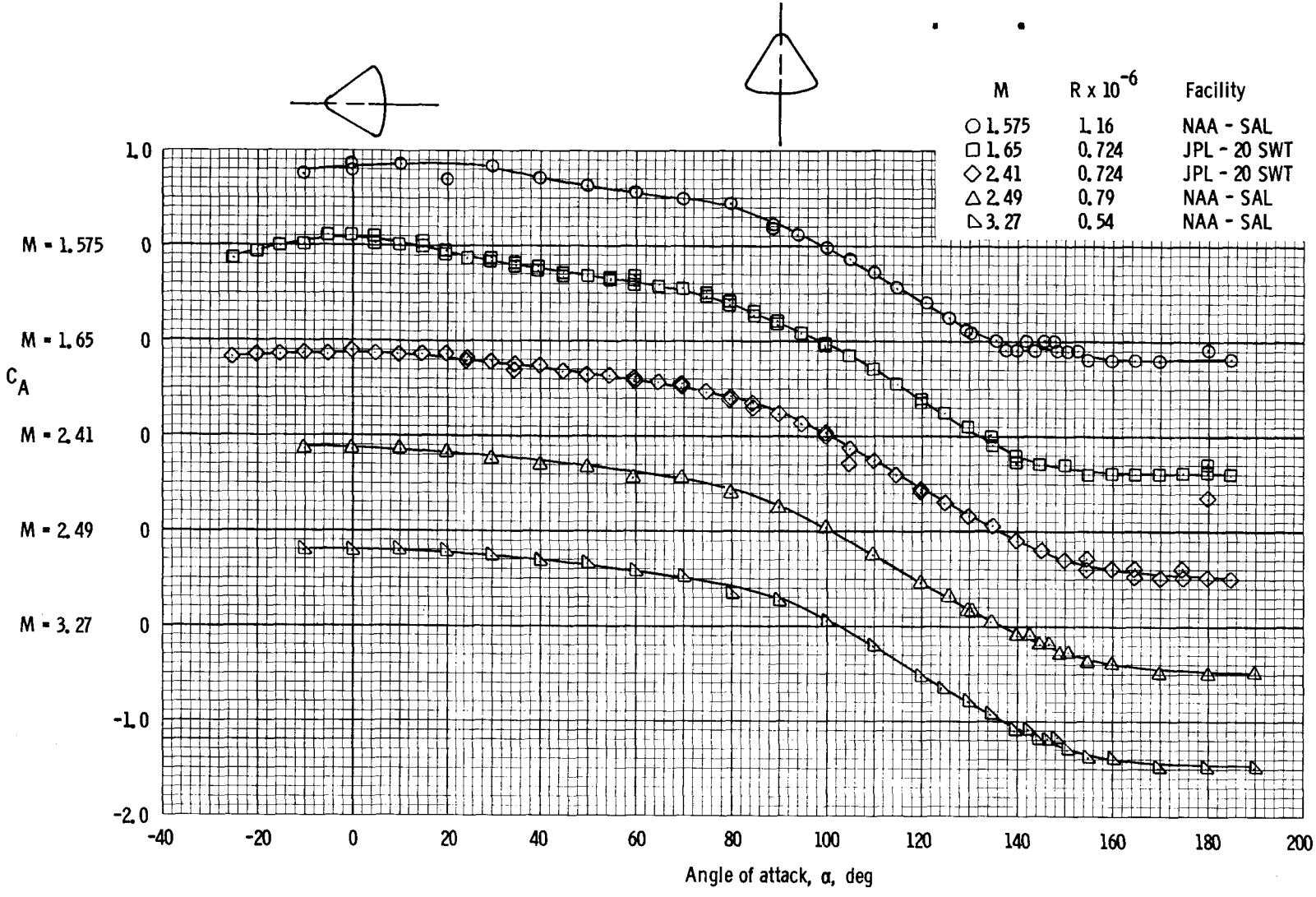

(d) Axial-force coefficient.

Figure 5. - Continued.

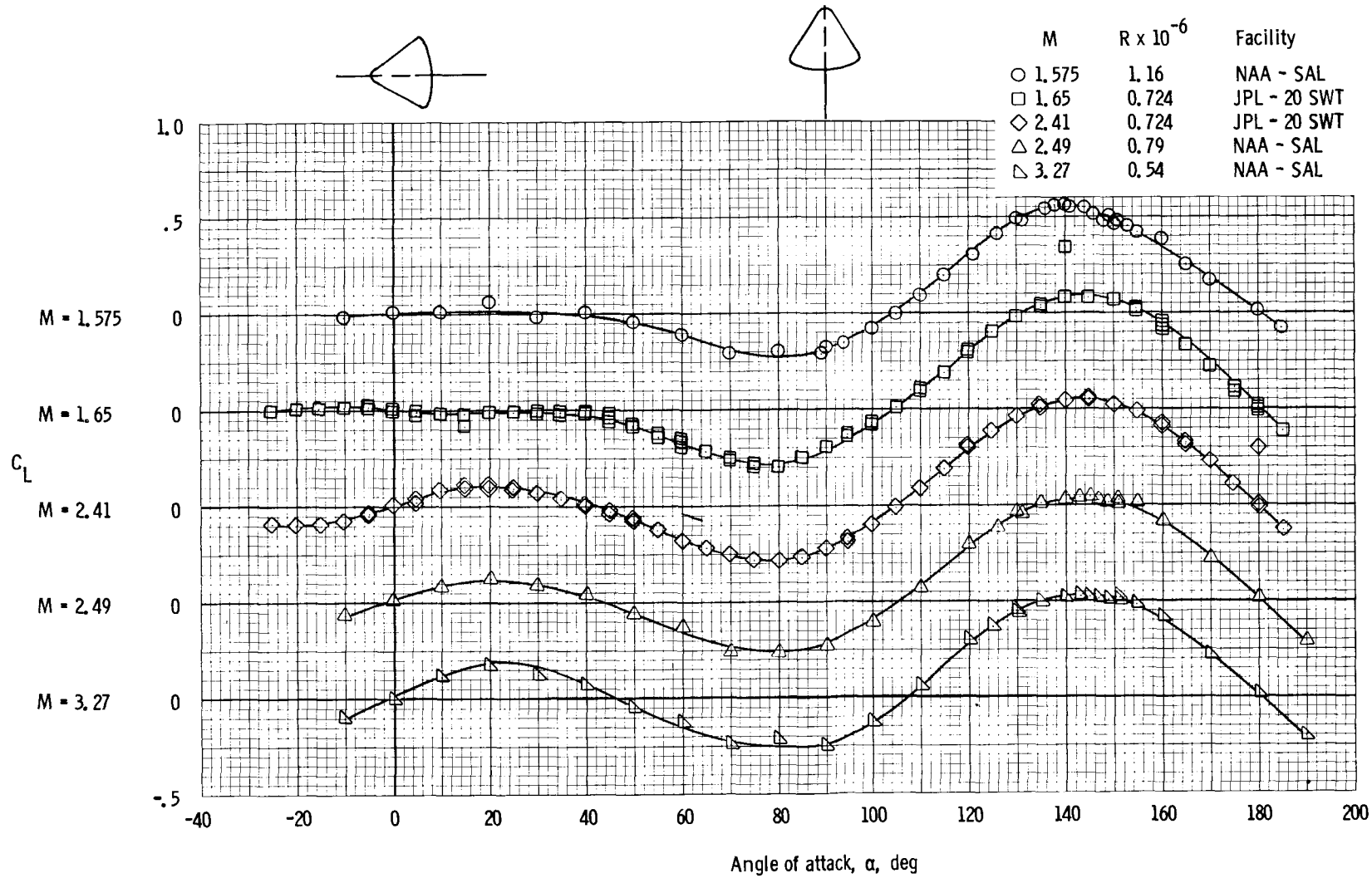

(e) Lift coefficient.

Figure 5. - Continued.

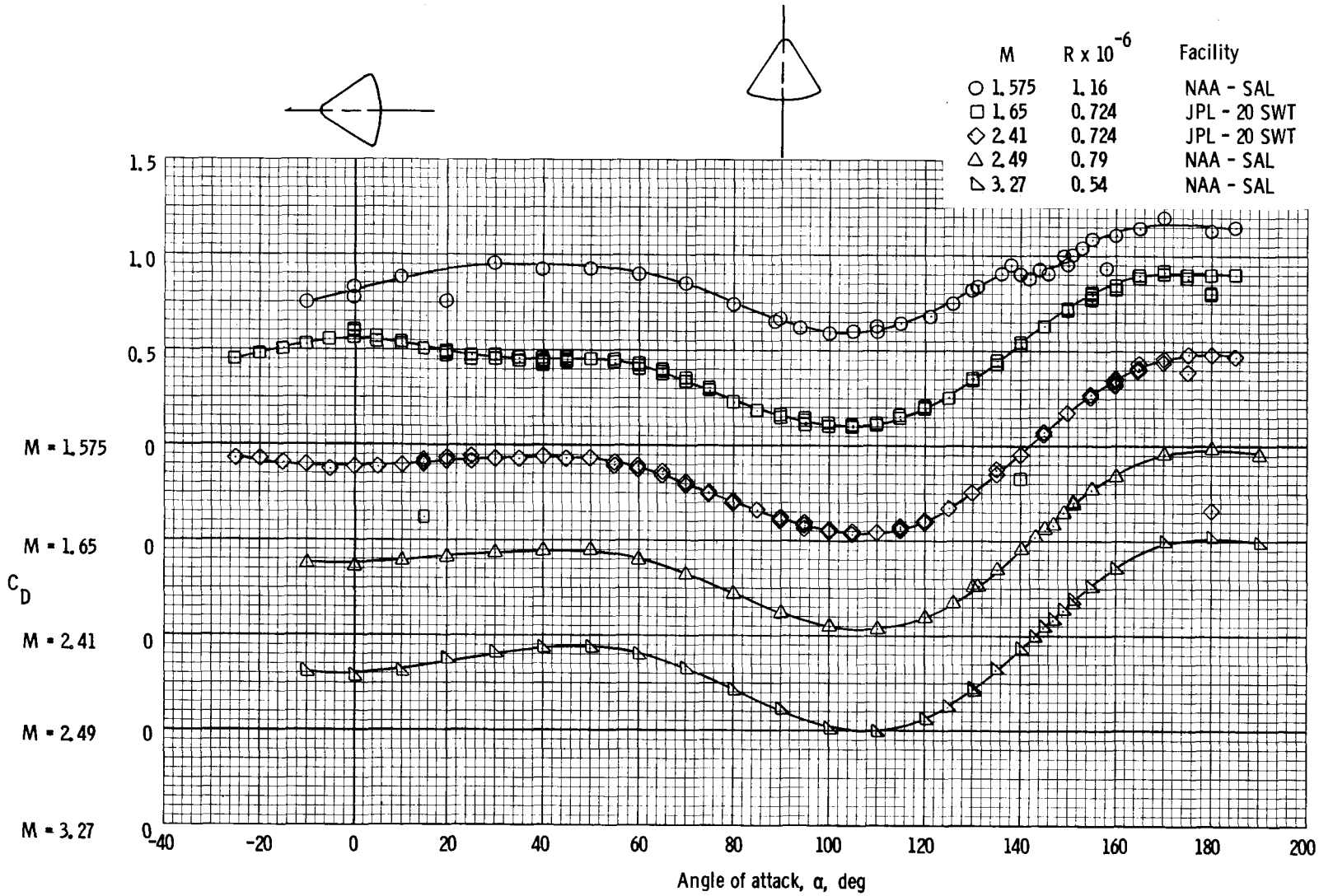

(f) Drag coefficient.

Figure 5. - Concluded.

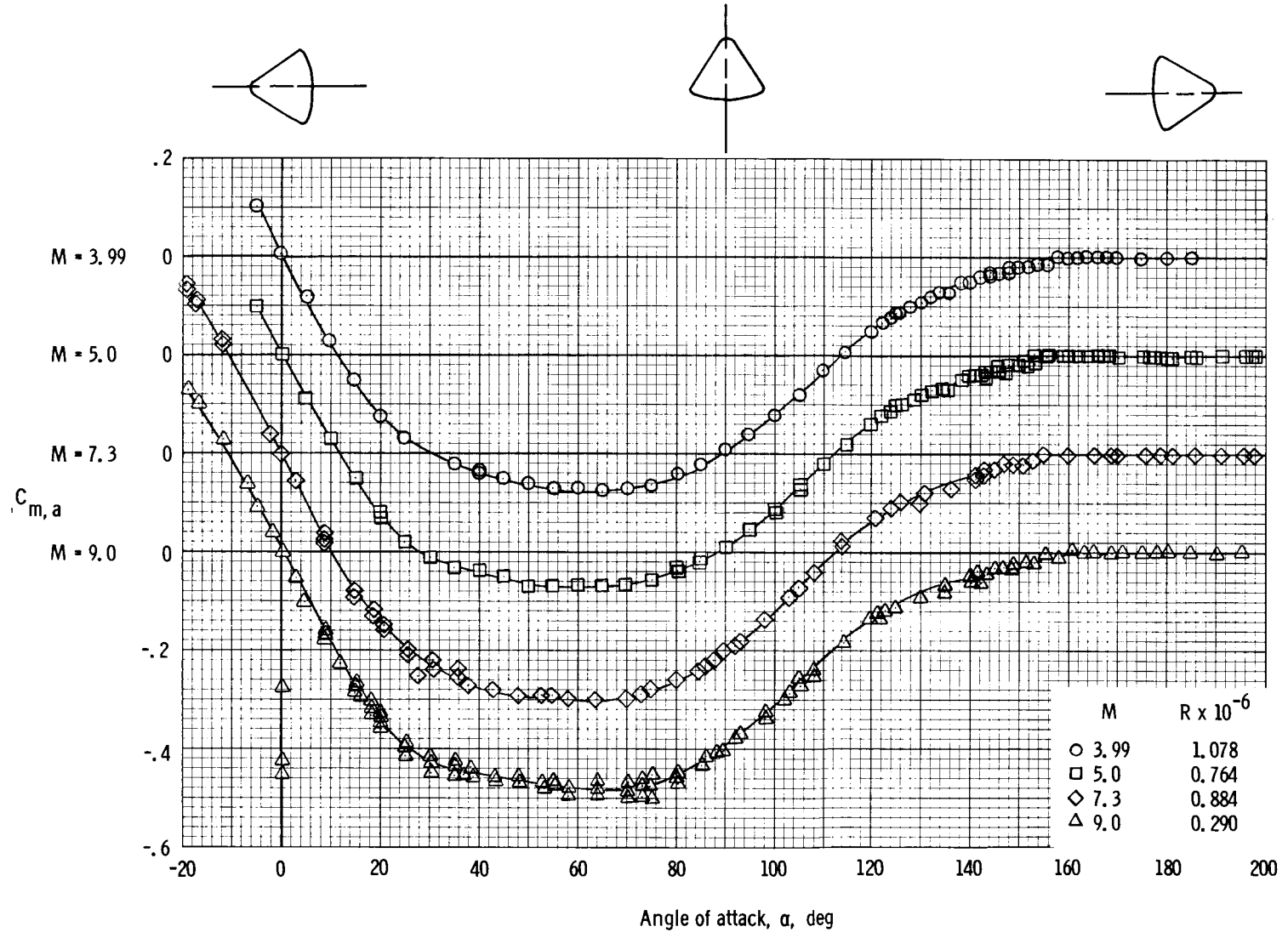

(a) Pitching-moment coefficient (apex).

Figure 6. - Aerodynamic characteristics of the Apollo command module (configuration C) obtained at JPL-20 SWT and JPL-21 HWT at M = 3.99 to 9.0 (c.g. = x/d = -0.685, z/d = 0.059).

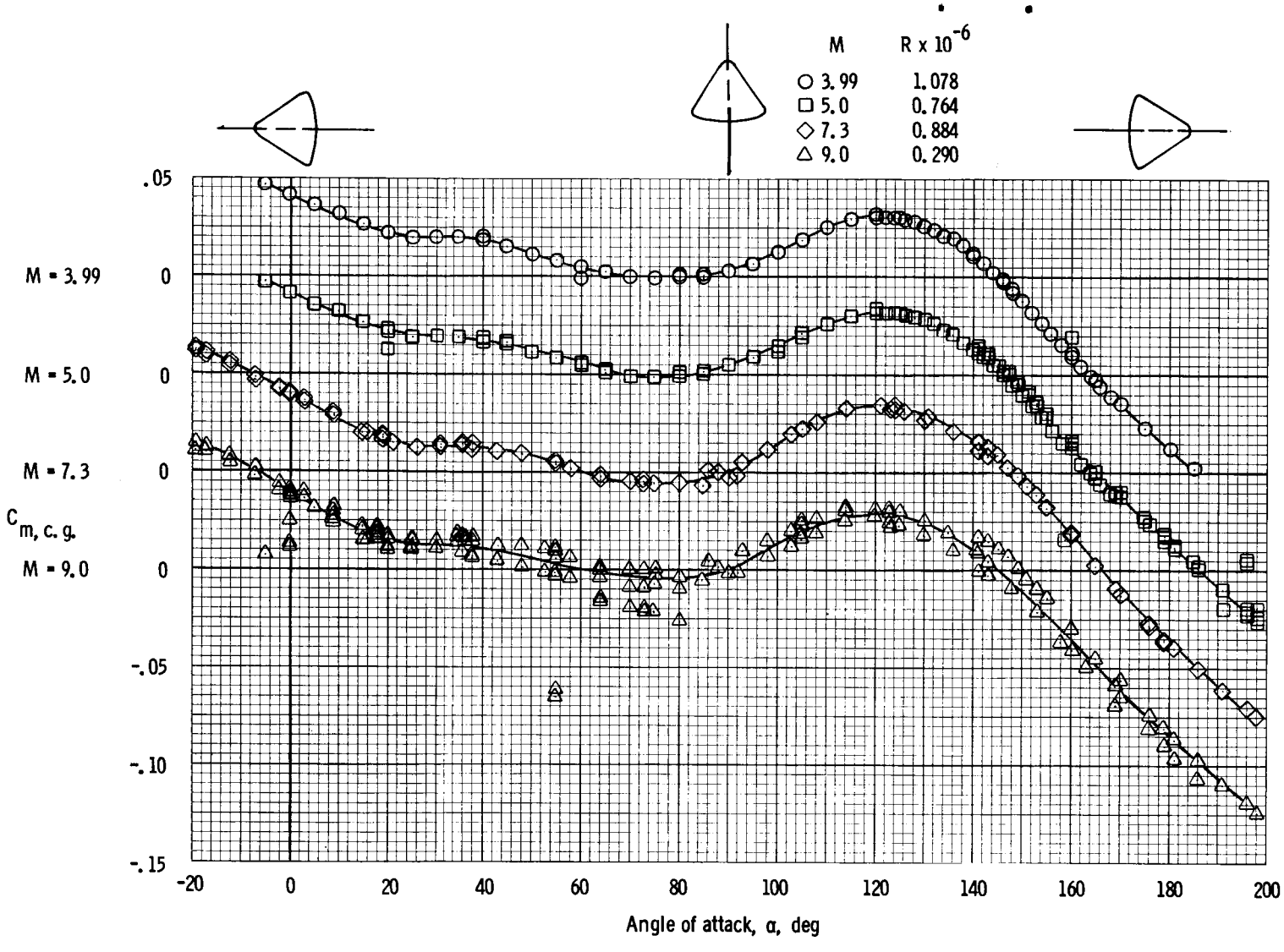

(b) Pitching-moment coefficient (c.g.).

Figure 6. - Continued.

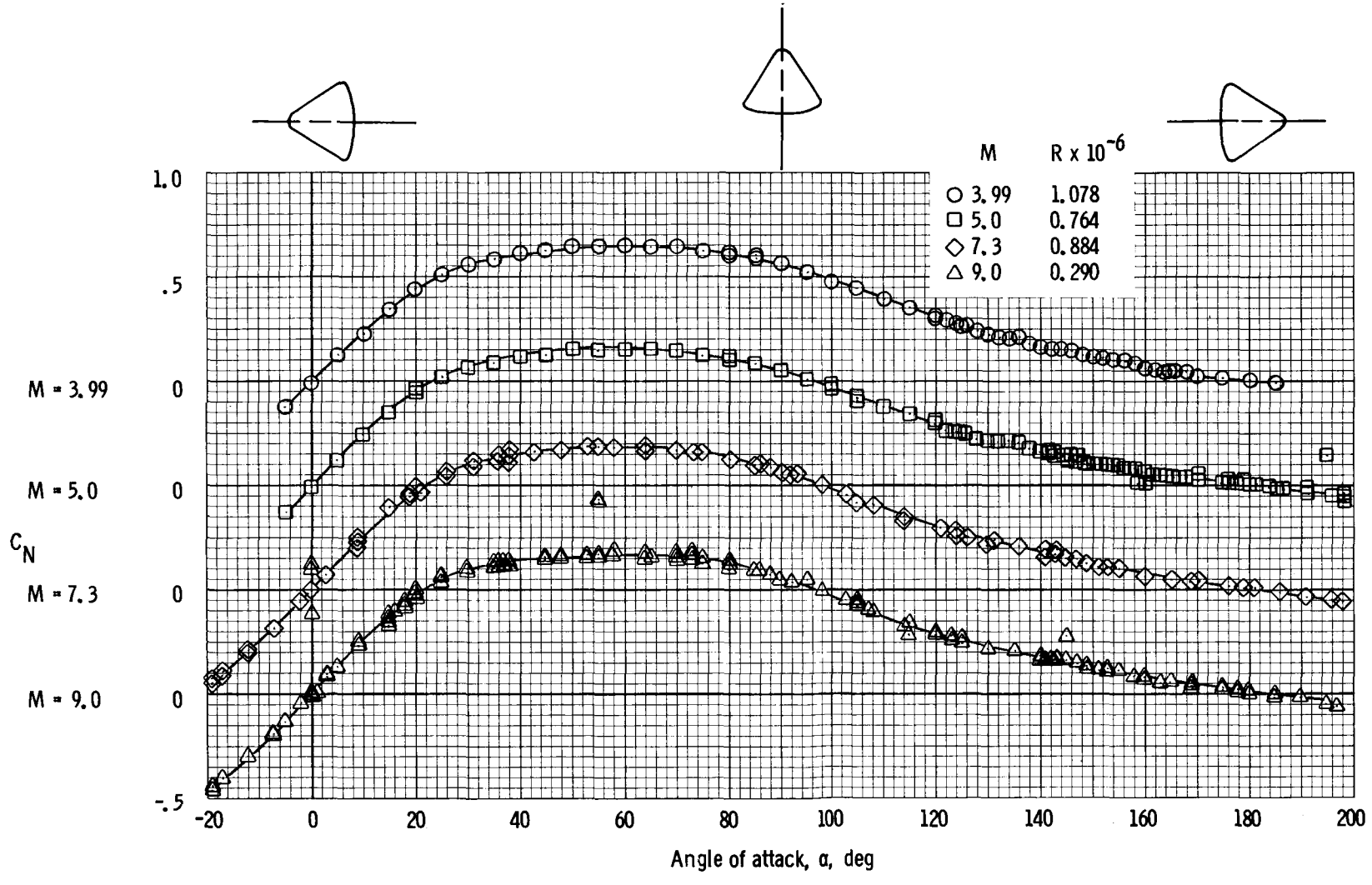

(c) Normal-force coefficient.

Figure 6. - Continued.

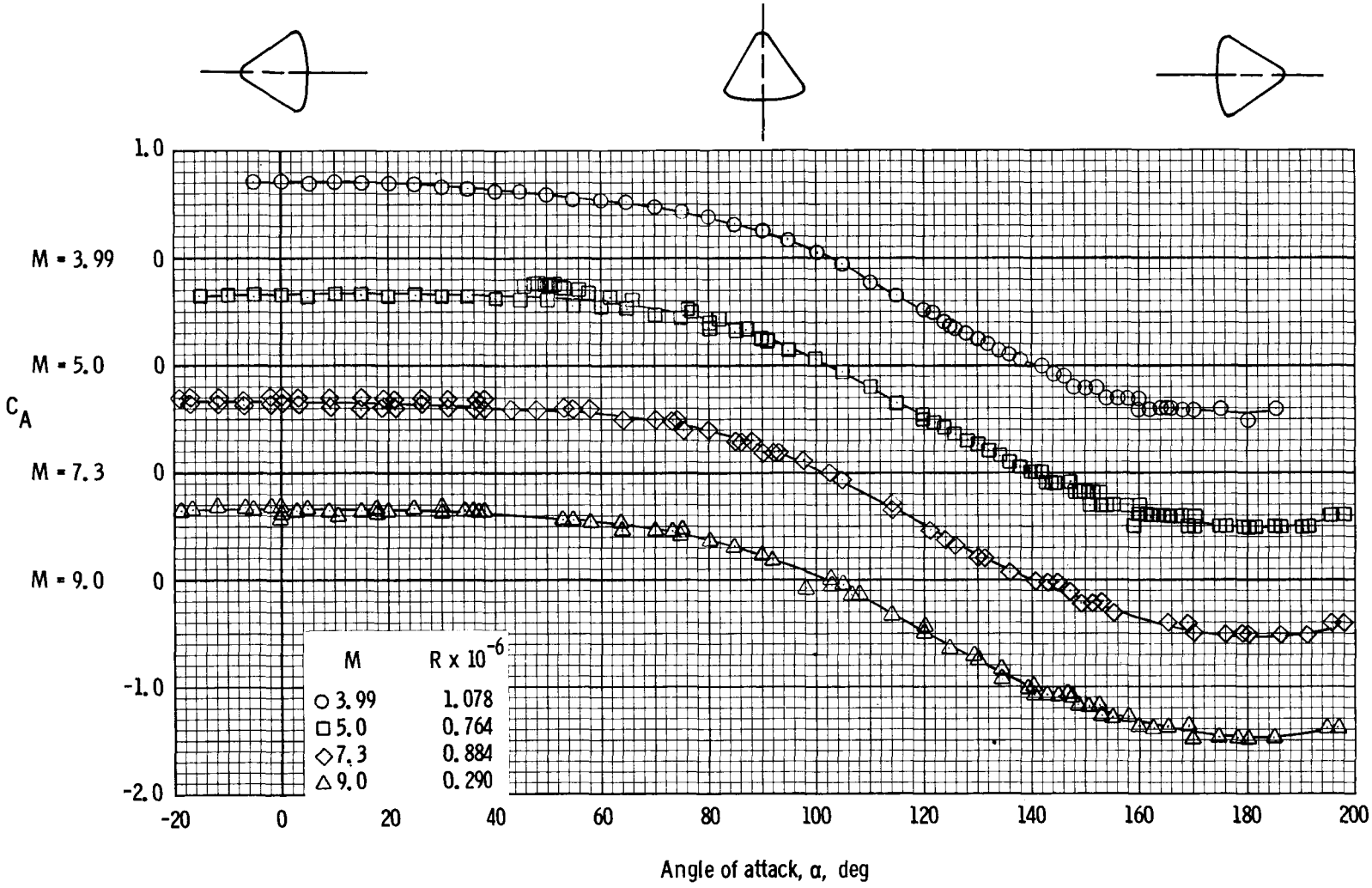

(d) Axial-force coefficient.

Figure 6. - Continued.

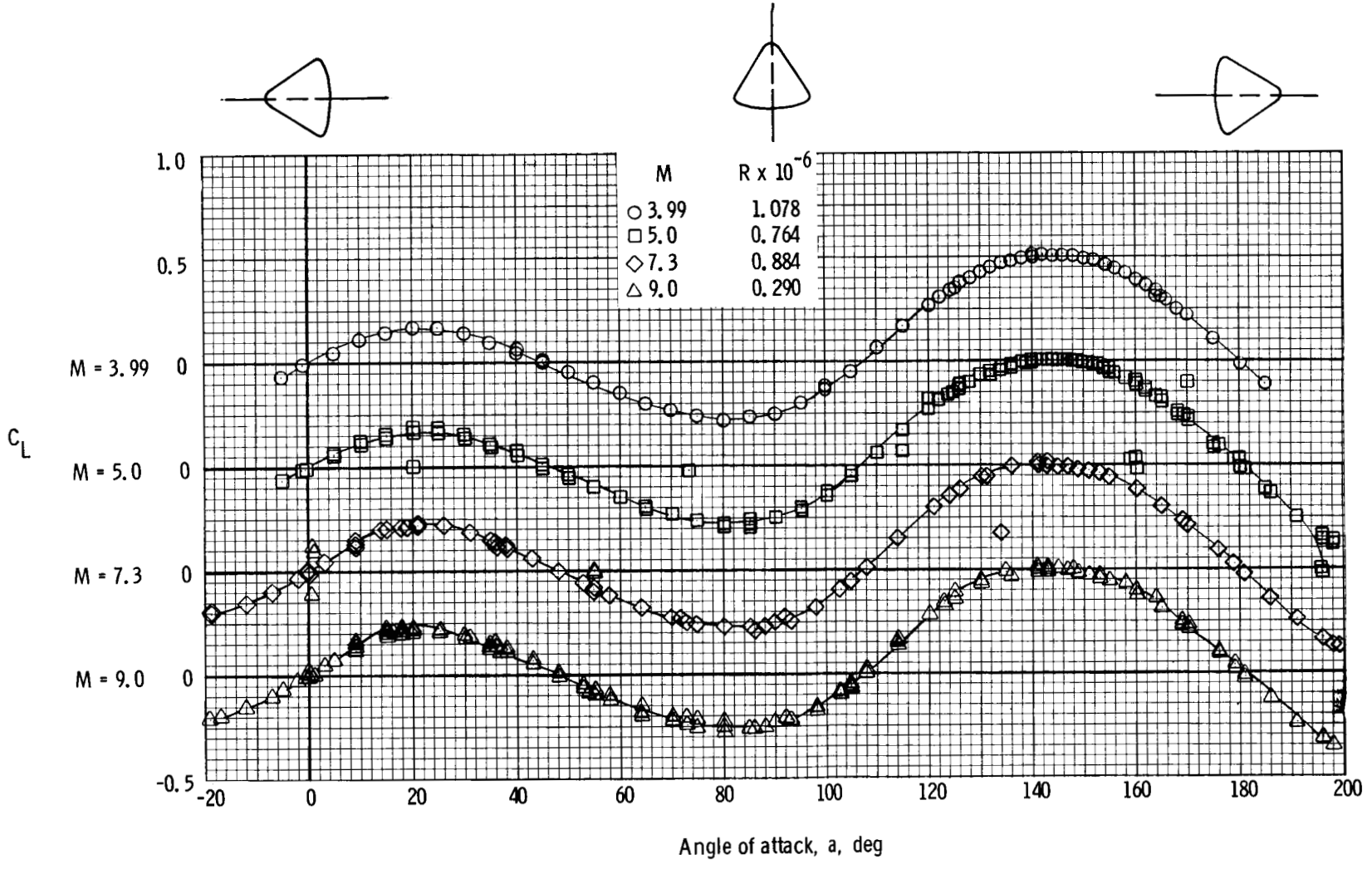

(e) Lift coefficient.

Figure 6. - Continued.

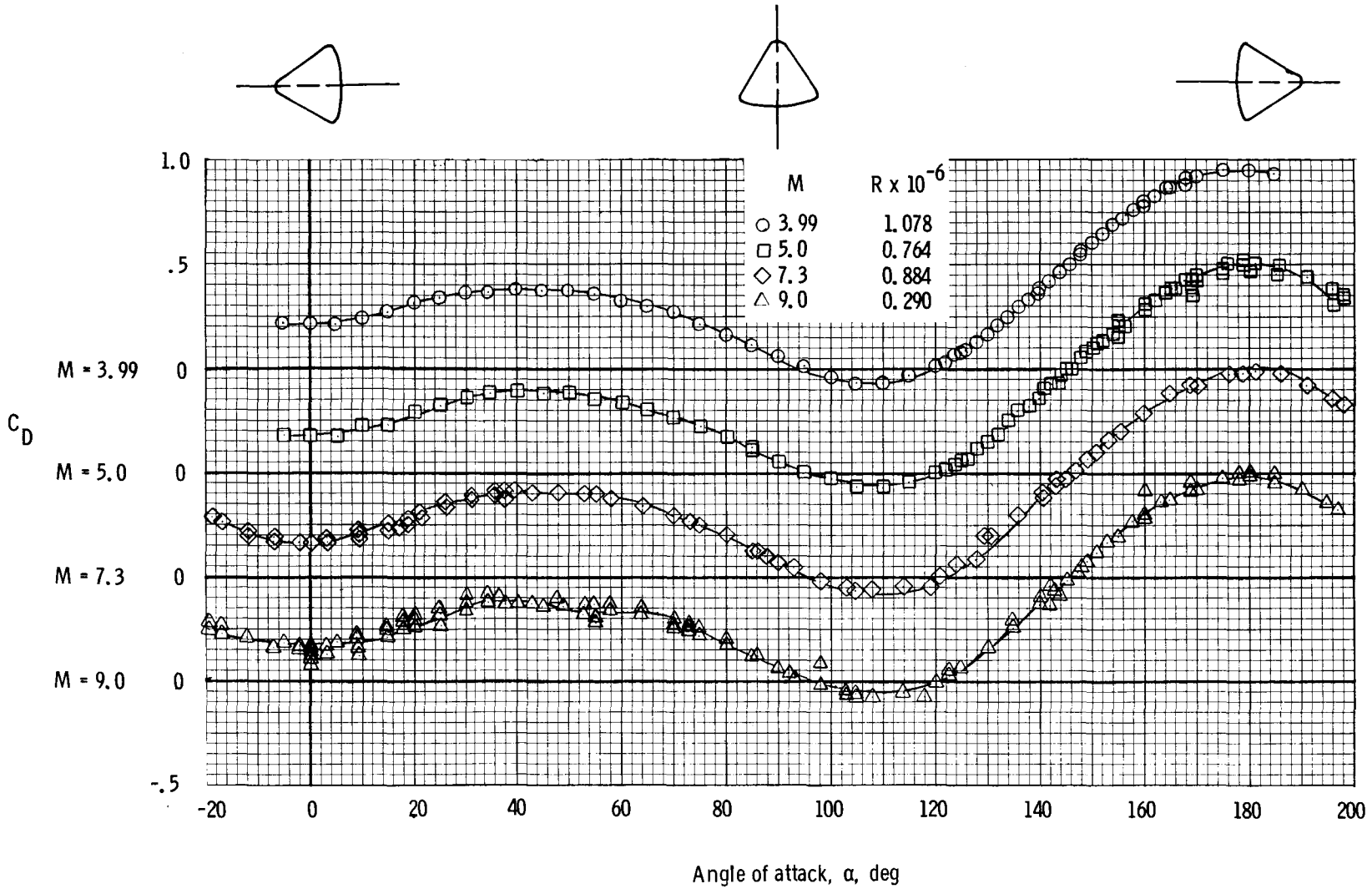

(f) Drag coefficient.

Figure 6. - Concluded.

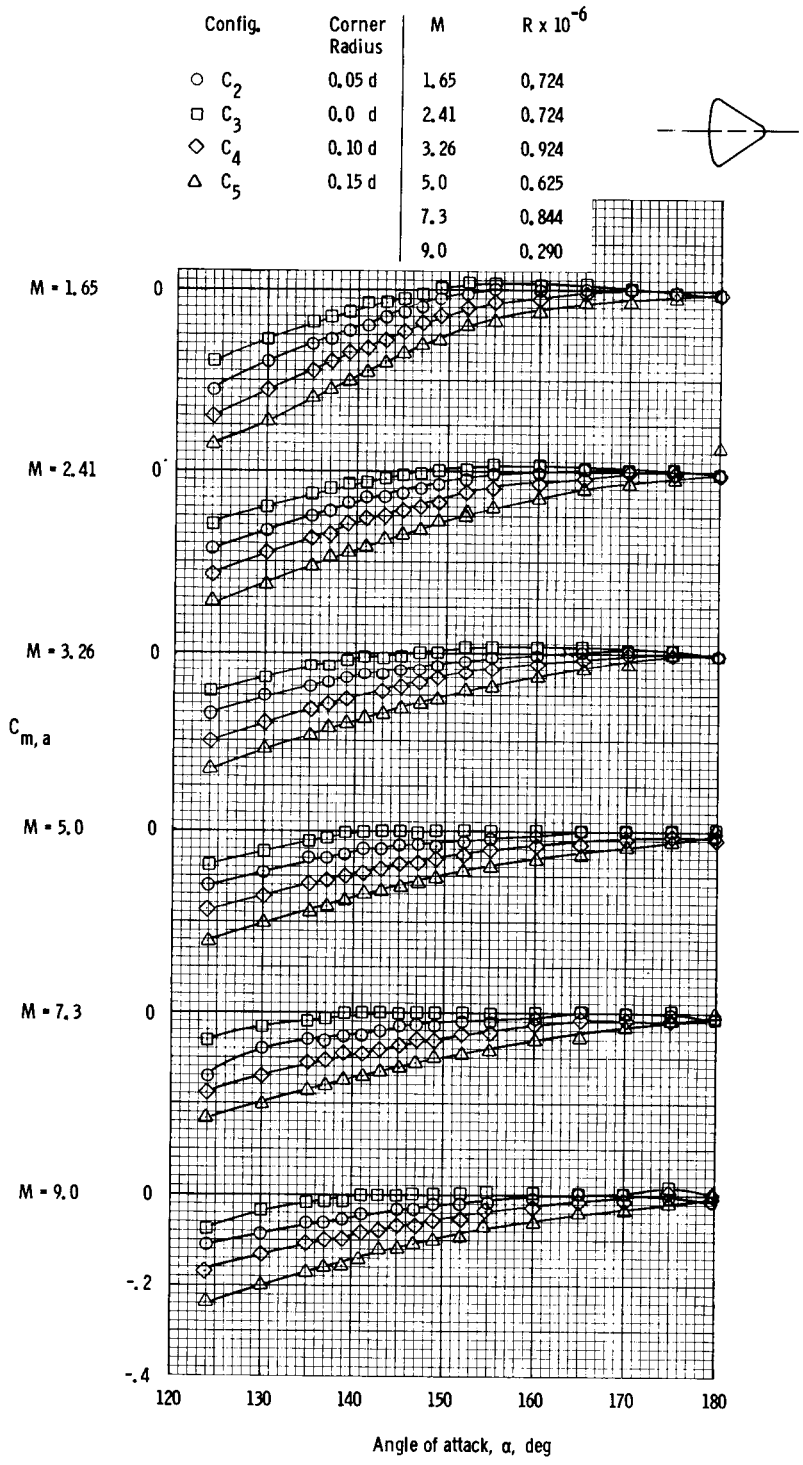

(a) Pitching-moment coefficient (apex).

Figure 7. - Aerodynamic characteristics of the Apollo command module with various corner radii obtained at JPL-20 SWT and JPL-21 HWT facilities at M = 1.65 to M = 9.0 (c.g. = x/d = -0.685, z/d = 0.059).

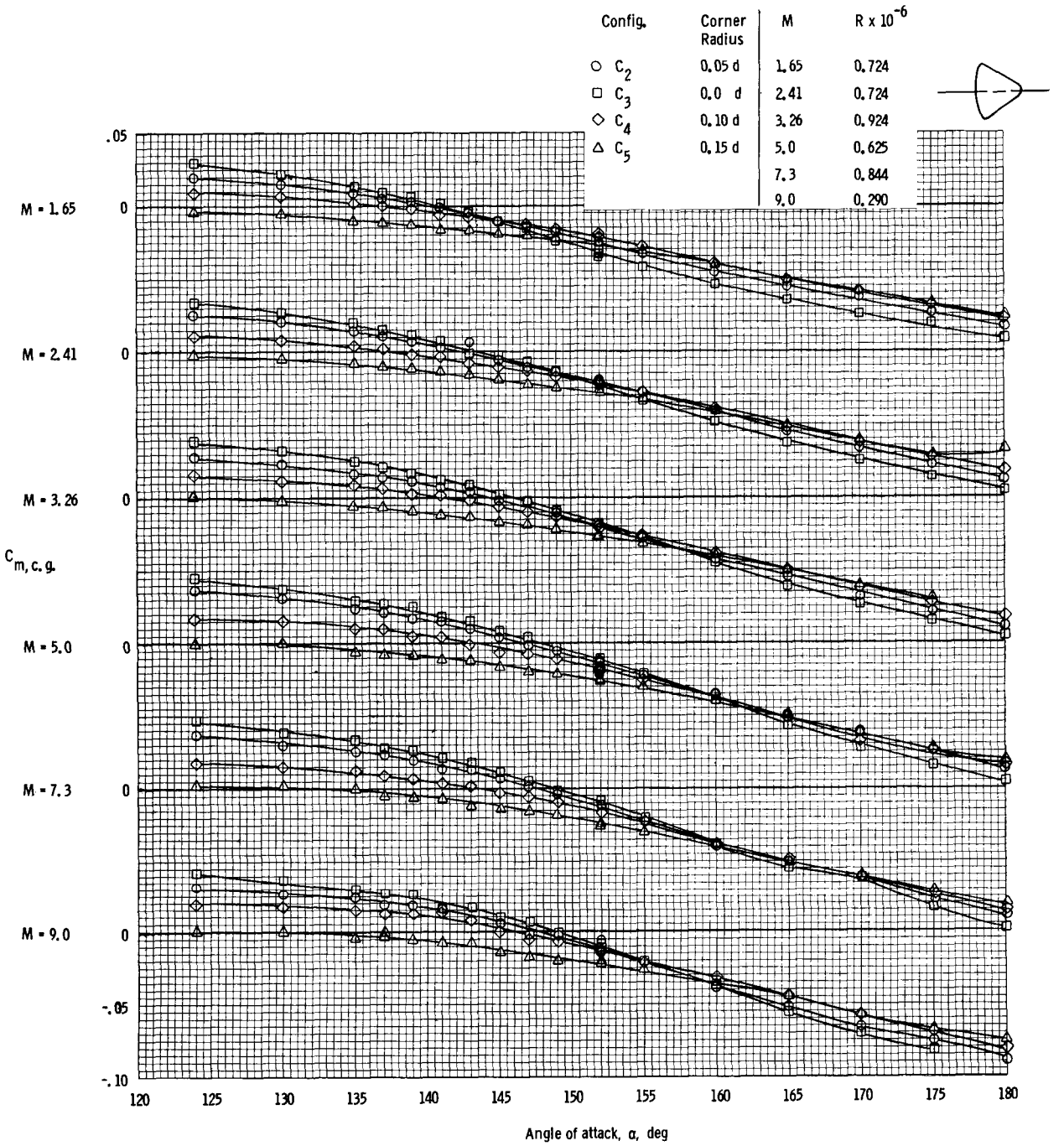

(b) Pitching-moment coefficient.

Figure 7. - Continued.

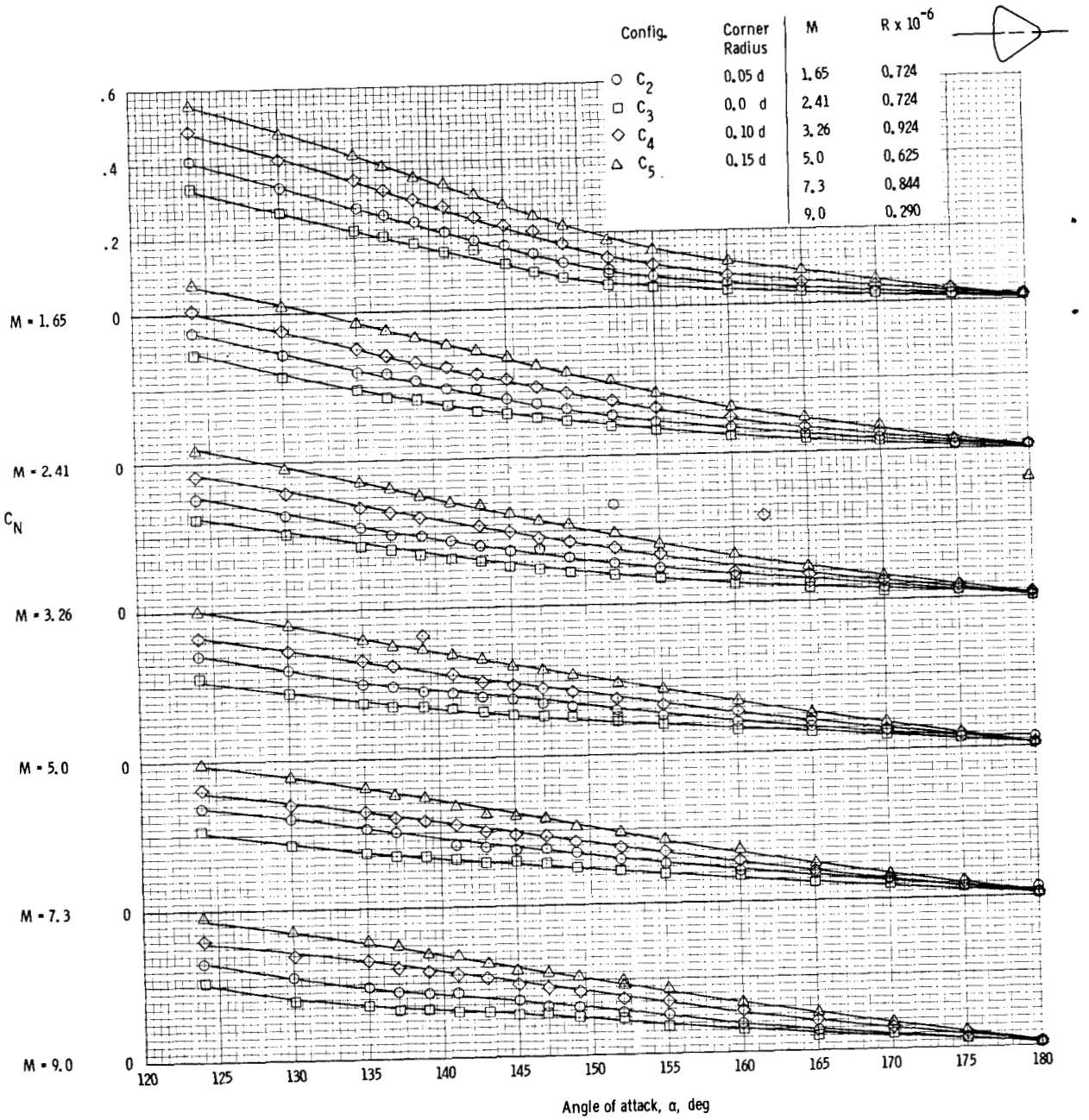

(c) Normal-force coefficient.

Figure 7. - Continued.

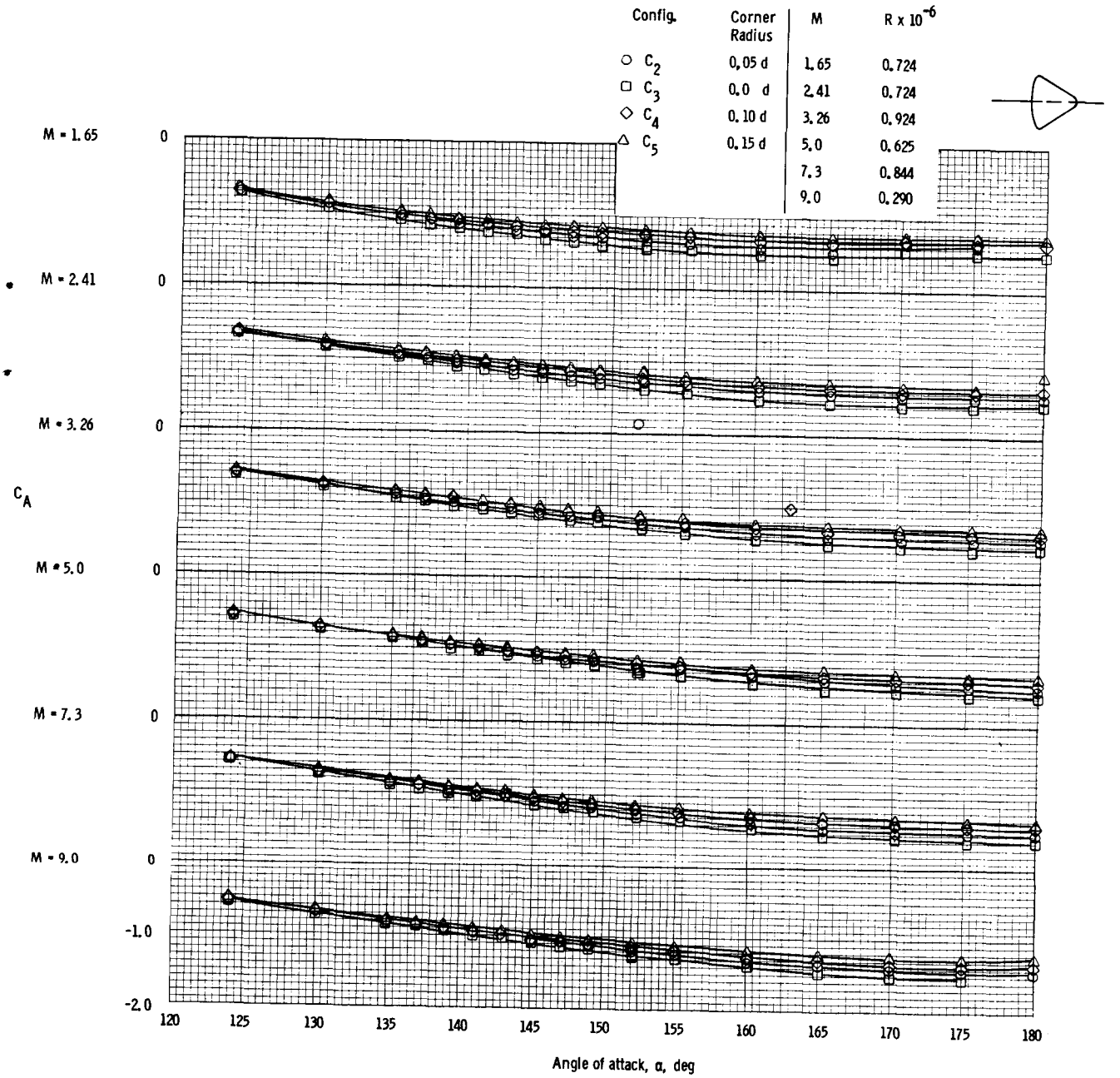

(d) Axial-force coefficient.

Figure 7. - Continued.

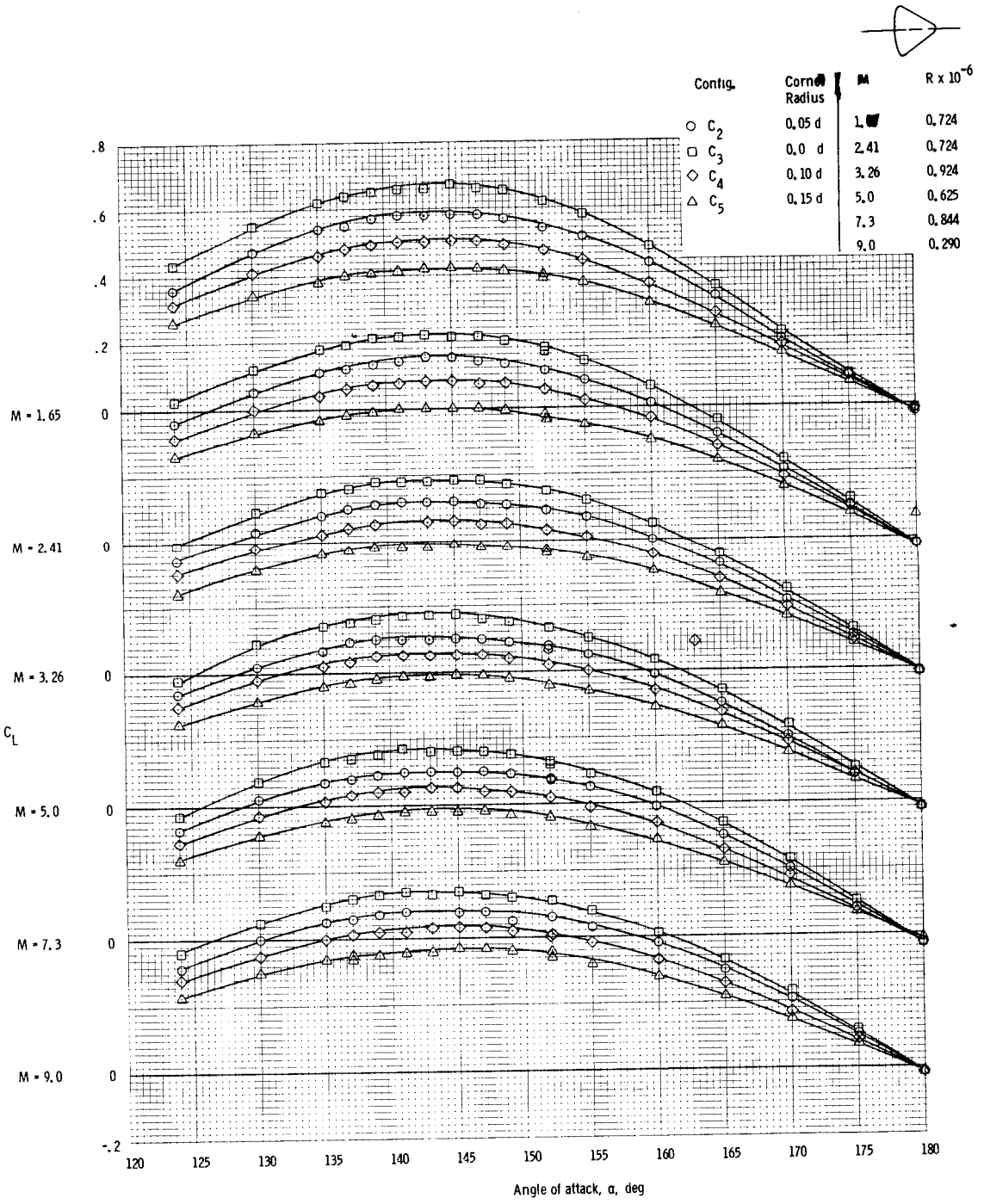

(e) Lift coefficient.

Figure 7. - Continued.

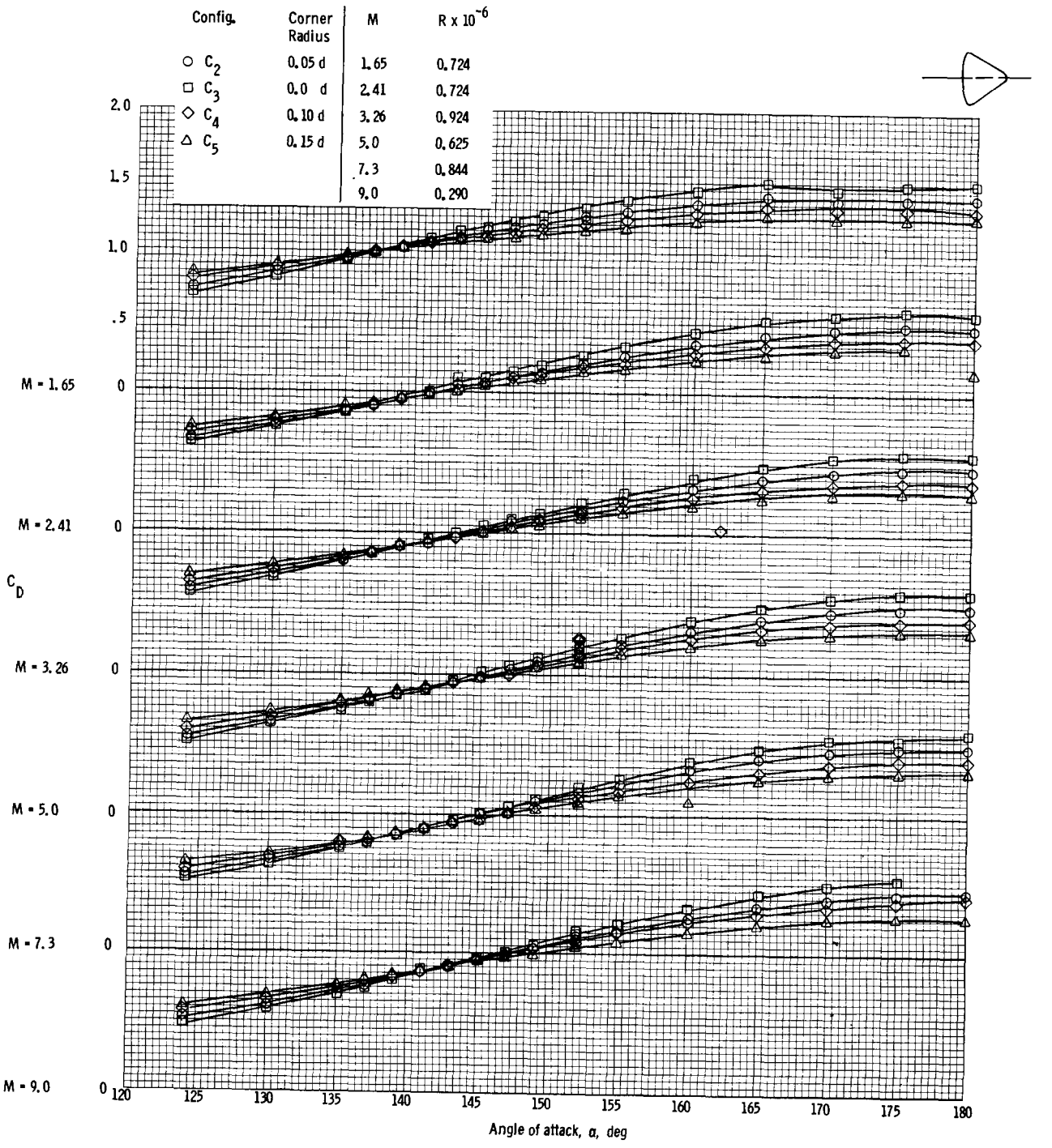

(f) Drag coefficient.

Figure 7. - Continued.

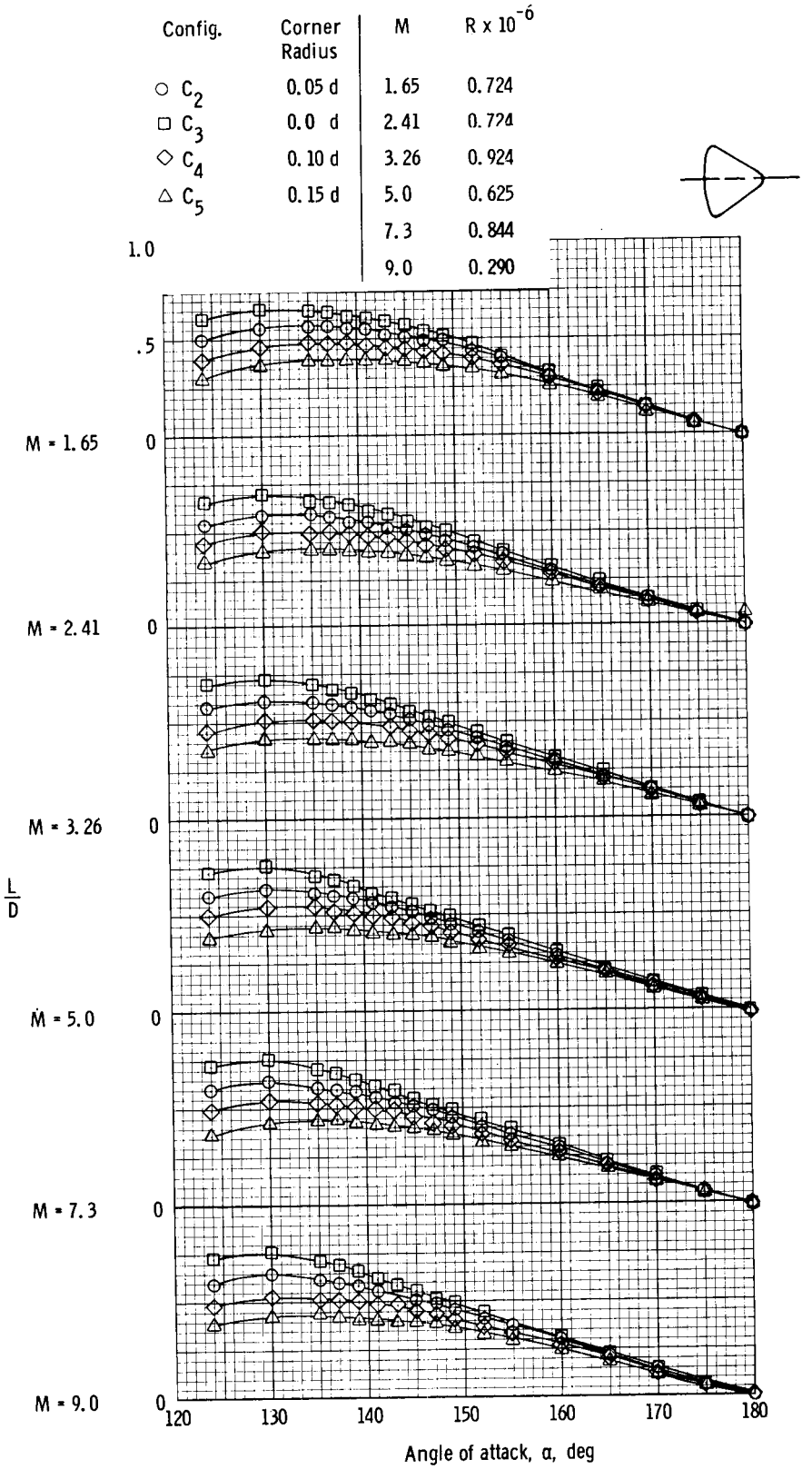

(g) Lift-to-drag ratio.

Figure 7. - Concluded.

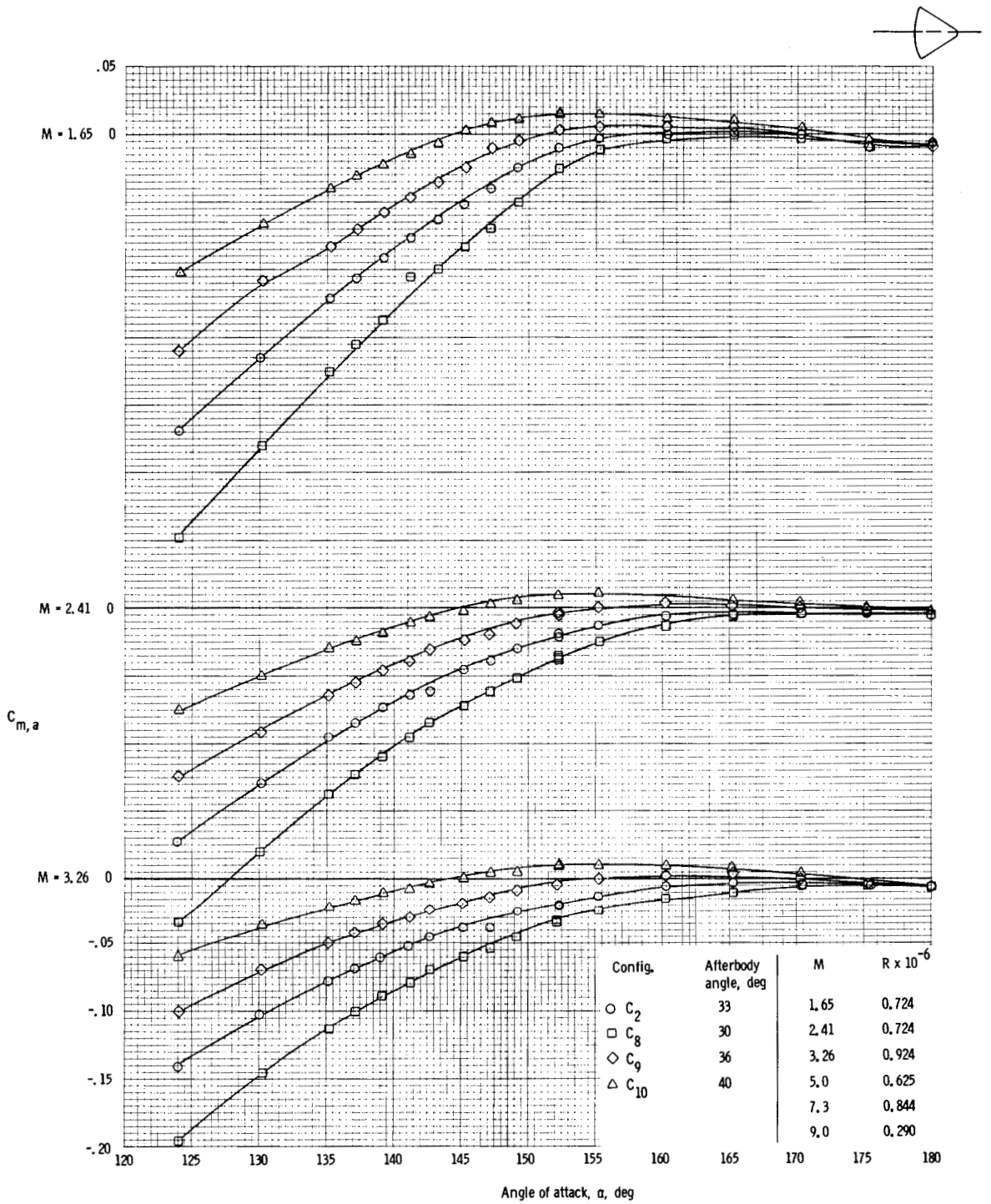

(a) Pitching-moment coefficient, apex (M = 1.65 to M = 3.26).

Figure 8. - Aerodynamic characteristics of the Apollo command module with various afterbody angles obtained at JPL-20 SWT and JPL-21 HWT facilities at M = 1.65 to M = 9.0.

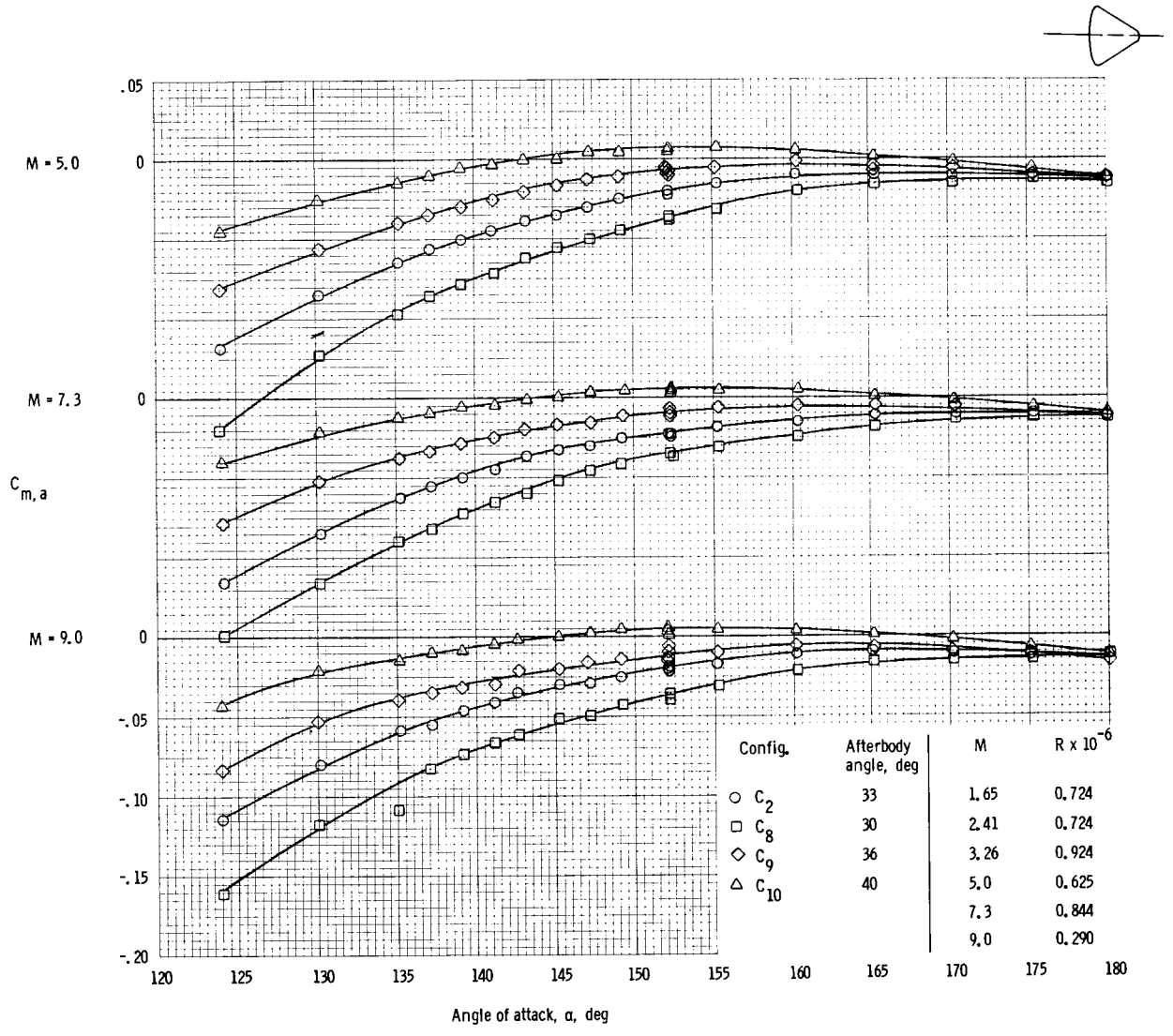

(b) Pitching-moment coefficient, apex (M = 5.0 to M = 9.0).

Figure 8. - Continued.

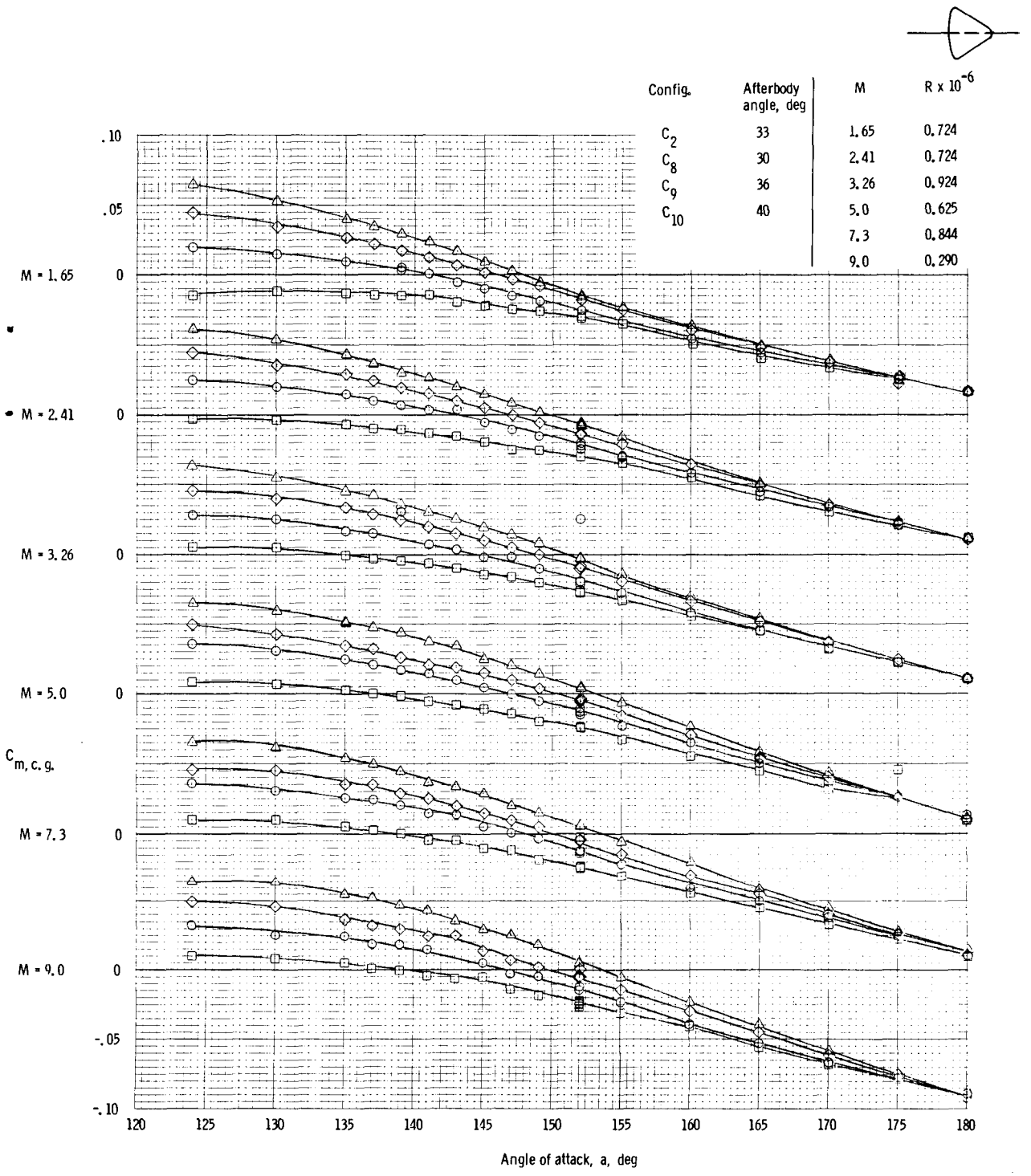

(c) Pitching-moment coefficient.

Figure 8. - Continued.

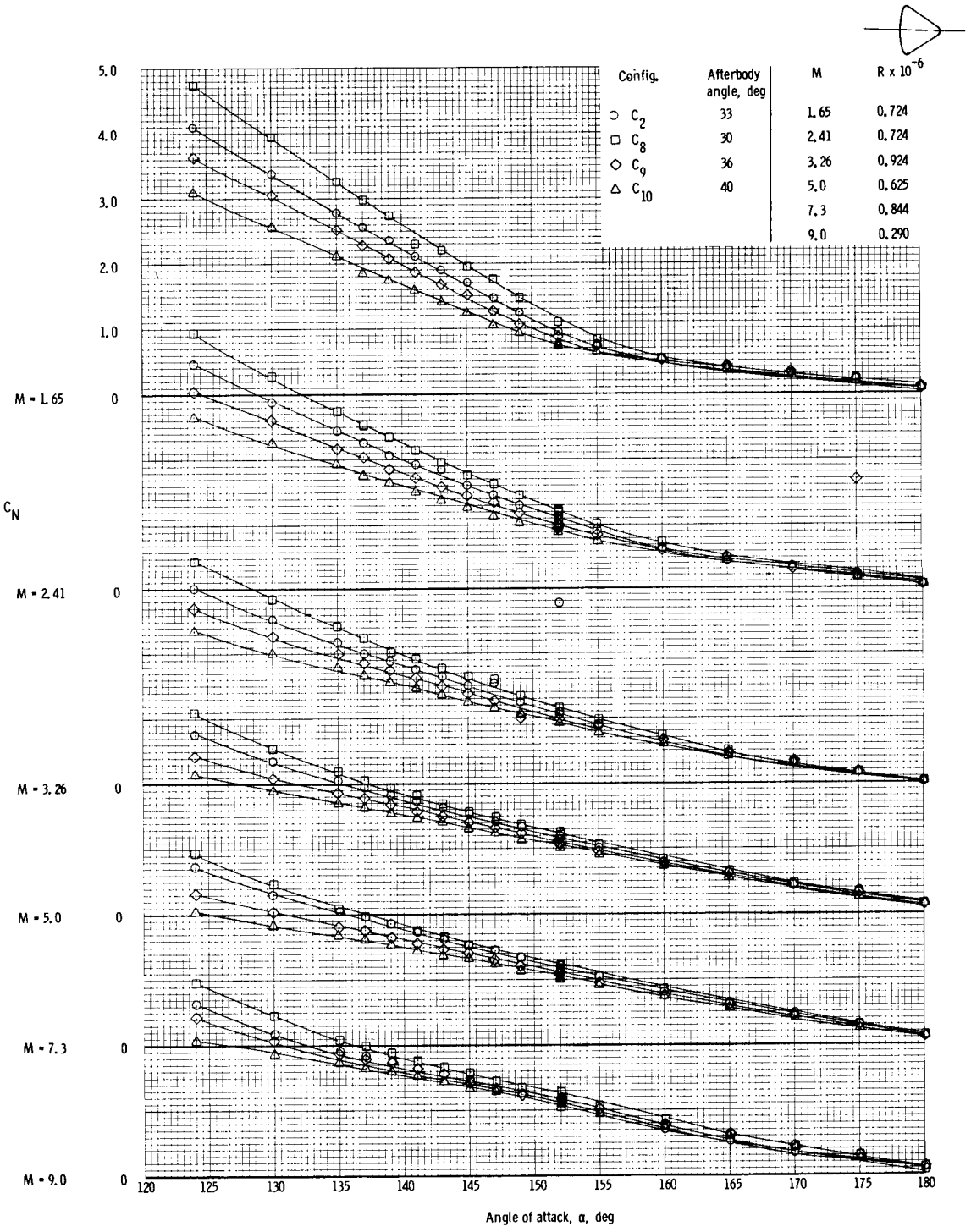

(d) Normal-force coefficient.

Figure 8. - Continued.

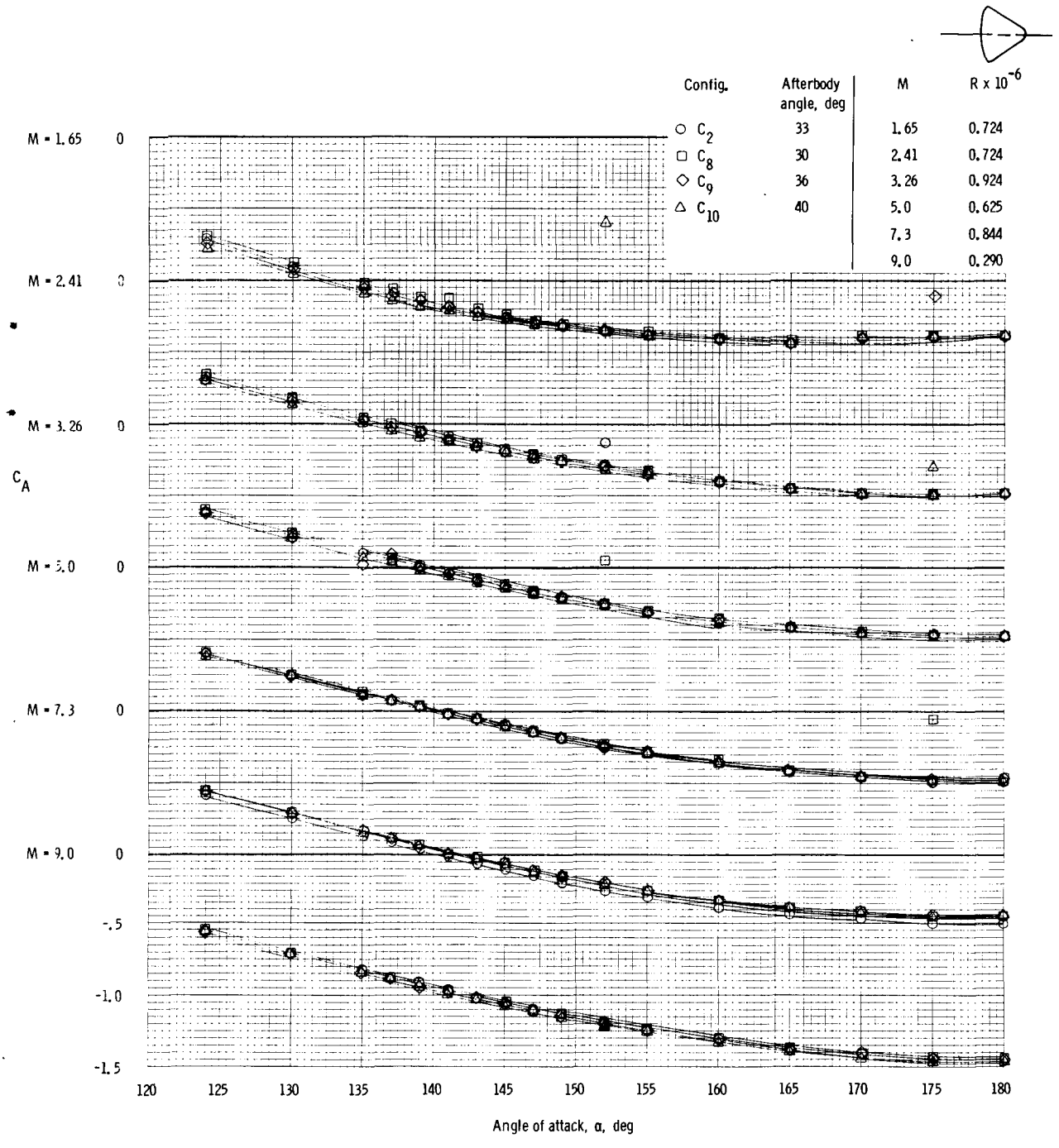

(e) Axial-force coefficient.

Figure 8. - Continued.

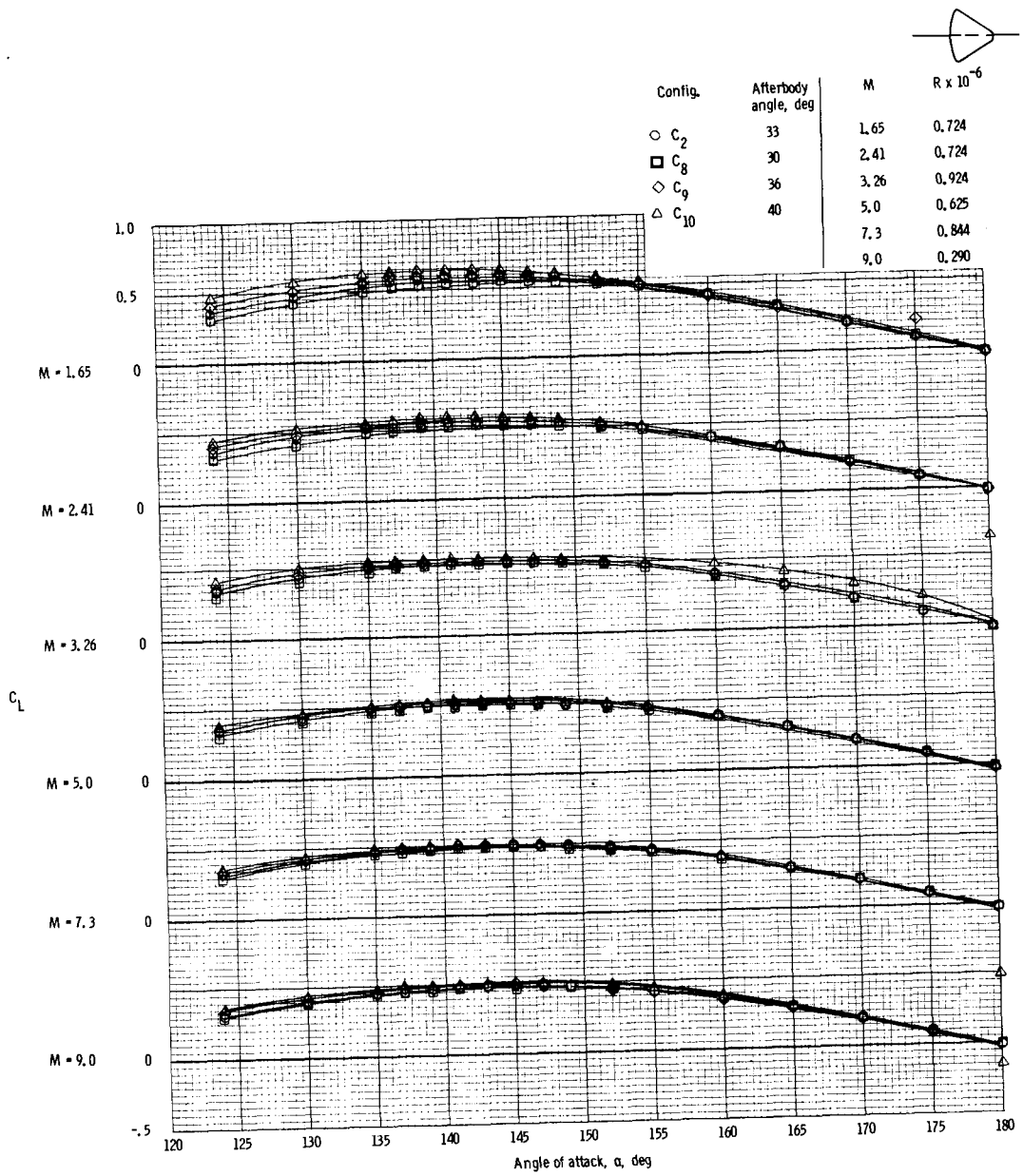

(f) Lift coefficient.

Figure 8. - Continued.

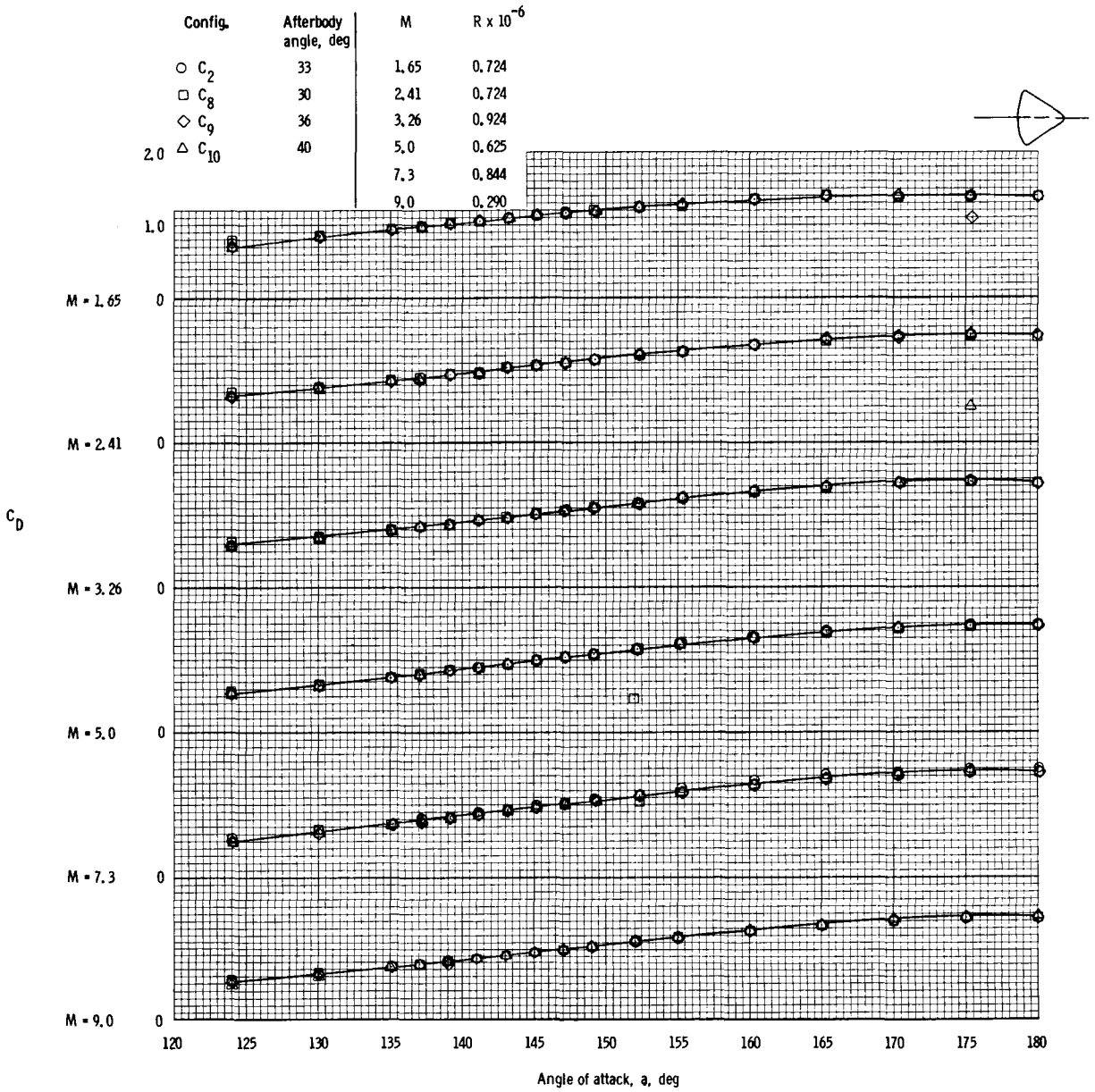

(g) Drag coefficient.

Figure 8. - Concluded.

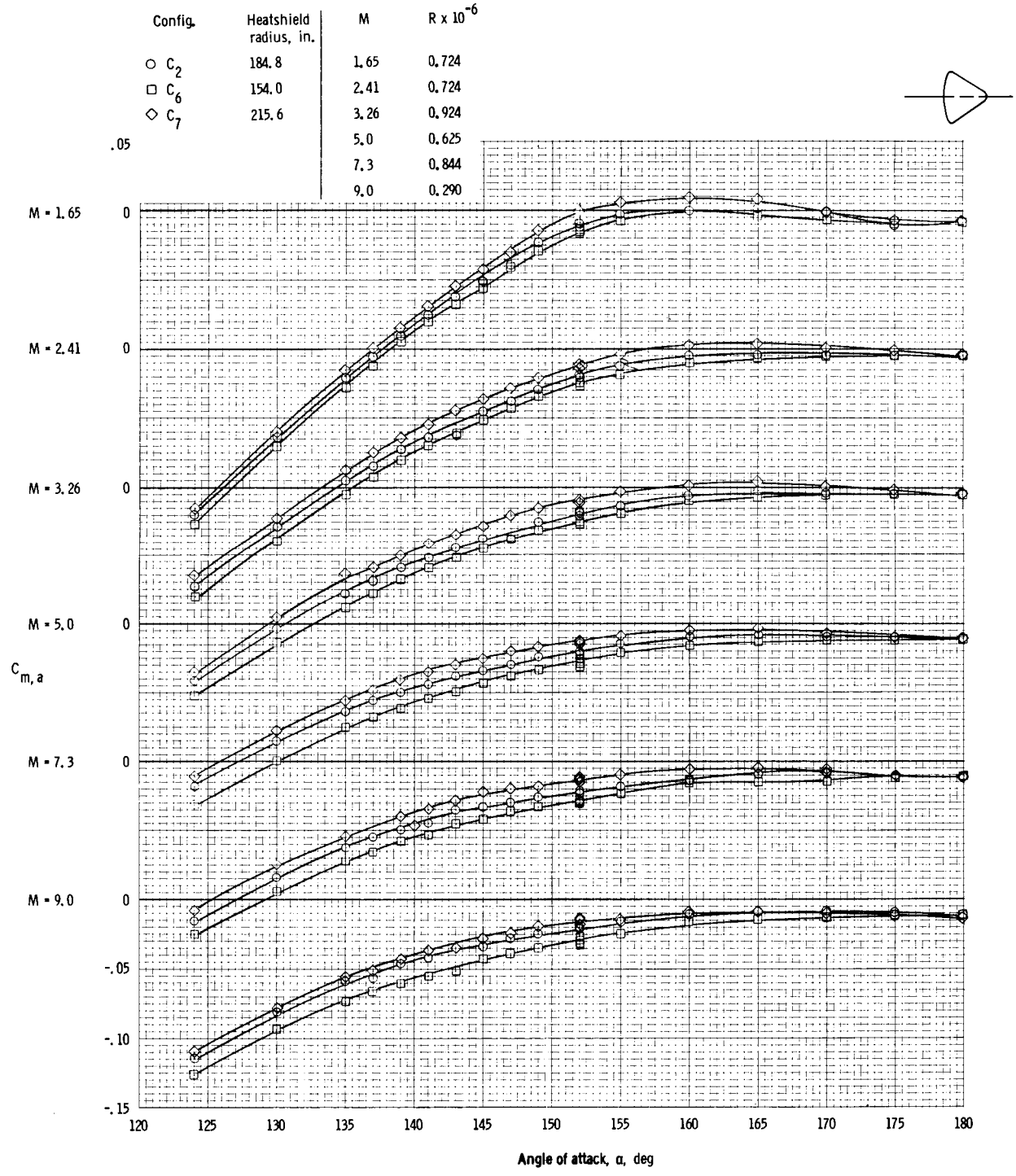

(a) Pitching-moment coefficient (apex).

Figure 9. - Aerodynamic characteristics of the Apollo command module with various heat-shield radii obtained at JPL-20 SWT and JPL-21 HWT facilities at M = 1.65 to M = 9.0.

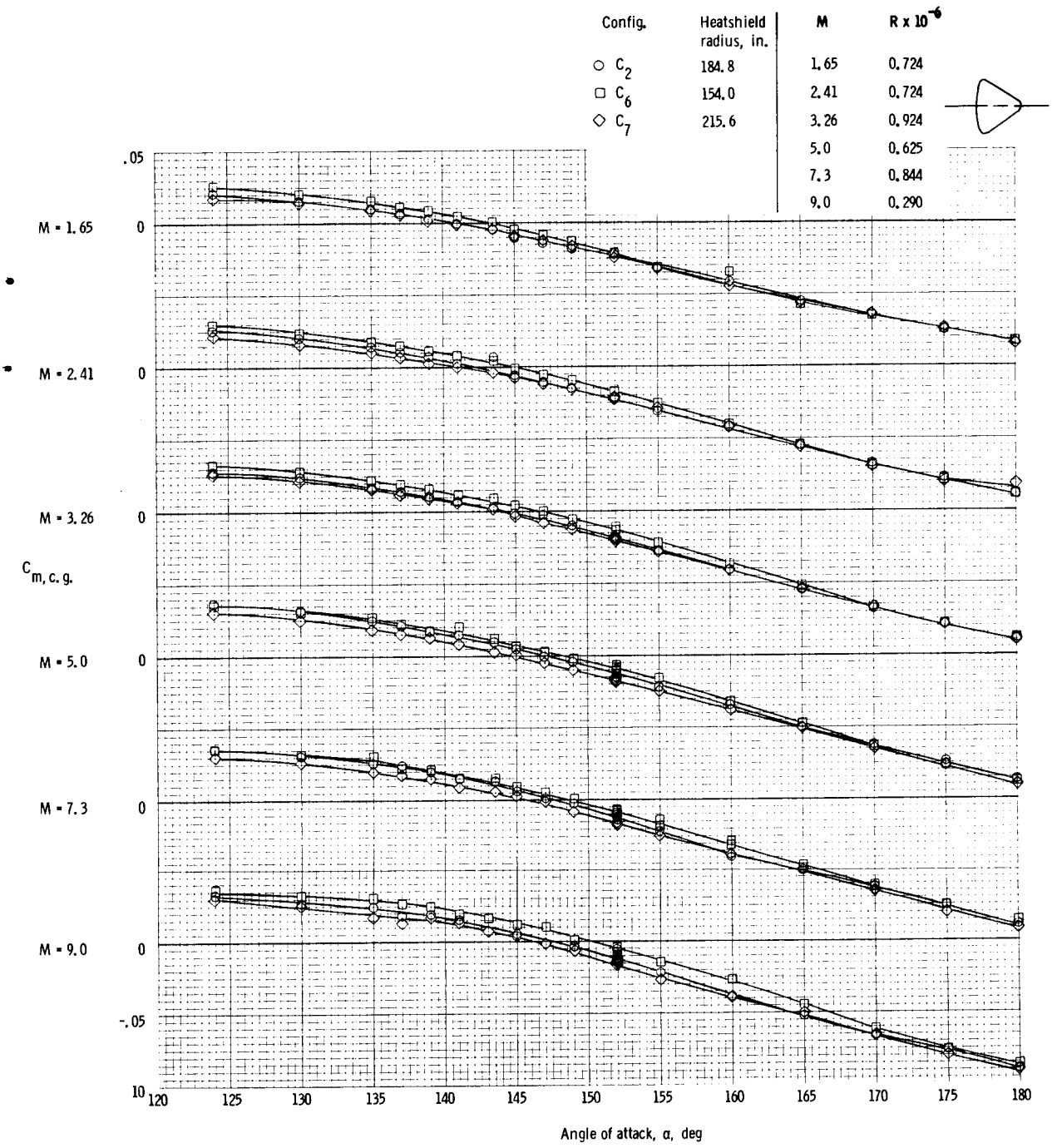

(b) Pitching-moment coefficient (c.g.).

Figure 9. - Continued.

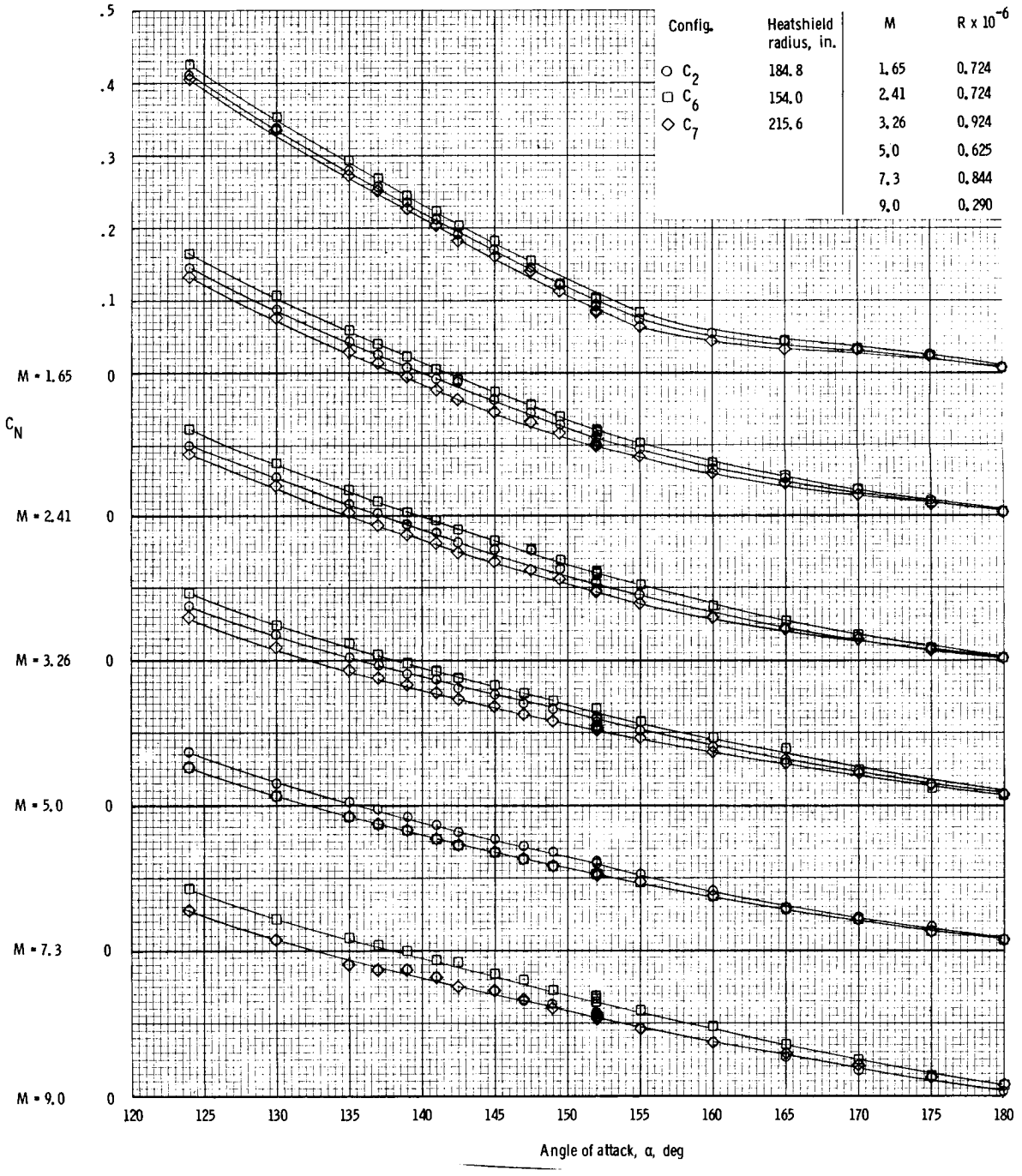

(c) Normal-force coefficient.

Figure 9. - Continued.

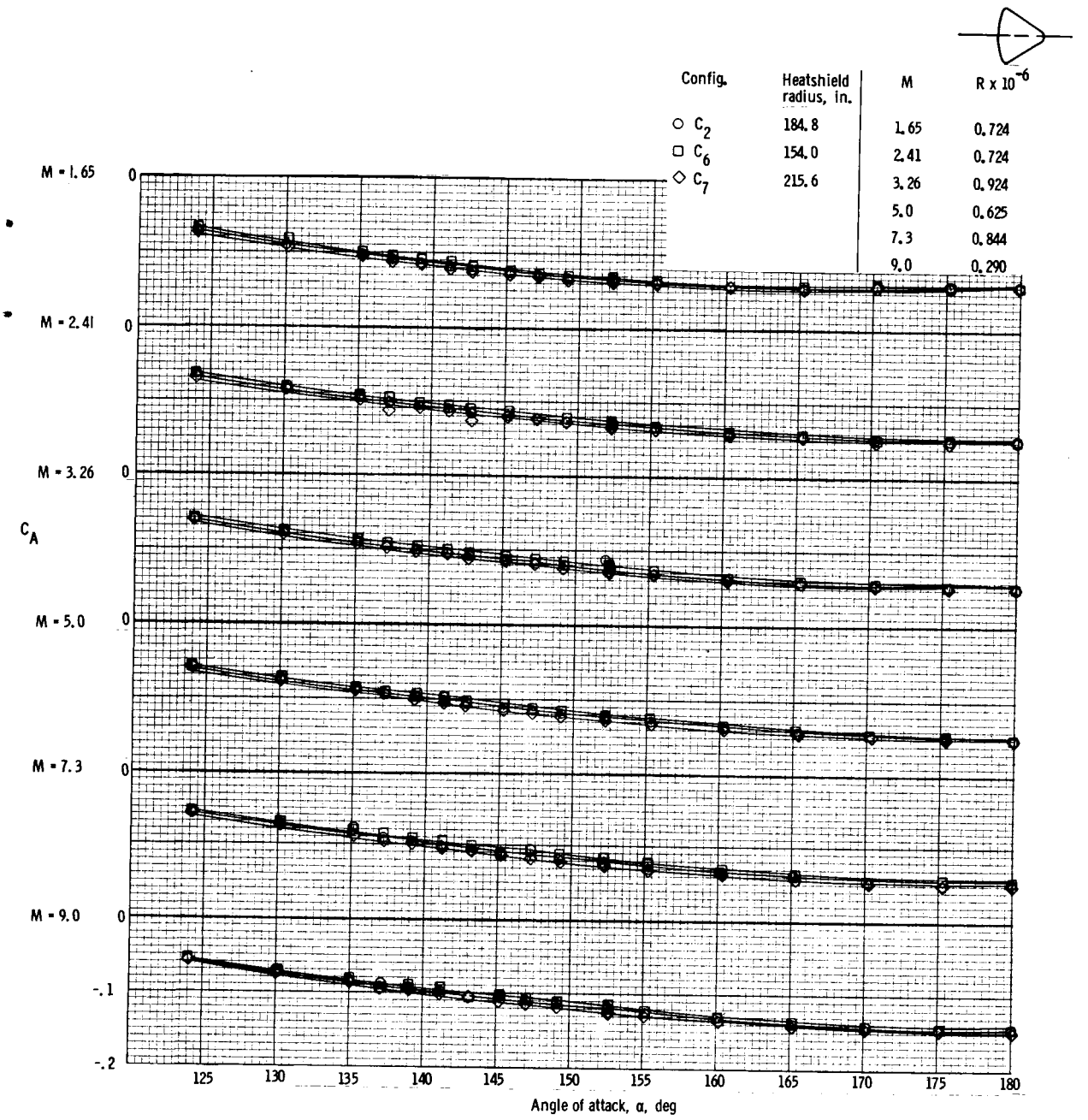

(d) Axial-force coefficient.

Figure 9. - Continued.

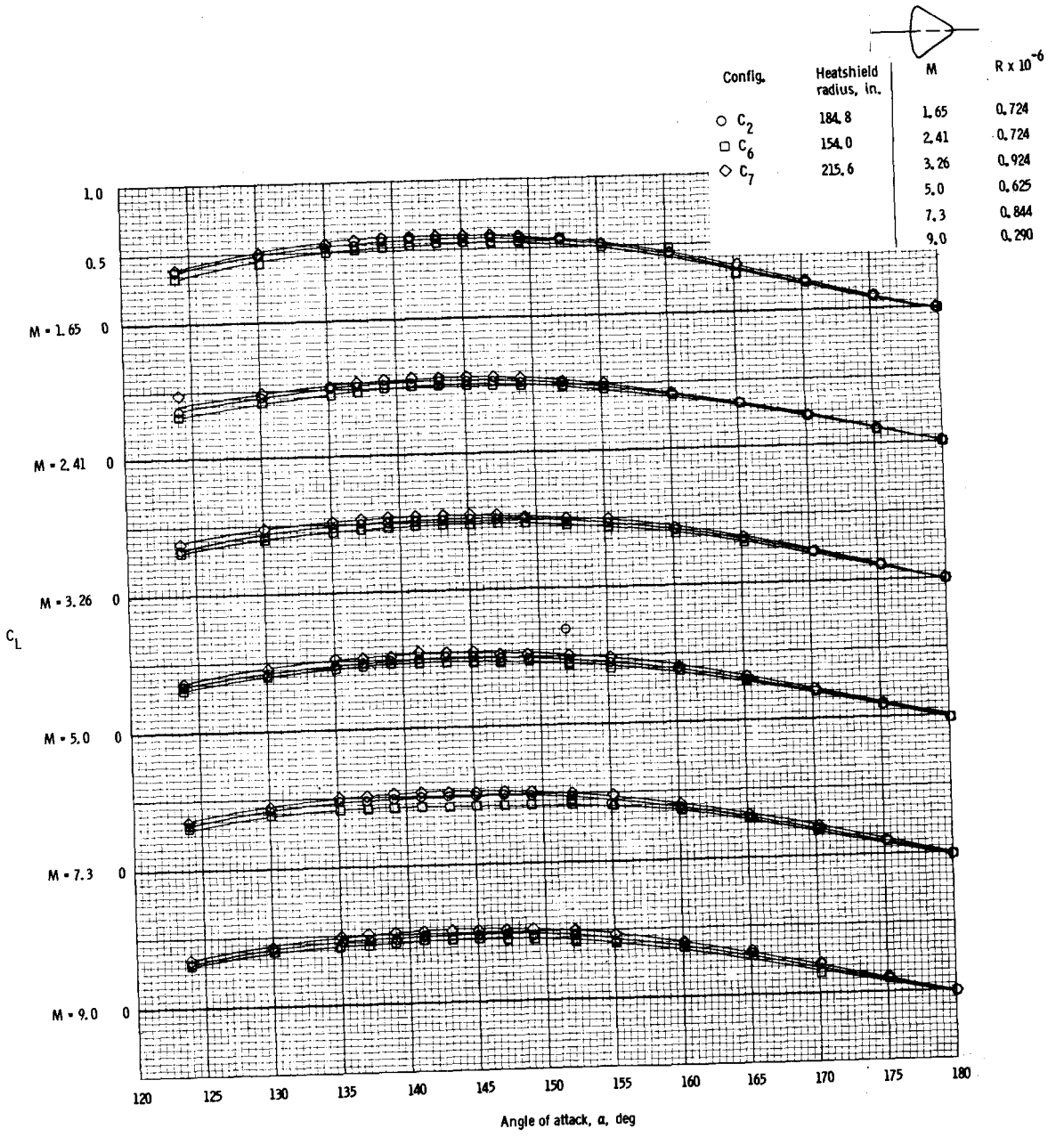

(e) Lift coefficient.

Figure 9. - Continued.

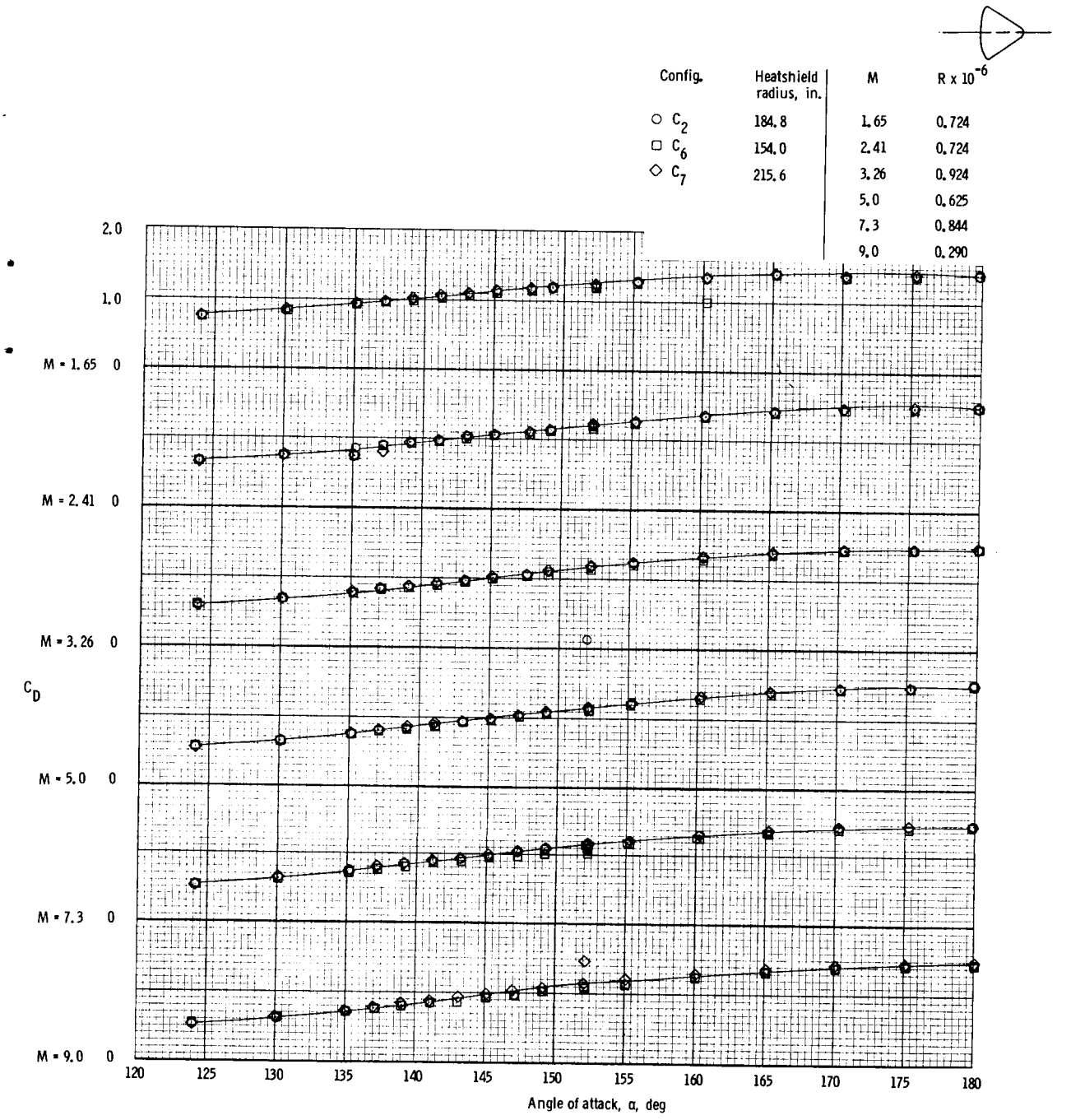

(f) Drag coefficient.

Figure 9. - Concluded.

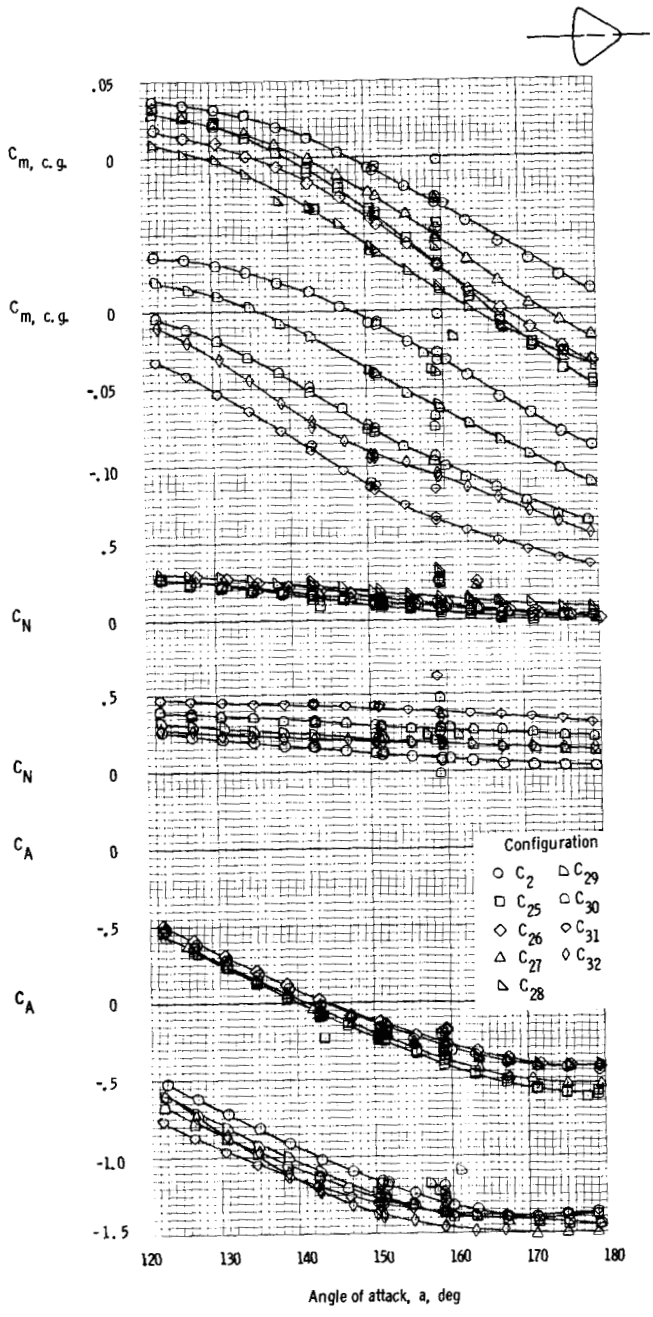

(a) Pitching-moment (c.g.), normal-force, and axial-force coefficients.

Figure 10. - Aerodynamic characteristics of the Apollo command module with heat-shield flaps (C_{25}), corner modifications (C_{26} and C_{27}), and canted heat shields (C_{28} to C_{32}) obtained at JPL-21 HWT facility at M = 7.3, $R \times 10^{-6}$ = 0.83 (c.g. = x/d = -0.685, z/d = 0.059).

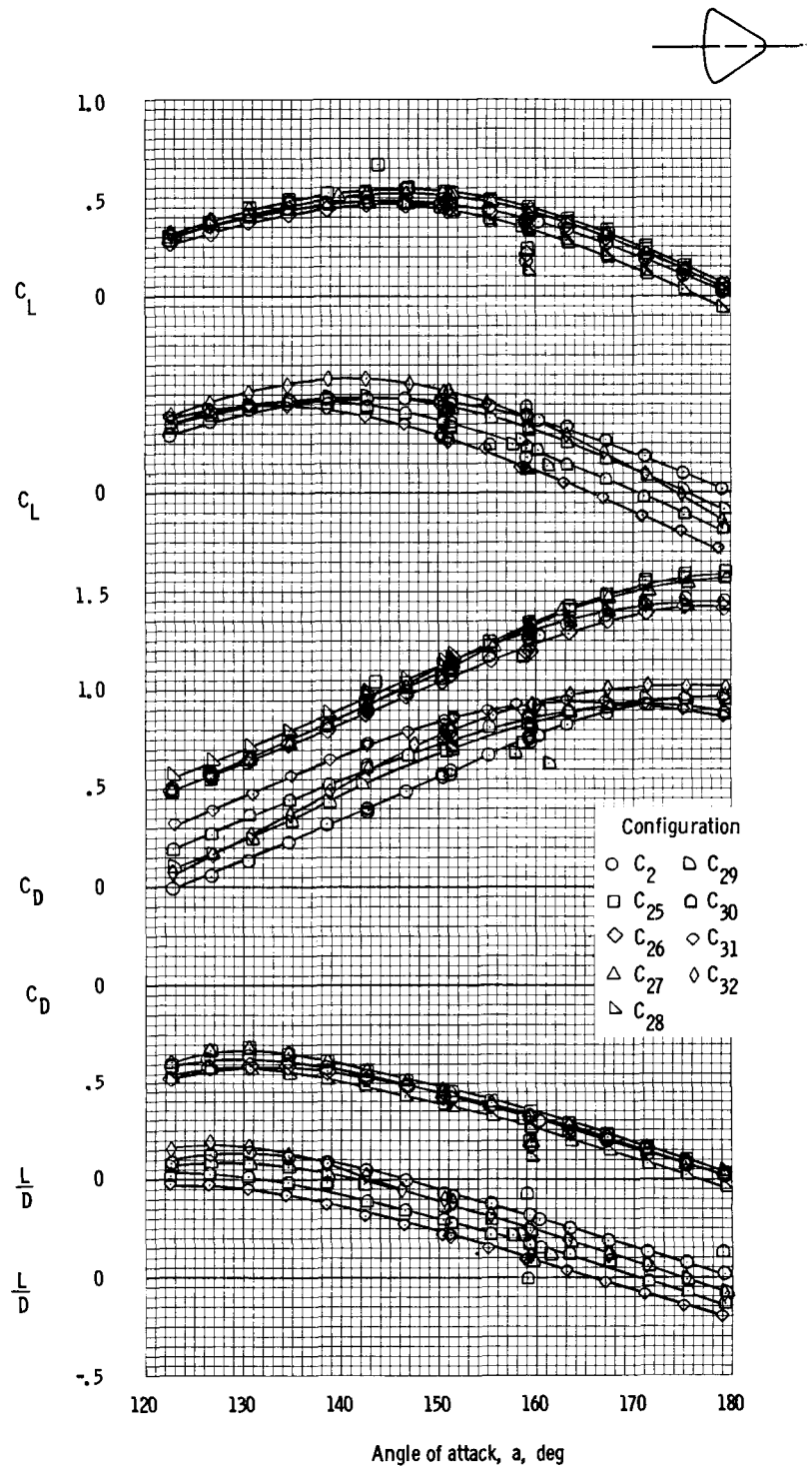

(b) Lift and drag coefficient and lift-to-drag ratio.

Figure 10. - Concluded.

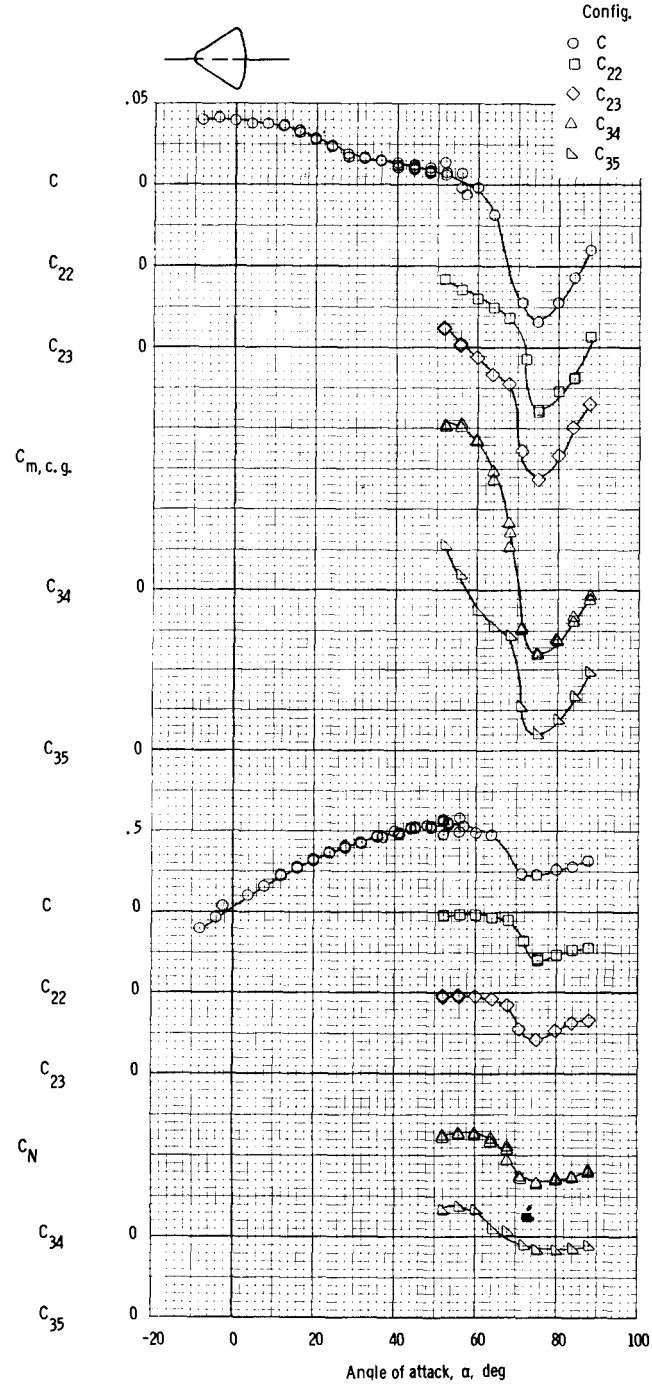

(a) Pitching-moment (c.g.) and normal-force coefficients.

Figure 11. - Aerodynamic characteristics of the Apollo command module with apex modifications obtained at Ames 2- by 2-foot TWT facility at M = 0.7, $R \times 10^{-6}$ = 2.1 (c.g. = x/d = -0.685, z/d = 0.059).

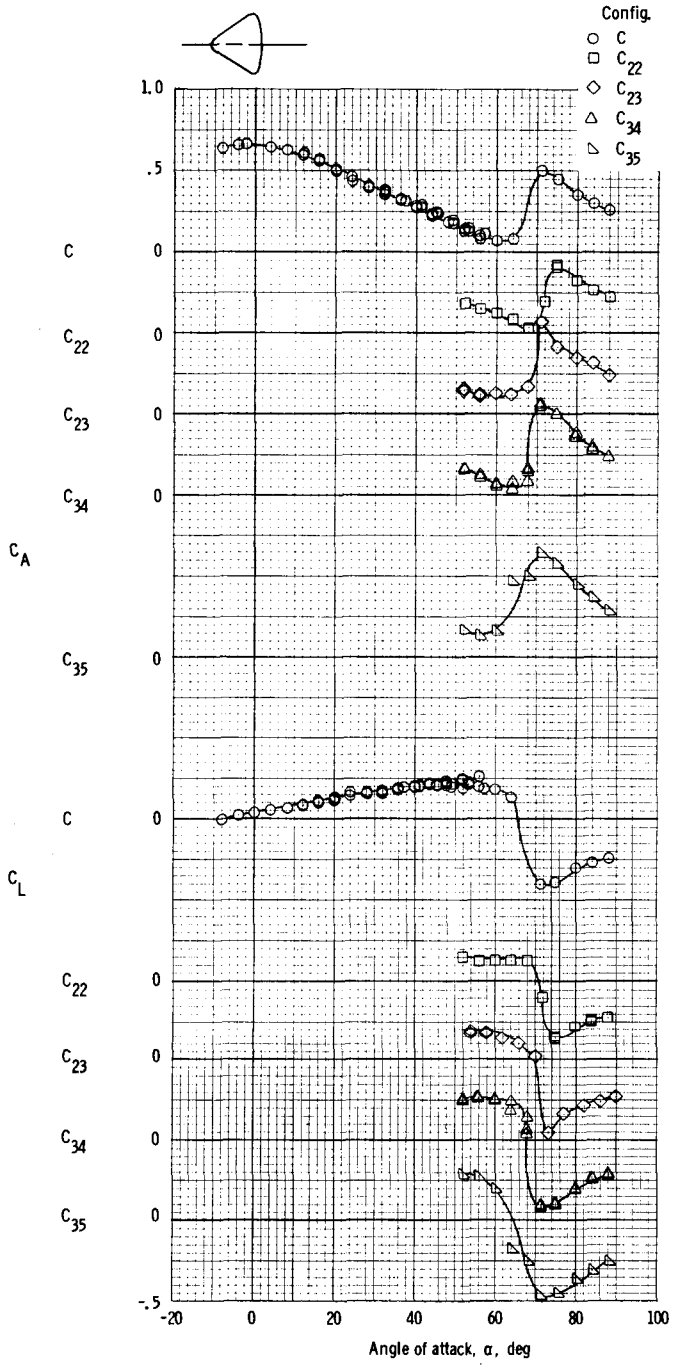

(b) Axial-force and lift coefficients.

Figure 11. - Continued.

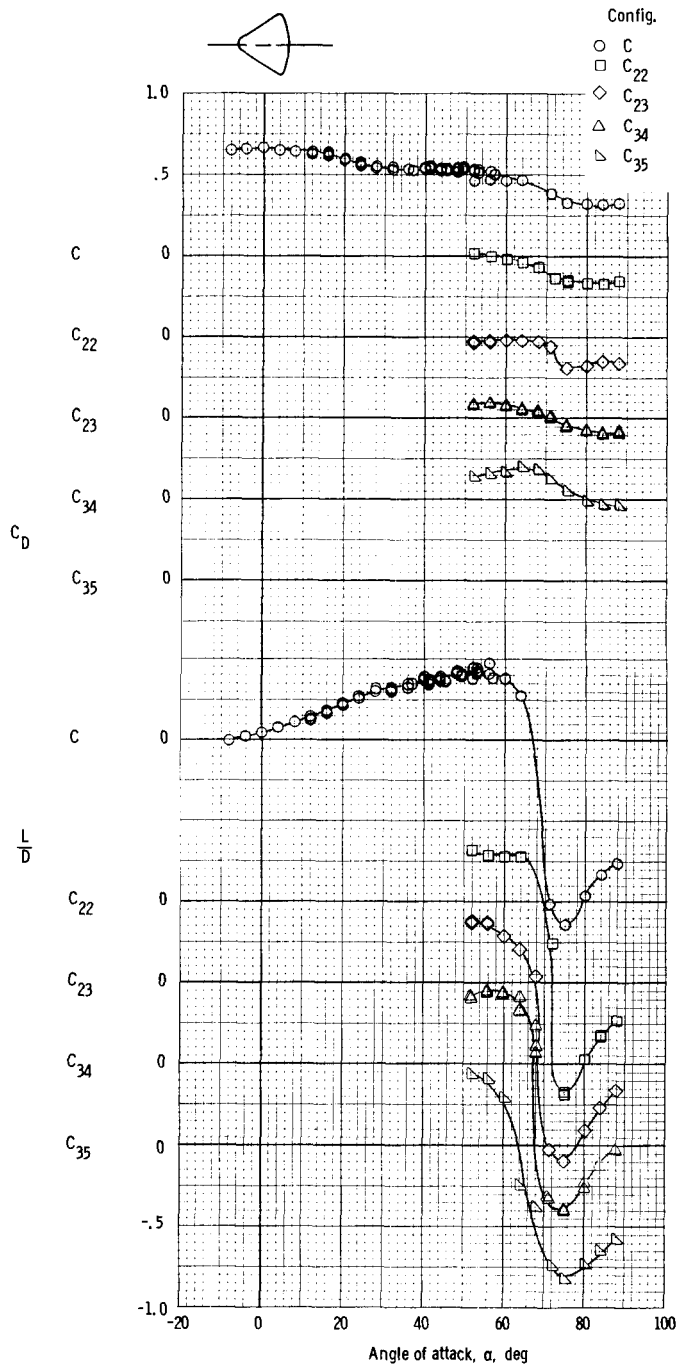

(c) Drag coefficient and lift-to-drag ratio.

Figure 11. - Concluded.

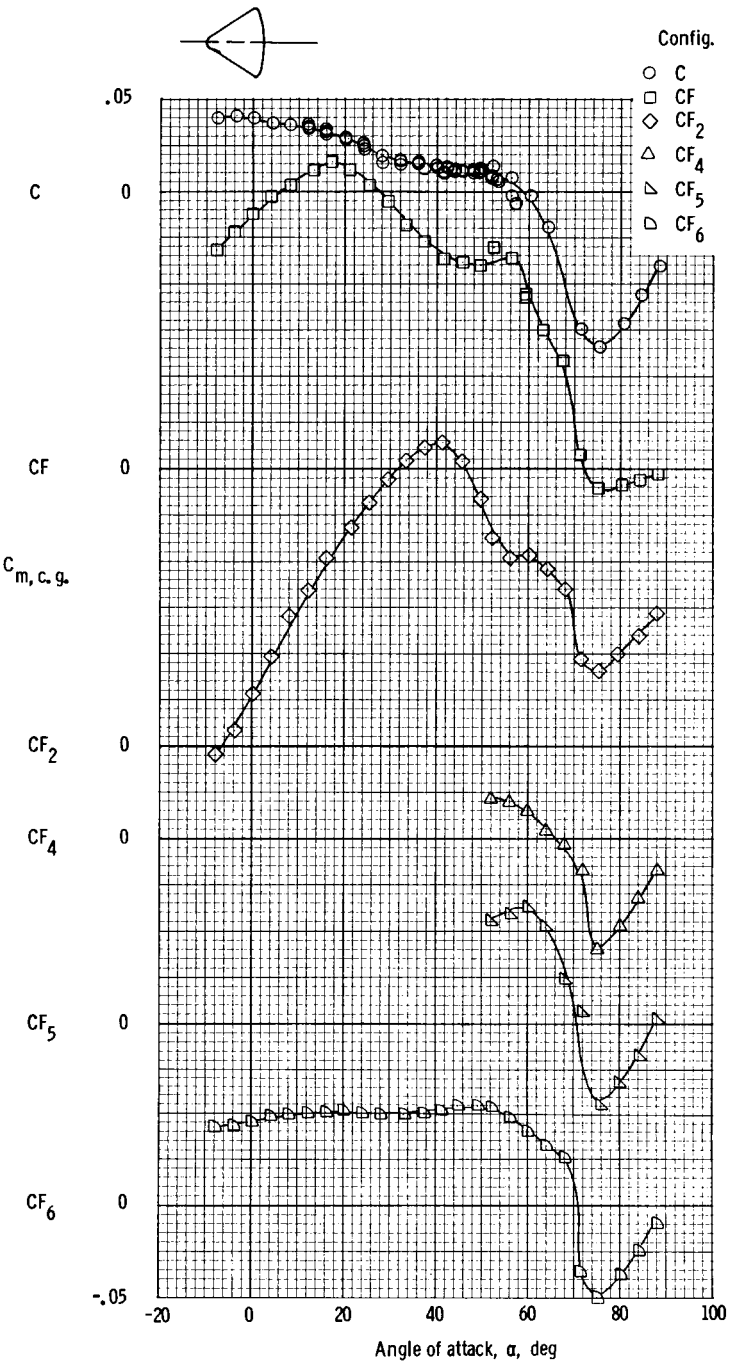

(a) Pitching-moment coefficient (c.g.).

Figure 12. - Aerodynamic characteristics of the Apollo command module with flaps obtained at the Ames 2- by 2-foot TWT facility at $M = 0.7$, $R \times 10^{-6} = 2.1$ (c.g. = x/d = -0.685, z/d = 0.059).

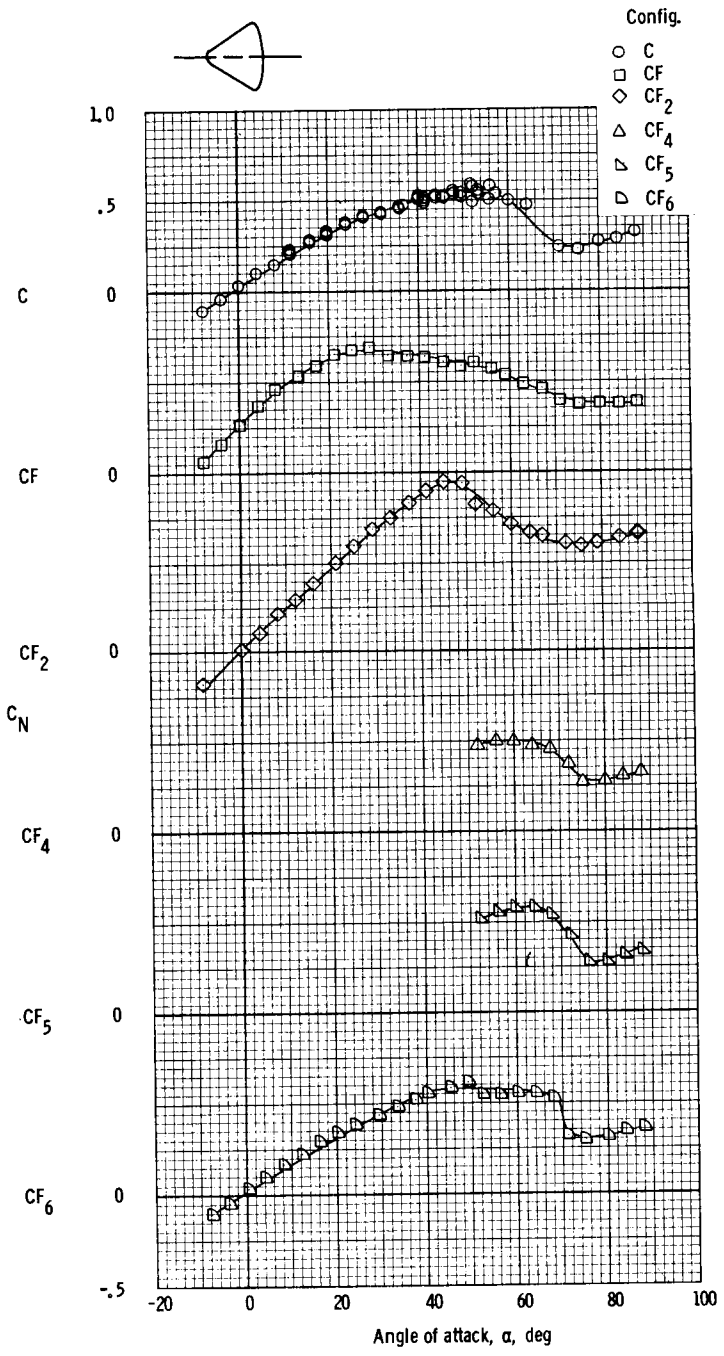

(b) Normal-force coefficient.

Figure 12. - Continued.

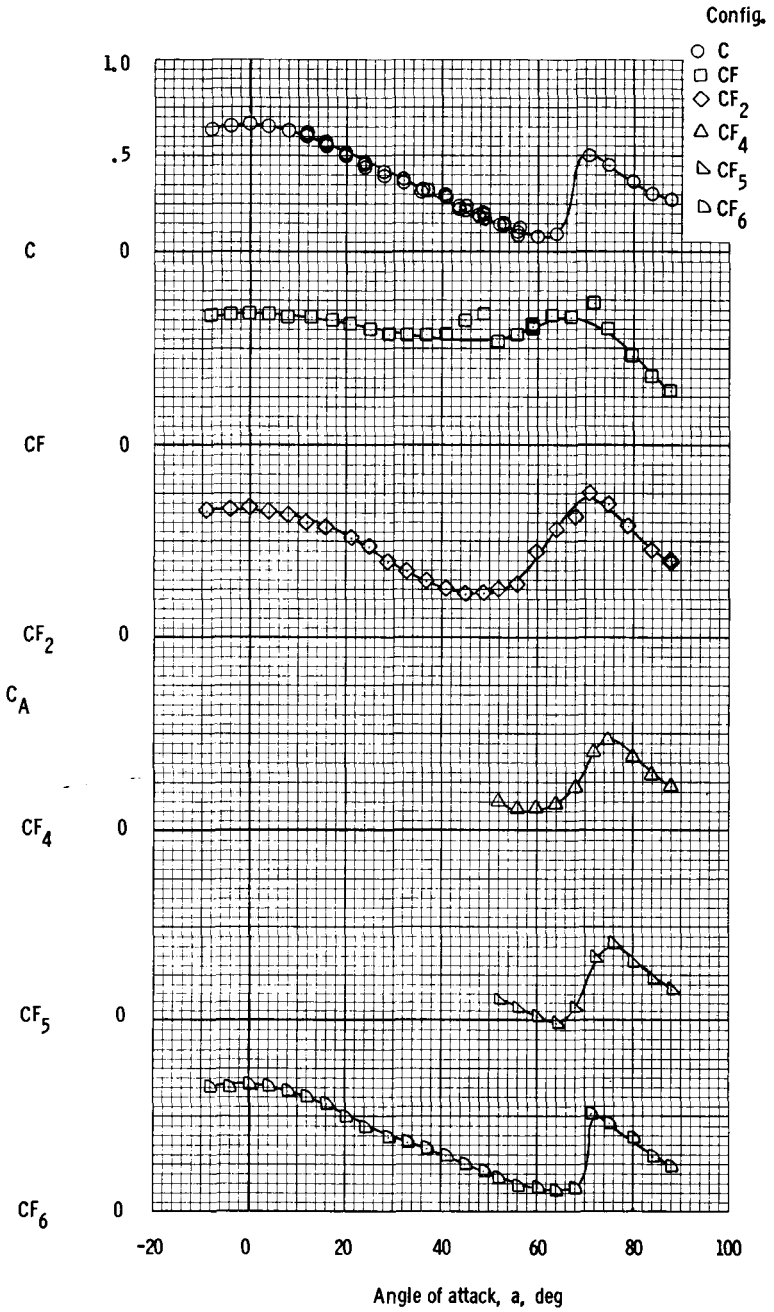

(c) Axial-force coefficient.

Figure 12. - Continued.

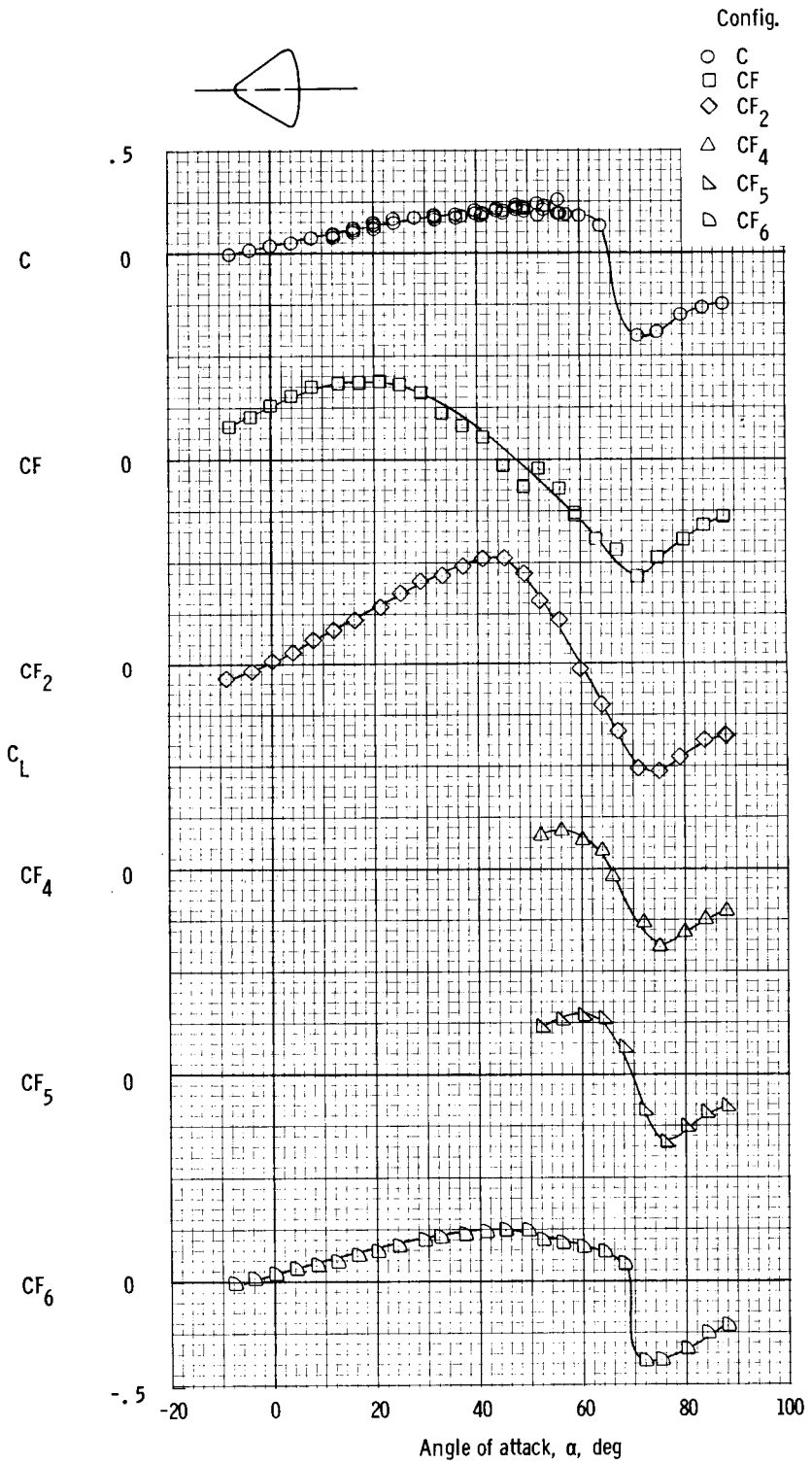

(d) Lift coefficient.

Figure 12. - Continued.

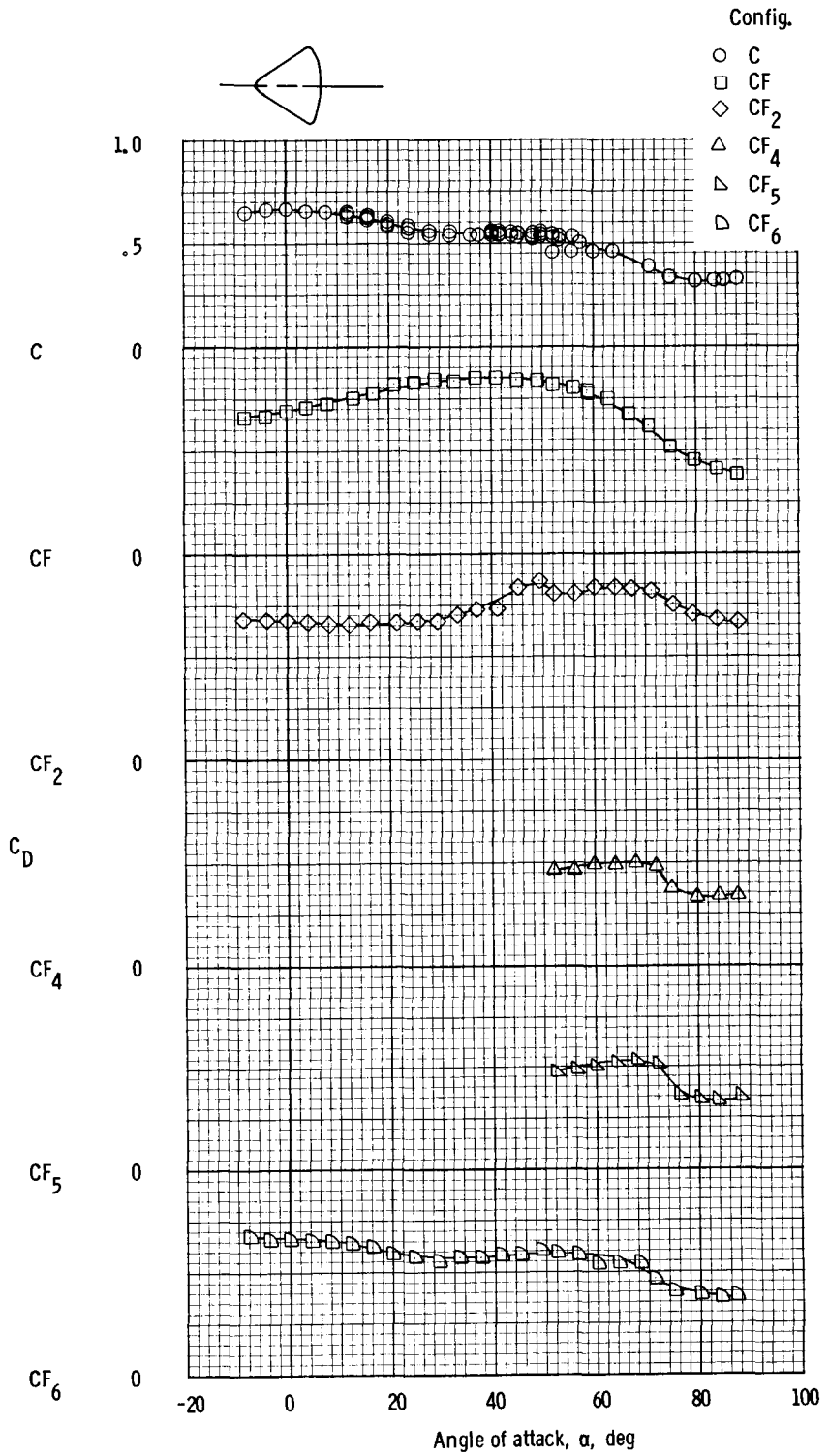

(e) Drag coefficient.

Figure 12. - Concluded.

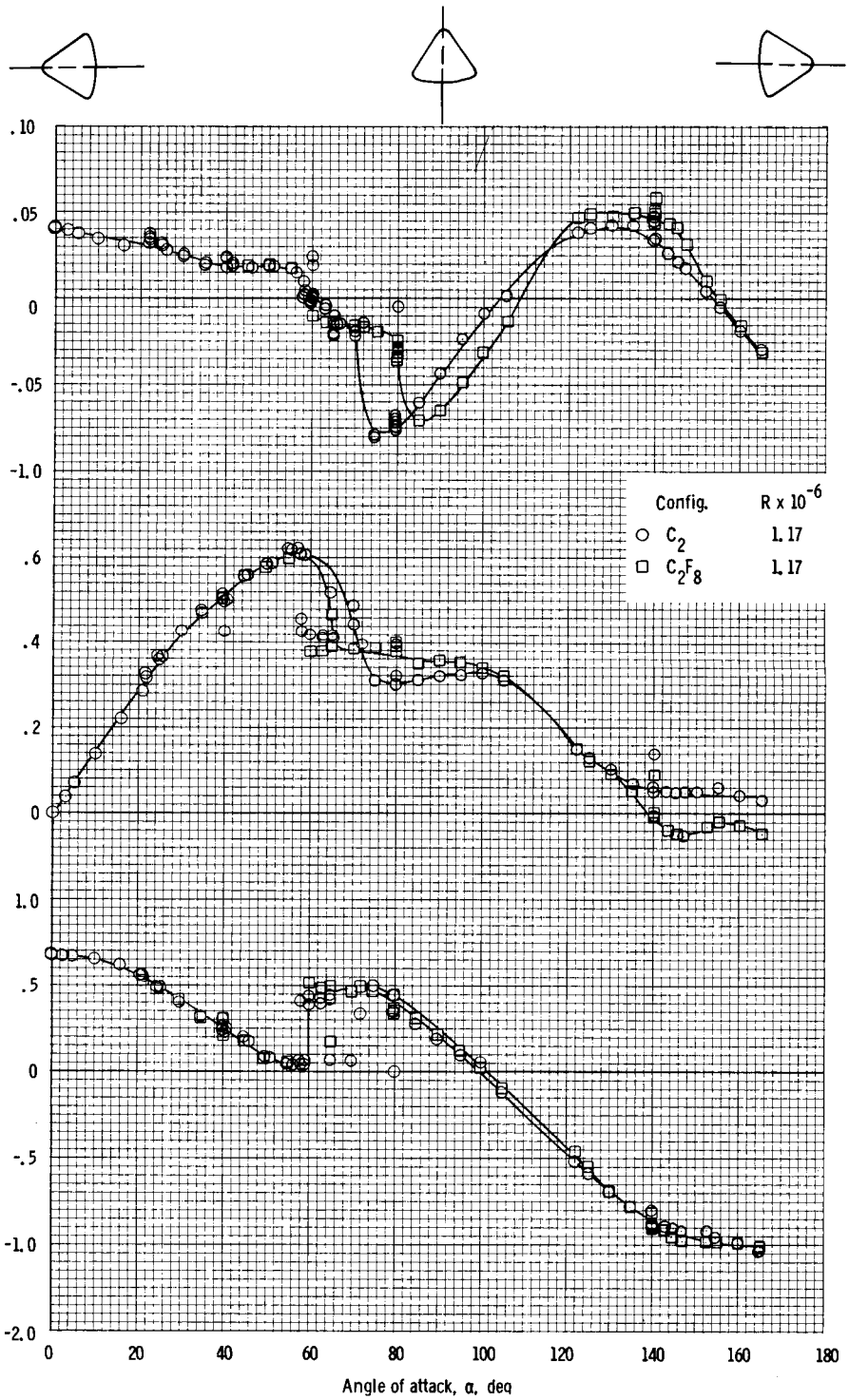

(a) Pitching-moment (c. g.), normal-force and axial-force coefficients.

Figure 13. - Aerodynamic characteristics of the Apollo command module with flaps obtained at JPL-20 SWT facility at M = 0. 7 (c. g. = x/d = -0. 685, z/d = 0. 059).

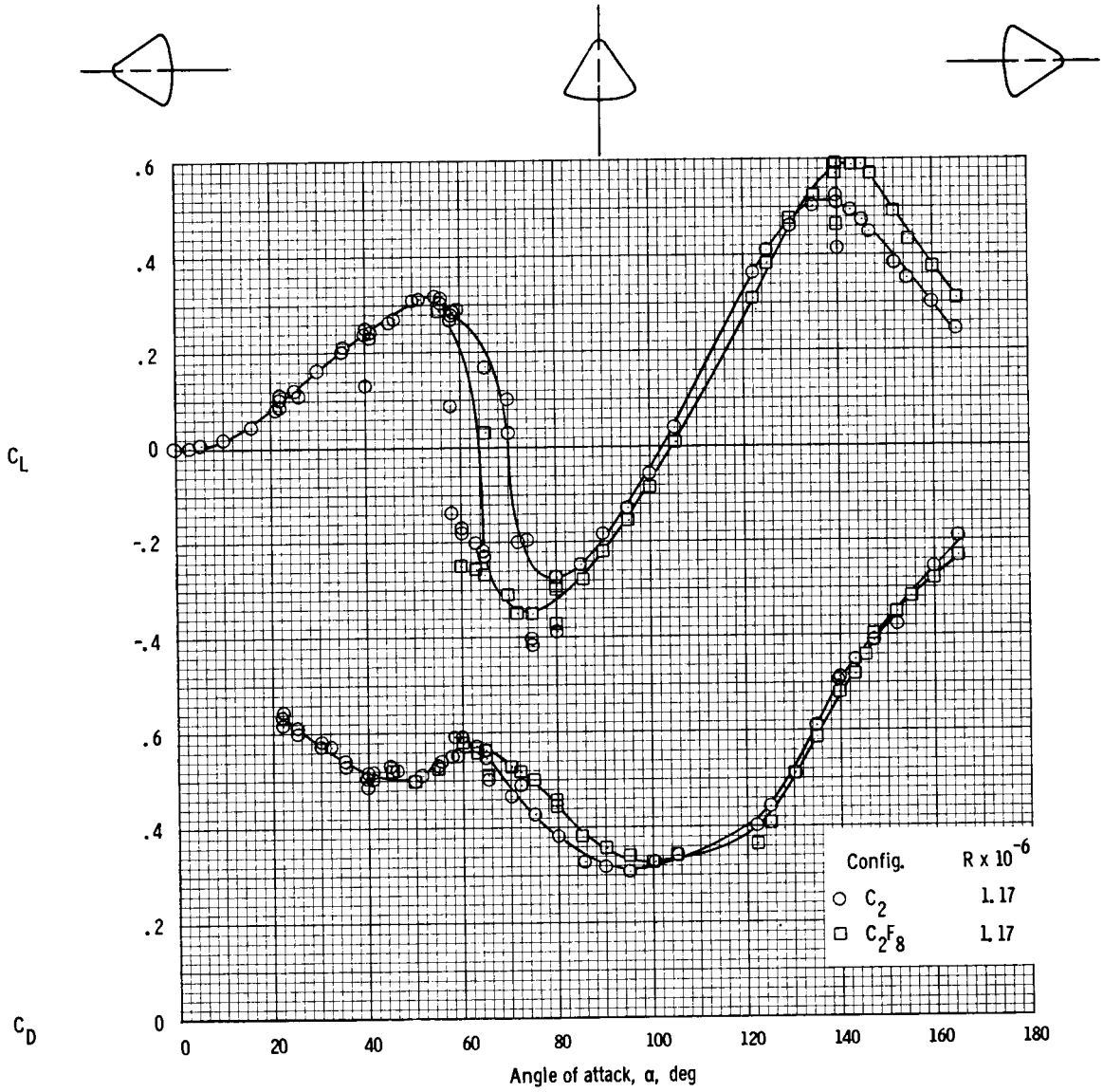

(b) Lift and drag coefficients.

Figure 13. - Concluded.

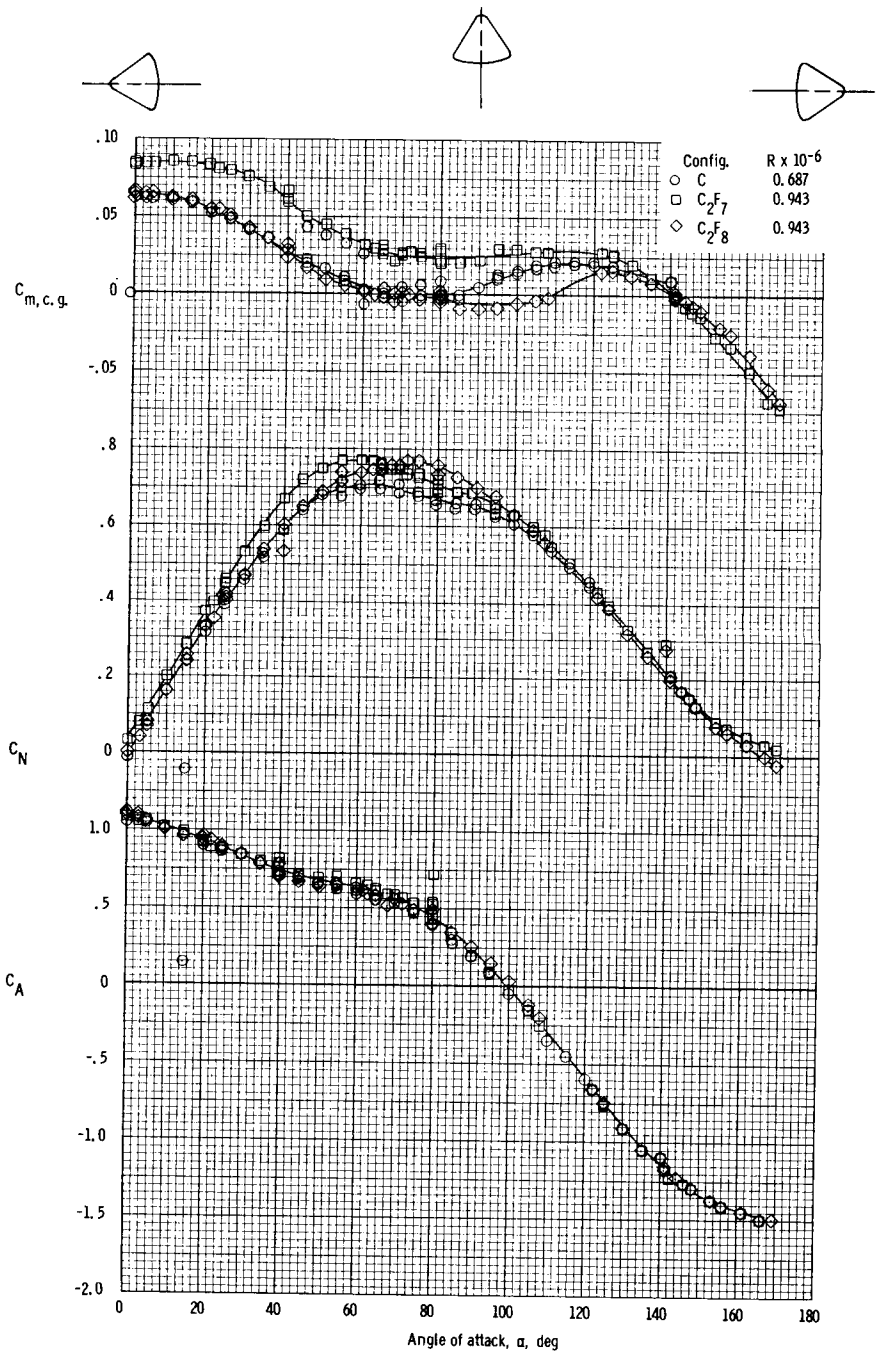

(a) Pitching-moment (c.g.), normal-force, and axial-force coefficients at M = 1.65.

Figure 14. - Aerodynamic characteristics of the Apollo command module with flaps obtained at JPL-20 SWT facility at M = 1.65 and M = 5.0 (c.g. = x/d = -0.685, z/d = 0.059).

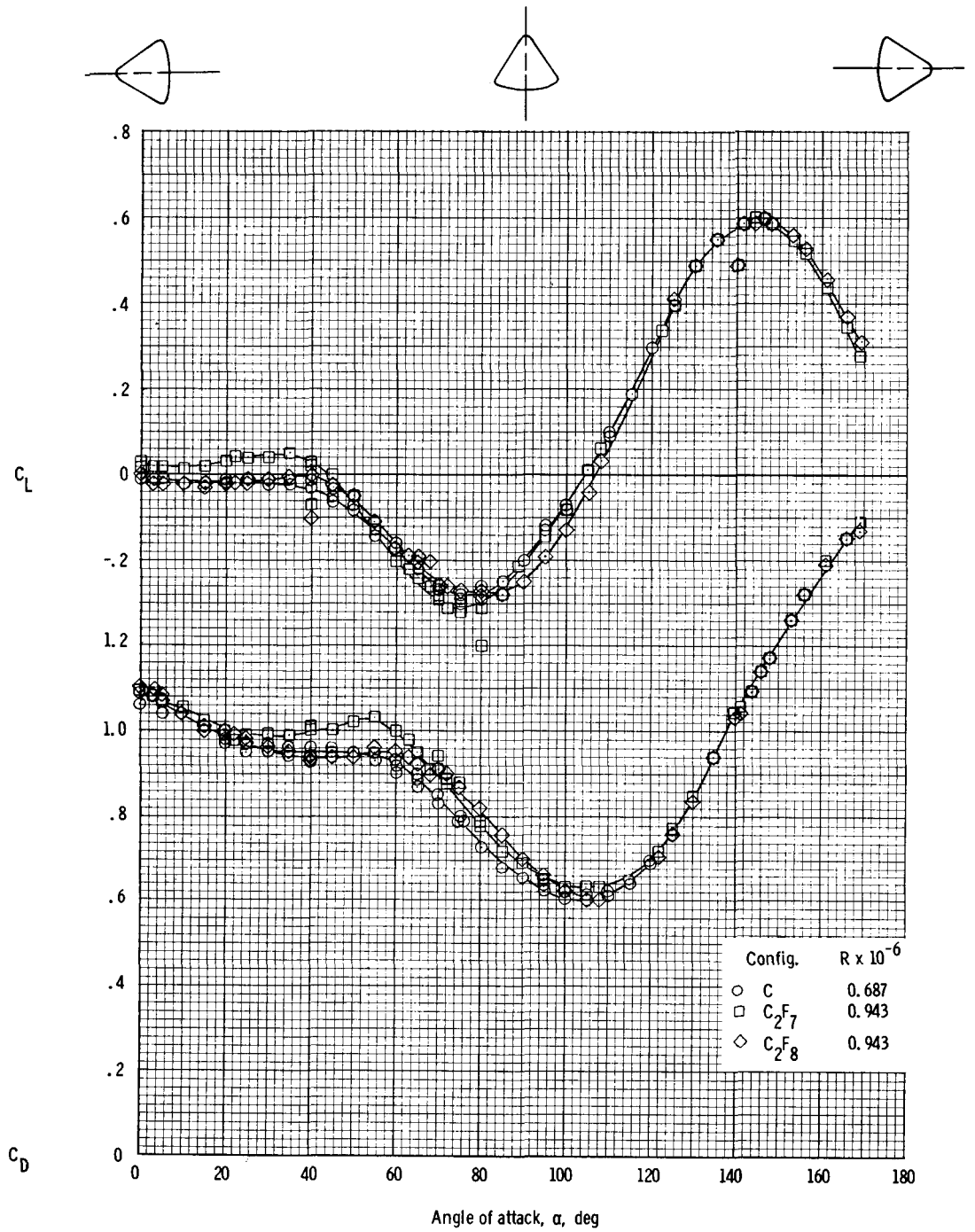

(b) Lift and drag coefficients.

Figure 14. - Continued.

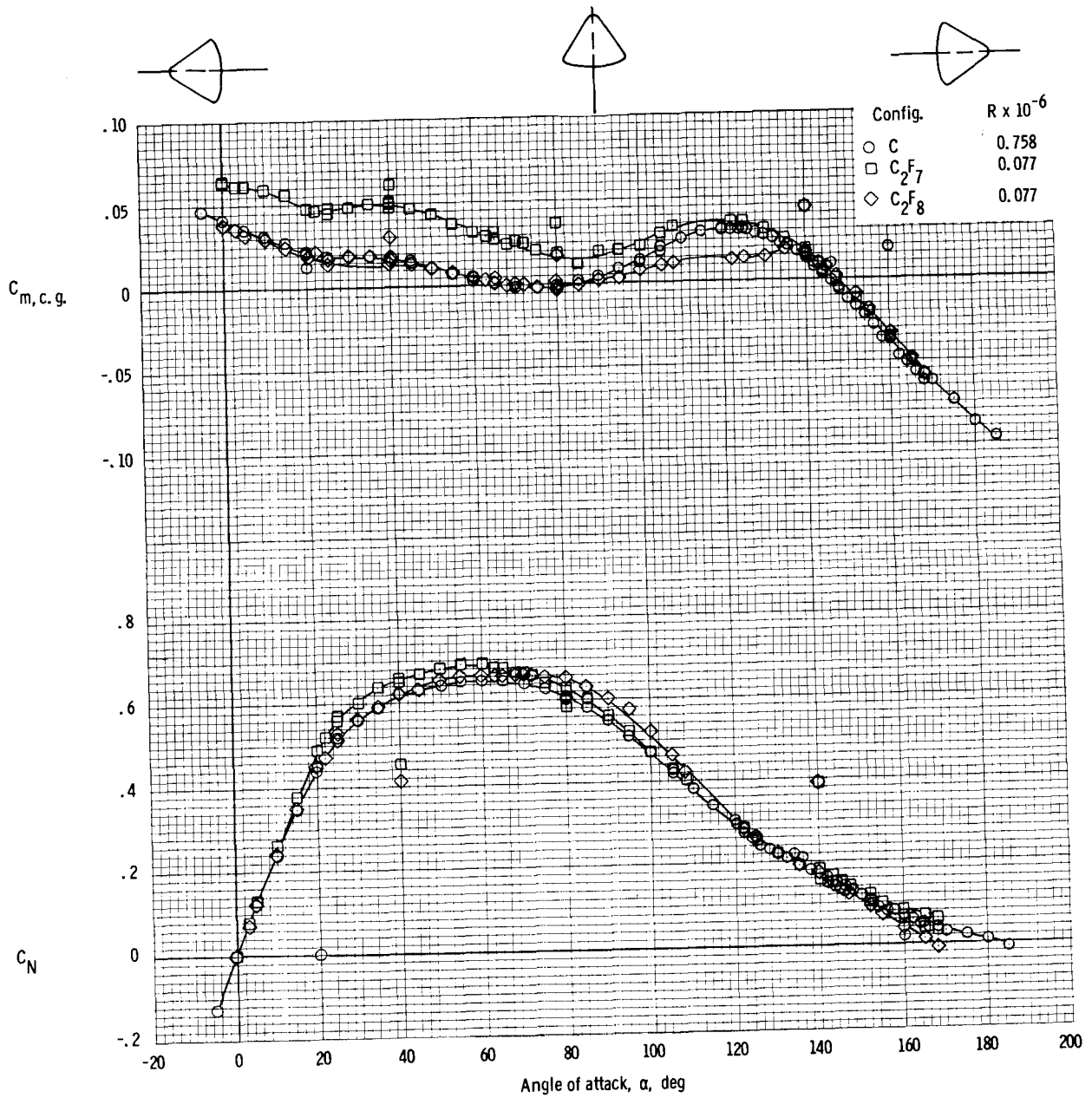

(c) Pitching-moment (c.g.) and normal-force coefficients.

Figure 14. - Continued.

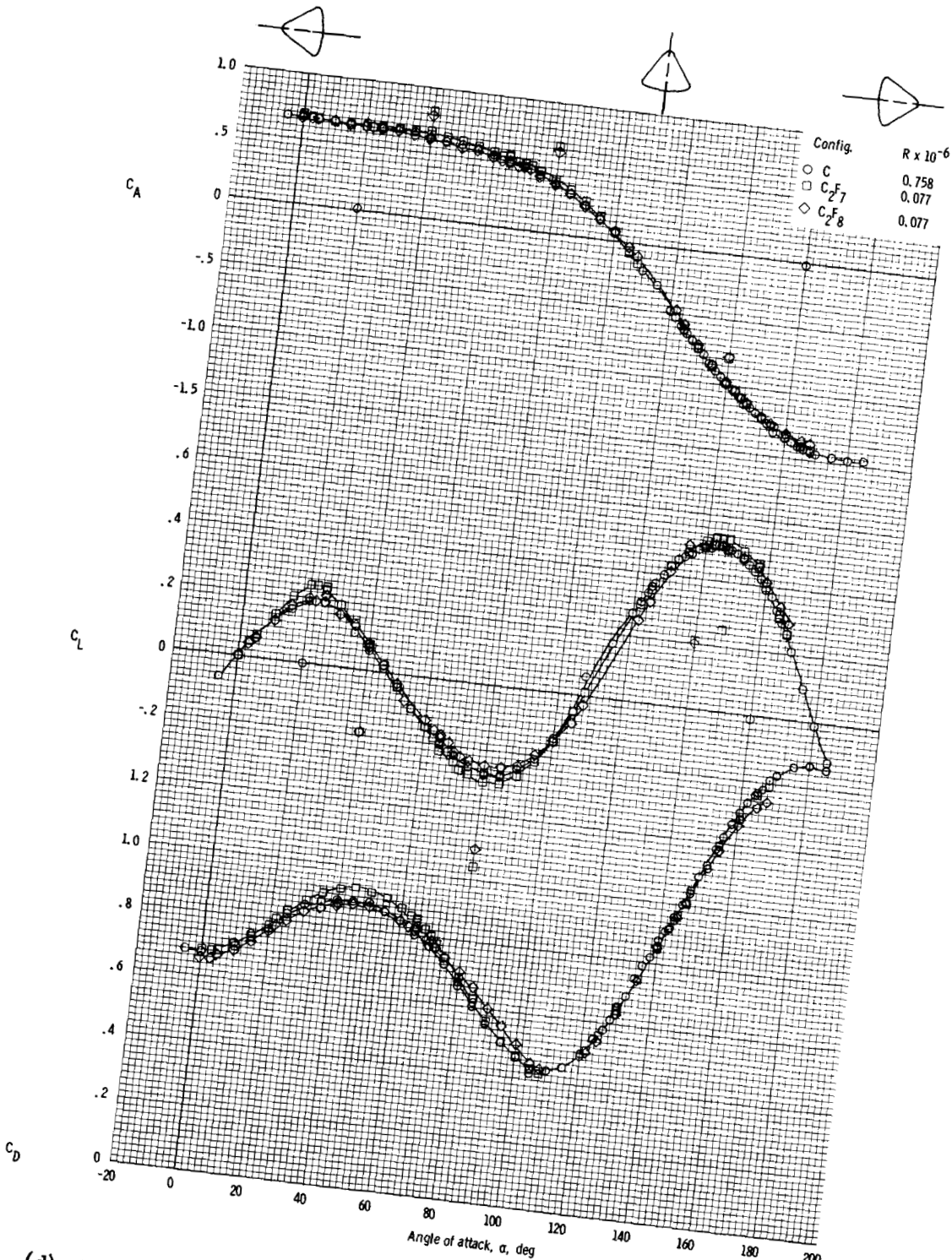

(d) Axial-force, lift, and drag coefficients at $M = 5.0$.

Figure 14. - Concluded.

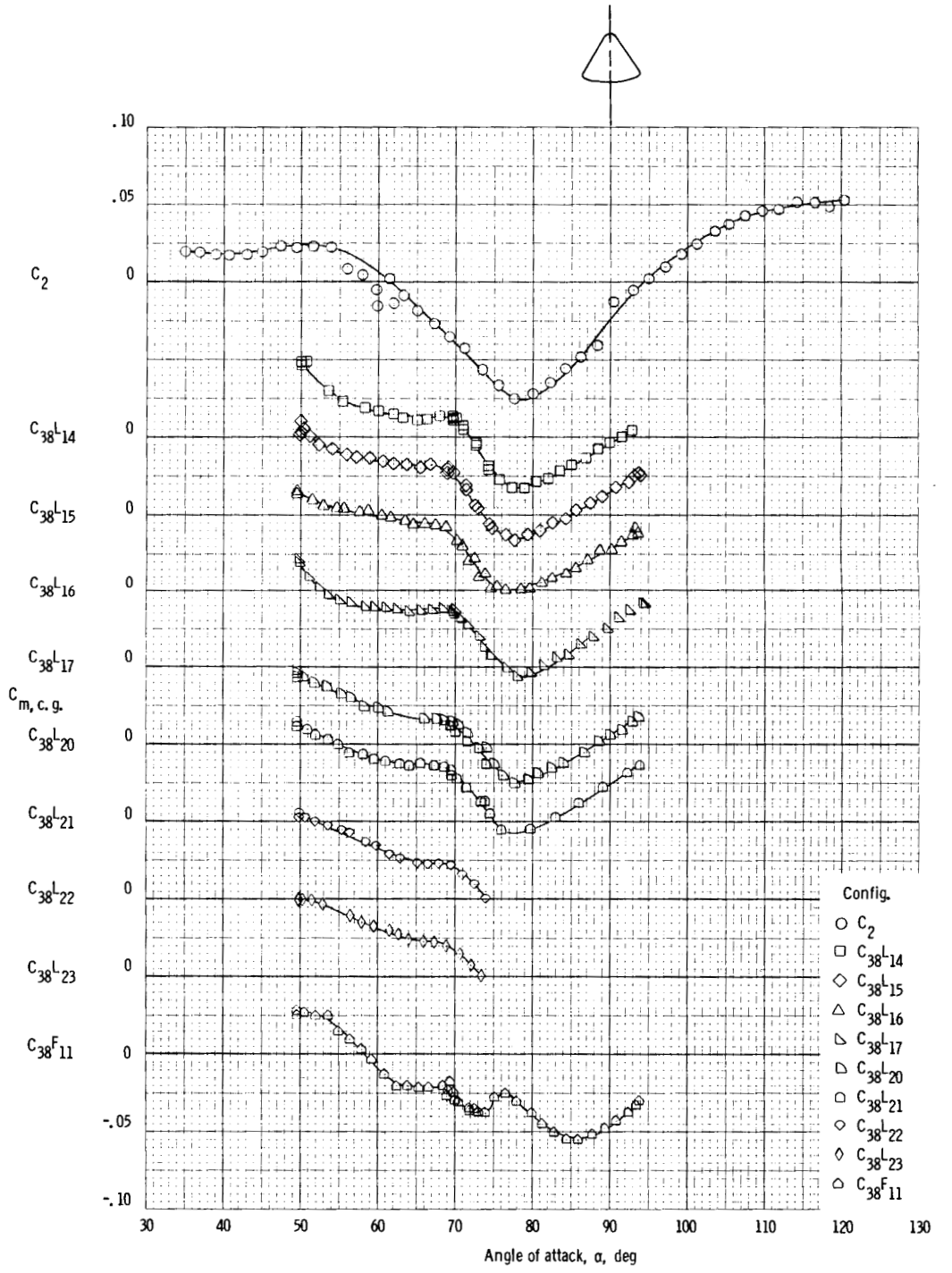

(a) Pitching-moment coefficient (c.g.).

Figure 15. - Aerodynamic characteristics of the Apollo command module with strakes and flaps obtained at NAA-TWT facility at $M = 0.7$, $R \times 10^{-6} = 13.0$ (c.g. = x/d = -0.685, z/d = 0.059).

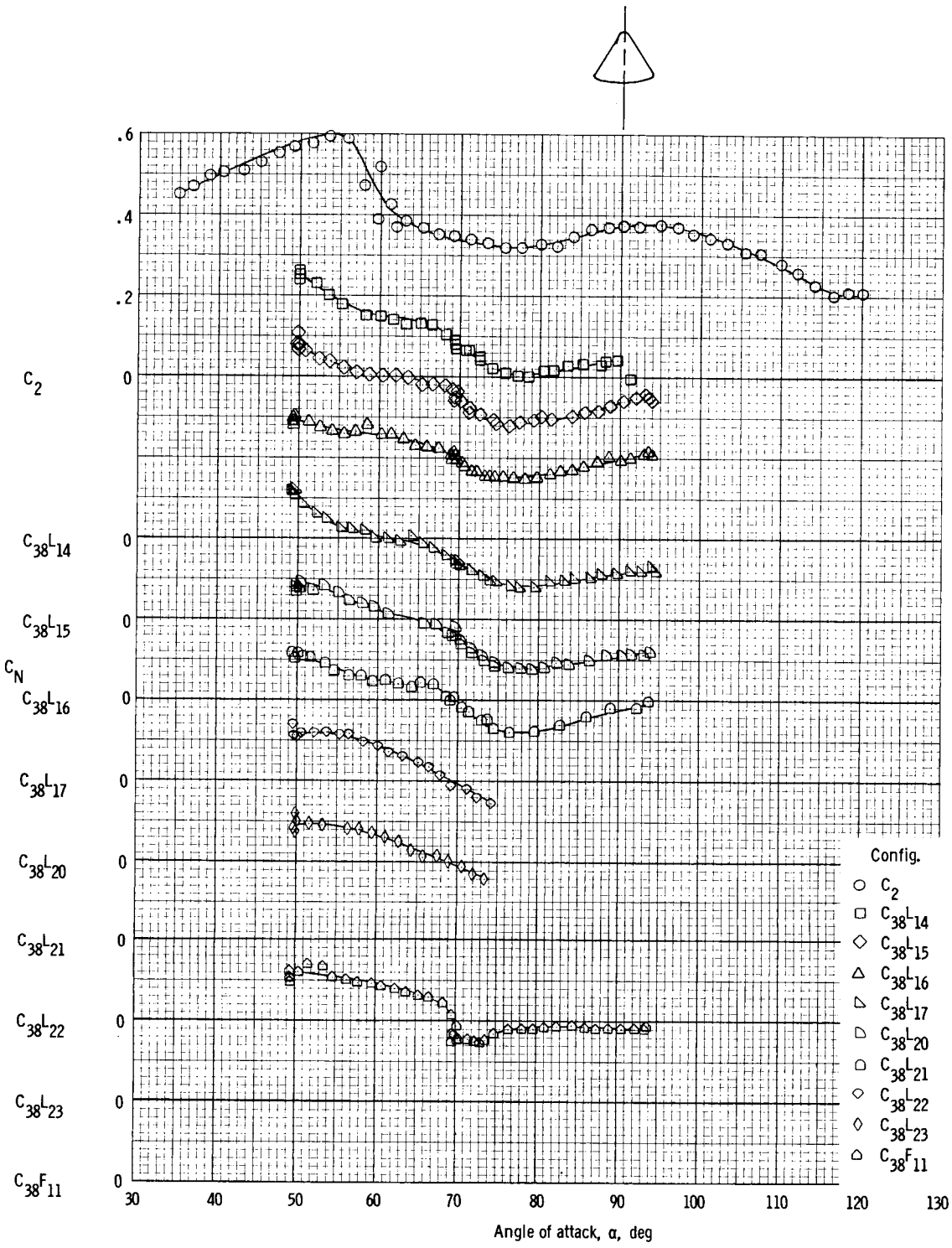

(b) Normal-force coefficient.

Figure 15. - Continued.

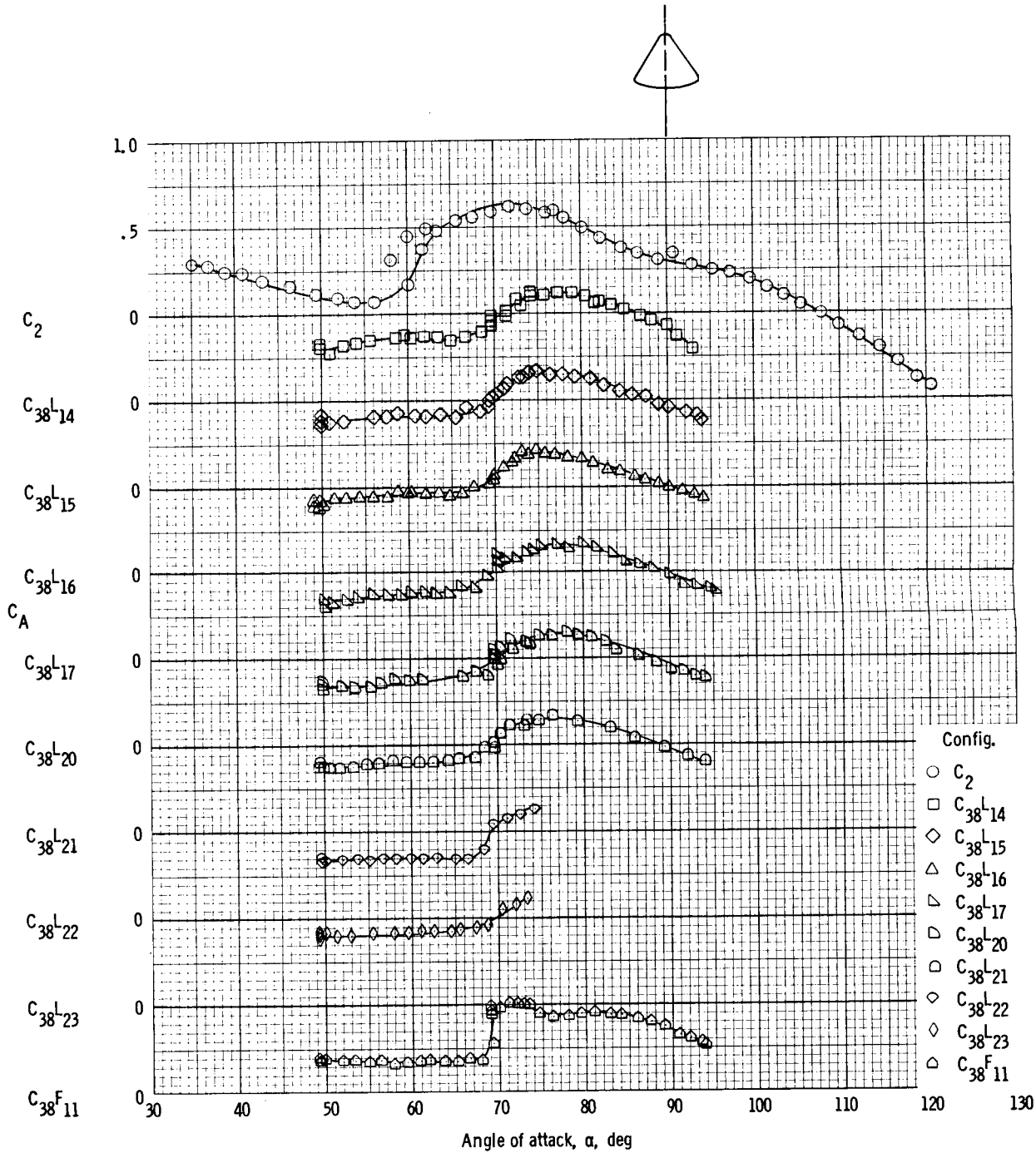

(c) Axial-force coefficient.

Figure 15. - Continued.

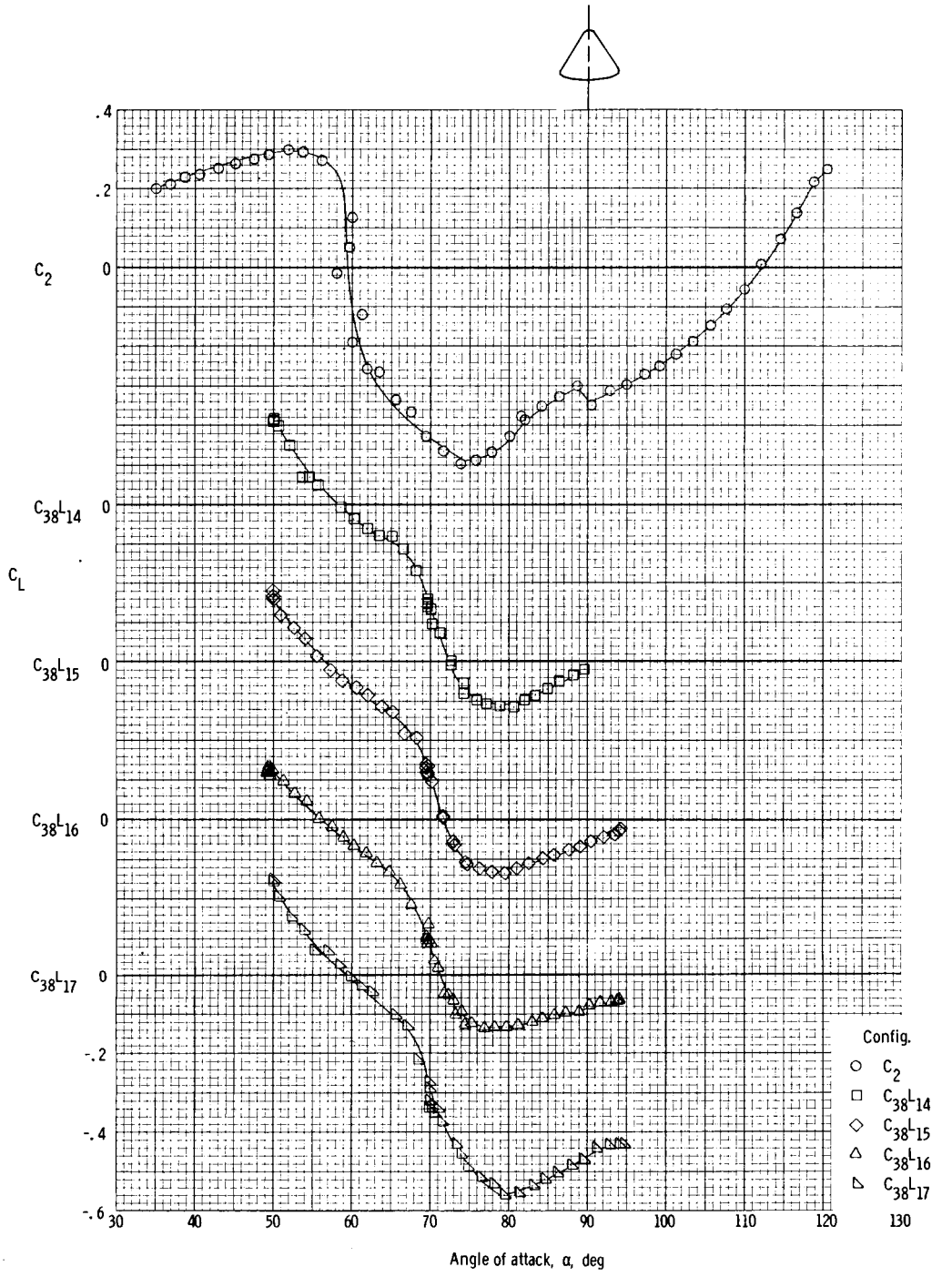

(d) Lift coefficient (C_2 and $C_{38}L_{14}$ to $C_{38}L_{17}$).

Figure 15. - Continued.

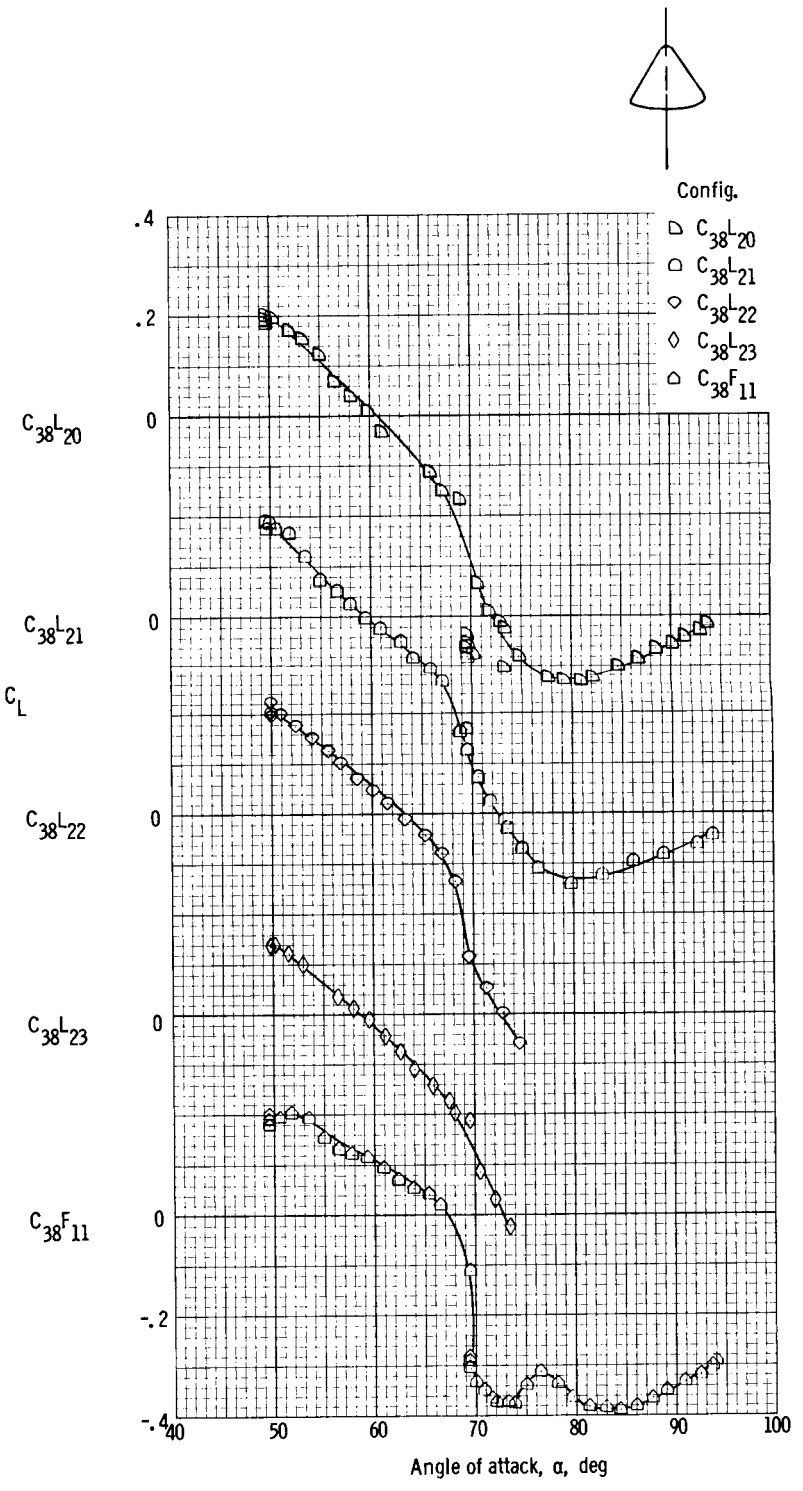

(e) Lift coefficient ($C_{38}L_{20}$ to $C_{38}L_{23}$, and $C_{38}L_{11}$).

Figure 15. - Continued.

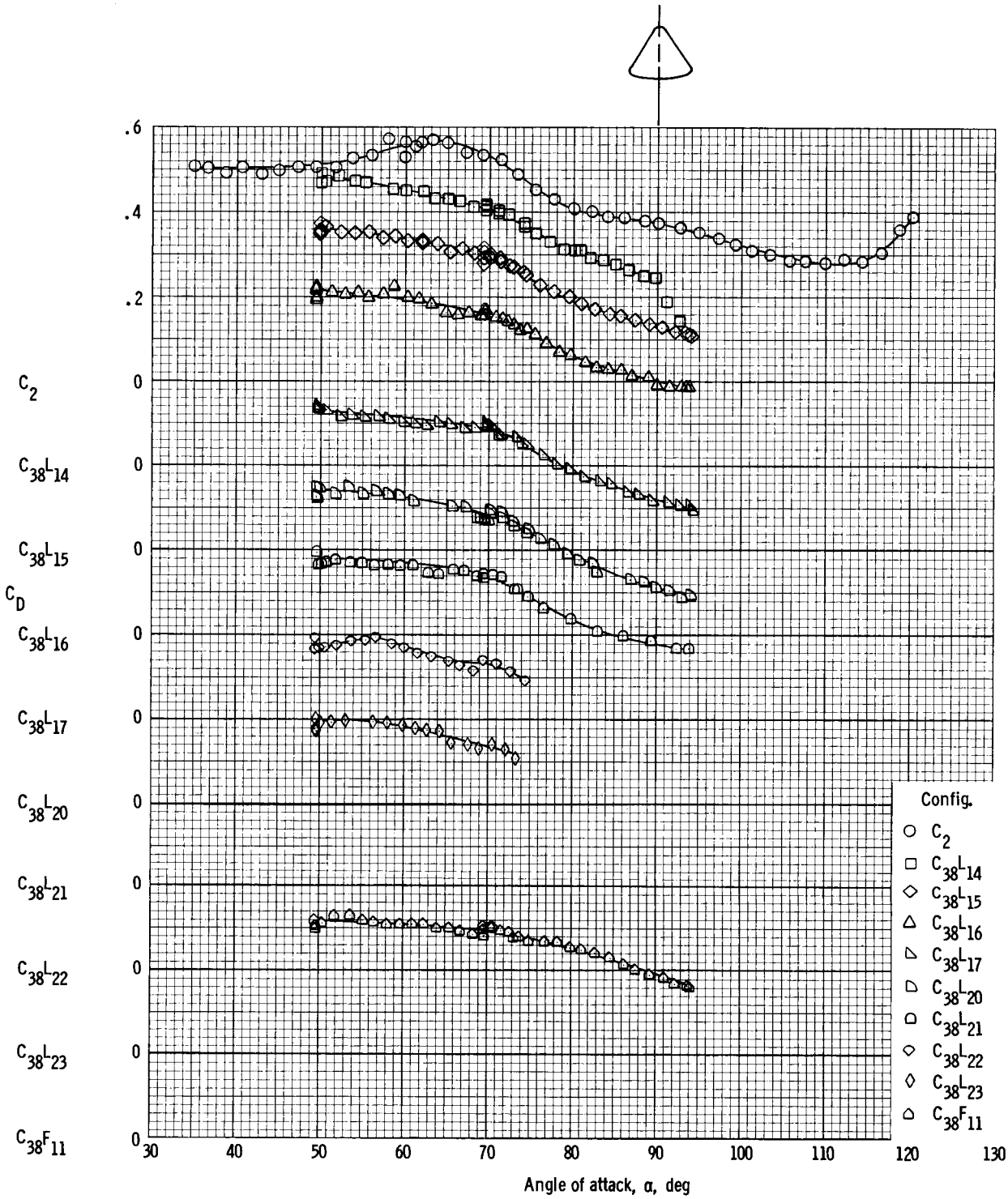

(f) Drag coefficient.

Figure 15. - Concluded.

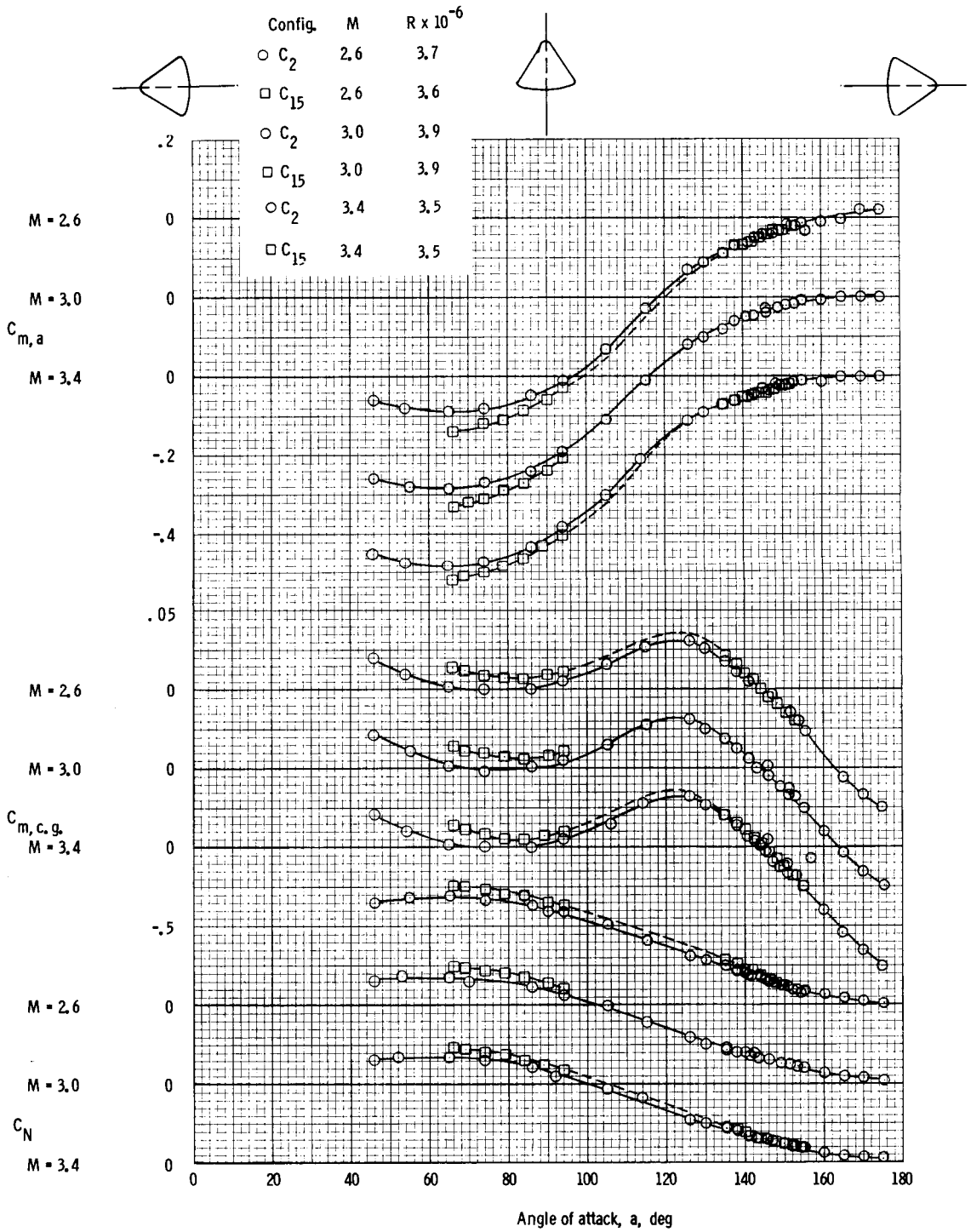

(a) Pitching-moment and normal-force coefficients.

Figure 16. - Aerodynamic characteristics of the Apollo command module with strakes obtained at Ames-UPWT facility at M = 2.6, M = 3.0, and M = 3.4.

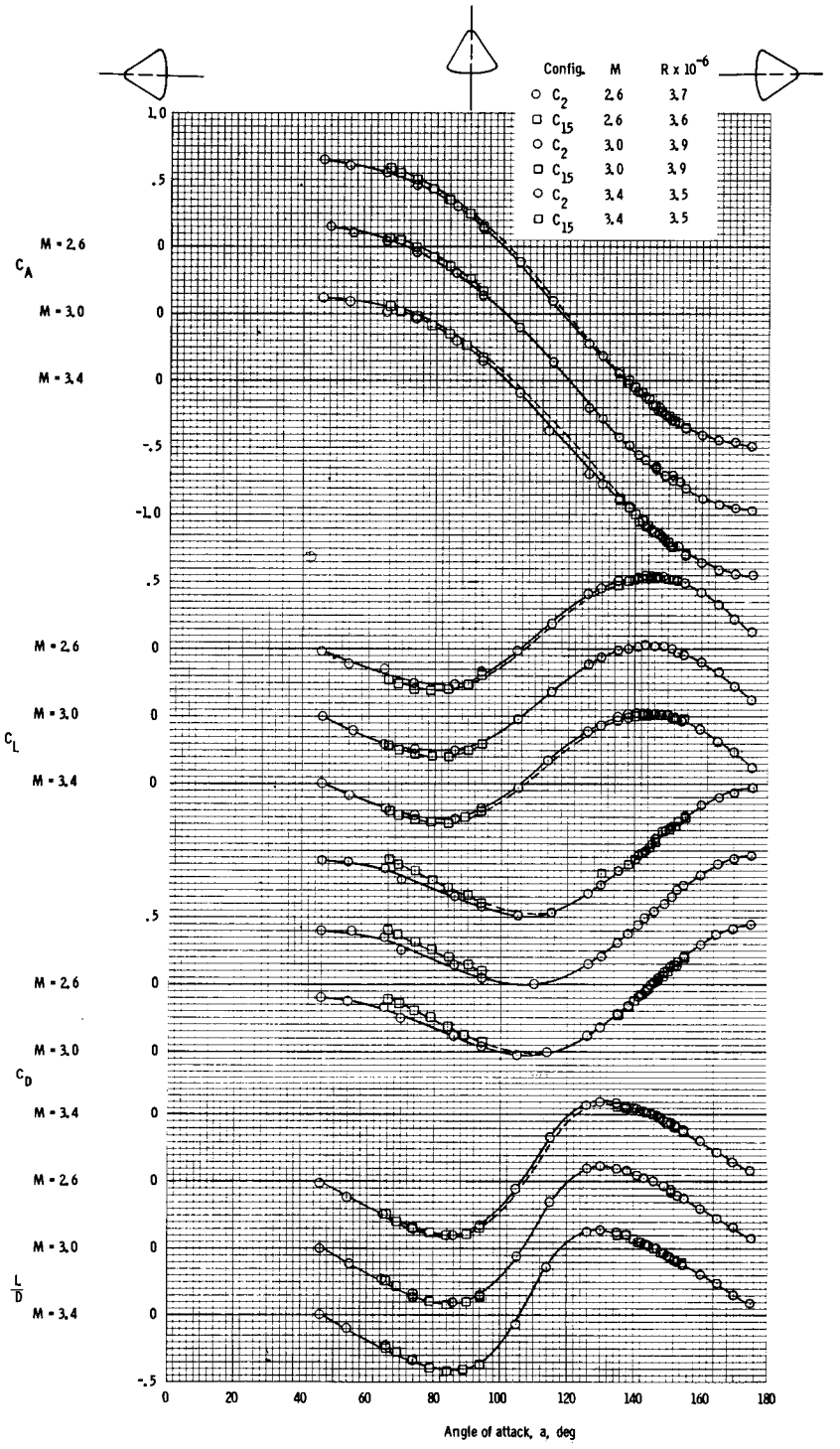

(b) Axial-force, lift and drag coefficients and lift-to-drag ratio.

Figure 16. - Concluded.

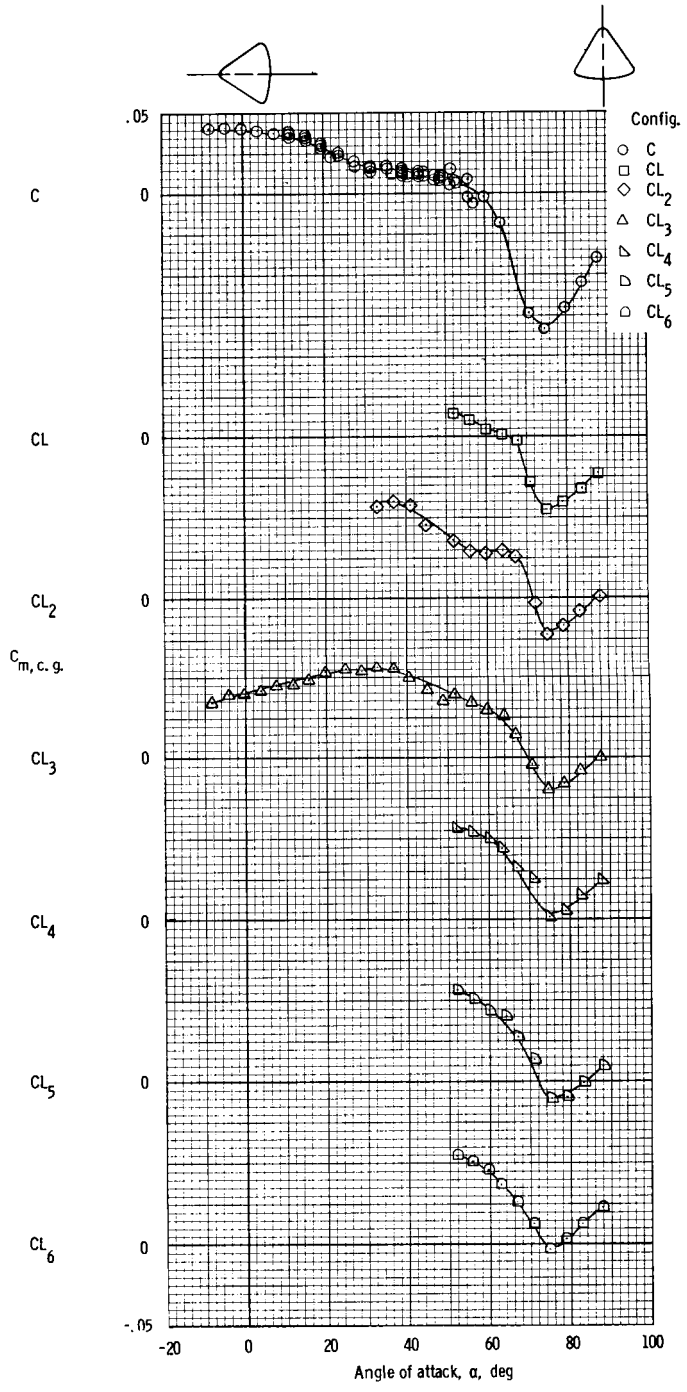

(a) Pitching-moment coefficient.

Figure 17. - Aerodynamic characteristics of the Apollo command module with strakes obtained at Ames 2- by 2-foot TWT facility at $M = 0.7$, $R \times 10^{-6} = 2.1$ (c.g. $= x/d = -0.685$, $z/d = 0.059$).

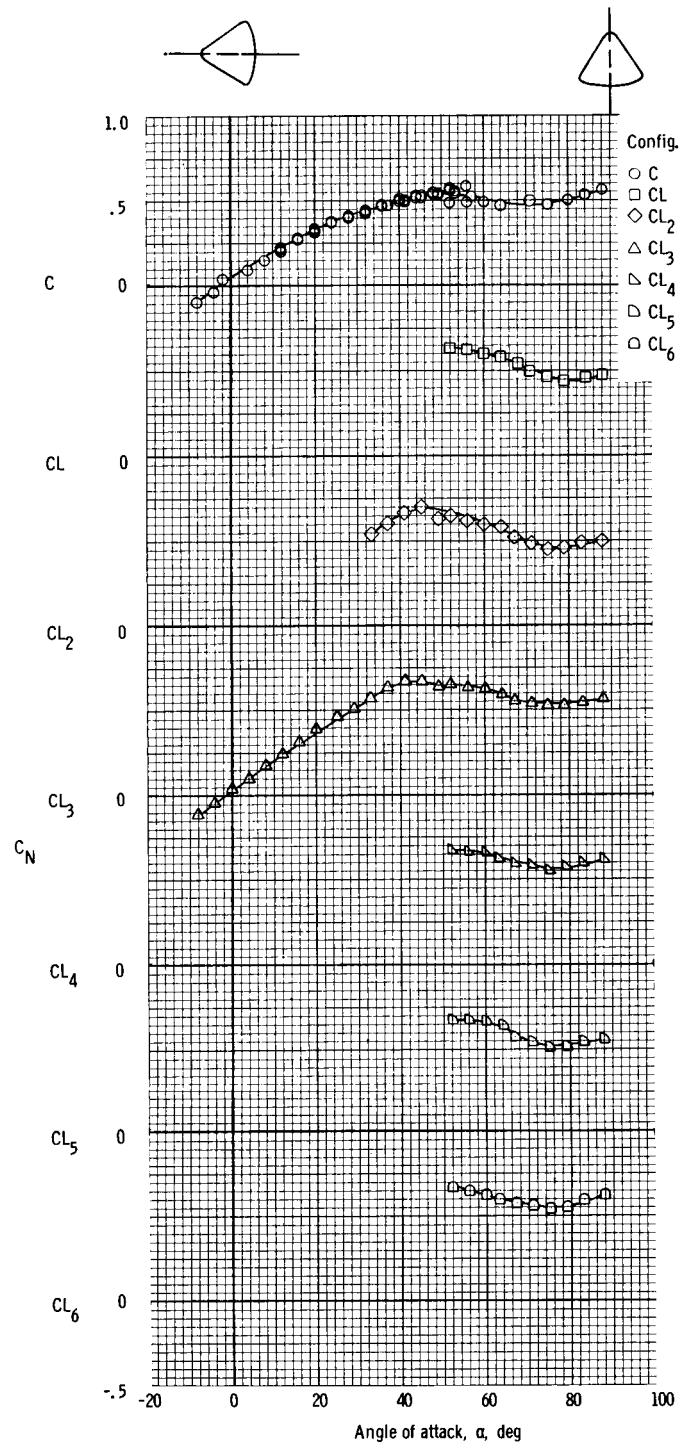

(b) Normal-force coefficient.

Figure 17. - Continued.

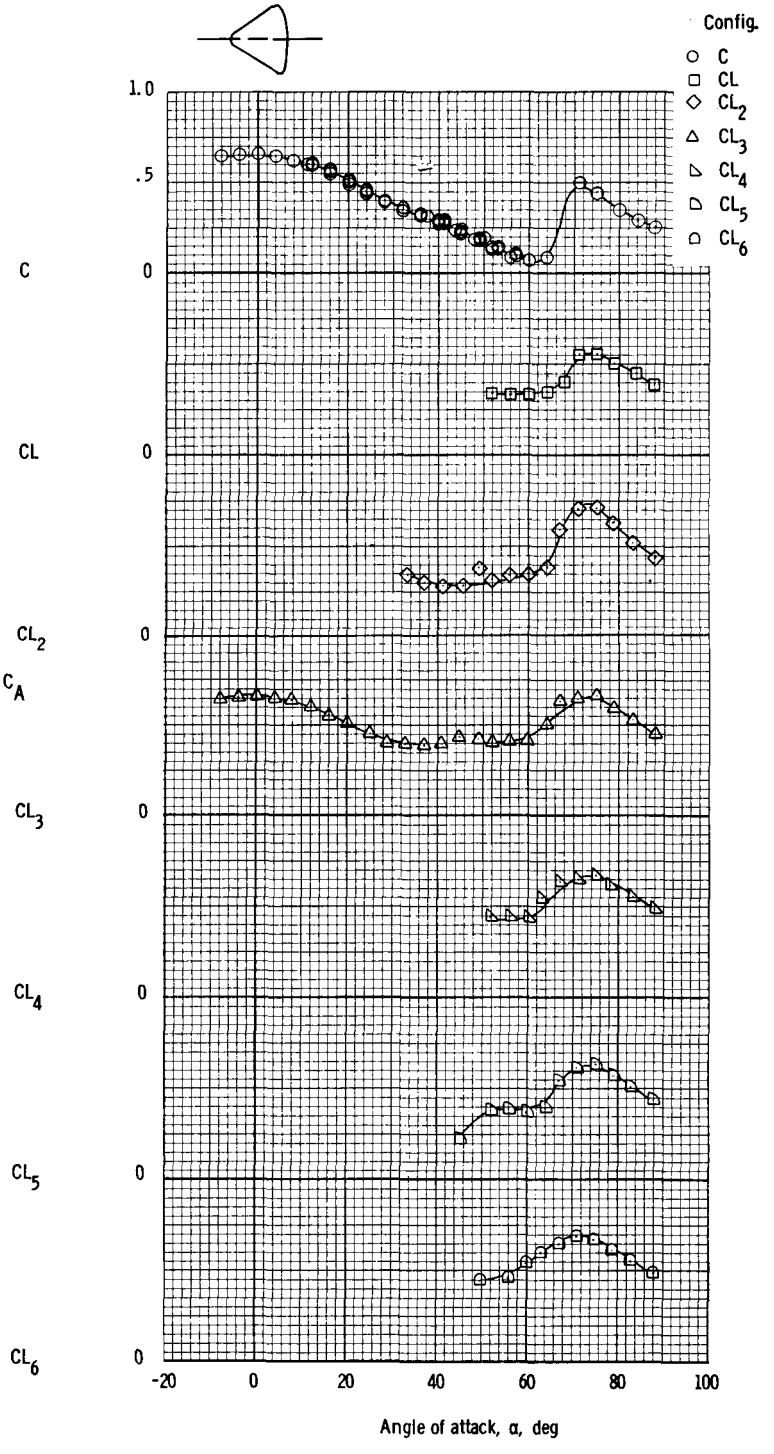

(c) Axial-force coefficient.

Figure 17. - Continued.

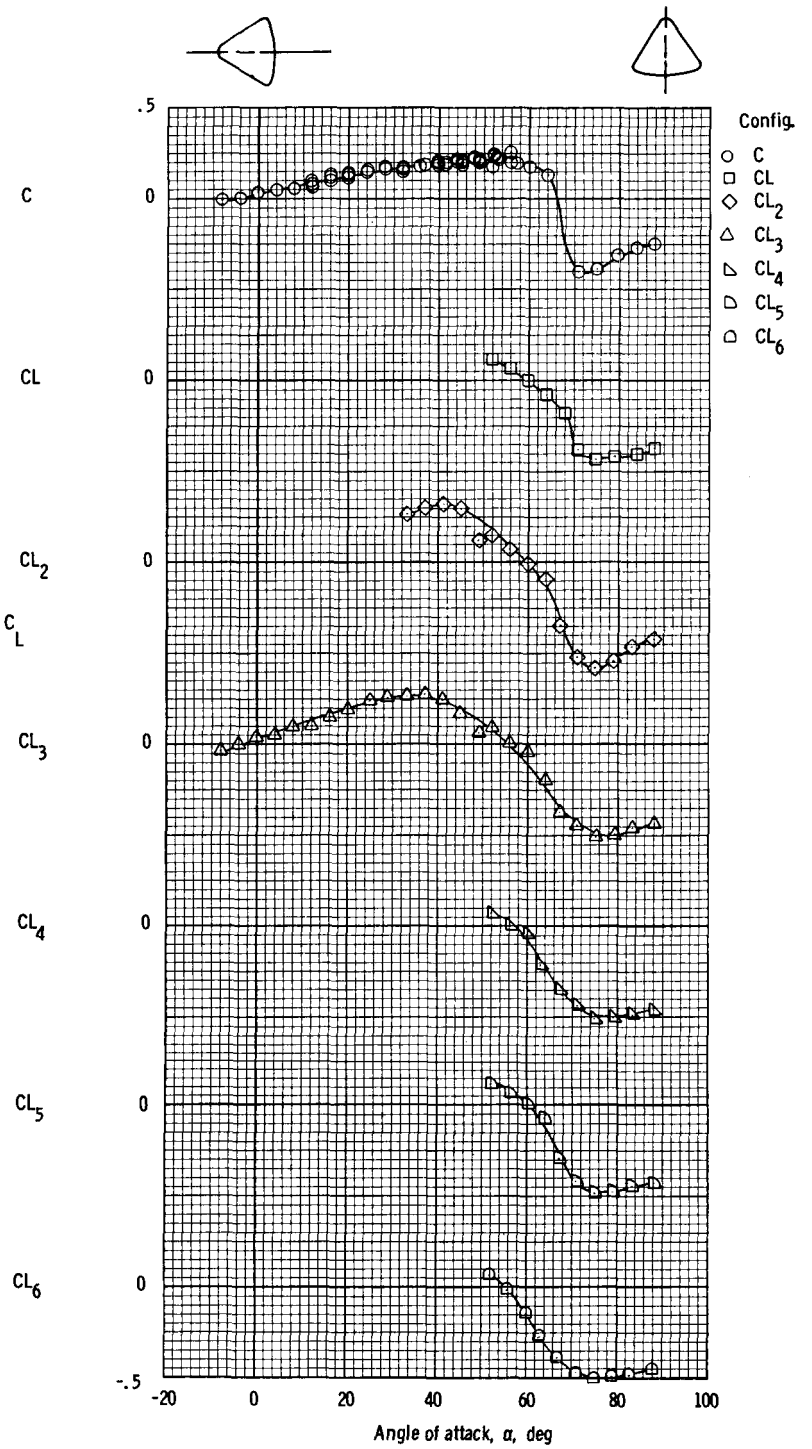

(d) Lift coefficient.

Figure 17. - Continued.

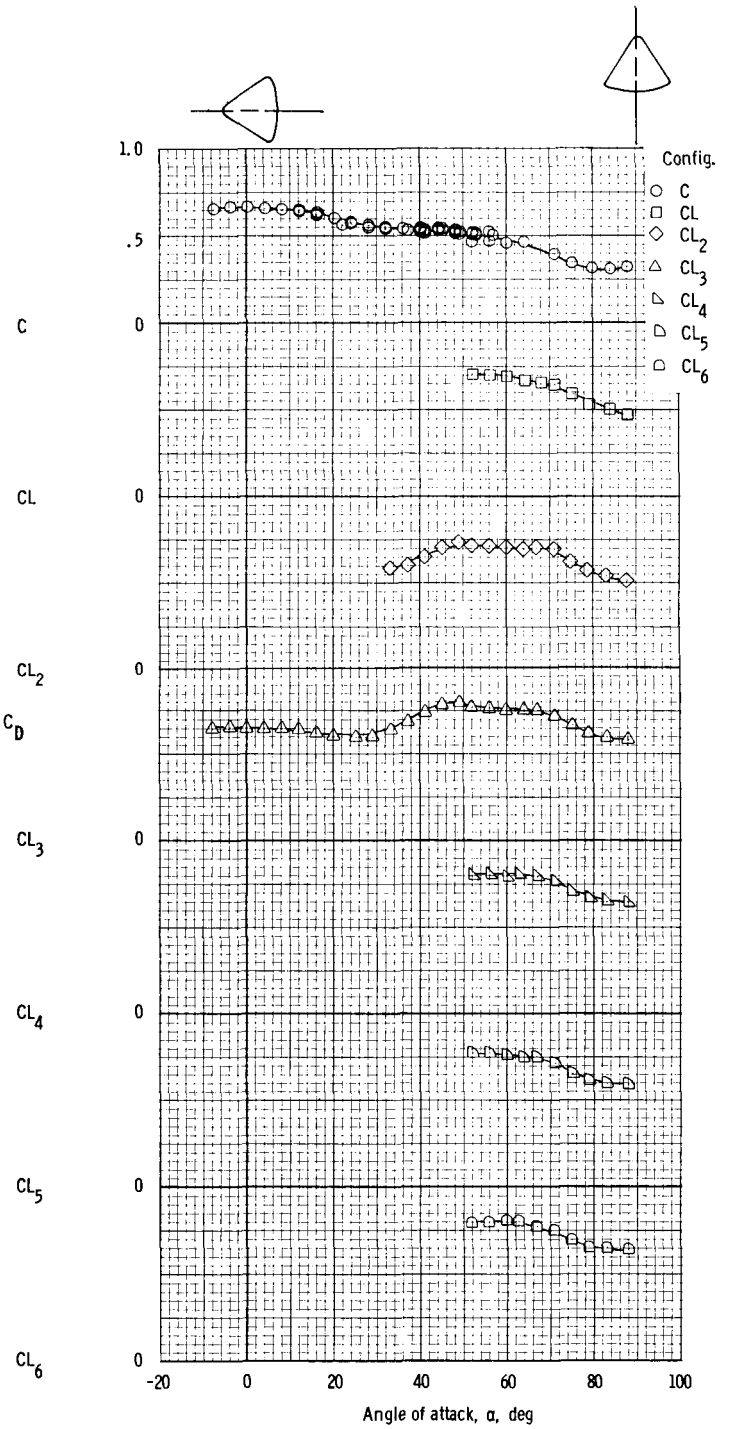

(e) Drag coefficient.

Figure 17. - Concluded.

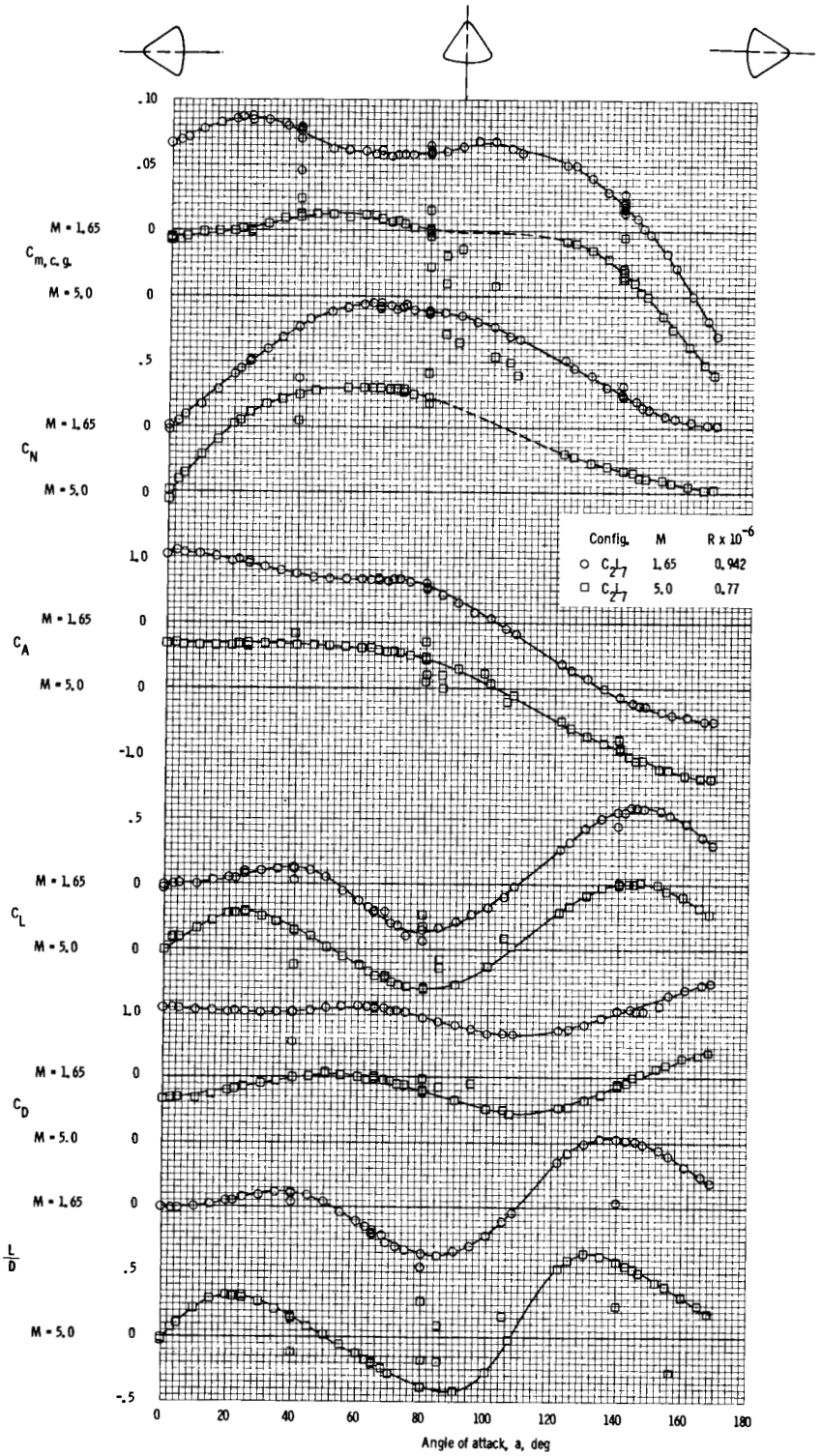

Figure 18. - Aerodynamic characteristics of the Apollo command module with strakes obtained at JPL-20 SWT facility at M = 1.65 and M = 5.0 (c.g. = x/d = -0.685, z/d = 0.059).

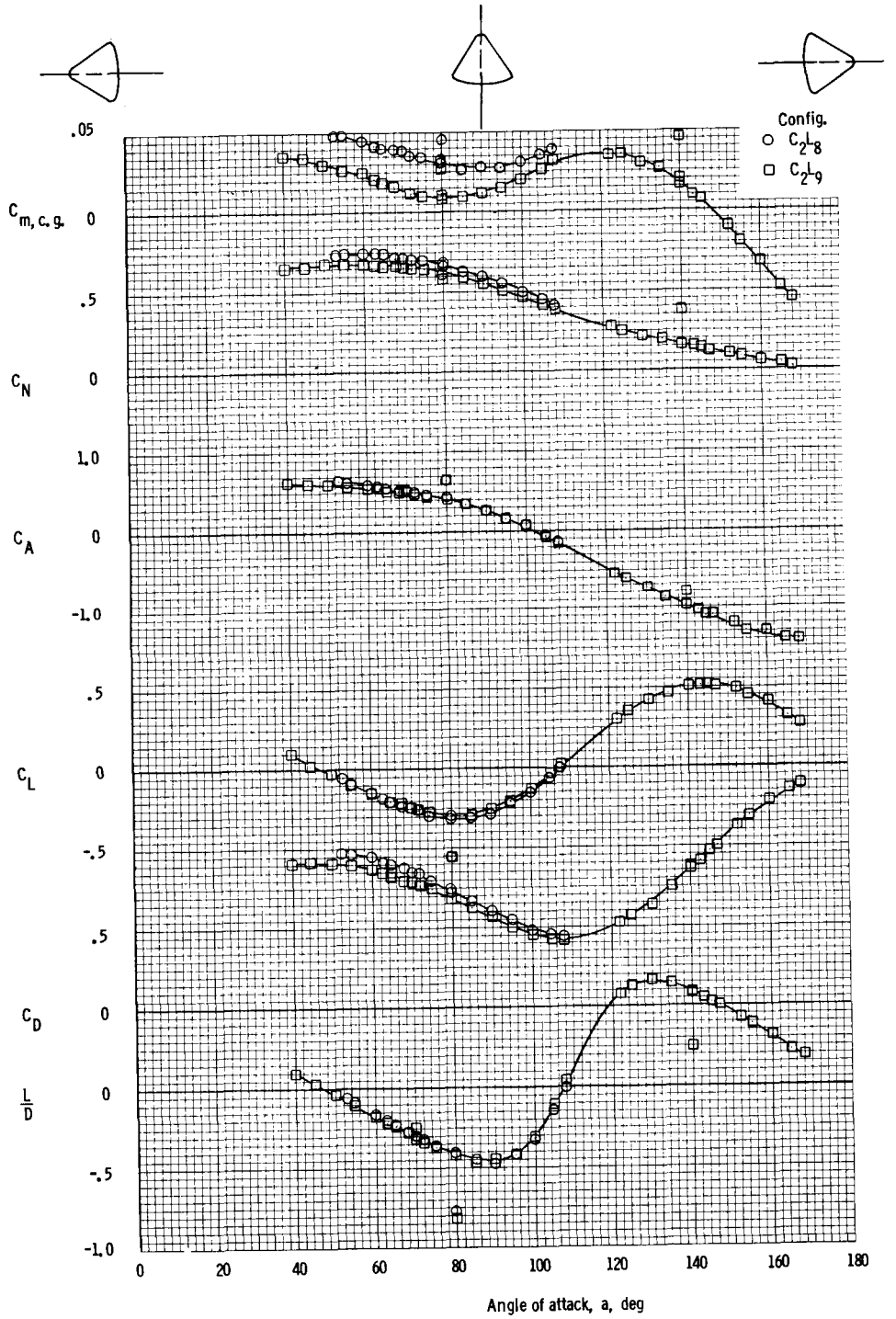

Figure 19. - Aerodynamic characteristics of the Apollo command module (strake configurations C_2L_8 and C_2L_9), obtained at JPL-20 SWT facility at M = 5.0, $R \times 10^{-6} = 0.77$ (c.g. = x/d = -0.685, z/d = 0.059).

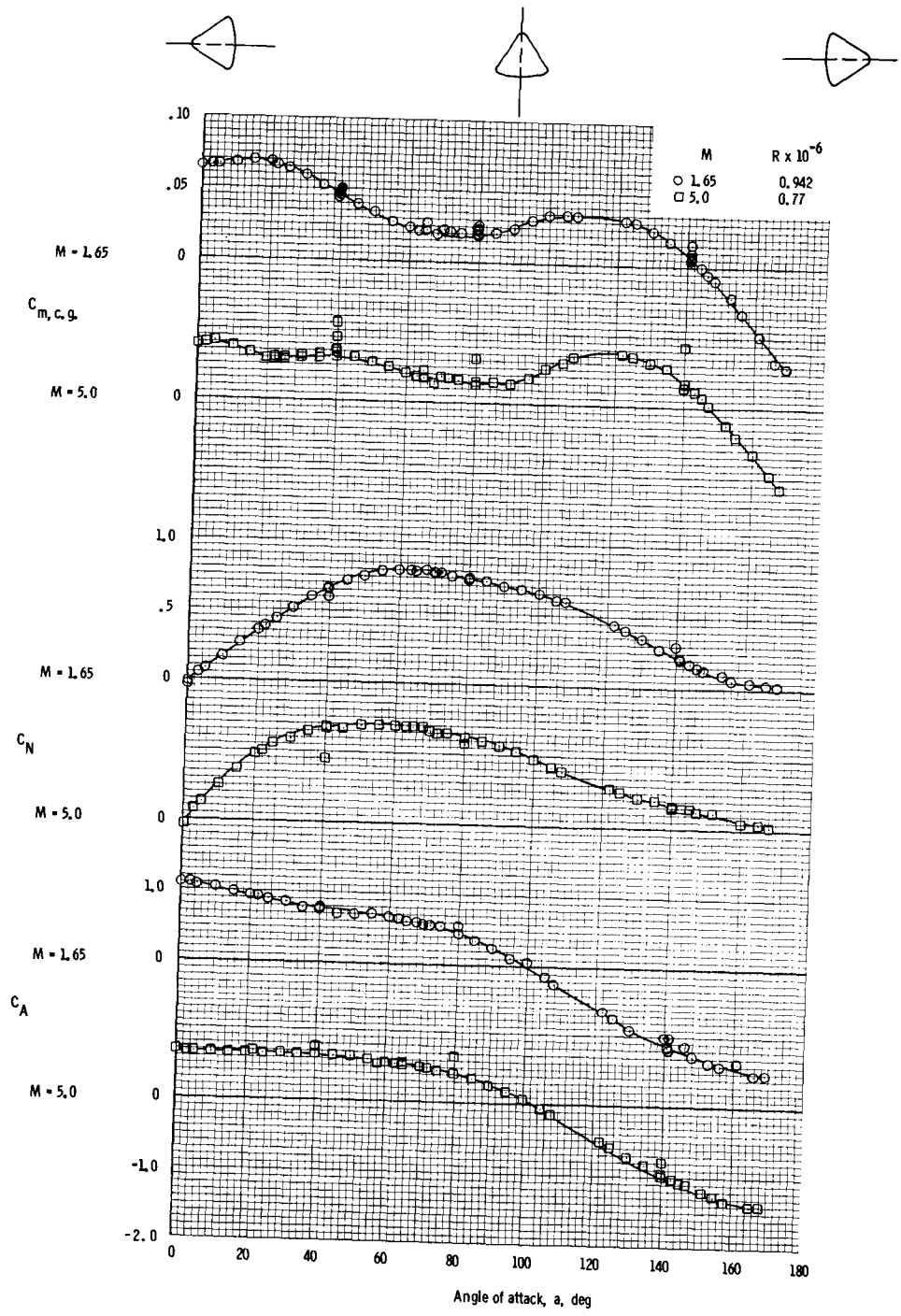

(a) Pitching-moment (c.g.), normal-force, and axial-force coefficients.

Figure 20. - Aerodynamic characteristics of the Apollo command module (strake configuration C_2L_{11}) obtained at JPL-20 SWT of M = 1.65 and M = 5.0 (c.g. = x/d = -0.685, z/d = 0.059).

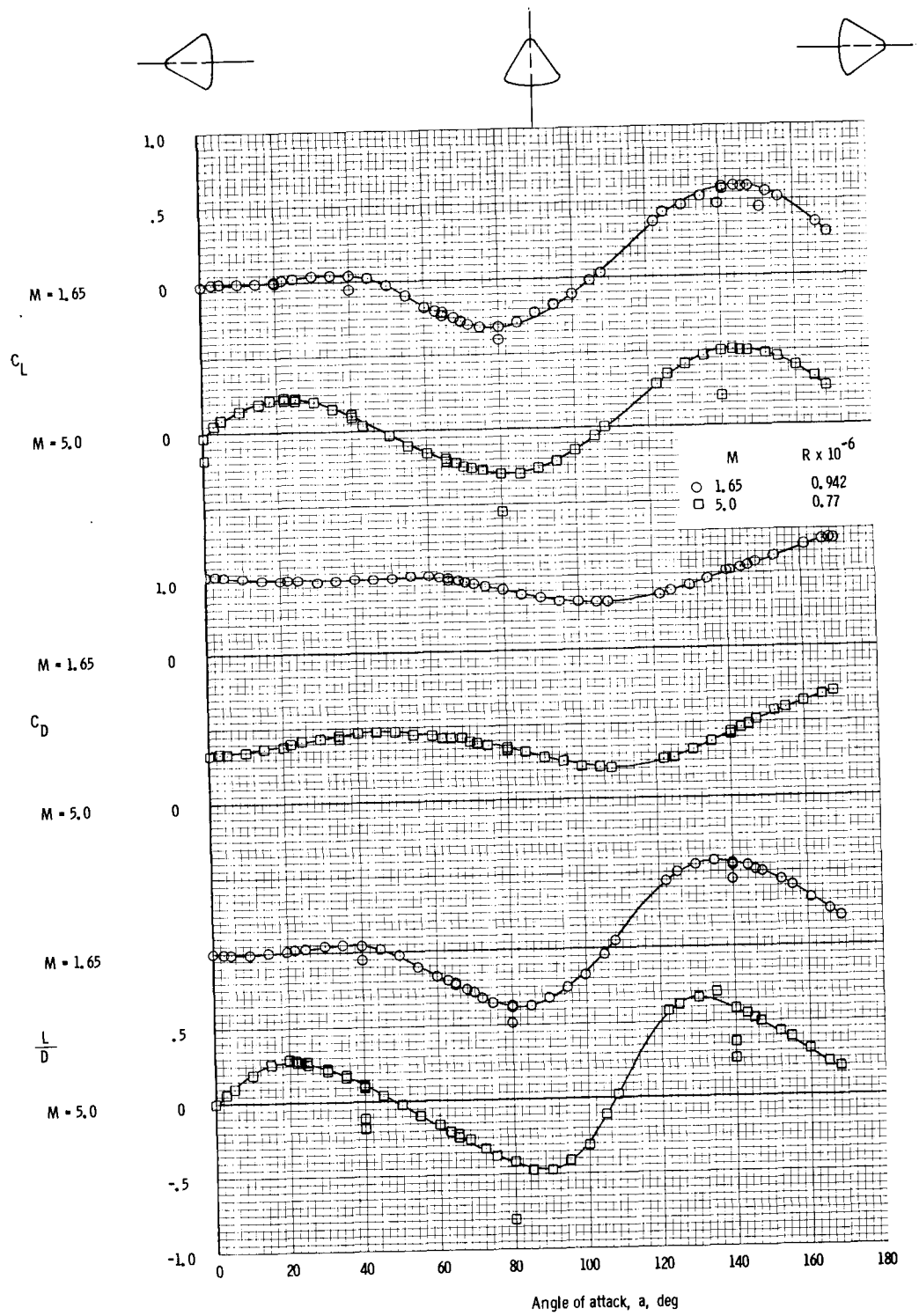

(b) Lift and drag coefficients and lift-to-drag ratio.

Figure 20. - Concluded.

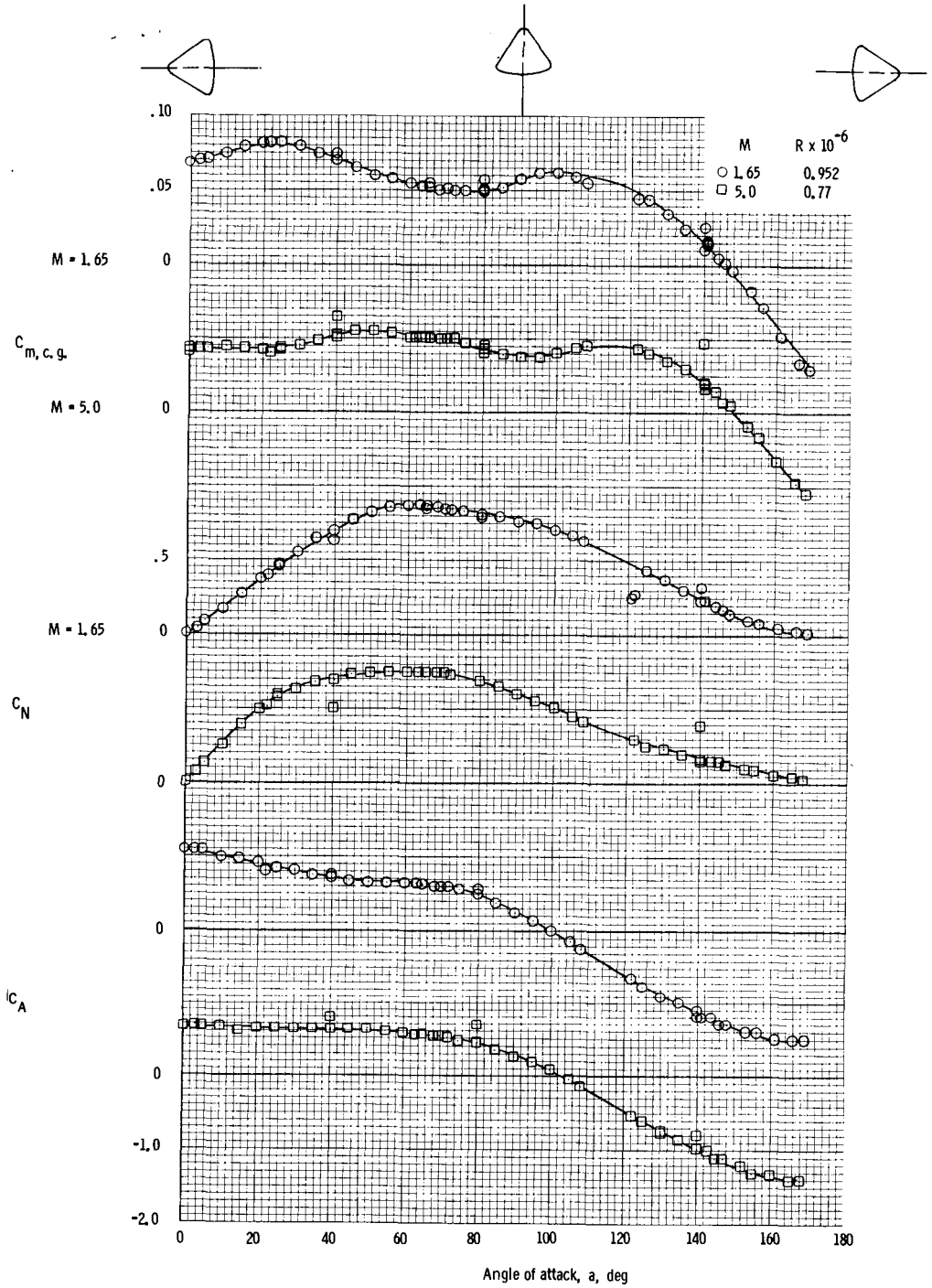

(a) Pitching-moment (c.g.), normal-force, and axial-force coefficients.

Figure 21. - Aerodynamic characteristics of the Apollo command module (strake configuration C_2L_{13}) obtained at JPL-20 SWT at M = 1.65 and M = 5.0 (c.g. = x/d = -0.685, z/d = 0.059).

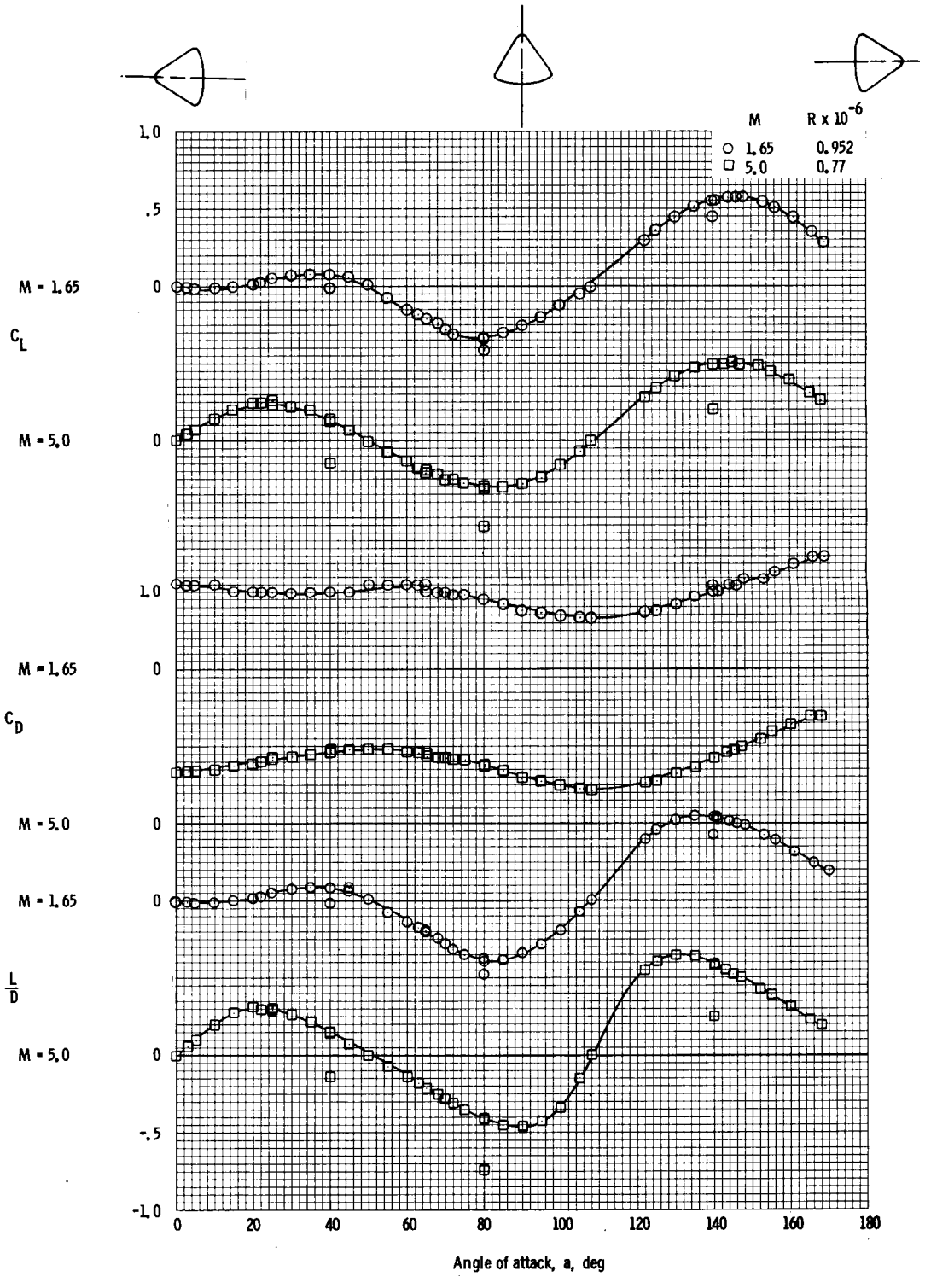

(b) Lift and drag coefficients and lift-to-drag ratio.

Figure 21. - Concluded.

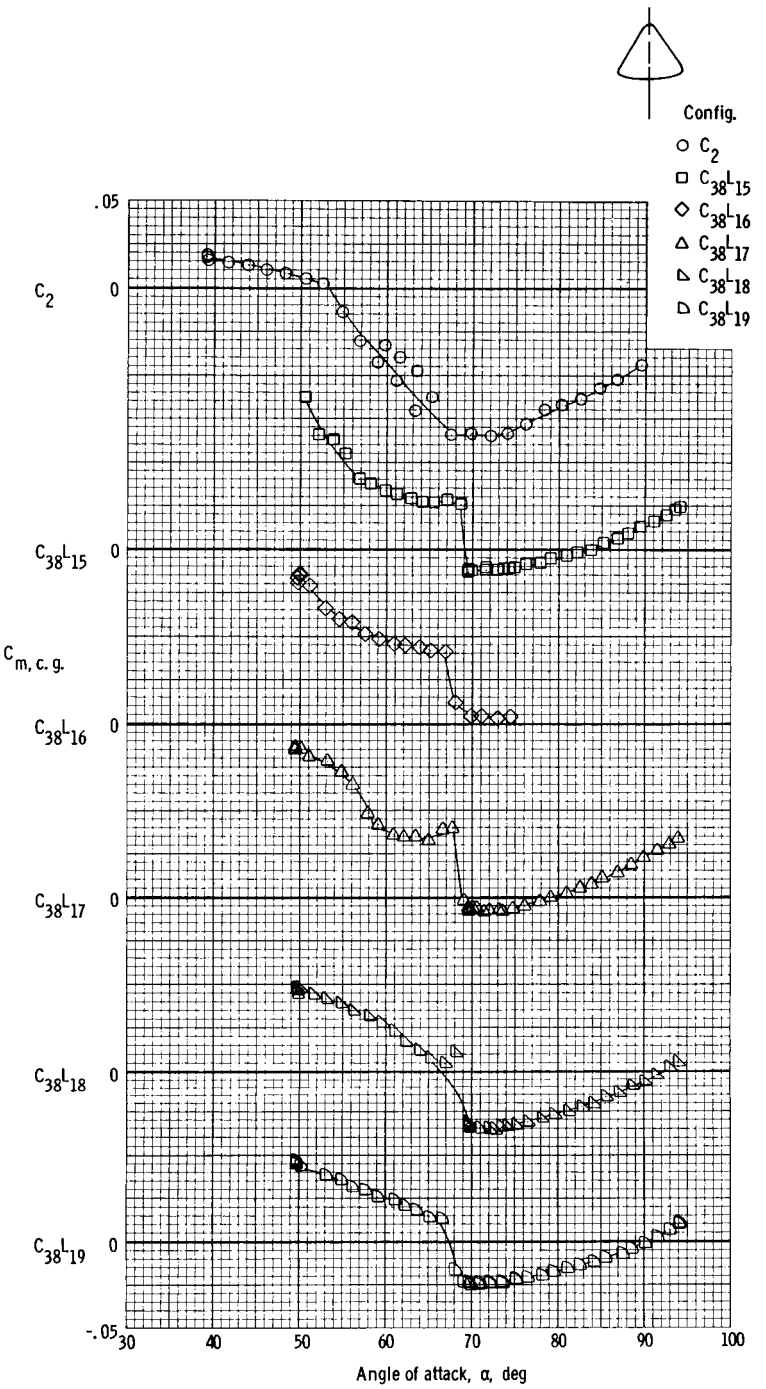

(a) Pitching-moment coefficient (c.g.).

Figure 22. - Aerodynamic characteristics of the Apollo command module with strakes obtained at NAA-TWT facility at $M = 0.4$, $R \times 10^{-6} = 11.0$ (c.g. = x/d = -0.685, z/d = 0.059).

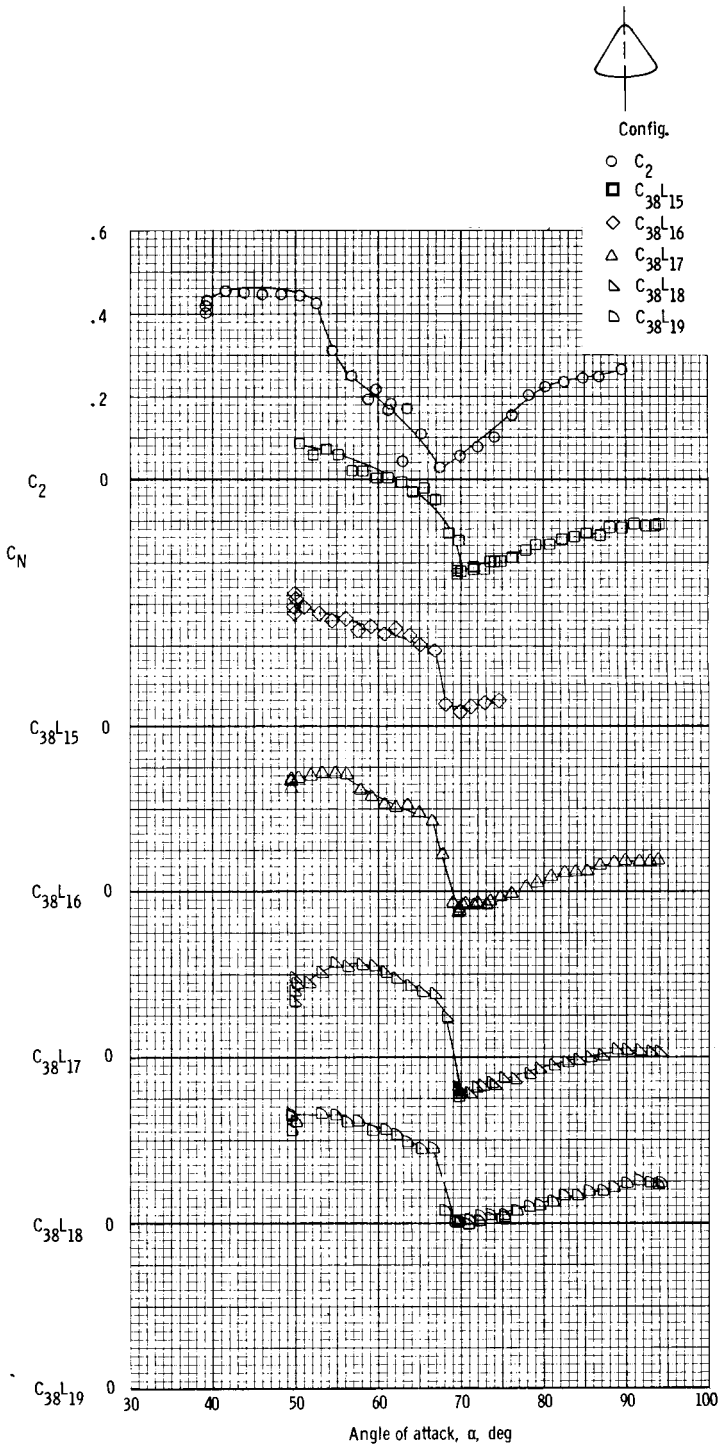

(b) Normal-force coefficient.

Figure 22. - Continued.

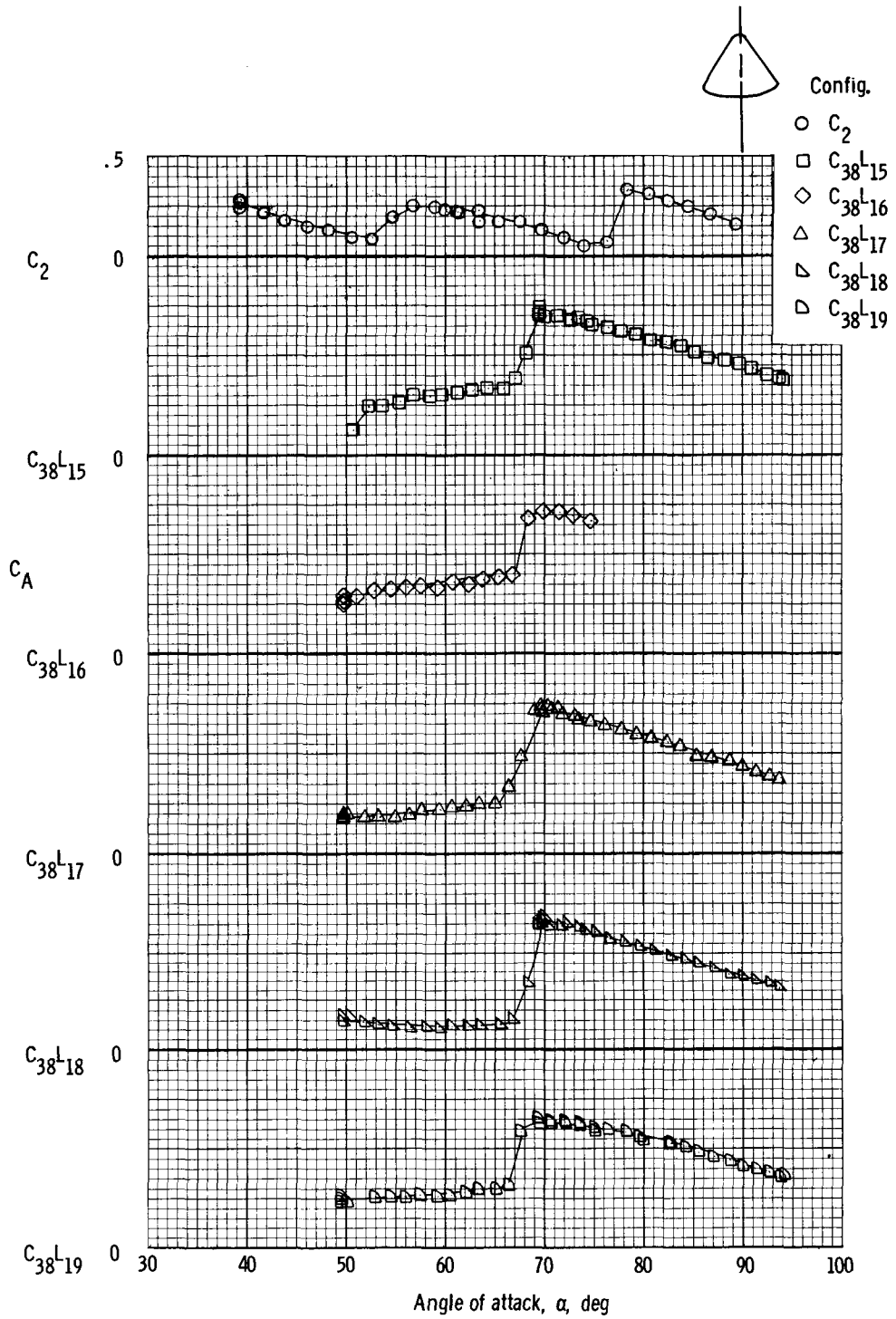

(c) Axial-force coefficient.

Figure 22. - Continued.

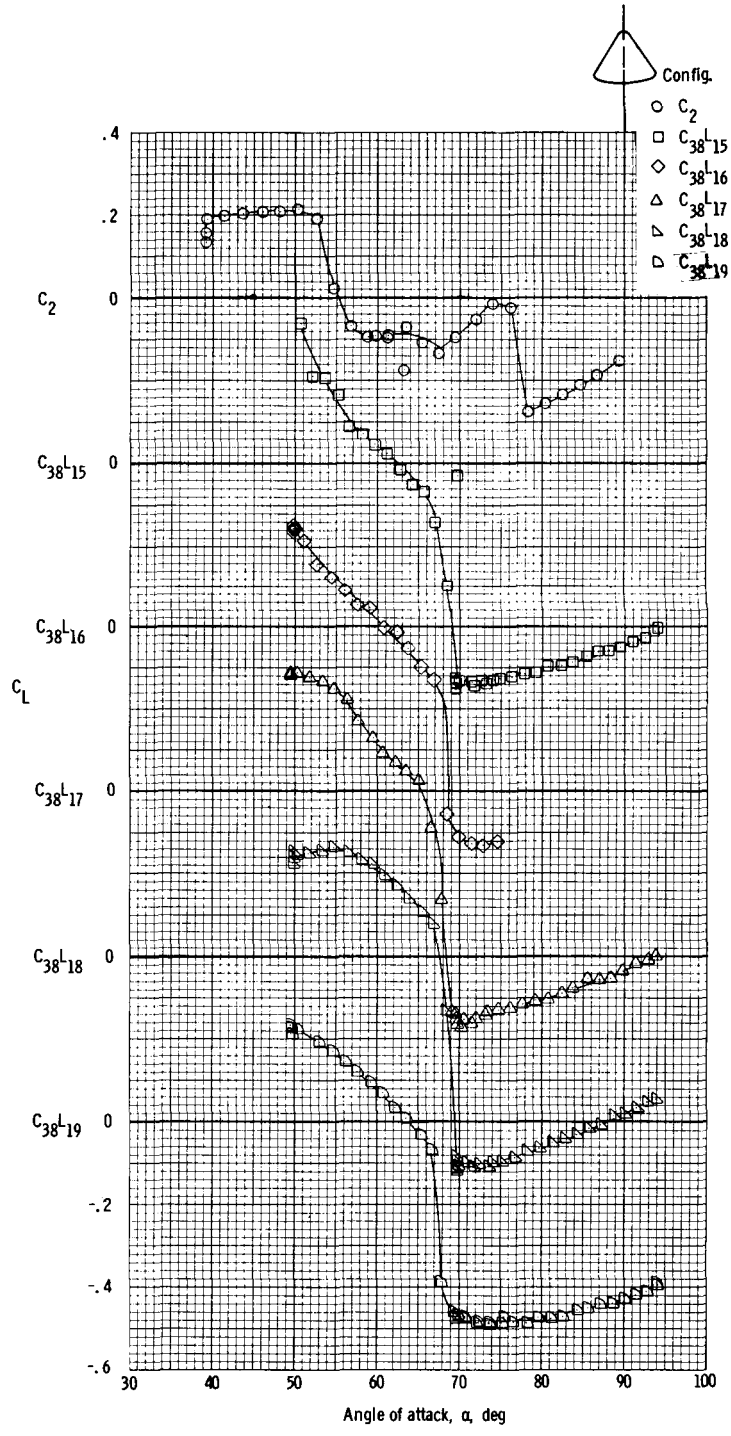

(d) Lift coefficient.

Figure 22. - Continued.

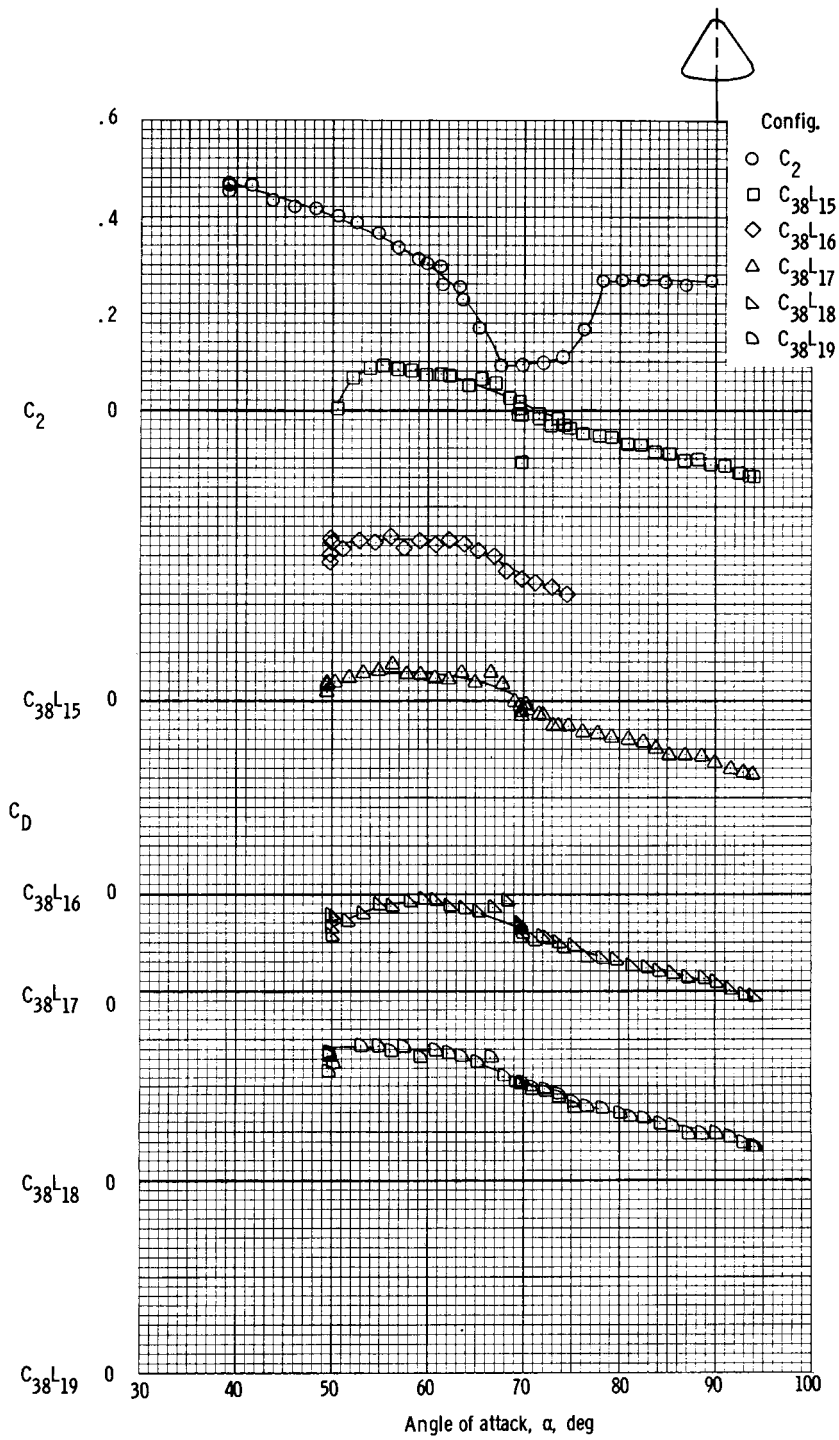

(e) Drag coefficient.

Figure 22. - Concluded.

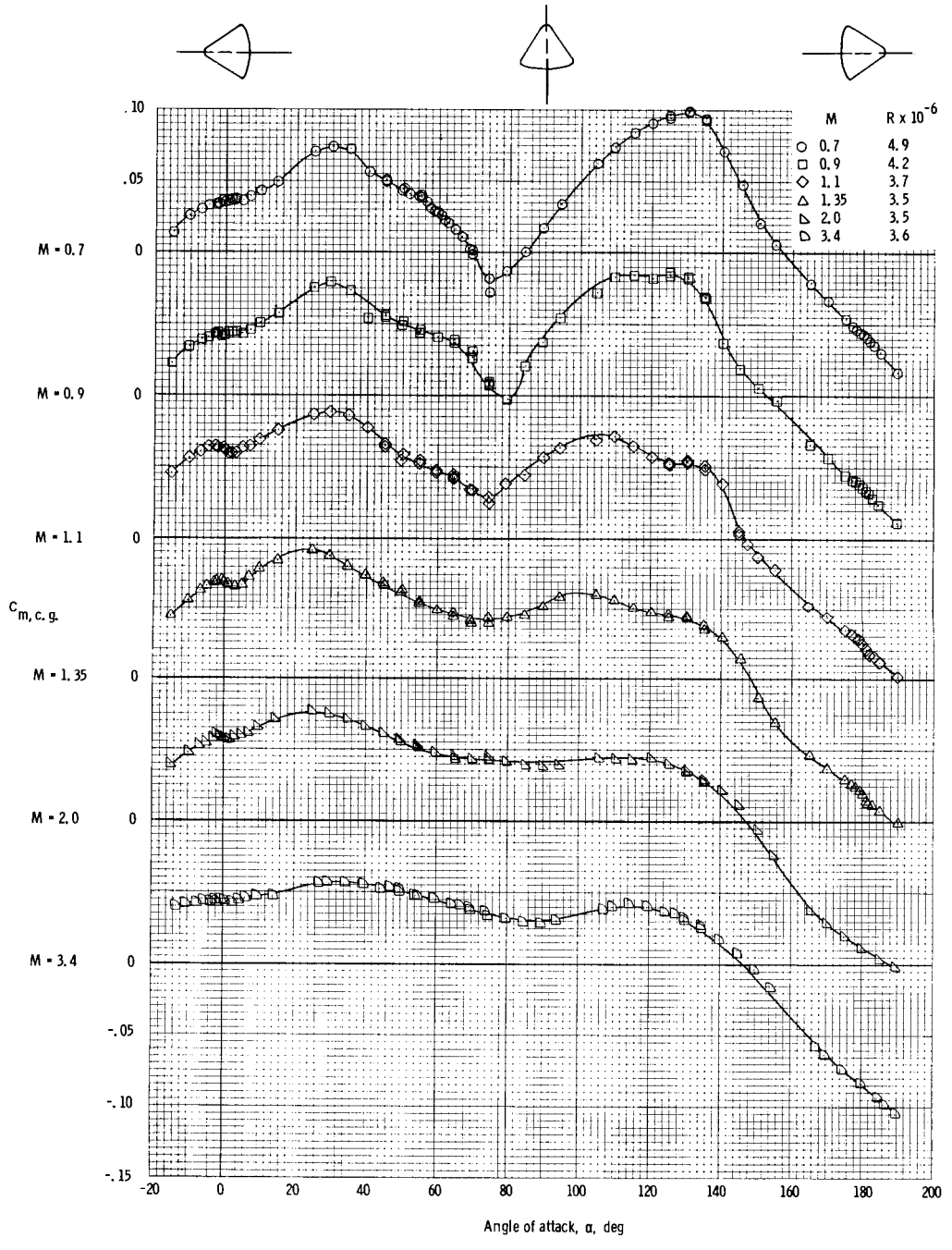

(a) Pitching-moment coefficient (c. g.).

Figure 23. - Aerodynamic characteristics of the Apollo command module (strake configuration $C_{39}L_{28}$) obtained at Ames-UPWT facilities at M = 0.7 to M = 3.4 (c. g. = x/d = -0.685, z/d = 0.059).

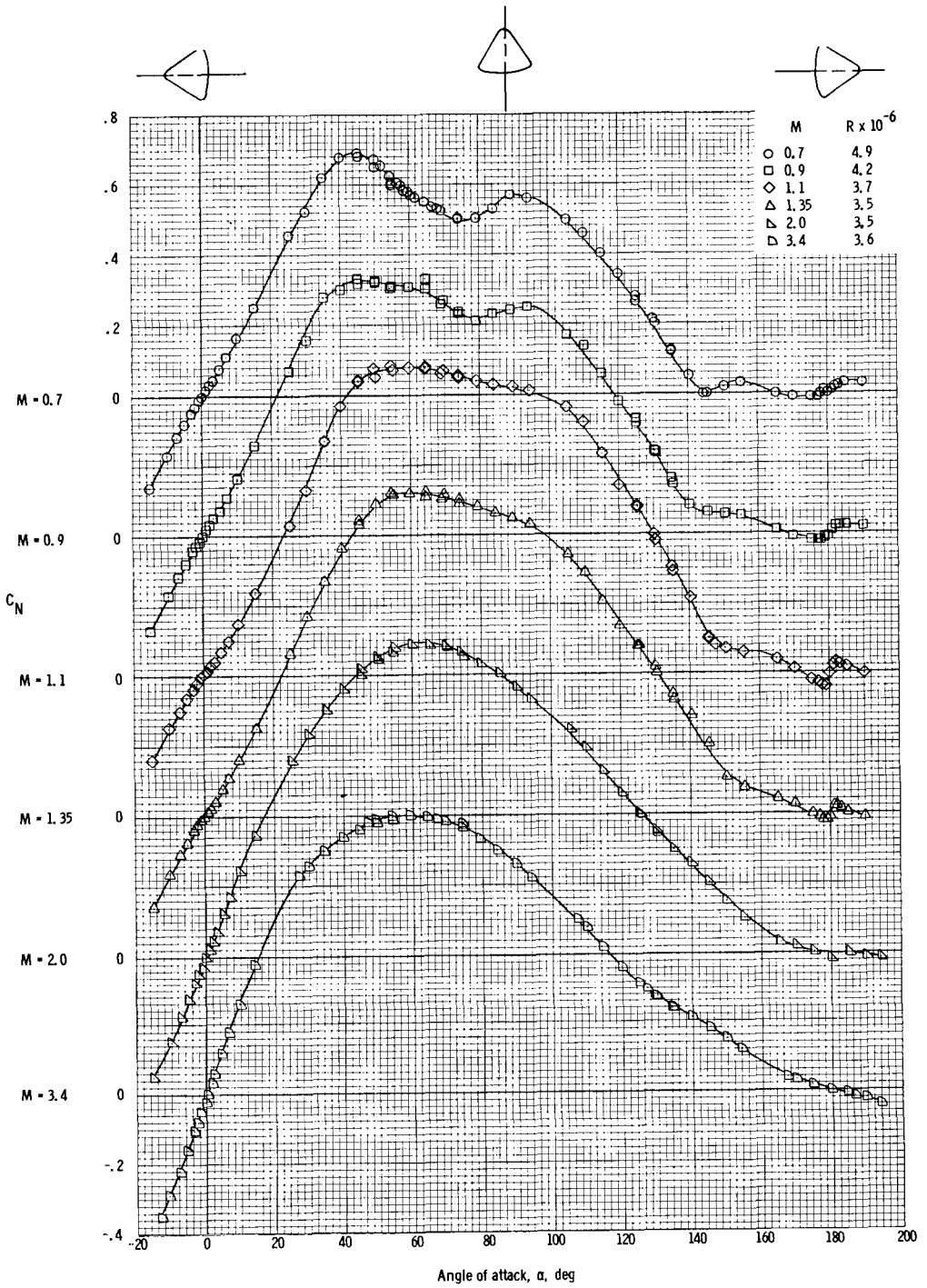

(b) Normal-force coefficient.

Figure 23. - Continued.

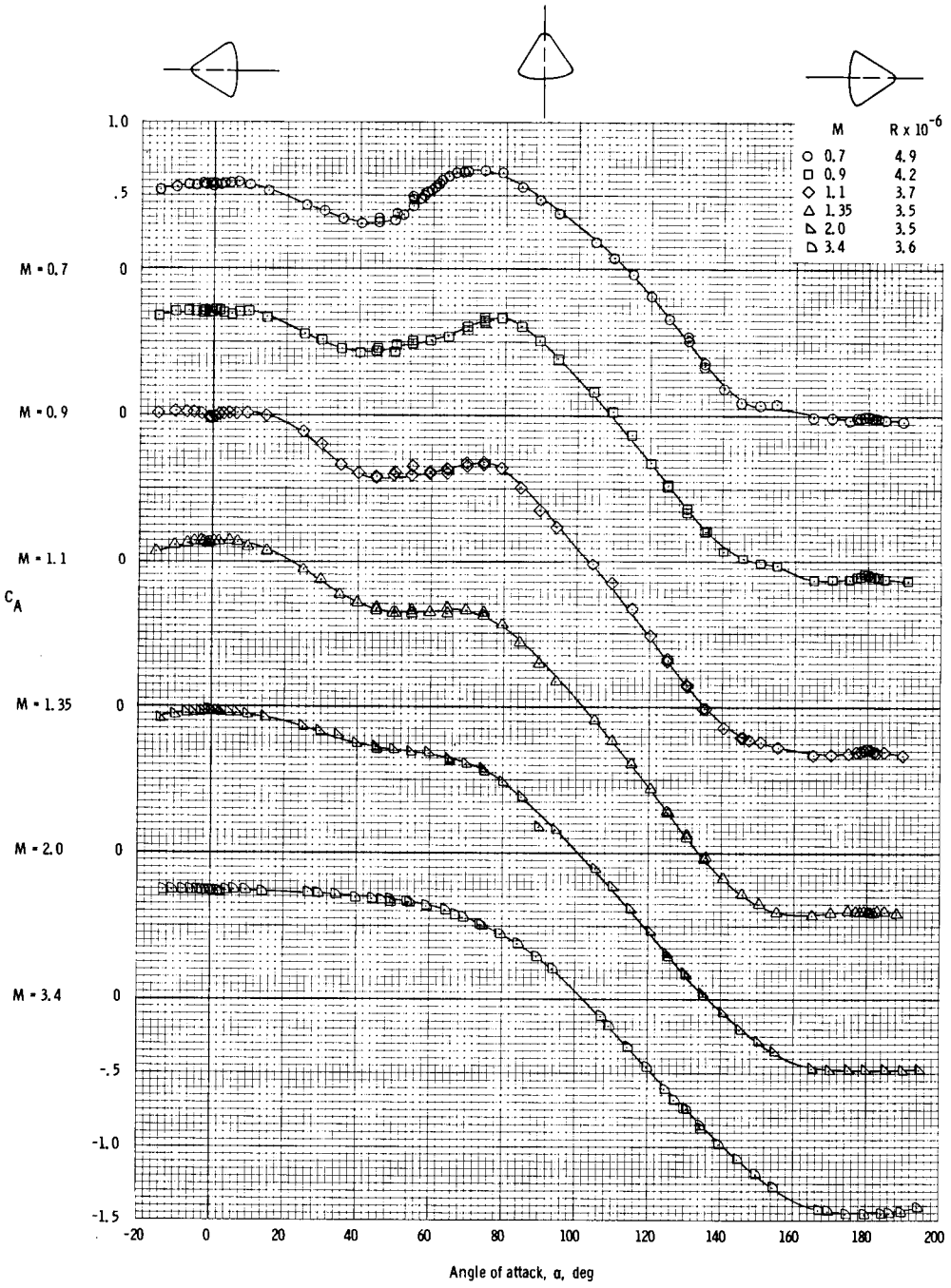

(c) Axial-force coefficient.

Figure 23. - Continued.

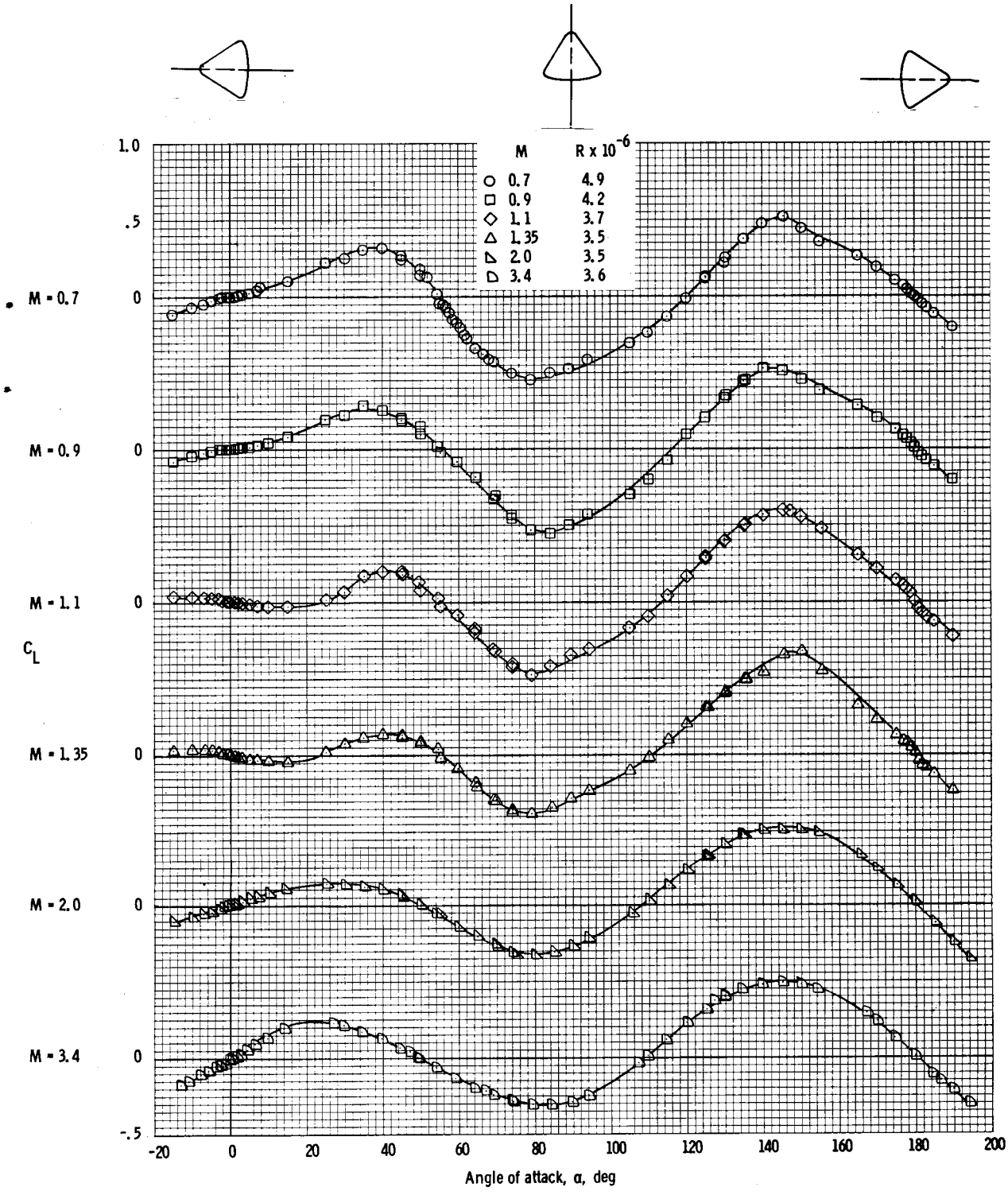

(d) Lift coefficient.

Figure 23. - Continued.

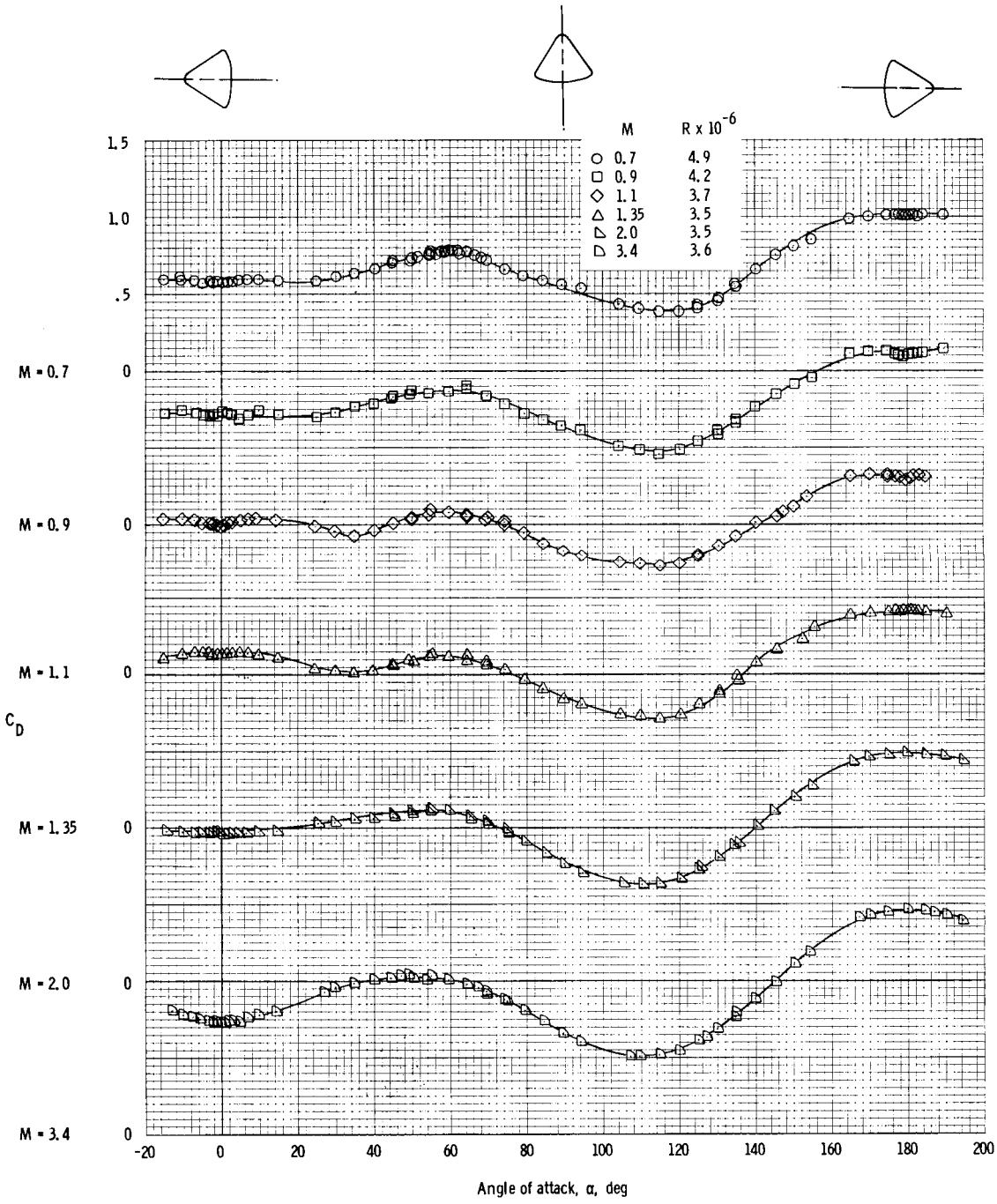

(e) Drag coefficient.

Figure 23. - Continued.

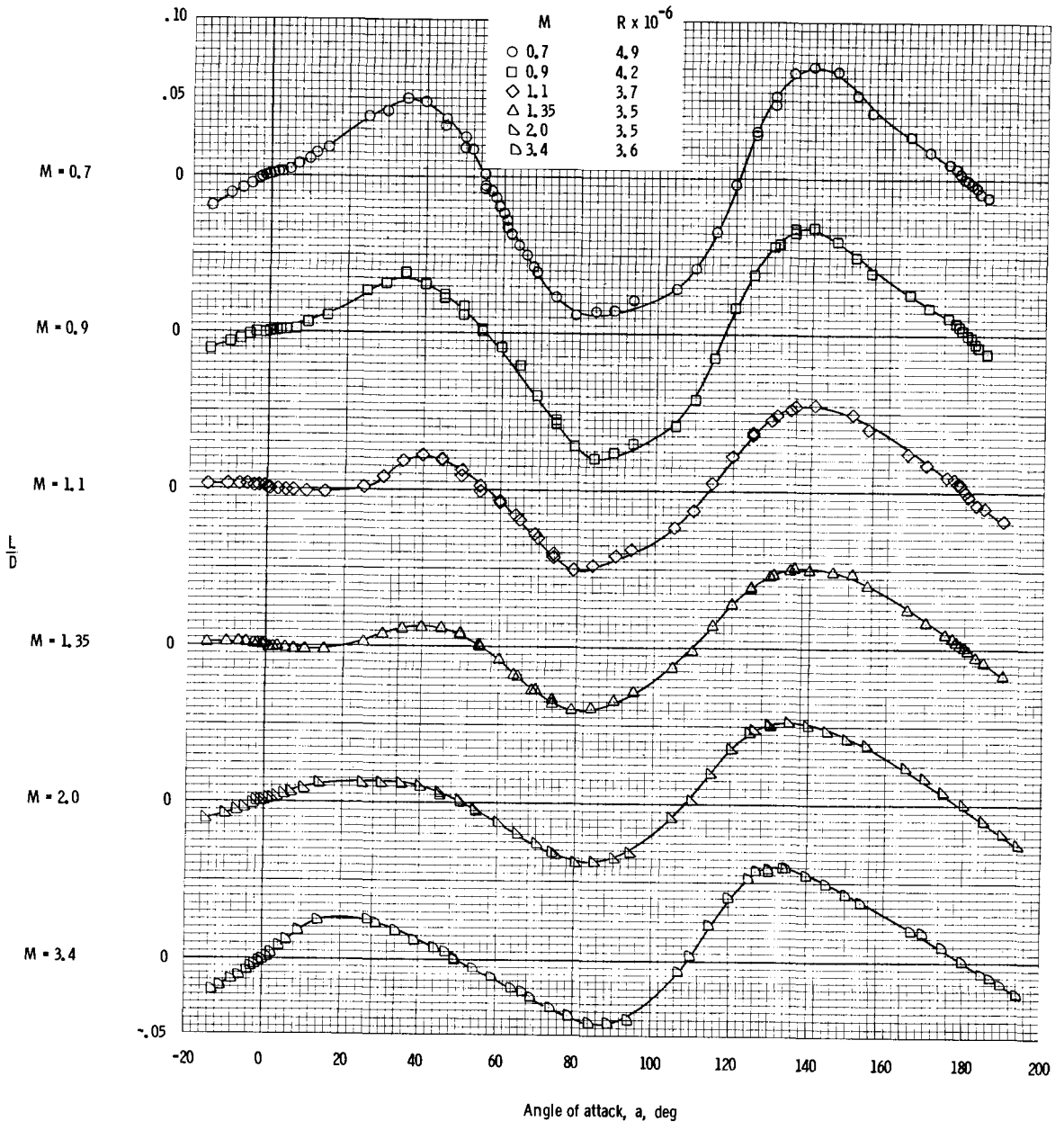

(f) Lift-to-drag ratio.

Figure 23. - Concluded.

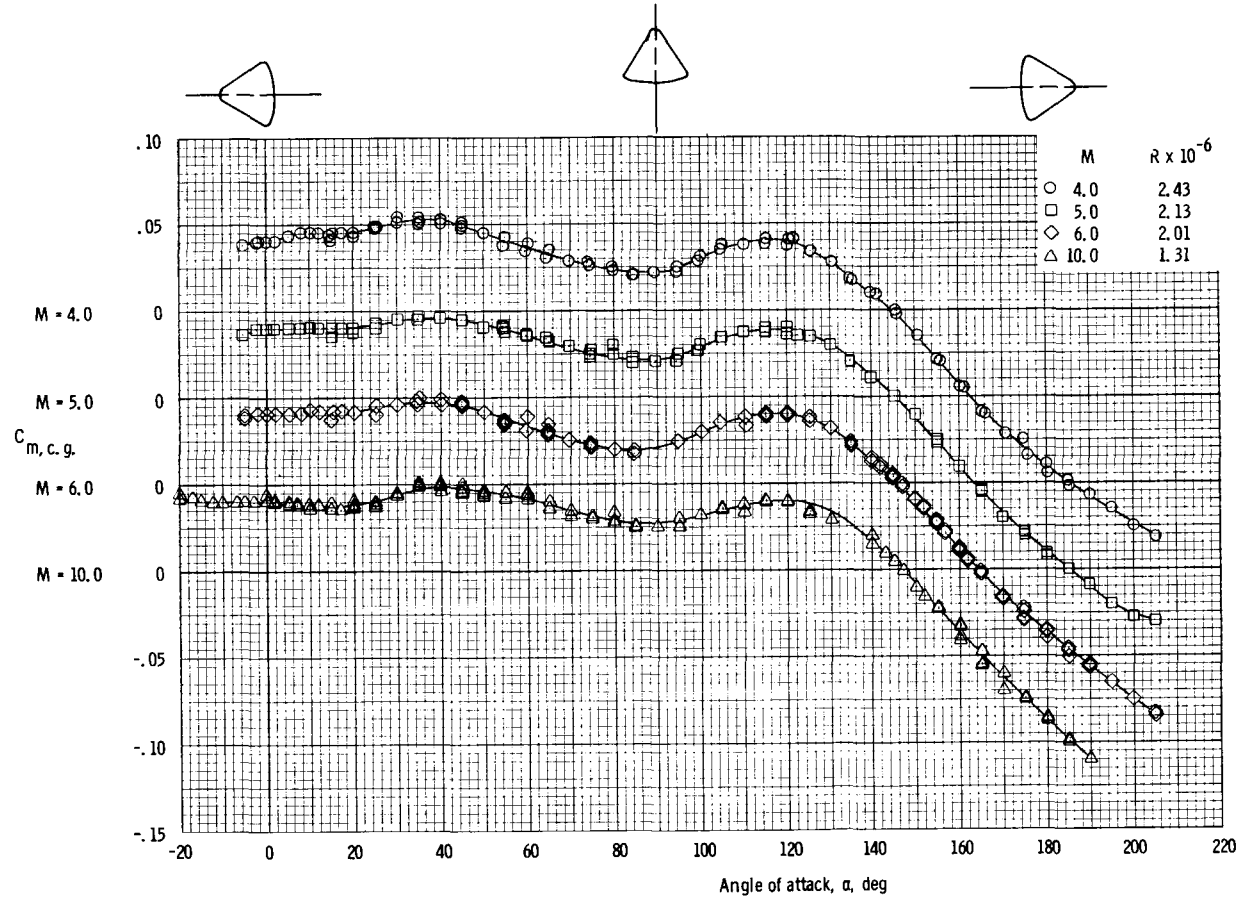

(a) Pitching-moment coefficient (c. g.).

Figure 24. - Aerodynamic characteristics of the Apollo command module (strake configuration $C_{38}L_{28}$) obtained at AEDC-A and AEDC-C facilities at M = 4.0 to M = 10.0 (c.g. = x/d = -0.685, z/d = 0.059).

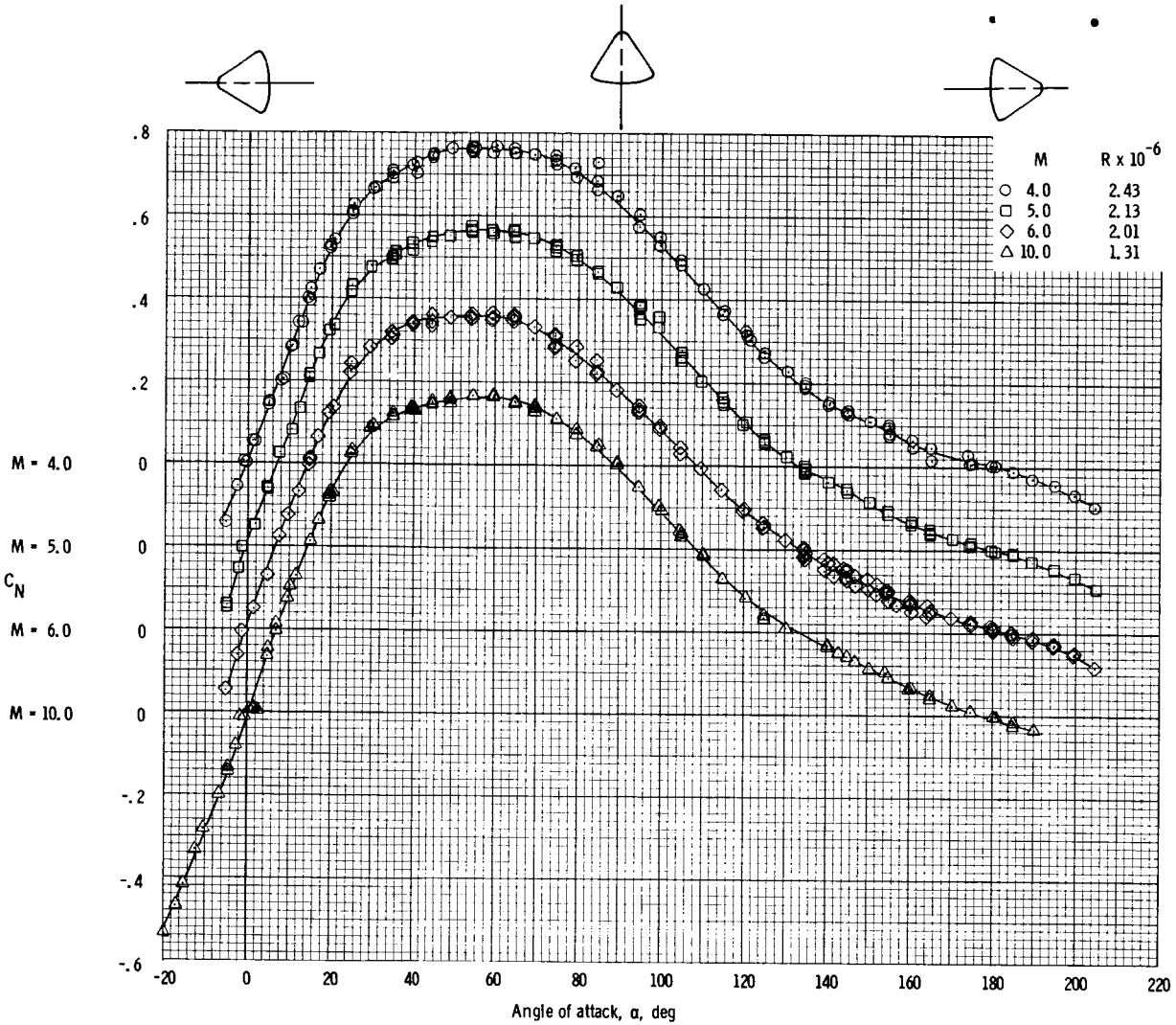

(b) Normal-force coefficient.

Figure 24. - Continued.

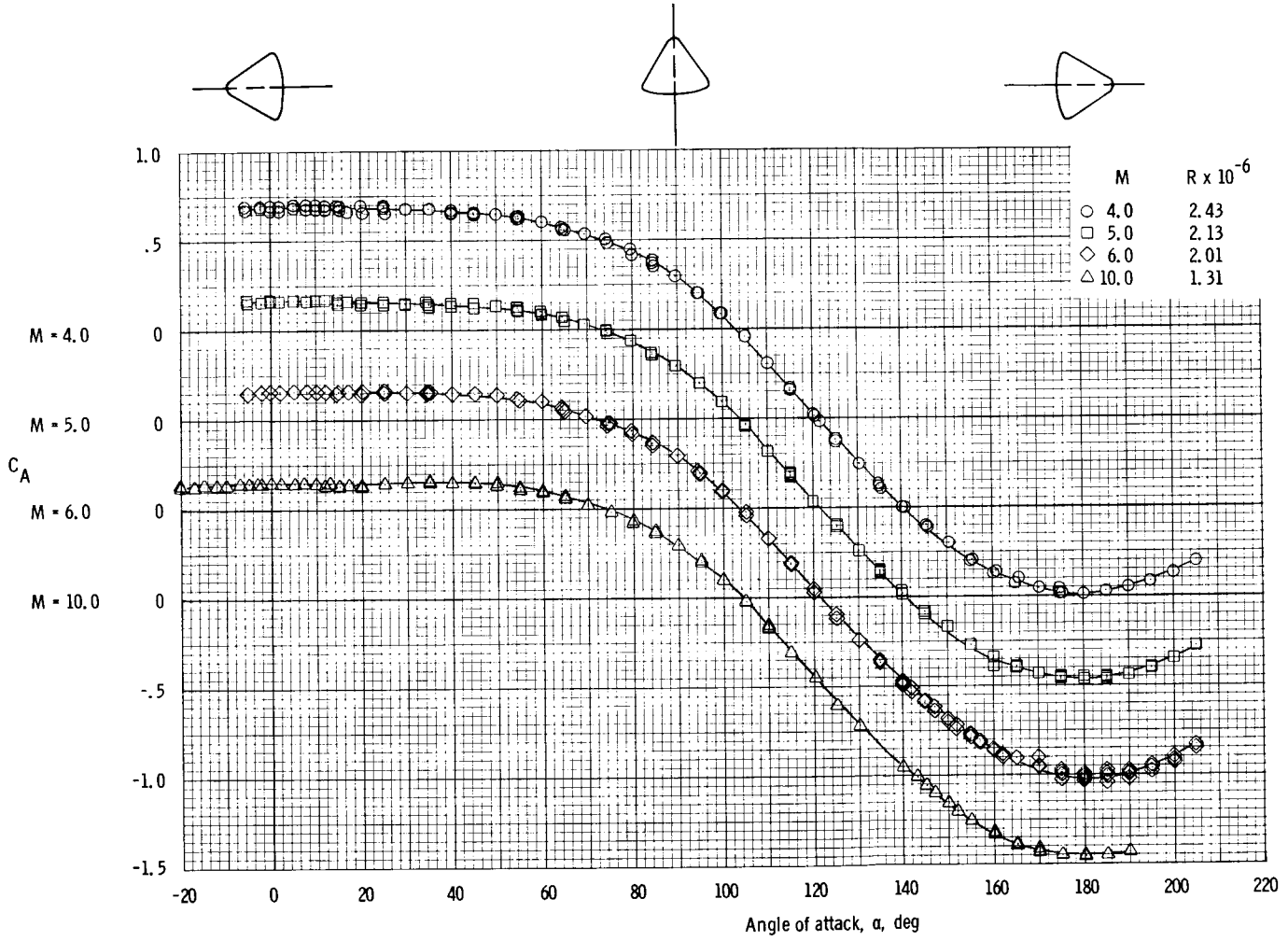

(c) Axial-force coefficient.

Figure 24. - Continued.

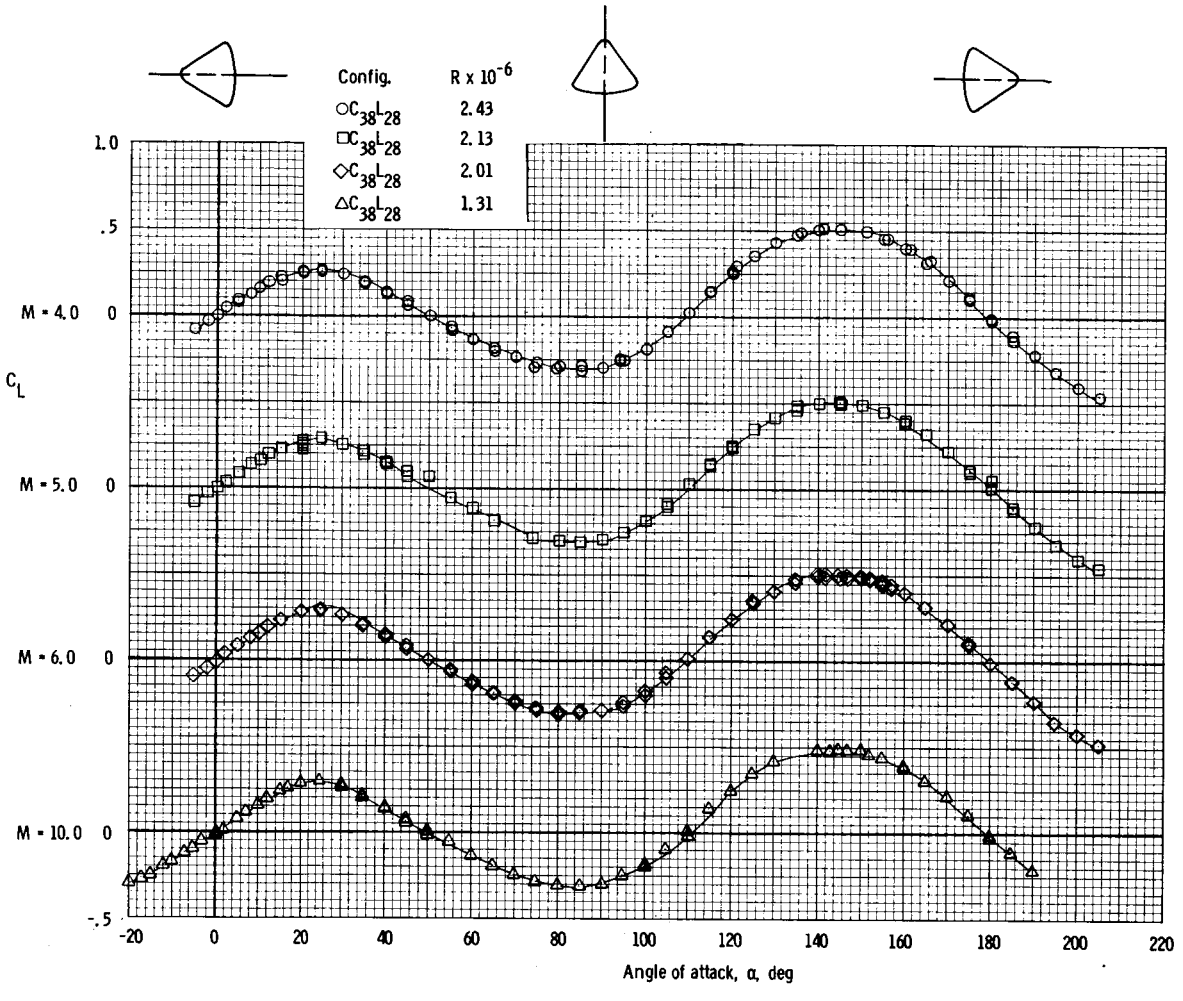

(d) Lift coefficient.

Figure 24. - Continued.

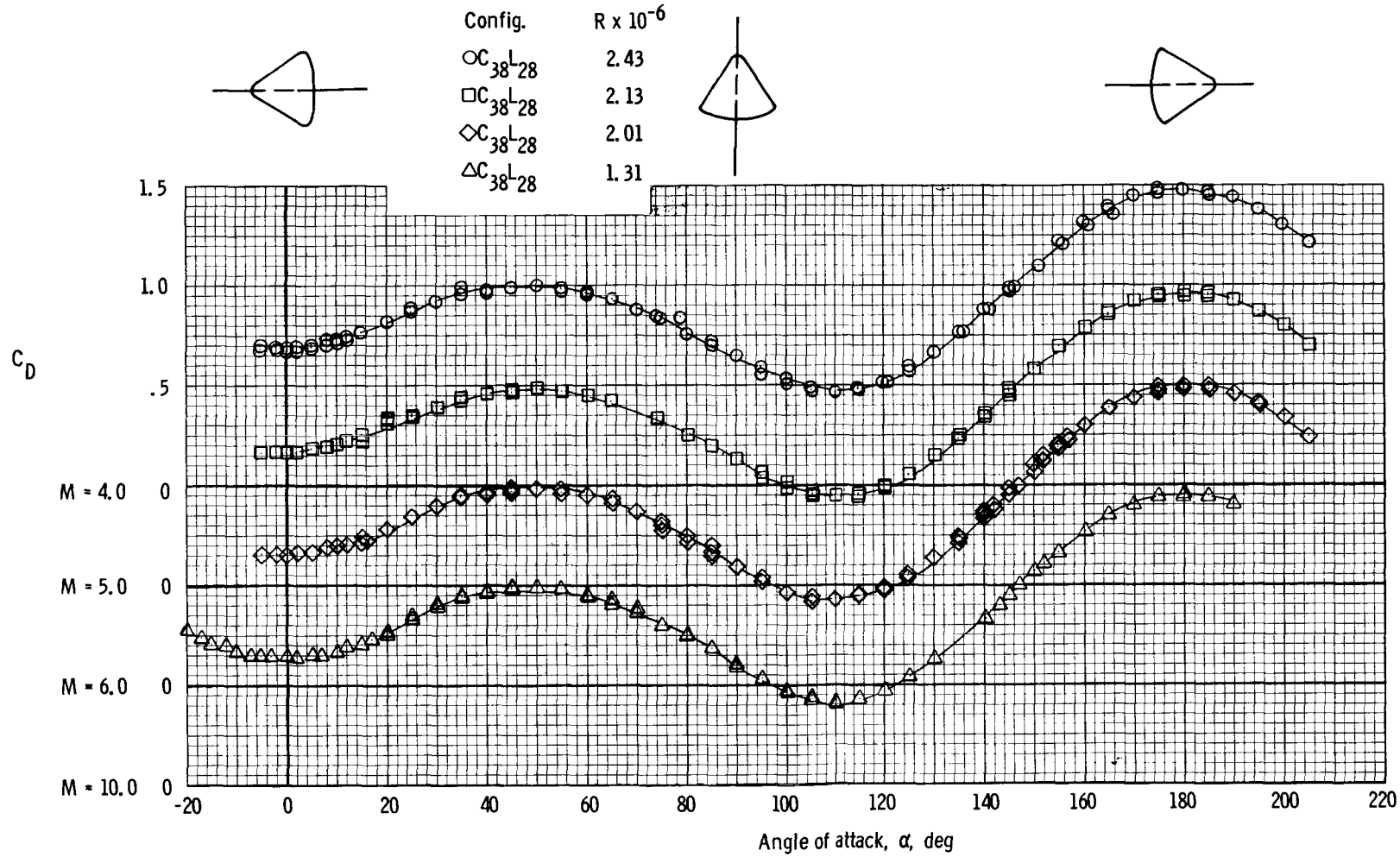

(e) Drag coefficient.

Figure 24. - Continued.

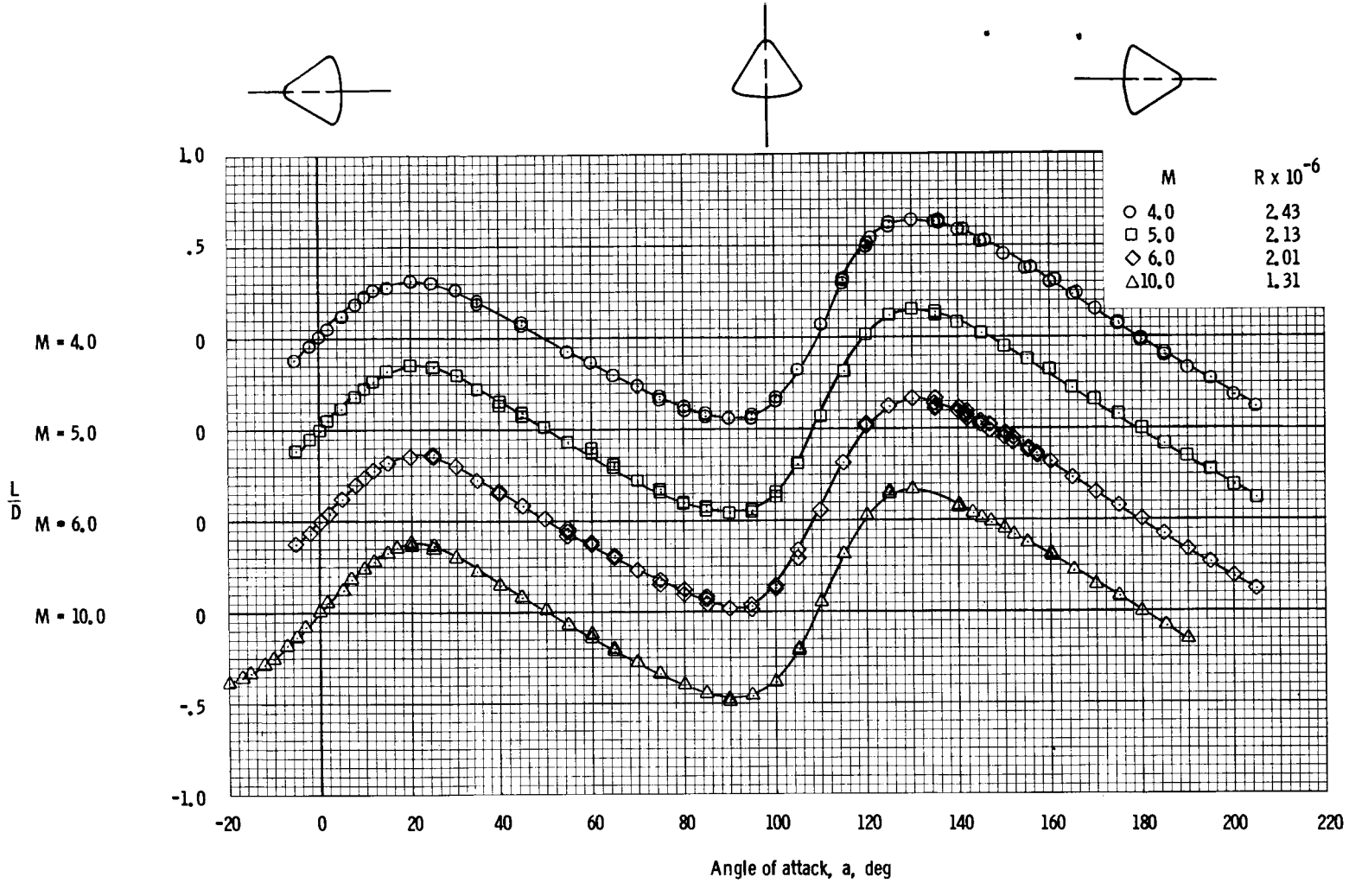

(f) Lift-to-drag ratio.

Figure 24. - Concluded.

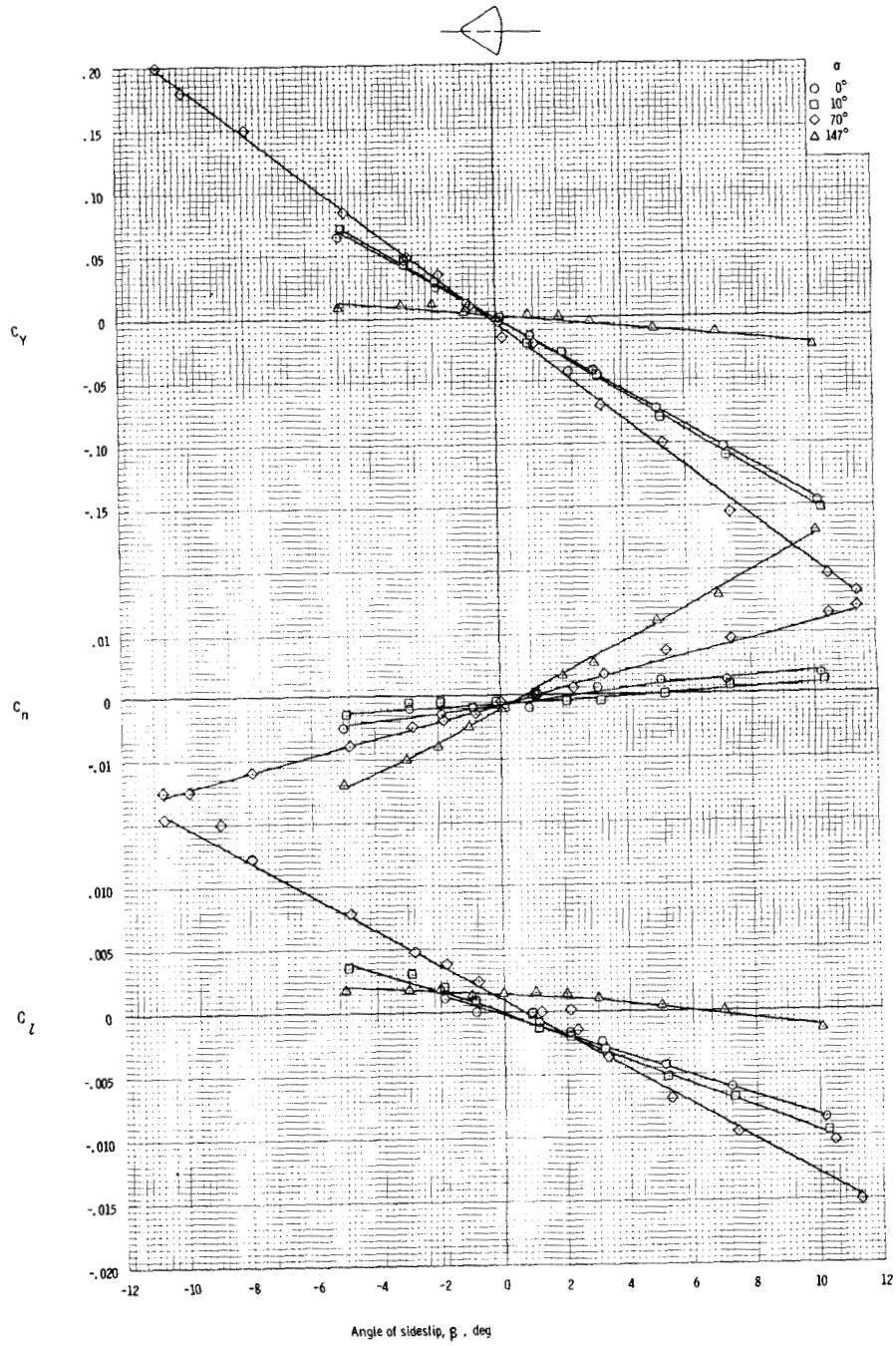

(a) Side-force, yawing-moment, and rolling-moment coefficients at $M = 0.7$, $R \times 10^{-6} = 4.9$.

Figure 25. - Aerodynamic characteristics of the Apollo command module (strake configuration $C_{39}L_{28}$) obtained at Ames-UPWT facilities at $M = 0.7$, $M = 1.35$, and $M = 3.0$ (c.g. = $x/d = -0.685$, $z/d = 0.059$).

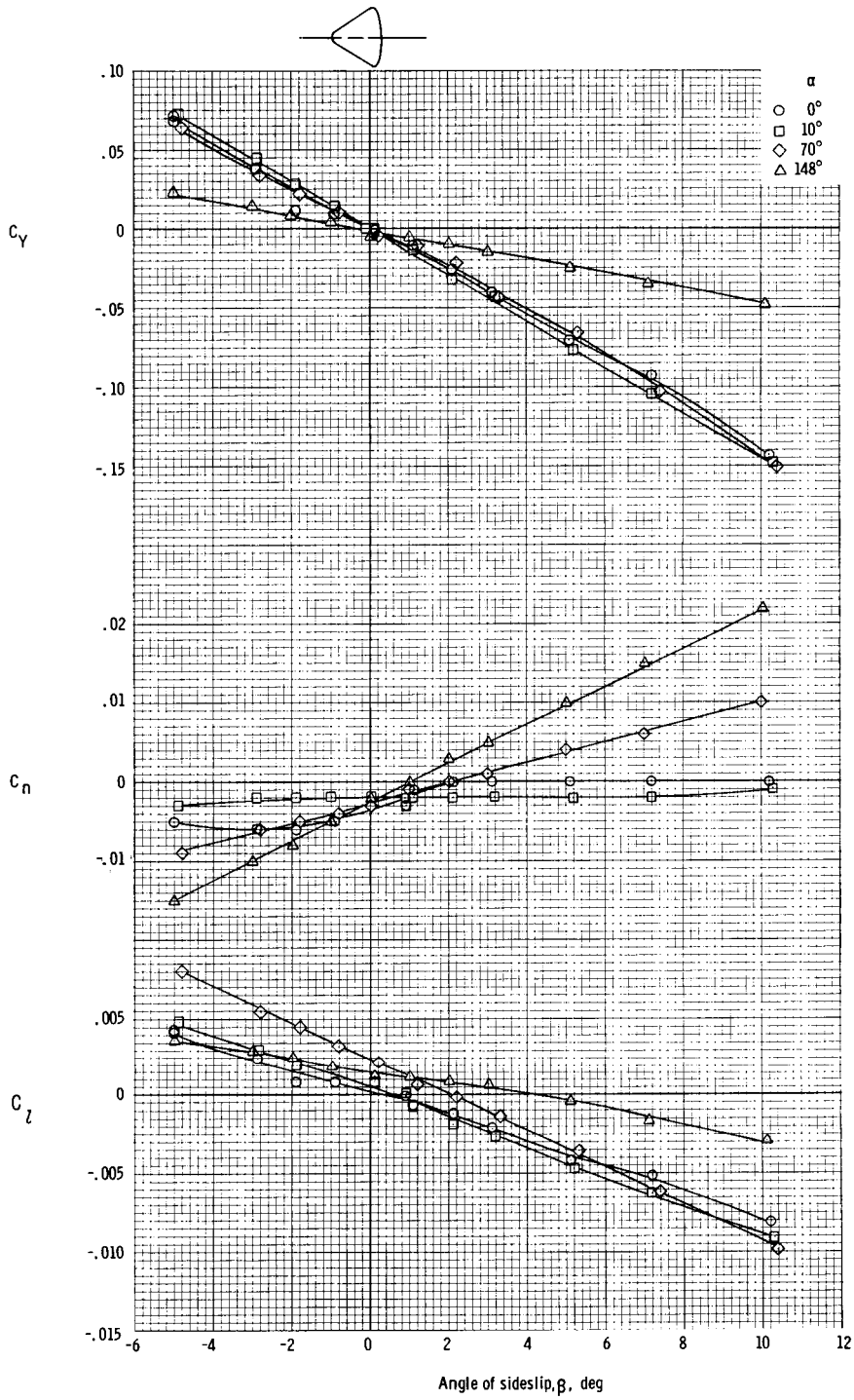

(b) Side-force, yawing-moment, and rolling-moment coefficients at $M = 1.35$, $R \times 10^{-6} = 4.9$.

Figure 25. - Continued.

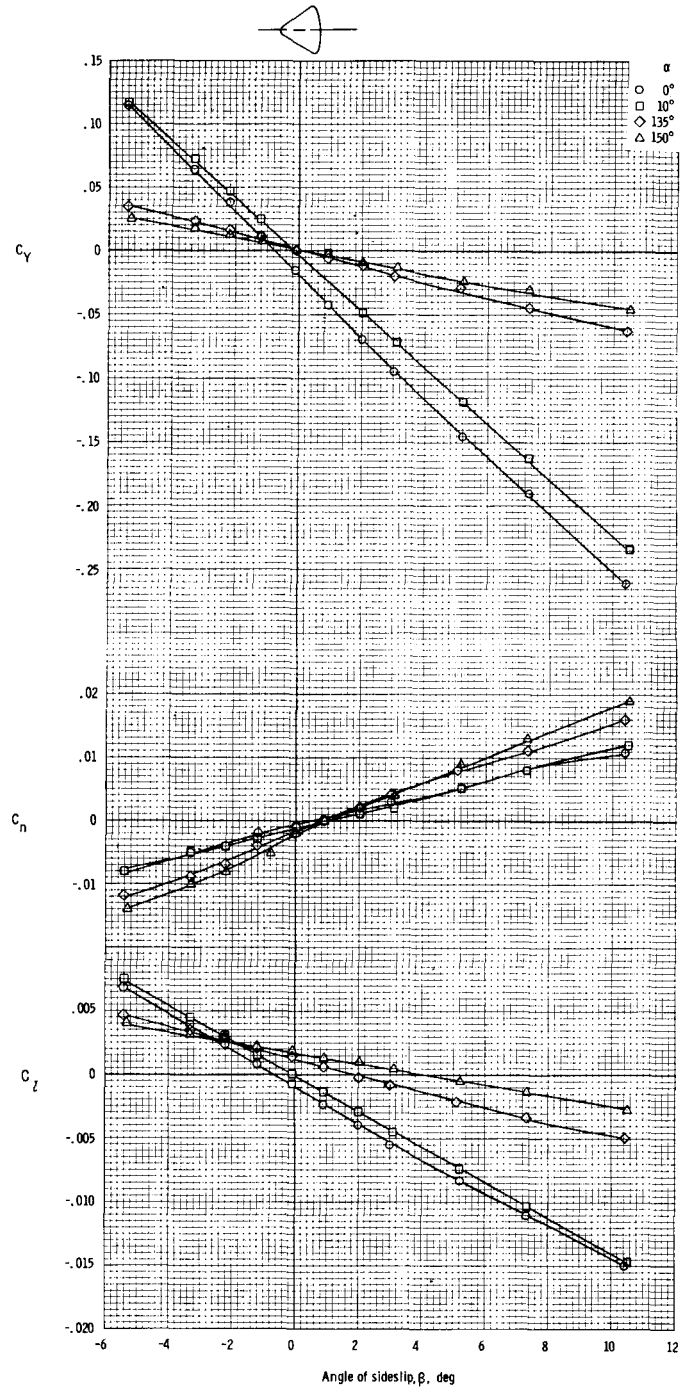

(c) Side-force, yawing-moment, and rolling-moment coefficients at $M = 3.0$, $R \times 10^{-6} = 3.9$.

Figure 25. - Concluded.

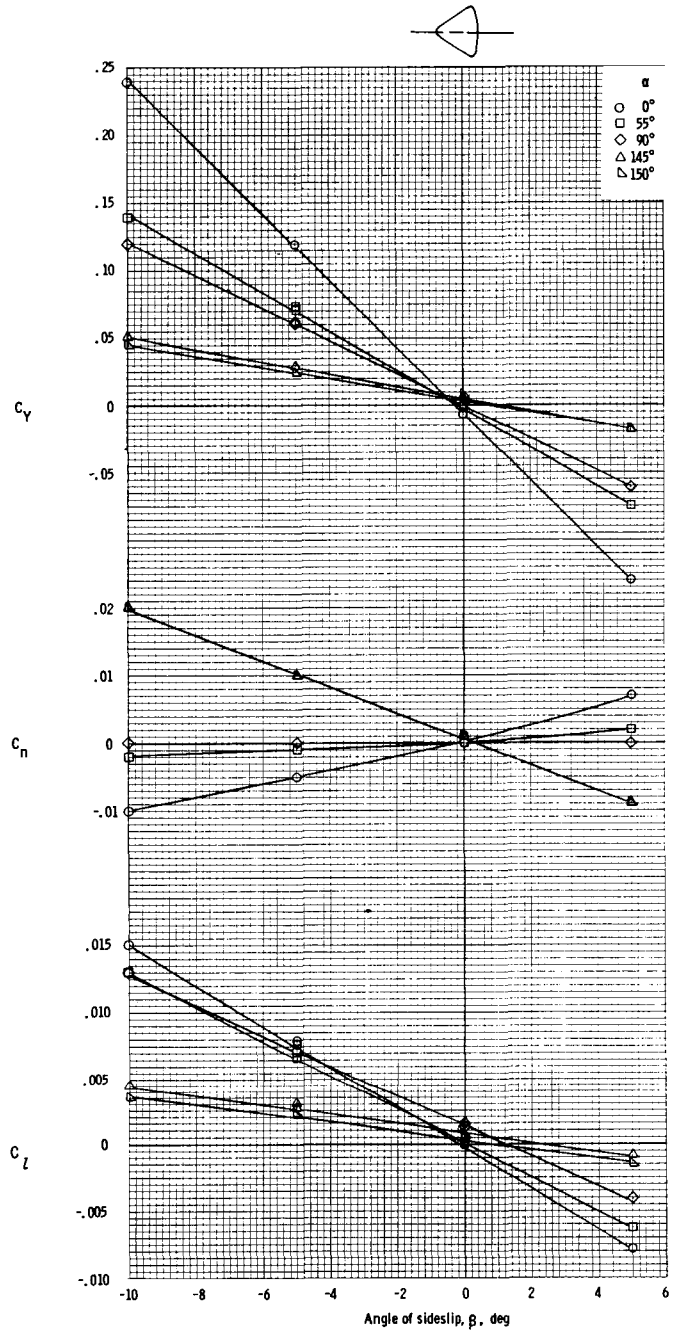

(a) Side-force, yawing-moment, and rolling-moment coefficients at $M = 4.0$, $R \times 10^{-6} = 2.43$.

Figure 26. - Aerodynamic characteristics of the Apollo command module (strake configuration $C_{38}L_{28}$) obtained at AEDC-A and AEDC-C facilities at $M = 4.0$, $M = 6.0$, and $M = 10.0$ (c.g. = x/d = -0.685, z/d = 0.059).

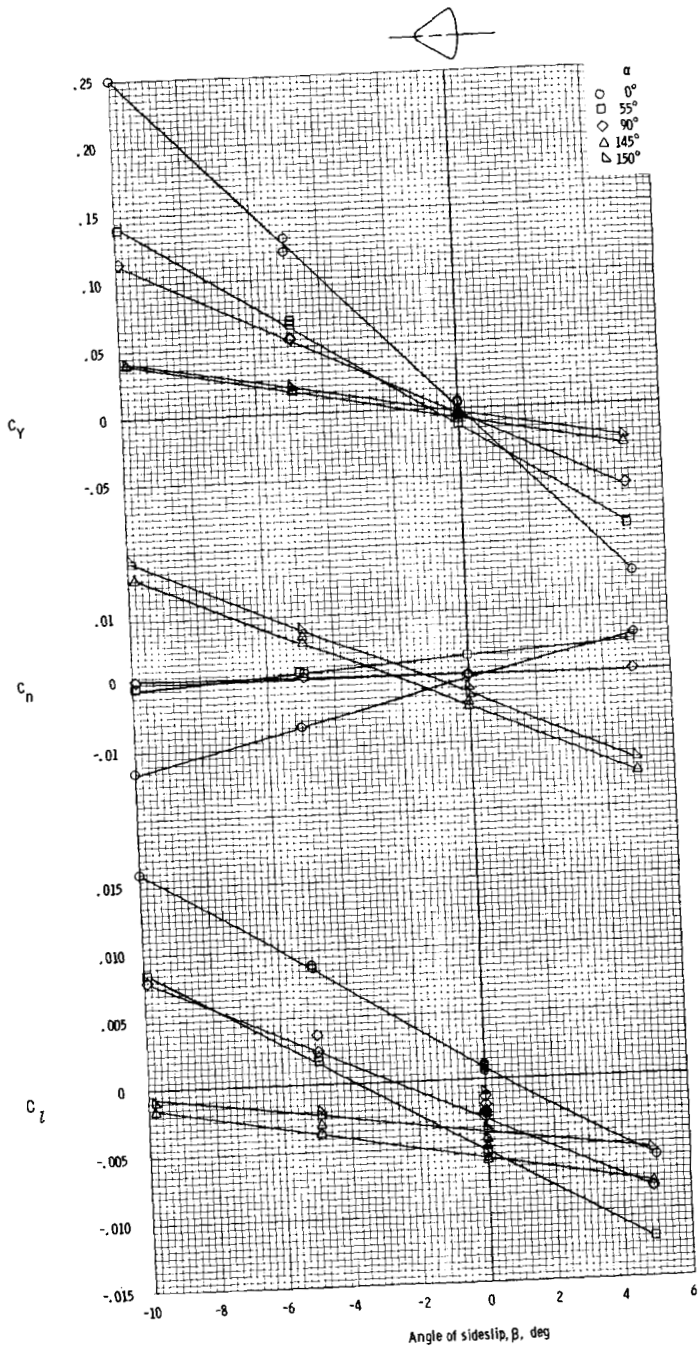

(b) Side-force, yawing-moment, and rolling-moment coefficients at $M = 6.0$, $R \times 10^{-6} = 2.01$.

Figure 26. - Continued.

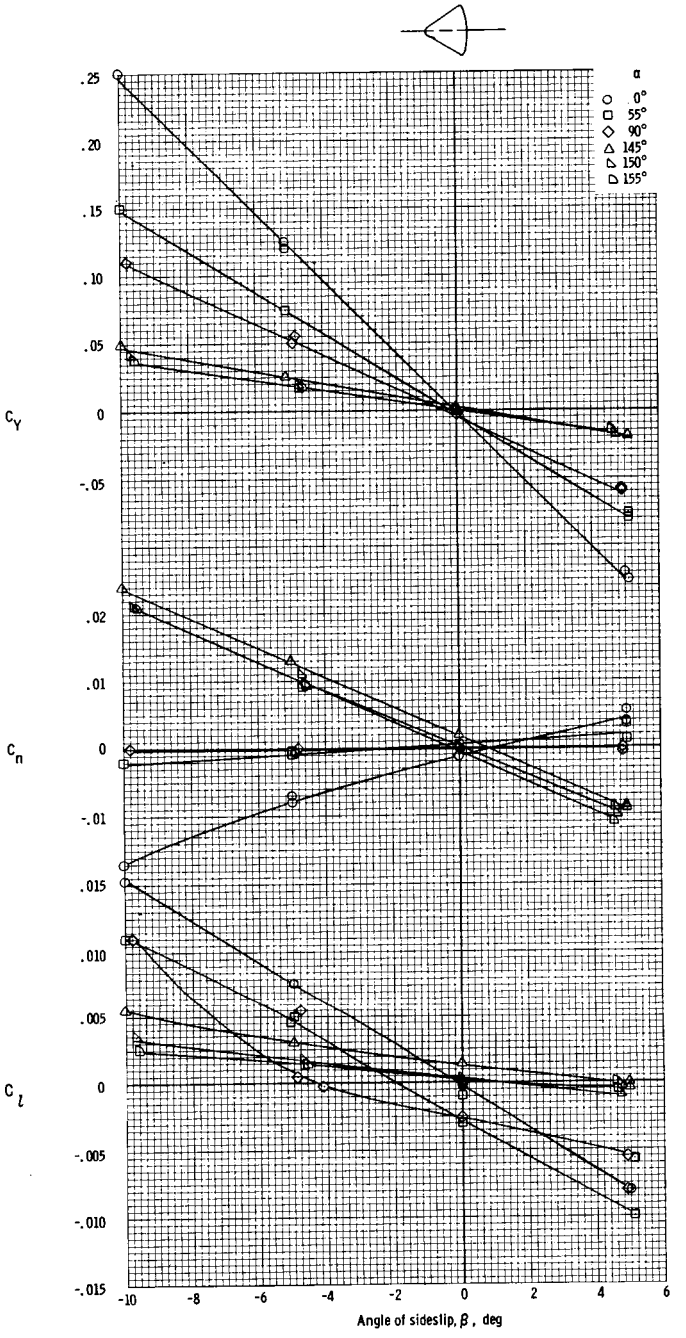

(c) Side-force, yawing-moment, and rolling-moment coefficients at $M = 10.0$, $R \times 10^{-6} = 1.31$.

Figure 26. - Concluded.

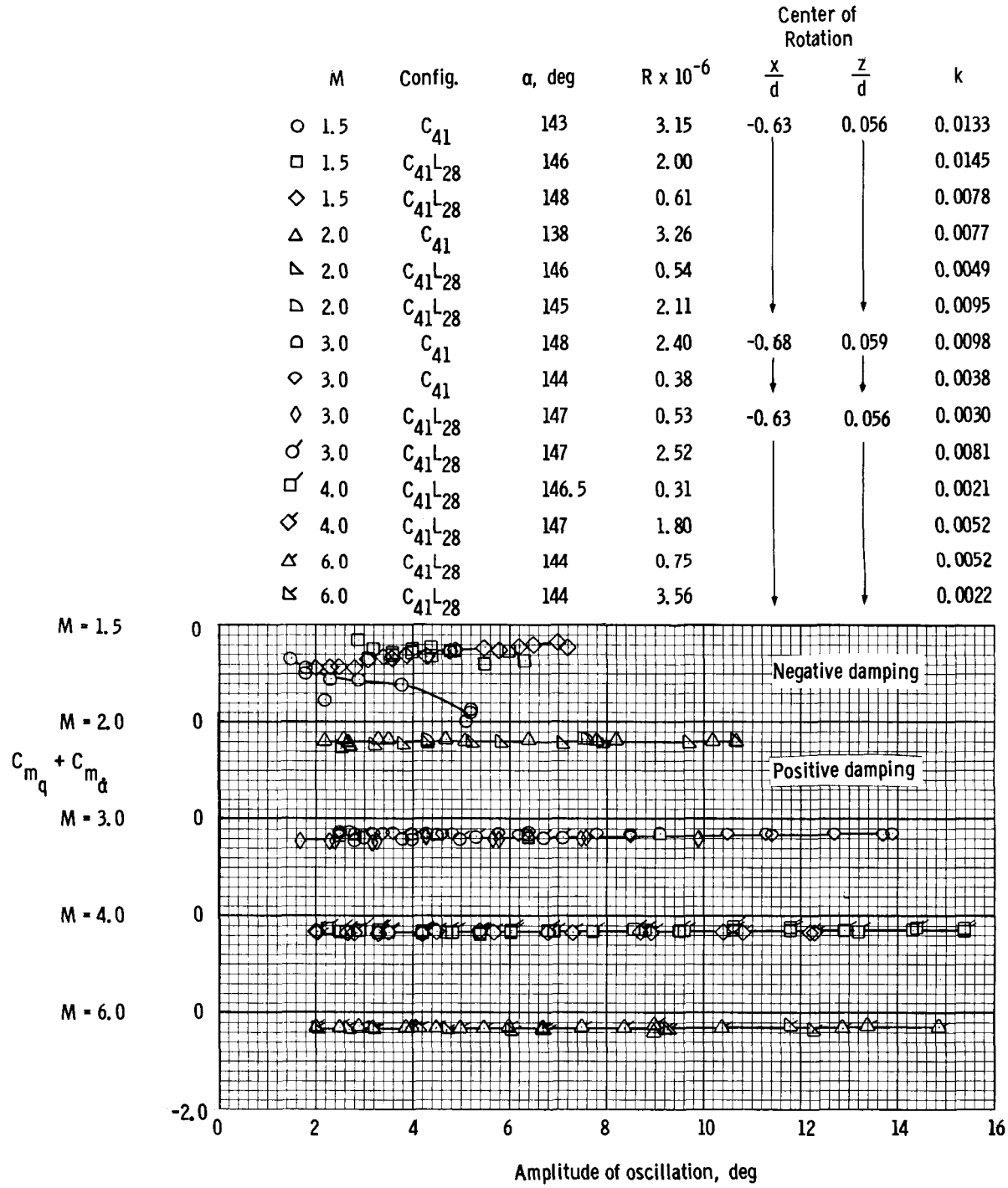

Figure 27. - Longitudinal oscillatory stability derivatives of the Apollo command module with strakes obtained at AEDC-A facility at M = 1.5 to M = 6.0.

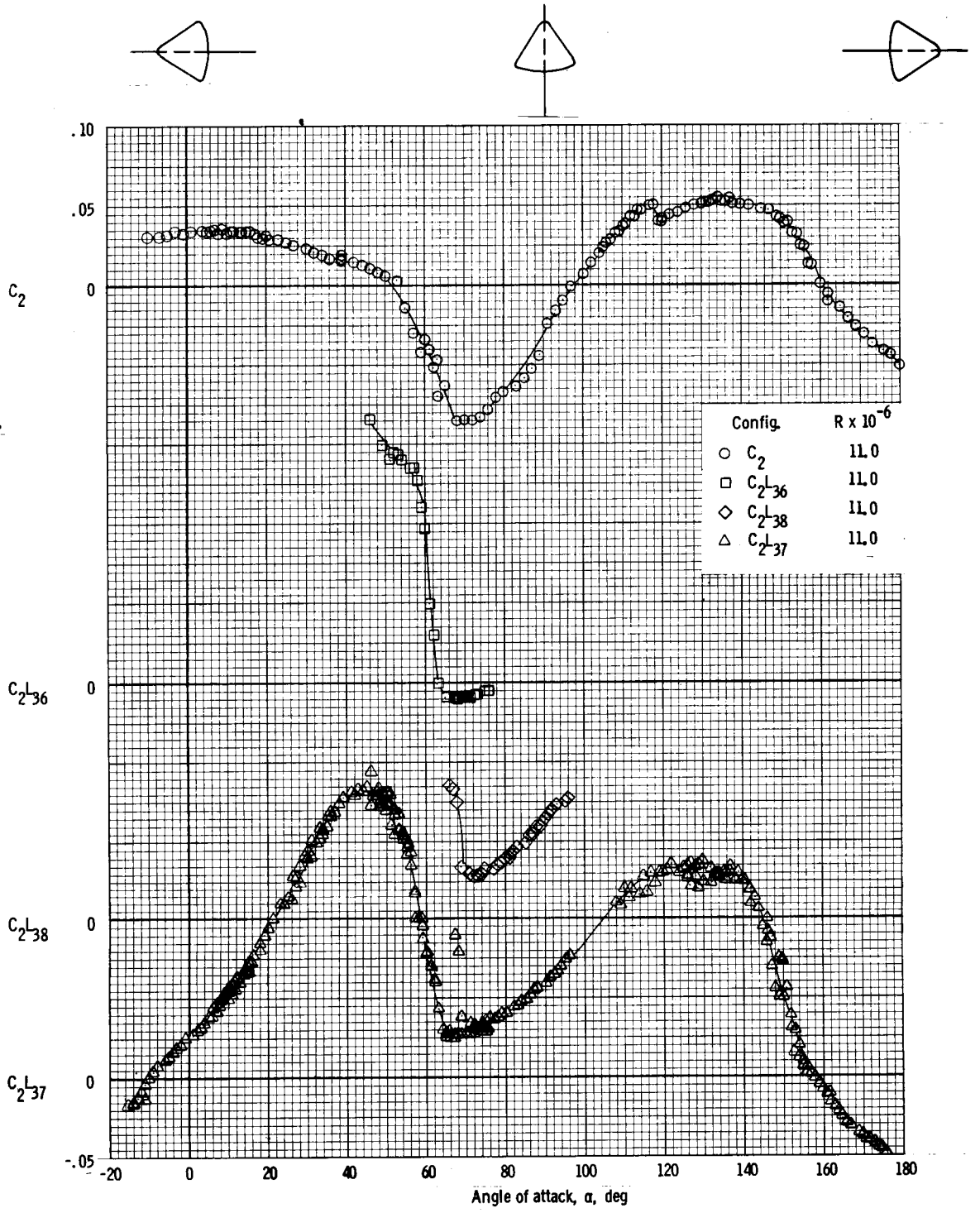

(a) Pitching-moment coefficient (c.g.).

Figure 28. - Aerodynamic characteristics of the Apollo command module with apex cover strake obtained at NAA-TWT facility at M = 0.4 (c.g. = x/d = -0.685, z/d = 0.059).

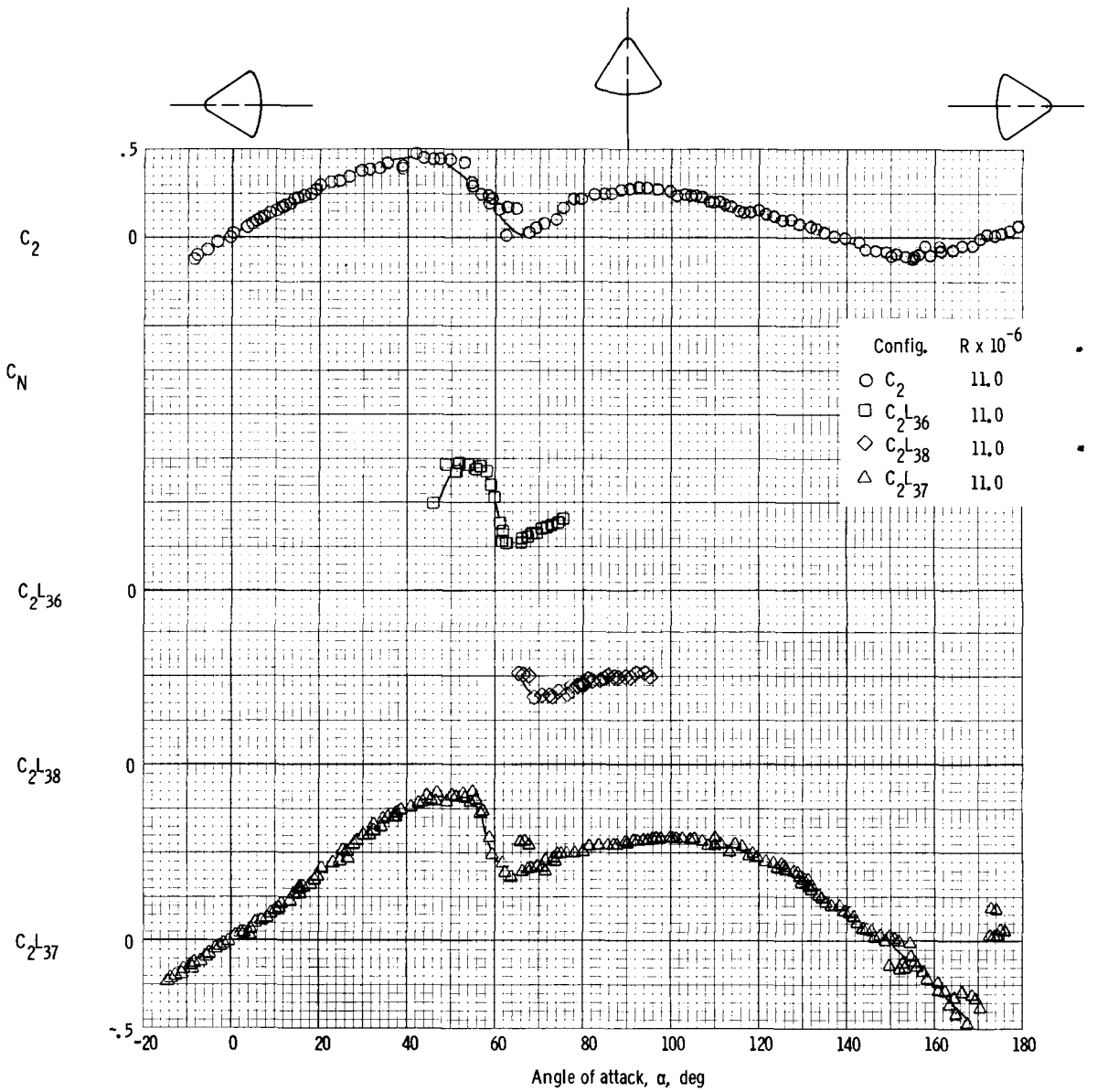

(b) Normal-force coefficient.

Figure 28. - Continued.

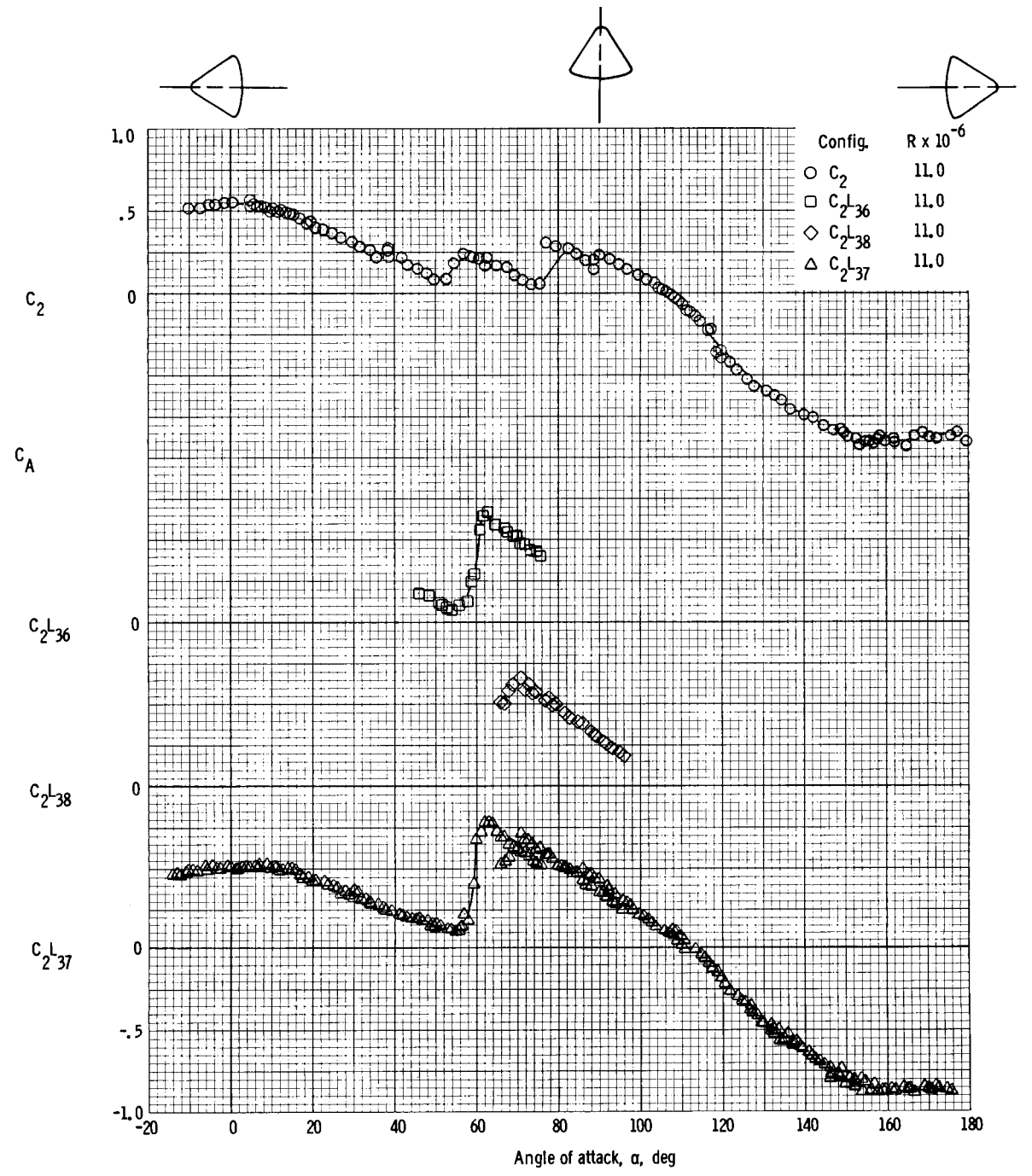

(c) Axial-force coefficient.

Figure 28. - Continued.

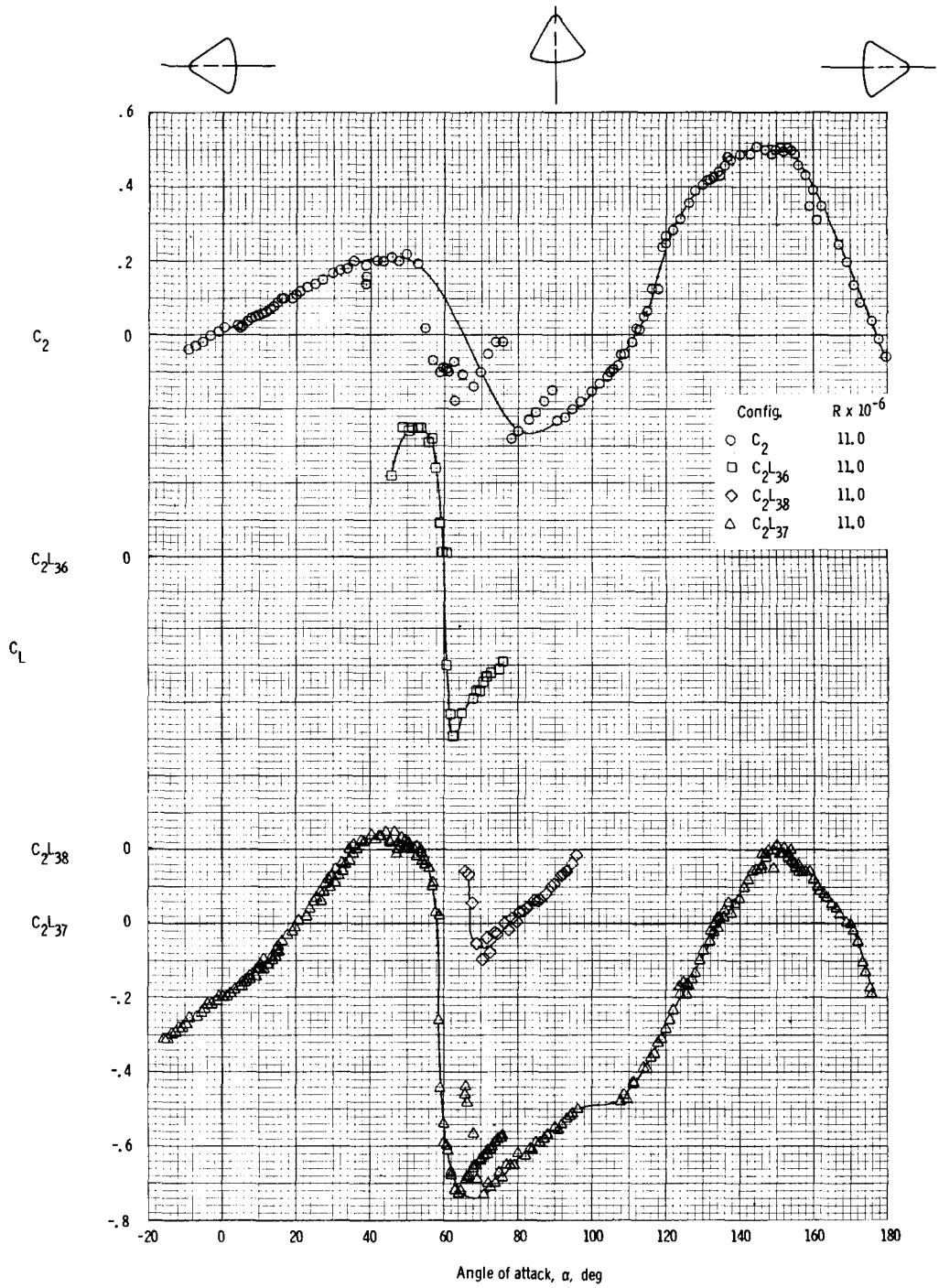

(d) Lift coefficient.

Figure 28. - Continued.

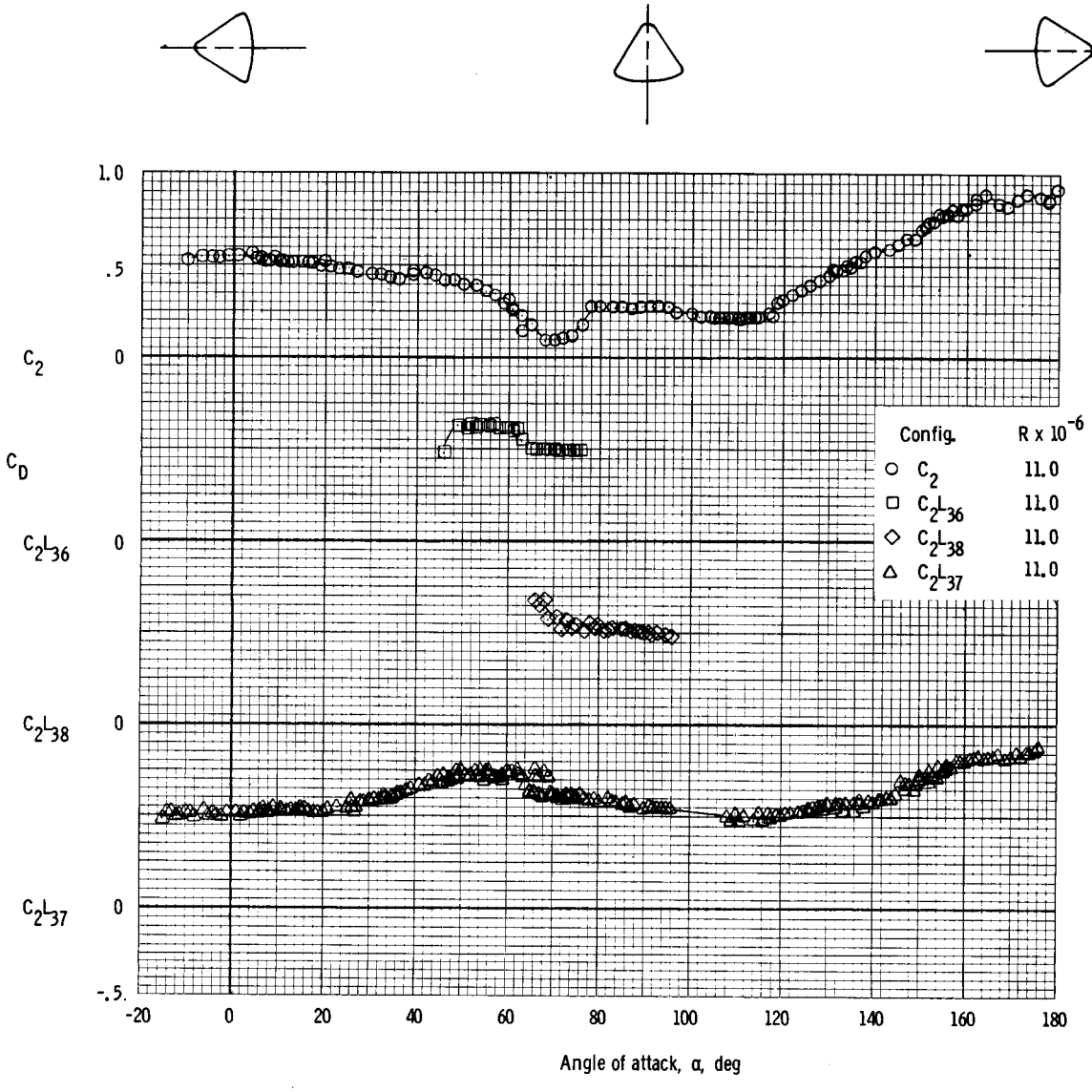

(e) Drag coefficient.

Figure 28. - Concluded.

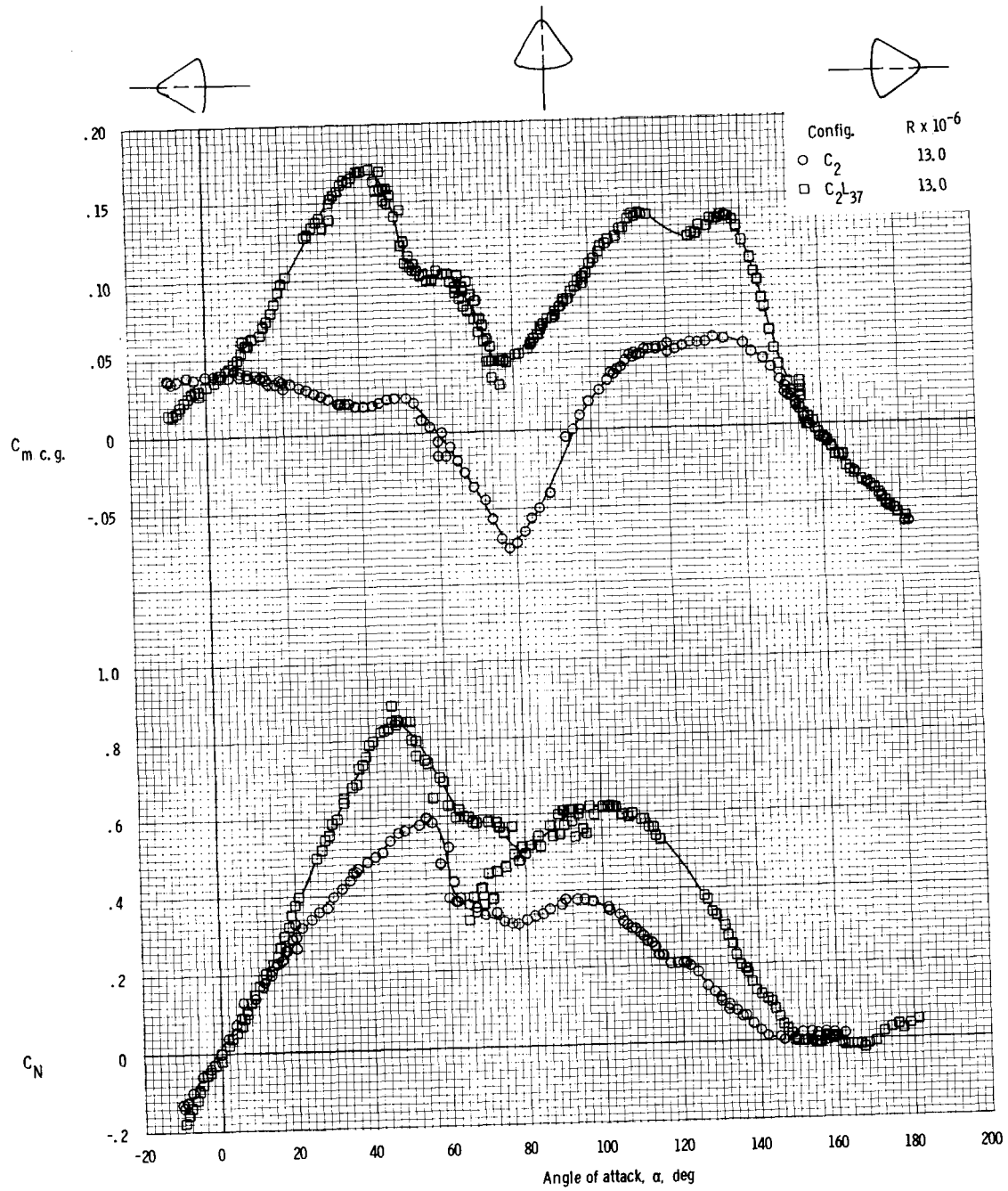

(a) Pitching-moment (c. g.) and normal-force coefficients.

Figure 29. - Aerodynamic characteristics of the Apollo command module with apex cover strake obtained at NAA-TWT facility at M = 0.7 (c. g. = x/d = -0. 685, z/d = 0. 059).

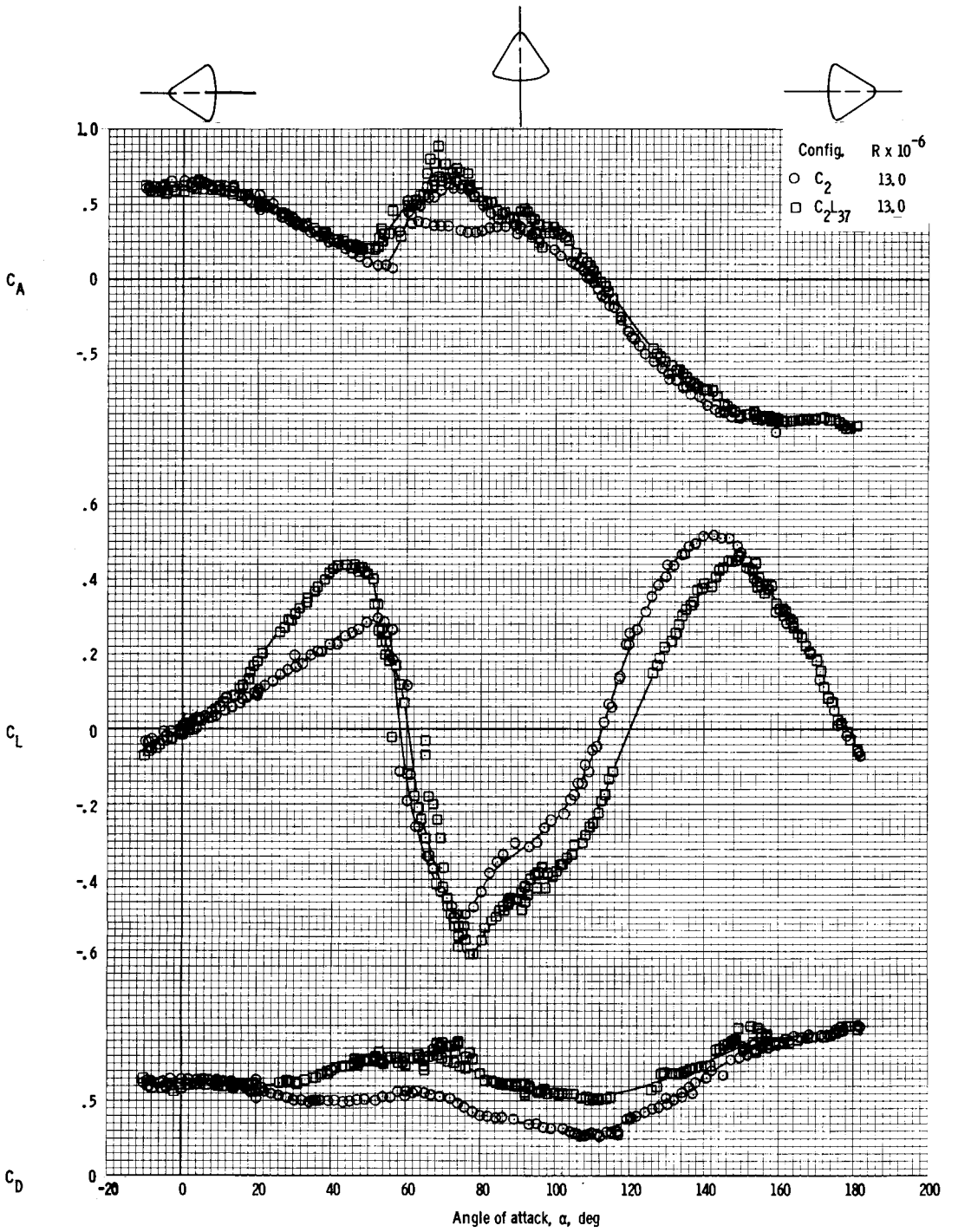

(b) Axial-force, lift, and drag coefficients.

Figure 29. - Concluded.

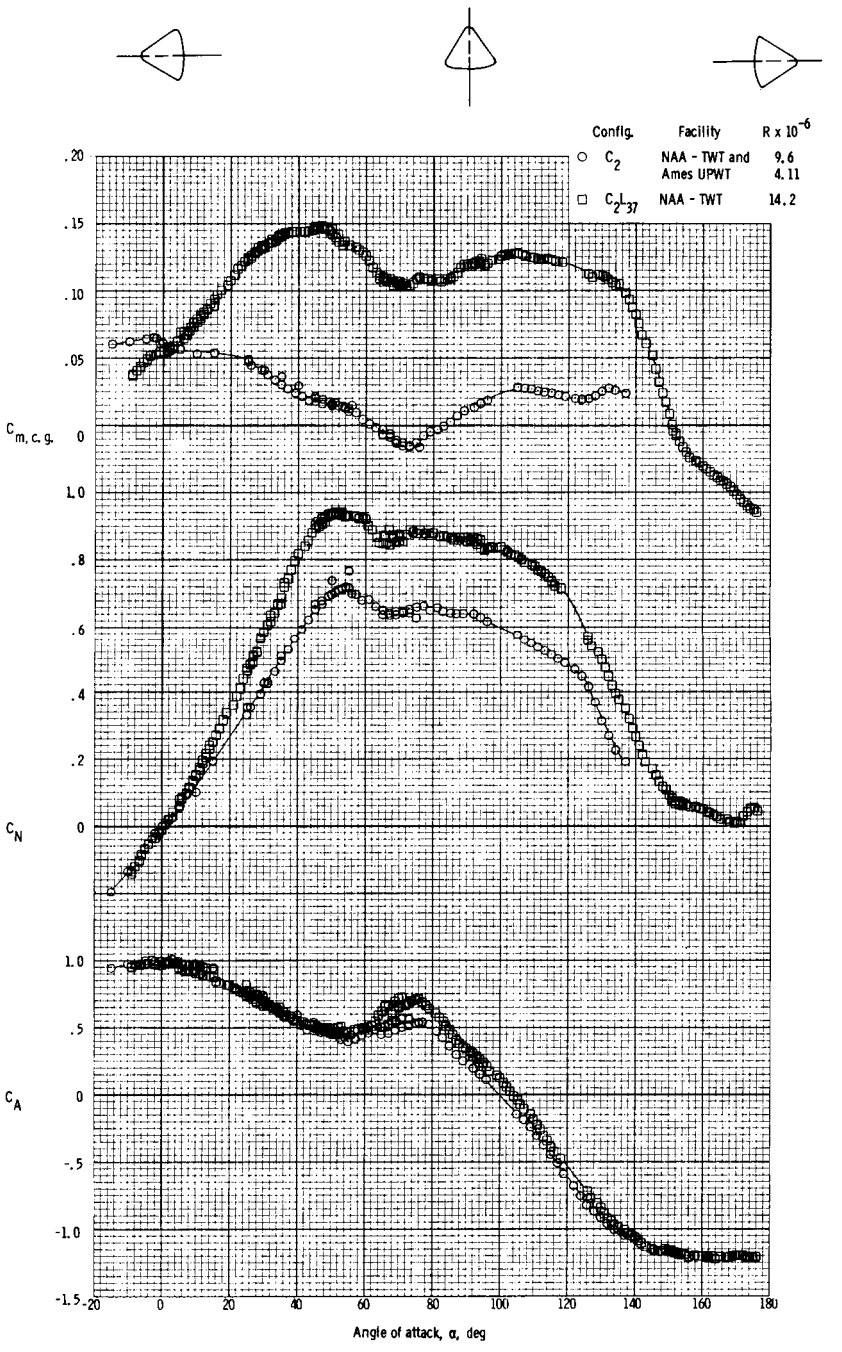

(a) Pitching-moment (c.g.), normal-force, and axial-force coefficients.

Figure 30. - Aerodynamic characteristics of the Apollo command module with apex cover strake obtained at Ames-UPWT and NAA-TWT at M = 1.2 (c.g. = x/d = -0.685, z/d = 0.059).

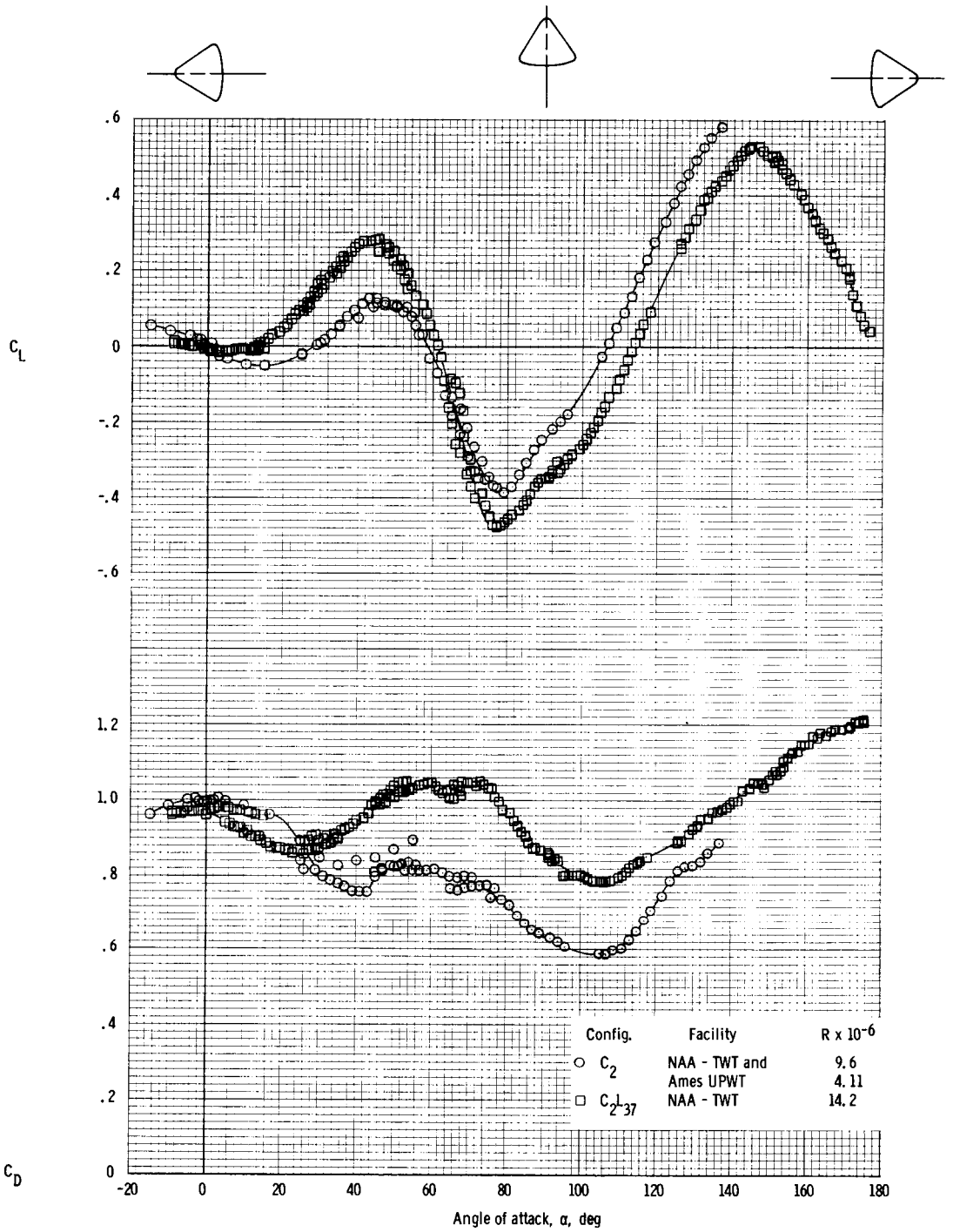

(b) Lift and drag coefficients.

Figure 30. - Concluded.

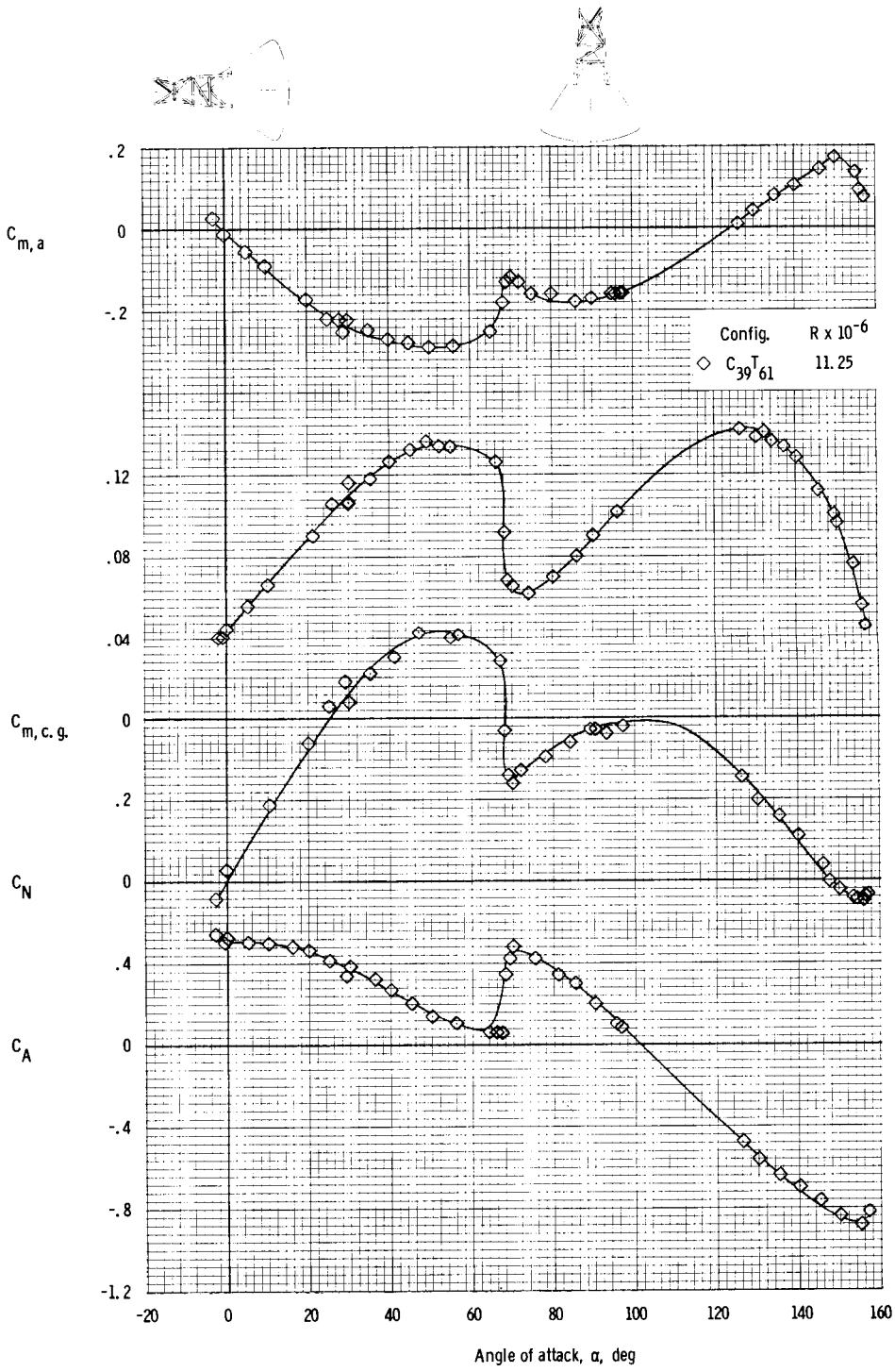

(a) Pitching-moment (apex and c. g.), normal-force, and axial-force coefficients at M = 0. 4.

Figure 31. - Aerodynamic characteristics of the Apollo command module and escape tower (with flap) obtained at NAA-TWT facility at M = 0. 4 to M = 3. 5.

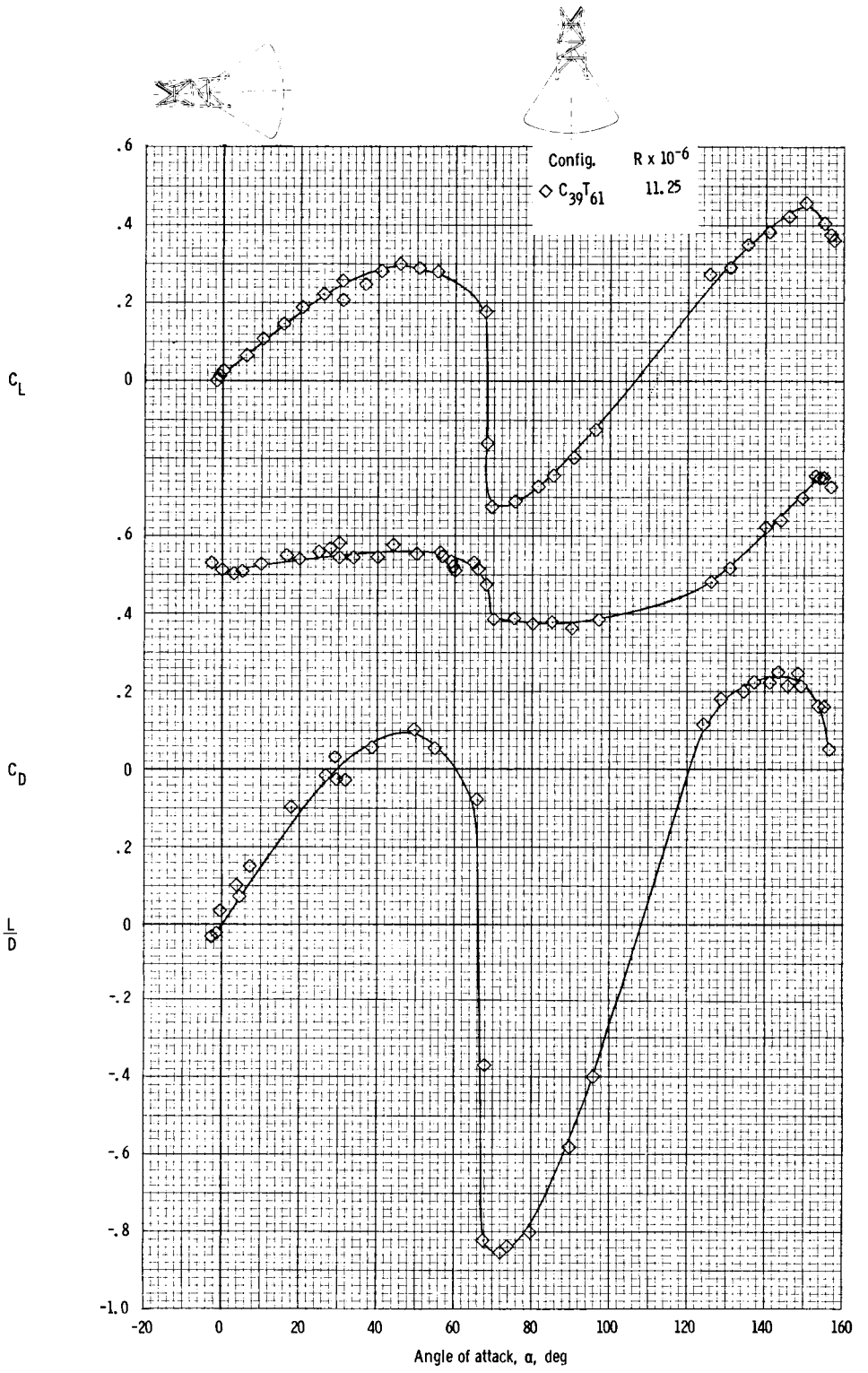

(b) Lift and drag coefficients, and lift-to-drag ratio at M = 0.4.

Figure 31. - Continued.

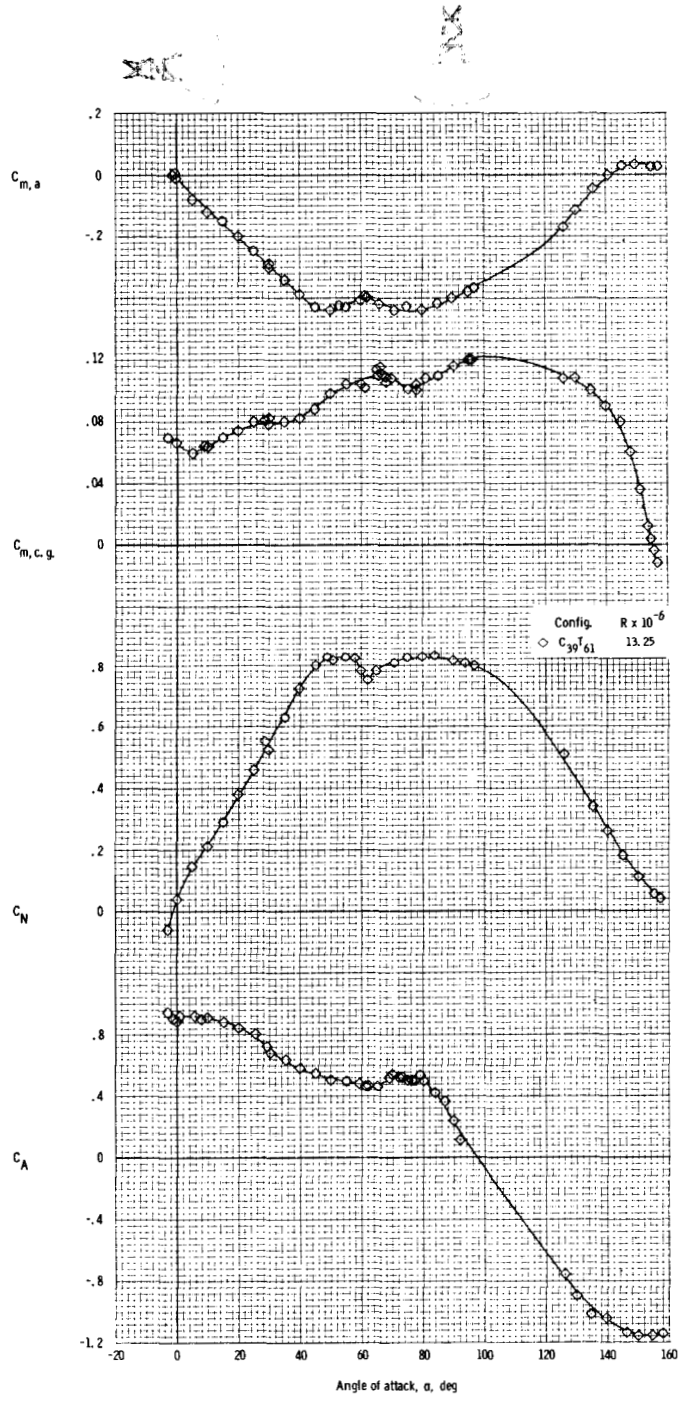

(c) Pitching-moment (apex and c. g.), normal-force, and axial-force coefficients at M = 1. 2.

Figure 31. - Continued.

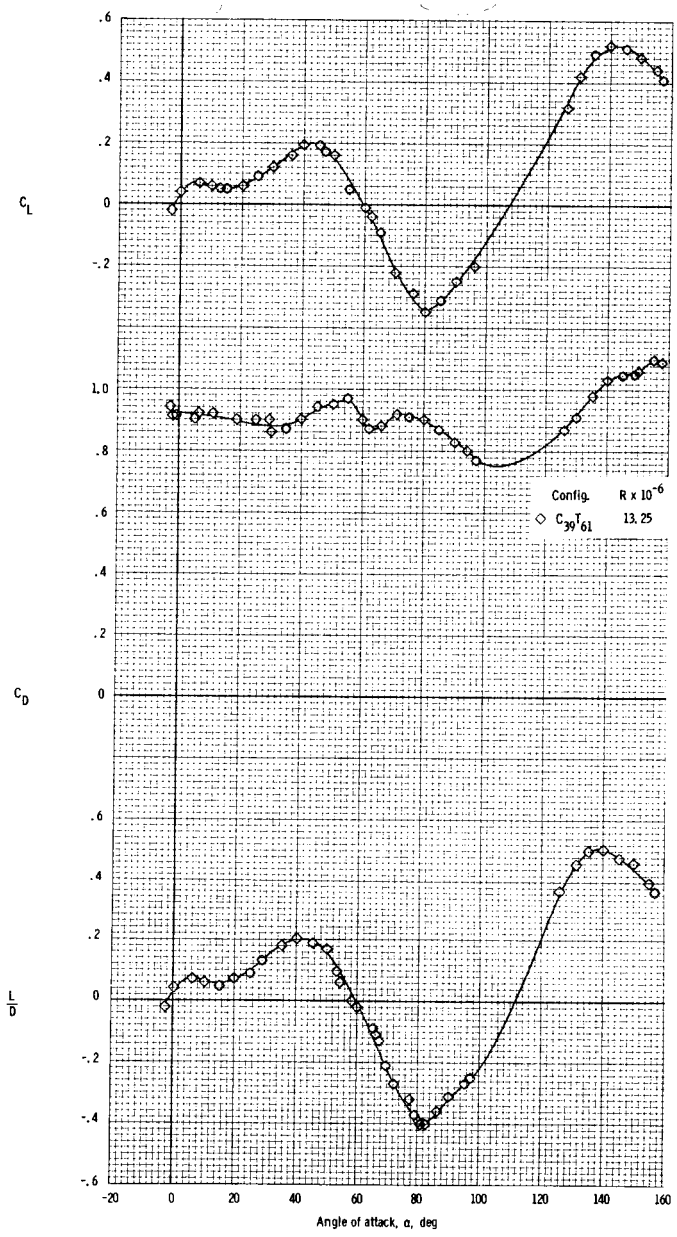

(d) Lift and drag coefficients, and lift-to-drag ratio at M = 1.2.

Figure 31. - Continued.

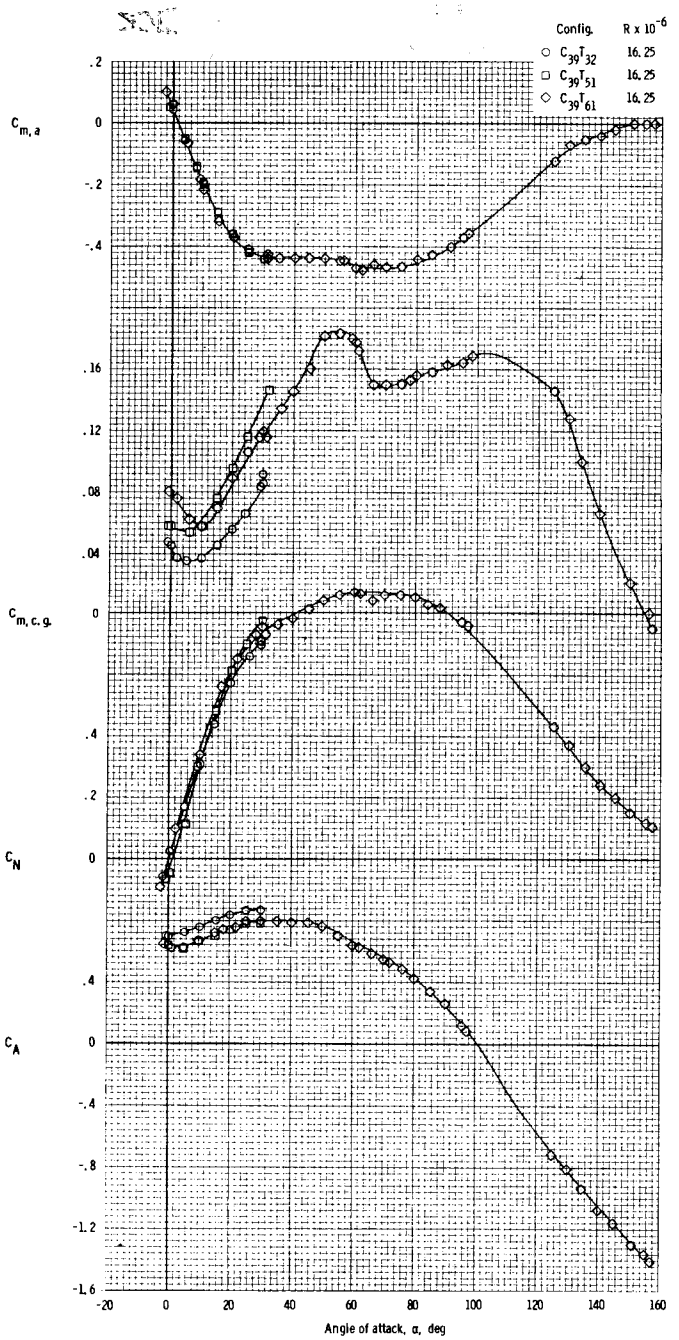

(e) Pitching-moment (apex and c.g.), normal-force, and axial-force coefficients at M = 3.5.

Figure 31. - Continued.

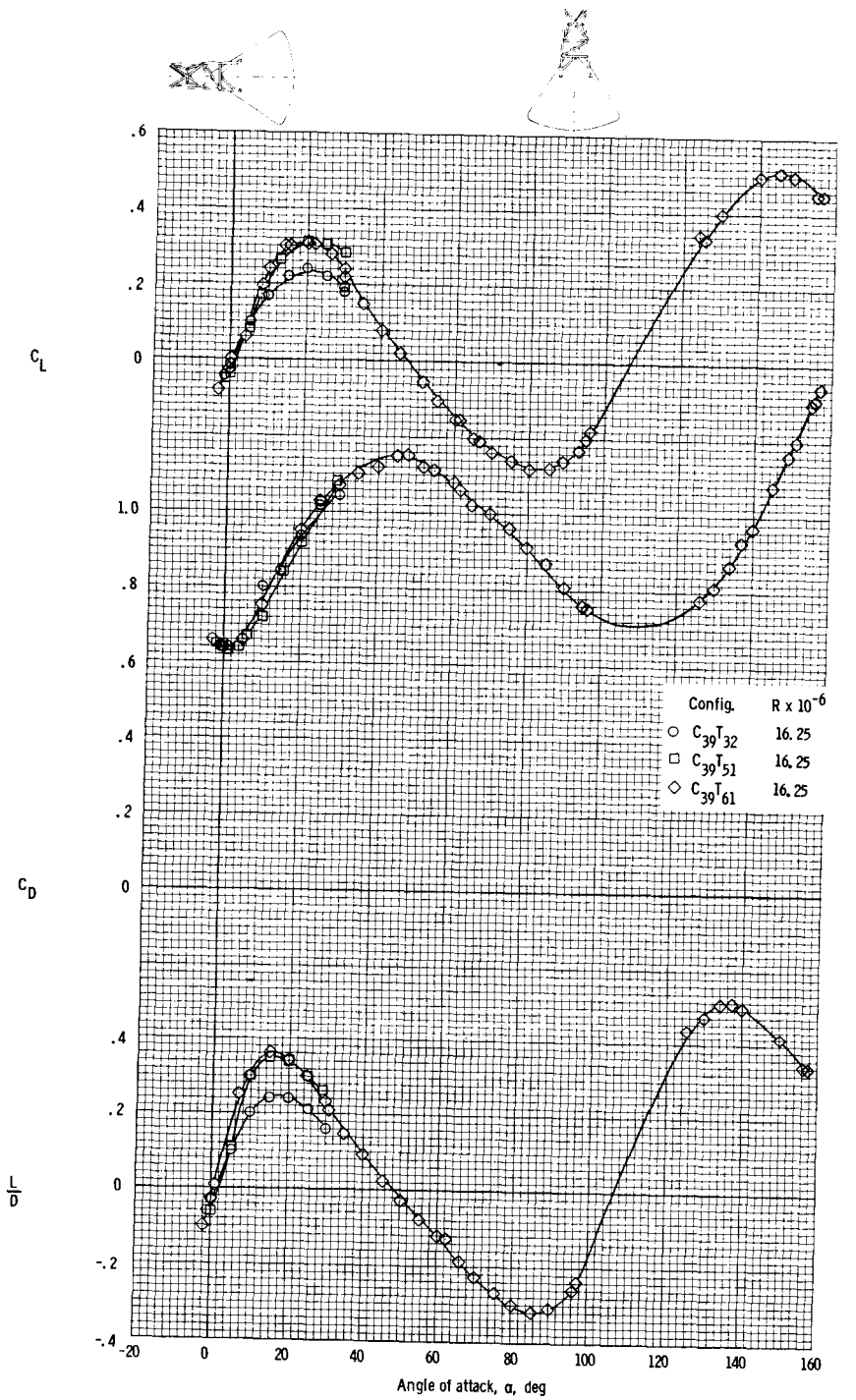

(f) Lift and drag coefficients, and lift-to-drag ratio at $M = 3.5$.

Figure 31. - Concluded.

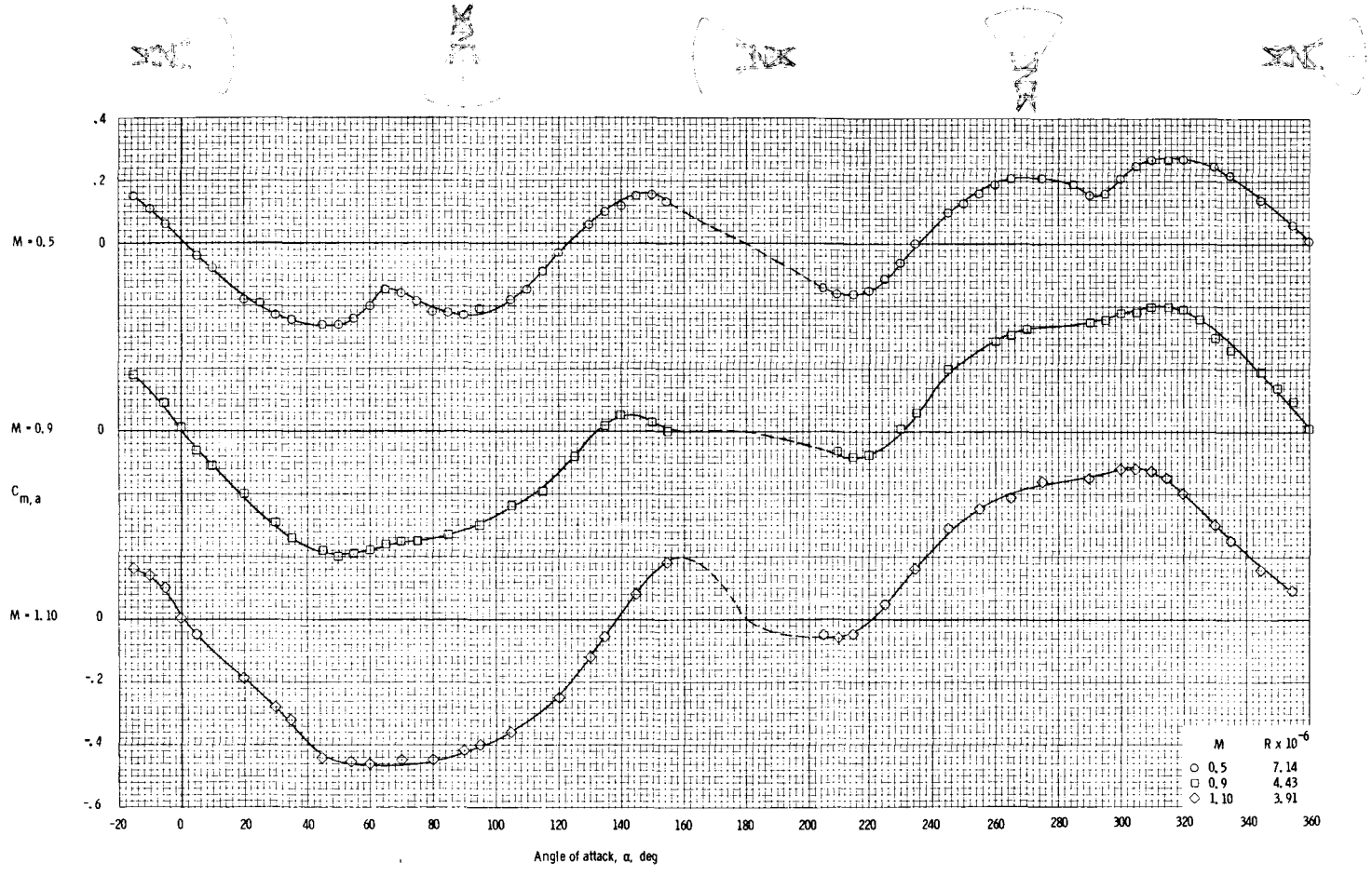

(a) Pitching-moment coefficient (apex) at M = 0.5 to M = 1.1.

Figure 32. - Aerodynamic characteristics of the Apollo command module (C_{43}) and escape tower with flap (T_{83}) obtained at Ames-UPWT facilities at M = 0.5 to M = 3.0.

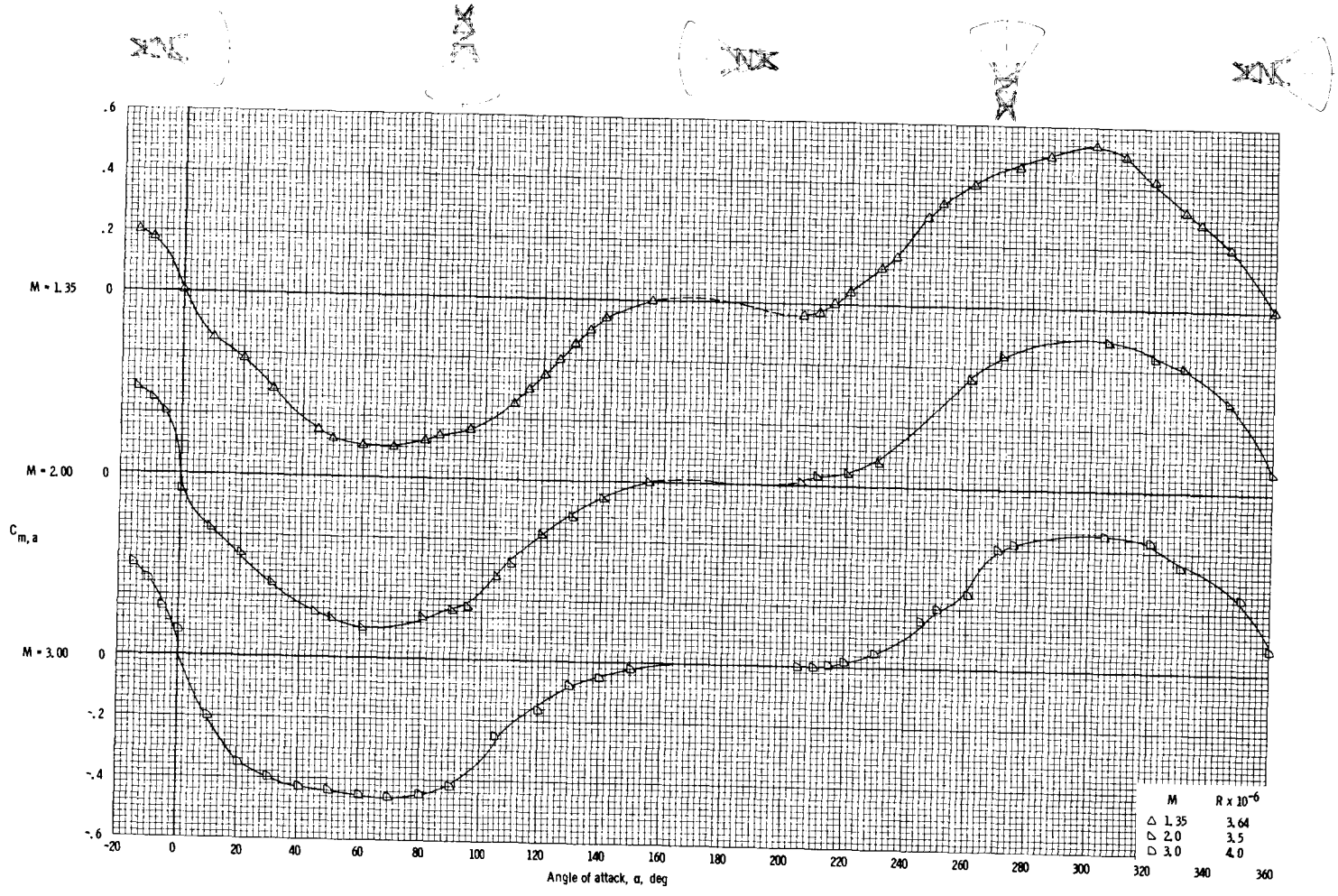

(b) Pitching-moment coefficient (apex) at M = 1.35 to M = 3.0.

Figure 32. - Continued.

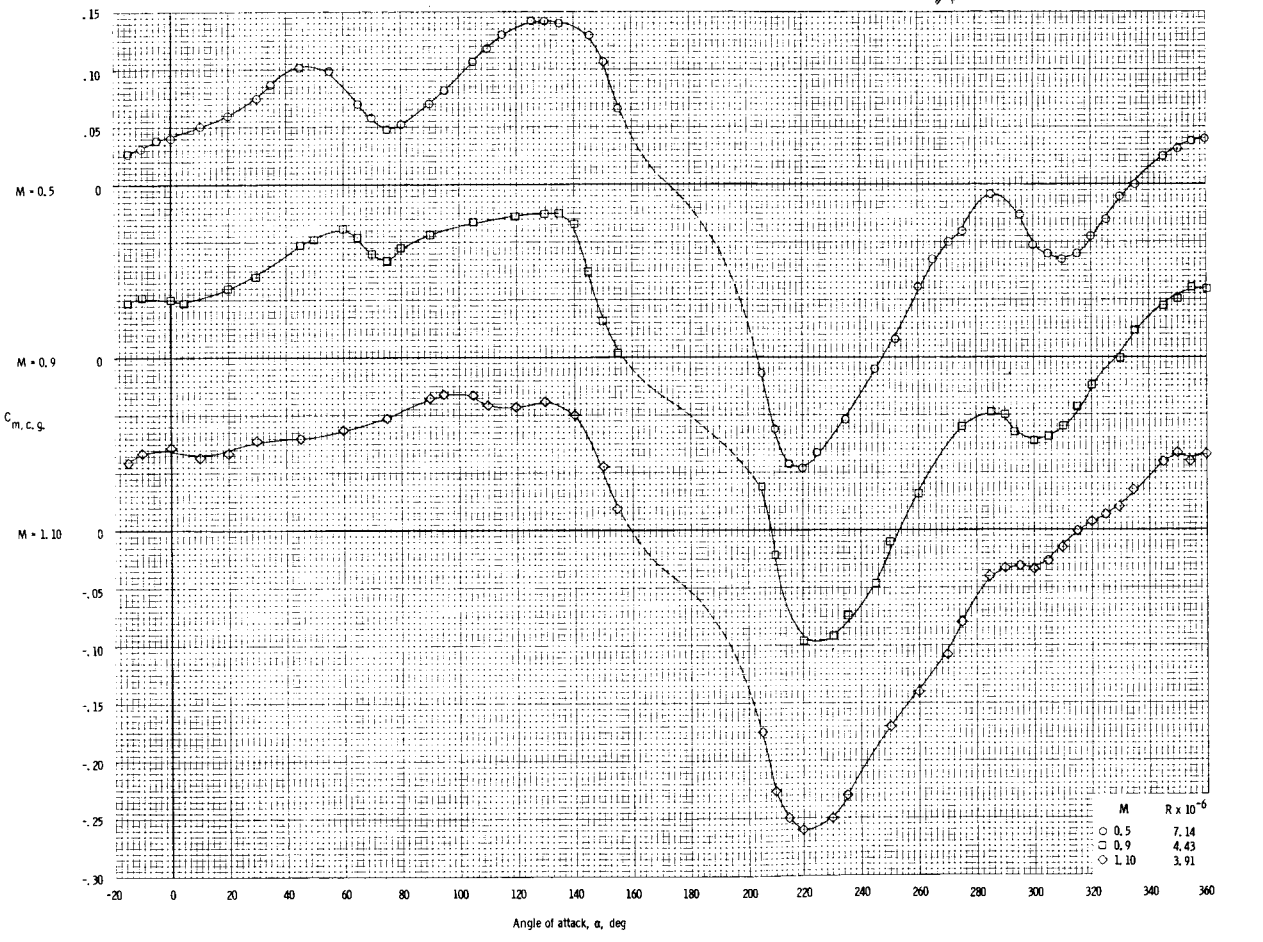

(c) Pitching-moment coefficient (c.g.) at M = 0.5 to M = 1.1 (c.g. = x/d = -0.602, z/d = 0.0474).

Figure 32. - Continued.

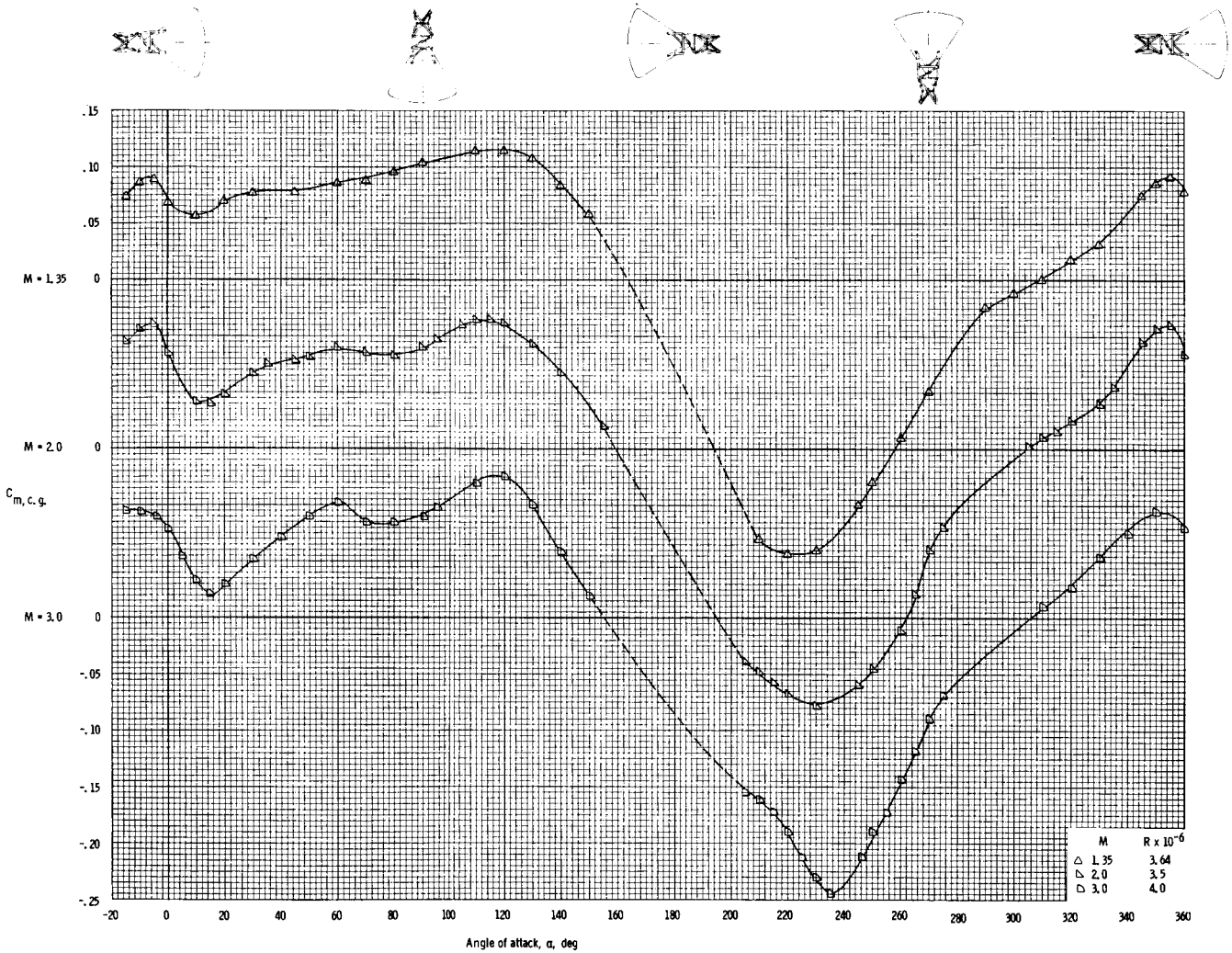

(d) Pitching-moment coefficient (c.g.) at M = 1.35 to M = 3.0 (c.g. = x/d = -0.602, z/d = 0.0474).

Figure 32. - Continued.

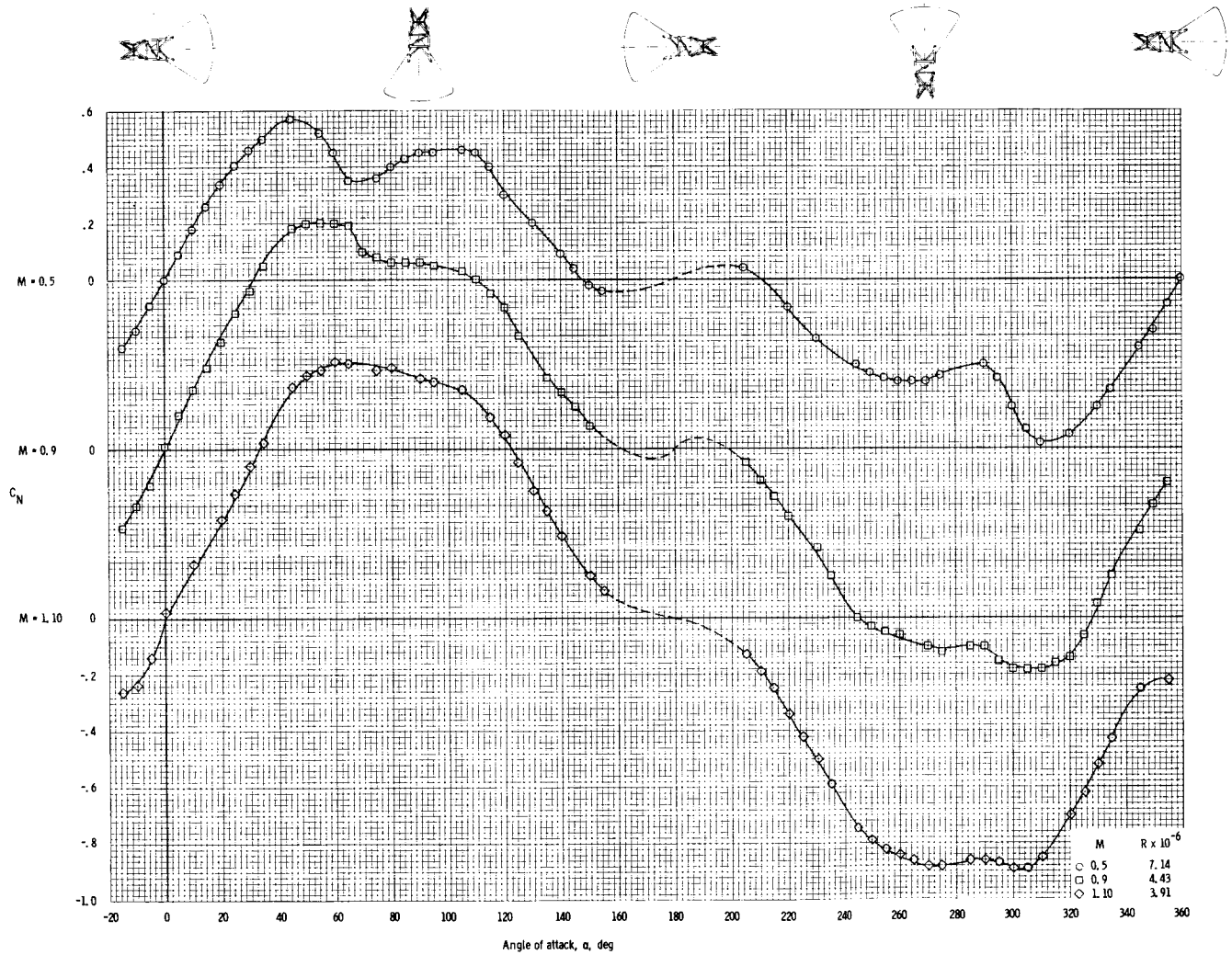

(e) Normal-force coefficient at M = 0.5 to M = 1.1.

Figure 32. - Continued.

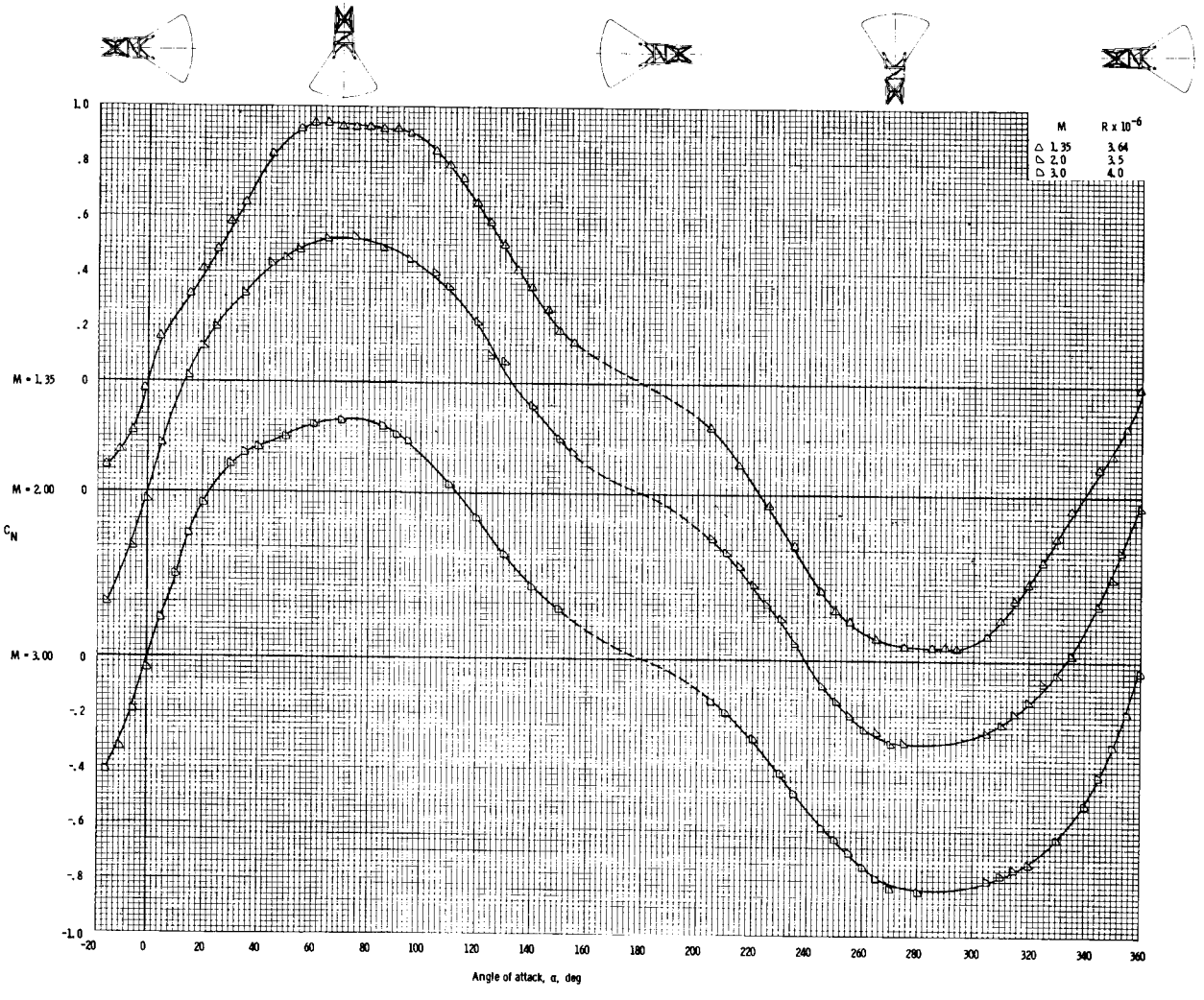

(f) Normal-force coefficient at M = 1.35 to M = 3.0.

Figure 32. - Continued.

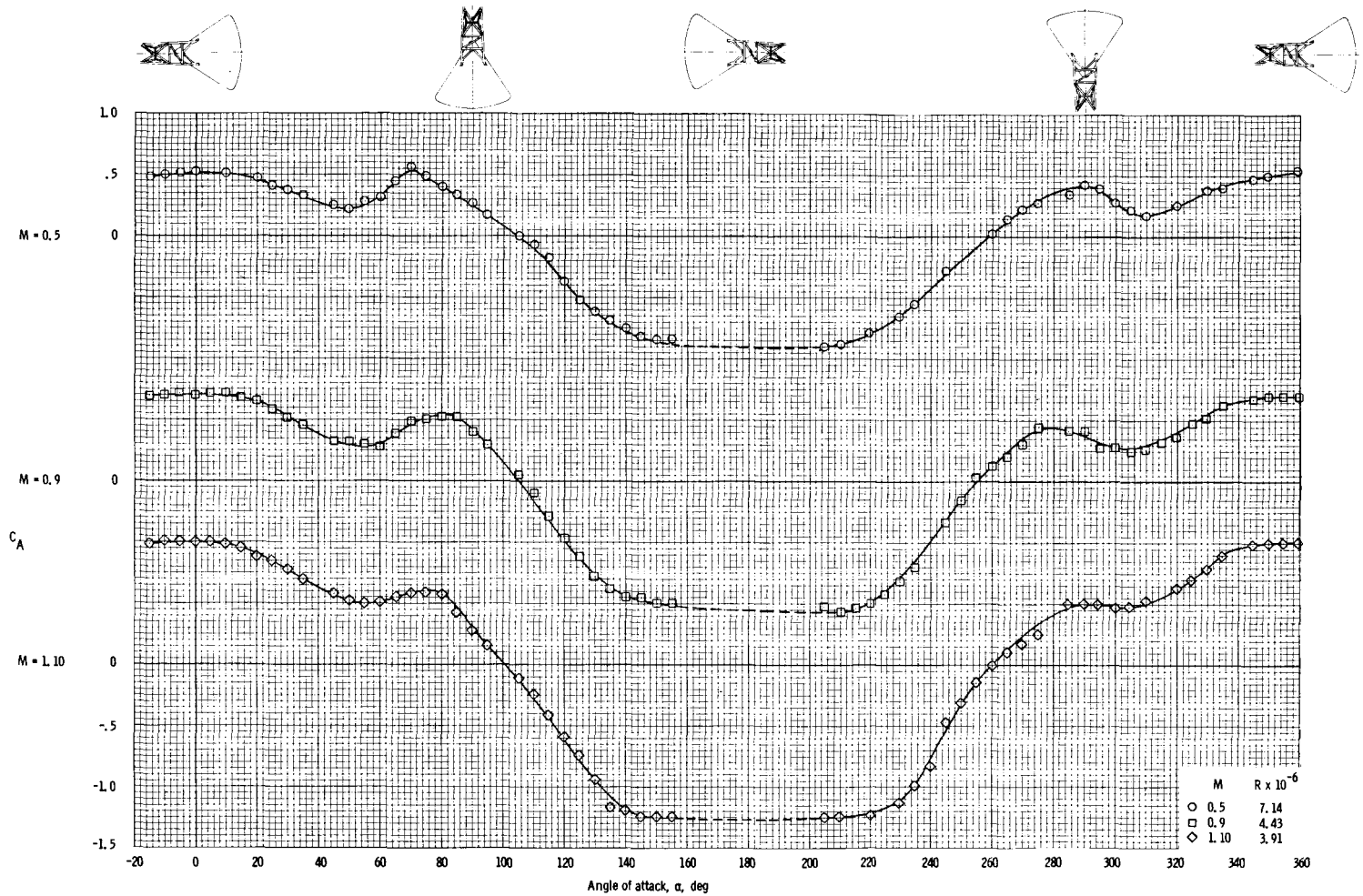

(g) Axial-force coefficient at M = 0.5 to M = 1.1.

Figure 32. - Continued.

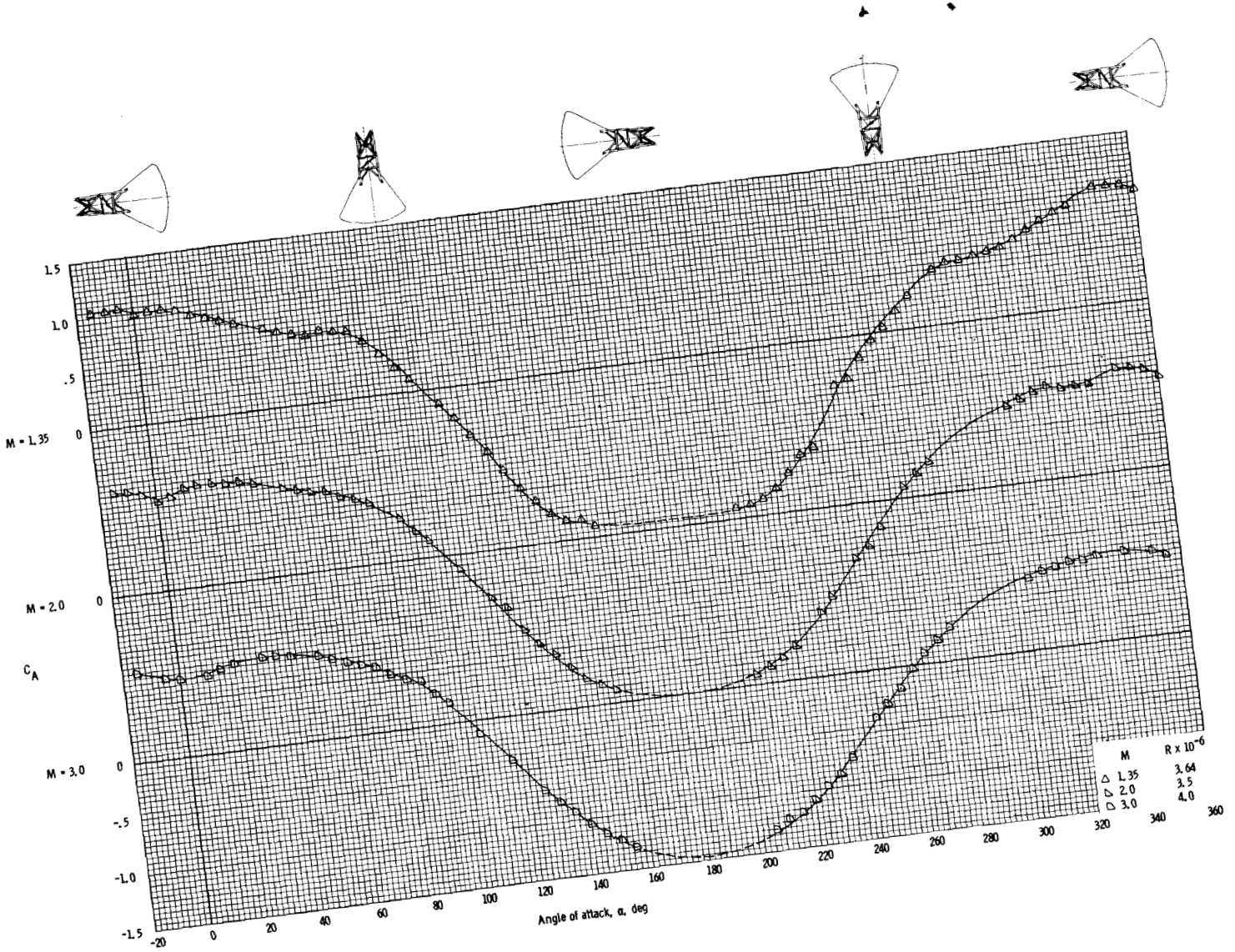

(h) Axial-force coefficient at M = 1.35 to M = 3.0.

Figure 32. - Continued.

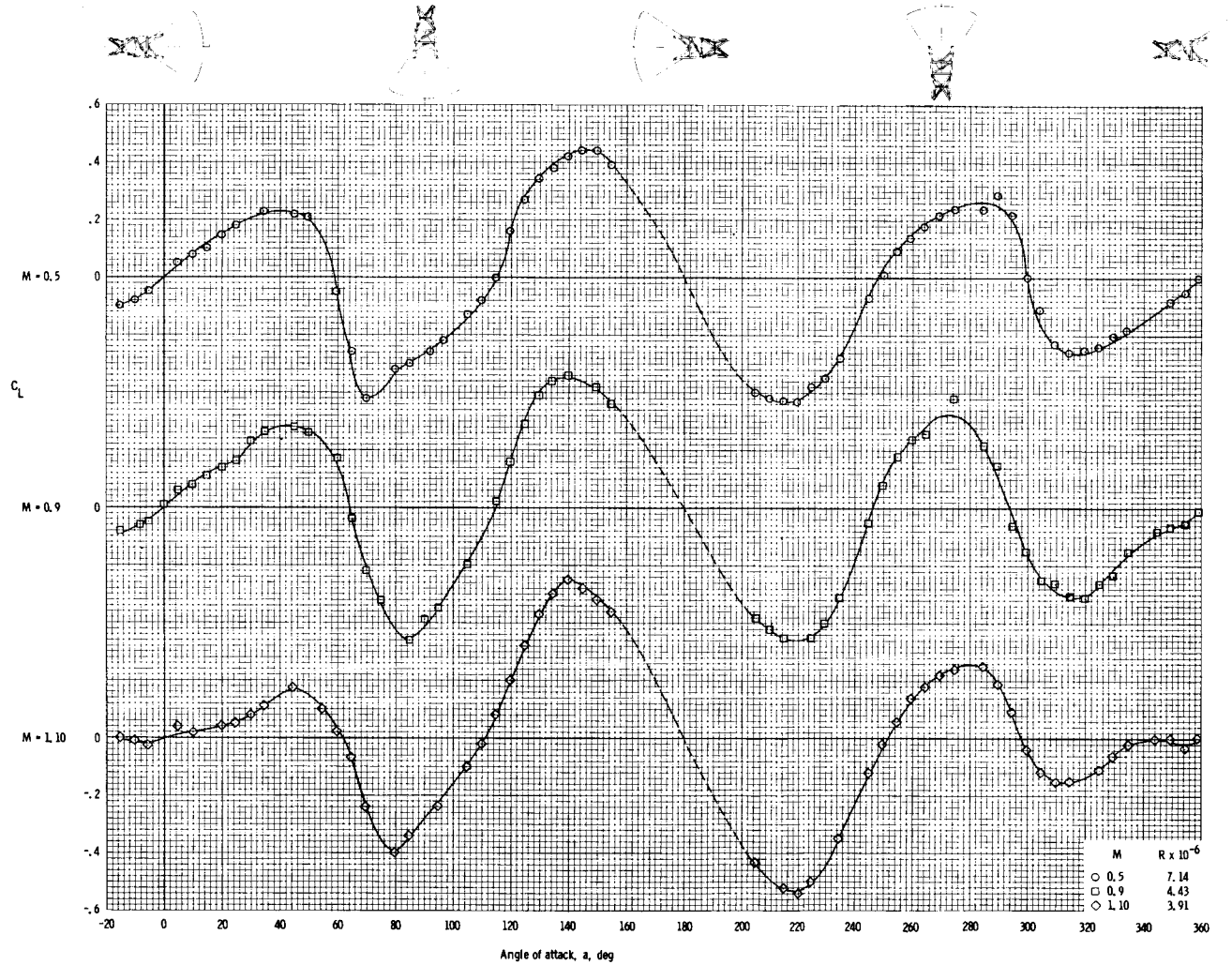

(i) Lift coefficient at M = 0.5 to M = 1.1.

Figure 32. - Continued.

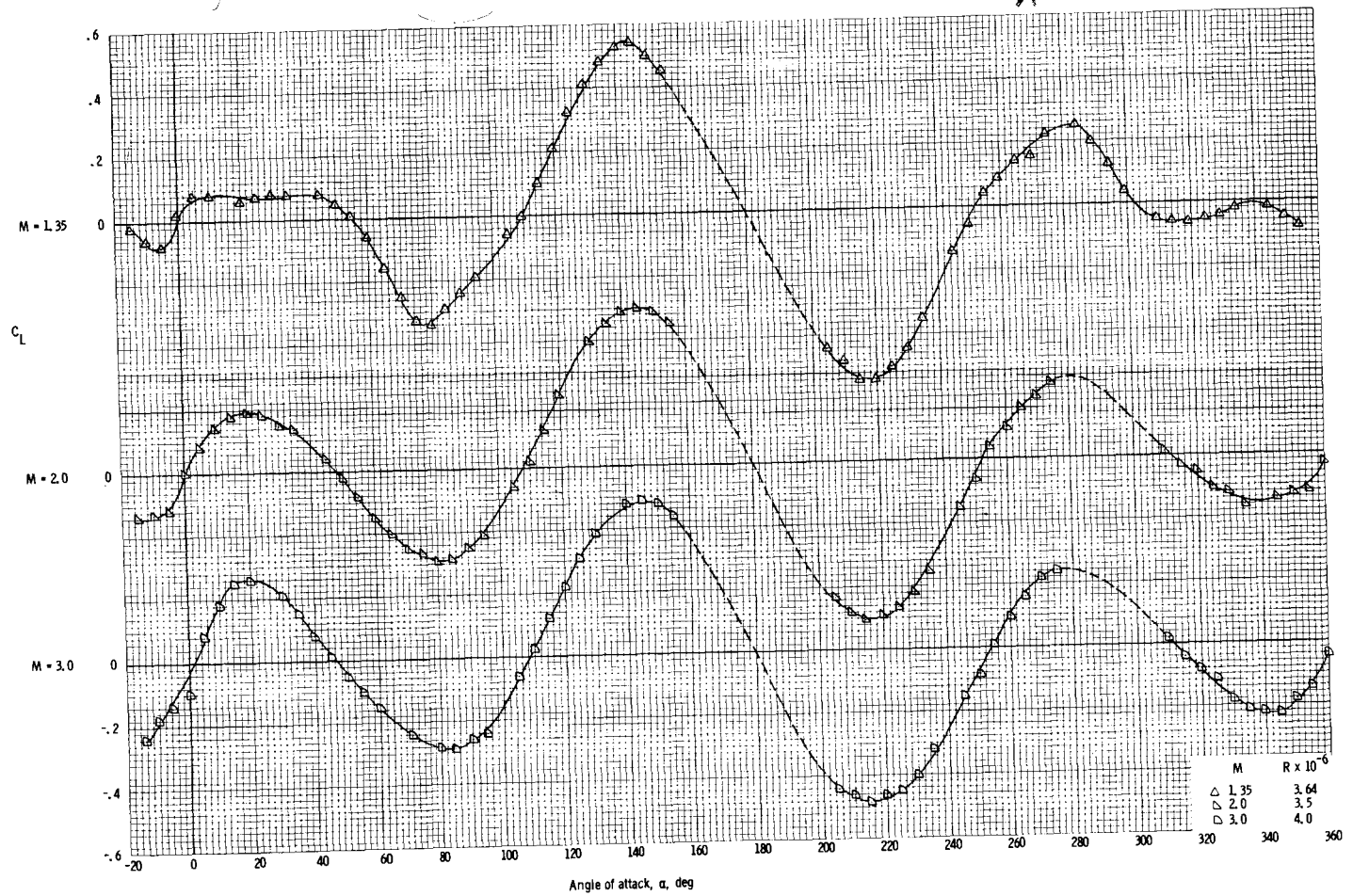

(j) Lift coefficient at M = 1.35 to M = 3.0.

Figure 32. - Continued.

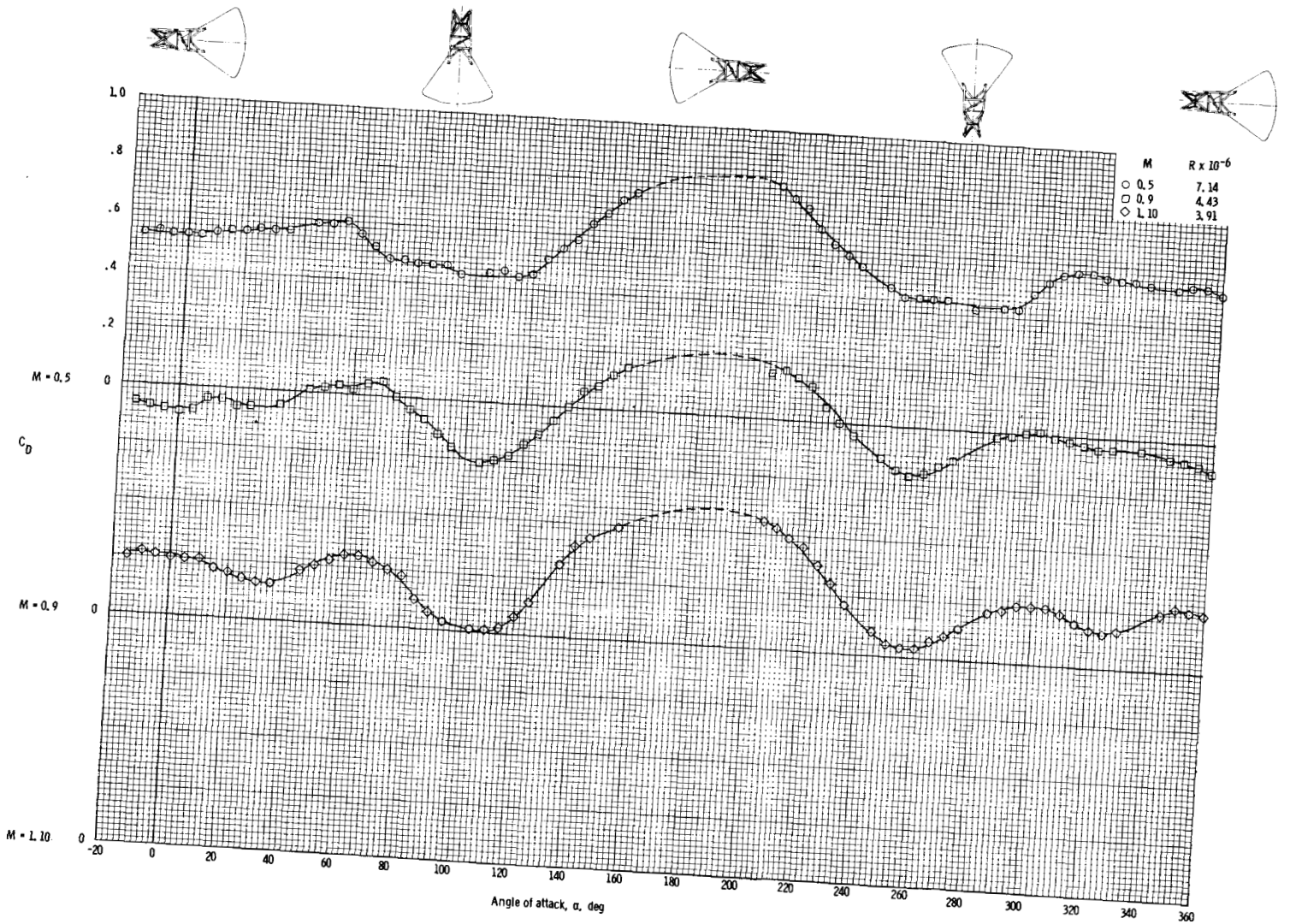

(k) Drag coefficient at M = 0.5 to M = 1.1.

Figure 32. - Continued.

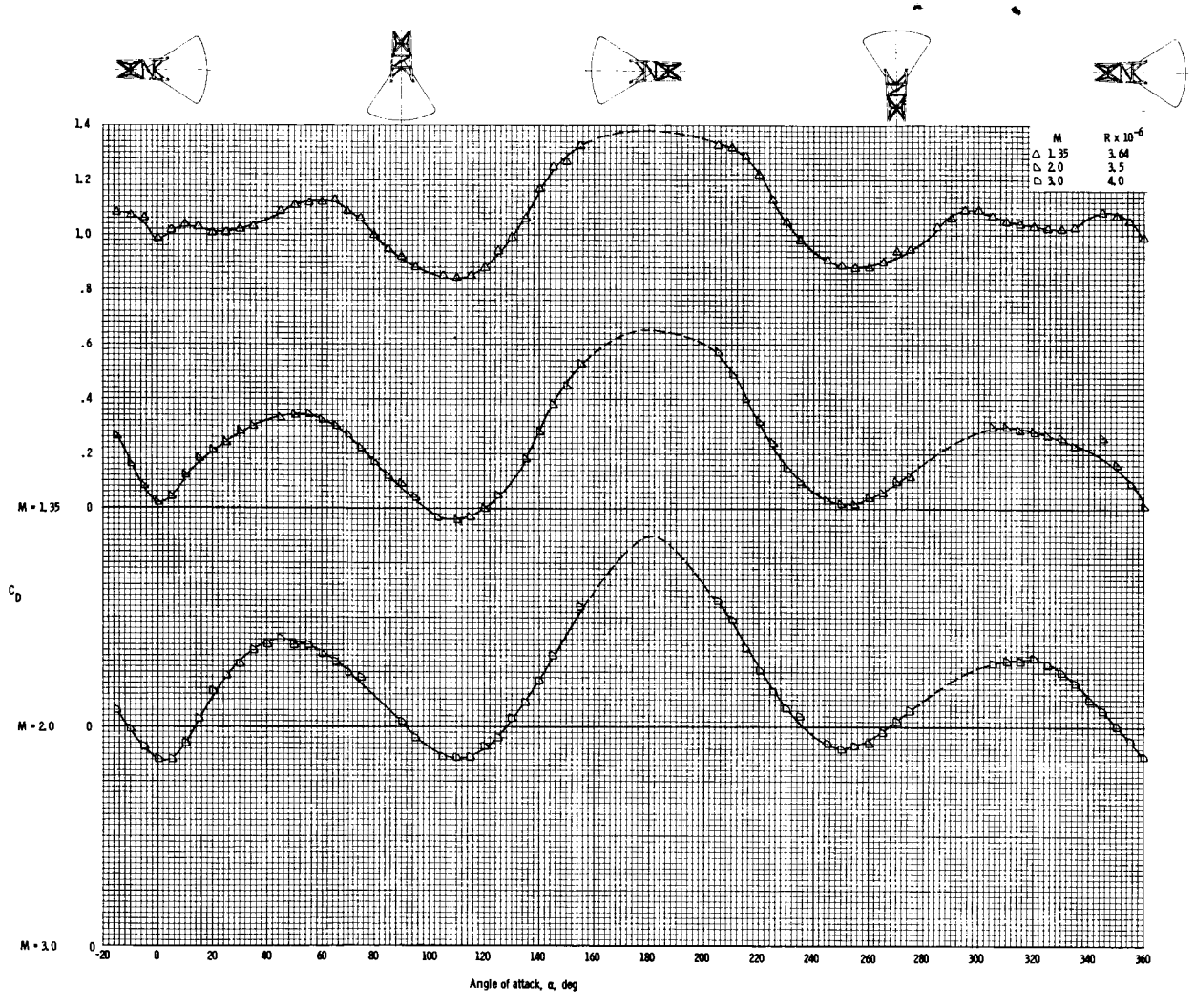

(l) Drag coefficient at M = 1.35 to M = 3.0.

Figure 32. - Continued.

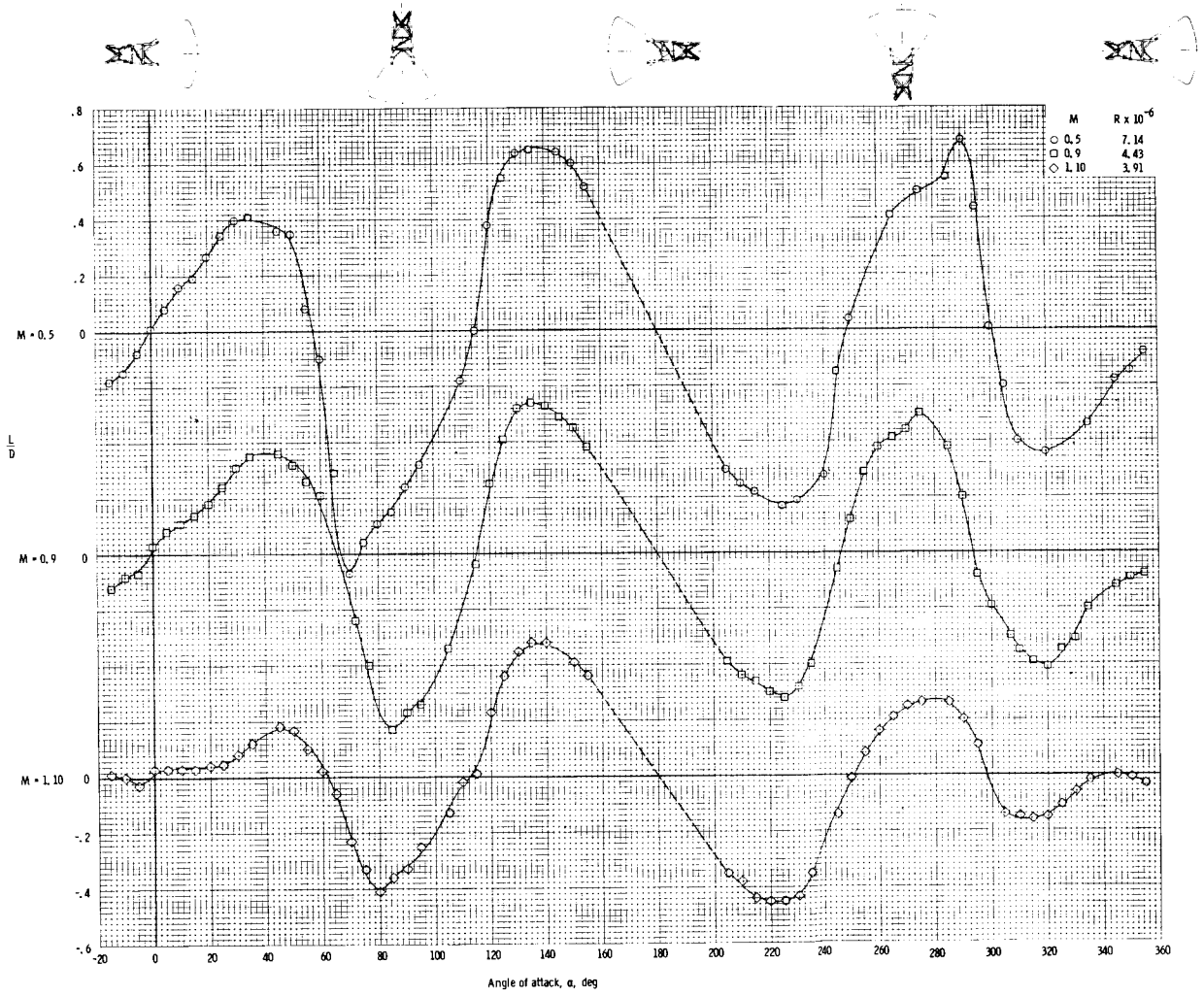

(m) Lift-to-drag ratio at M = 0.5 to M = 1.1.

Figure 32. - Continued.

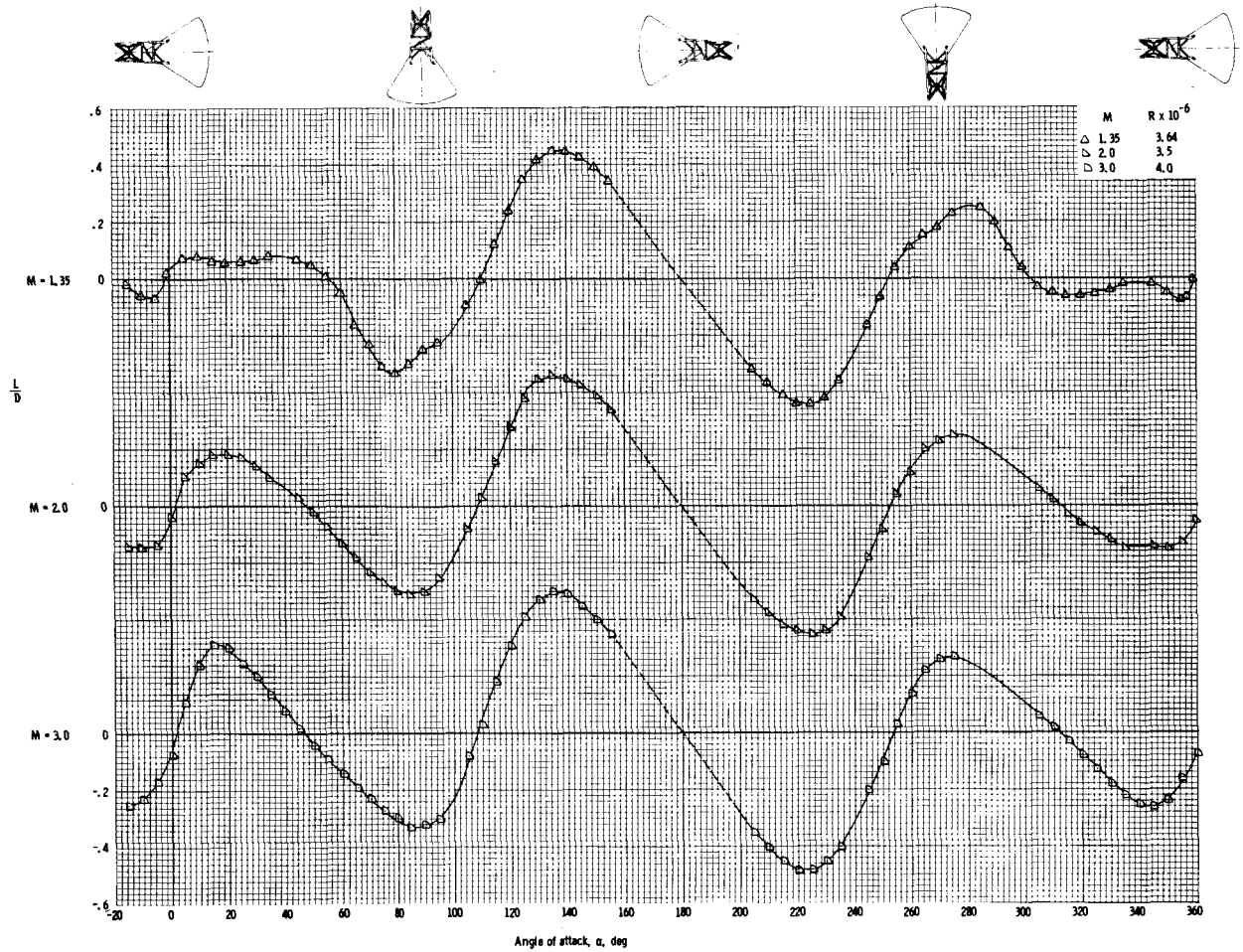

(n) Lift-to-drag ratio at M = 1.35 to M = 3.0.

Figure 32. - Concluded.

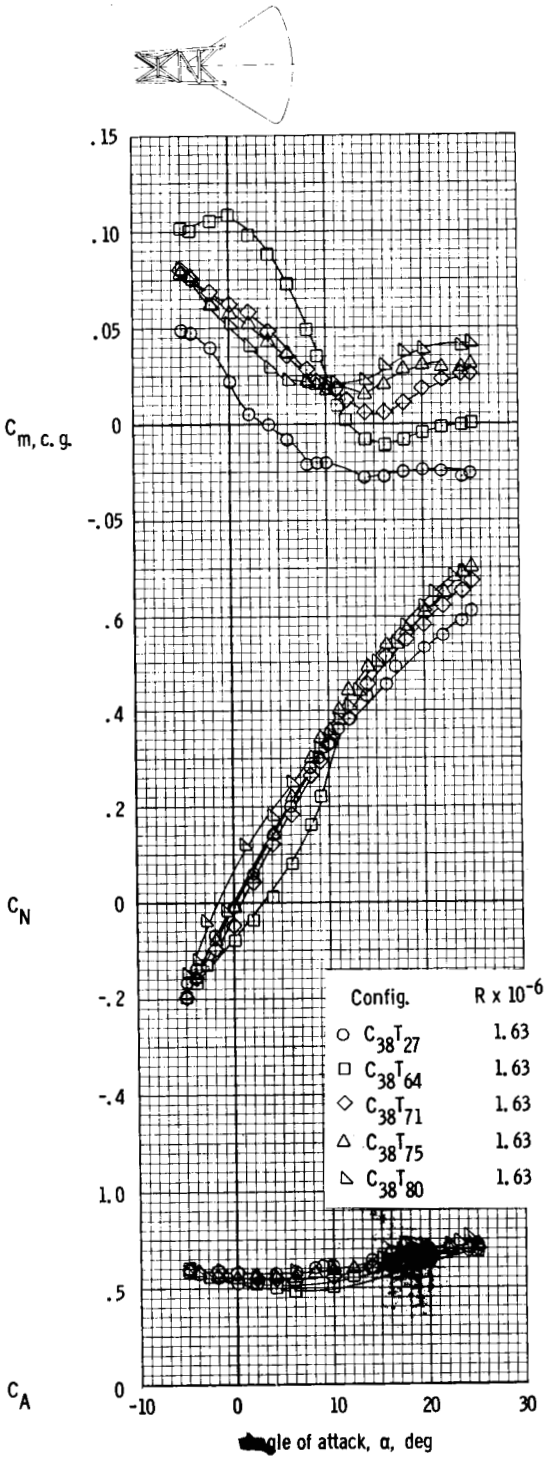

Figure 33. - Aerodynamic characteristics of the Apollo command module and escape tower (with flap) obtained at AEDC-A facility at M = 6.0 (c.g. = x/d = -0.582, z/d = 0.0438).

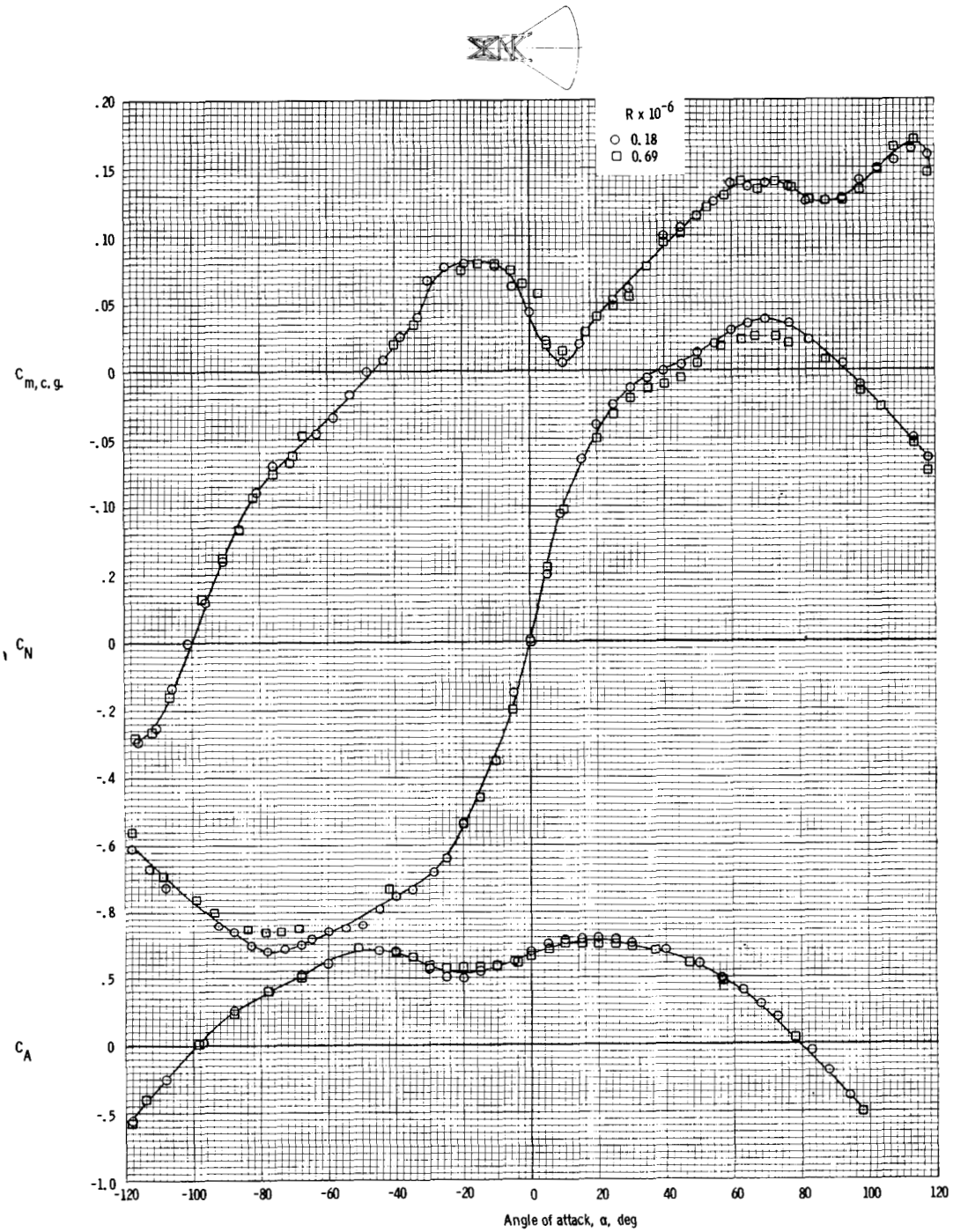

Figure 34. - Aerodynamic characteristics of the Apollo command module (C_{38}) and escape tower with flap (T_{62}) obtained at AEDC-C facility at M =10.0 (c.g. = x/d = -0.612, z/d = 0.0539).

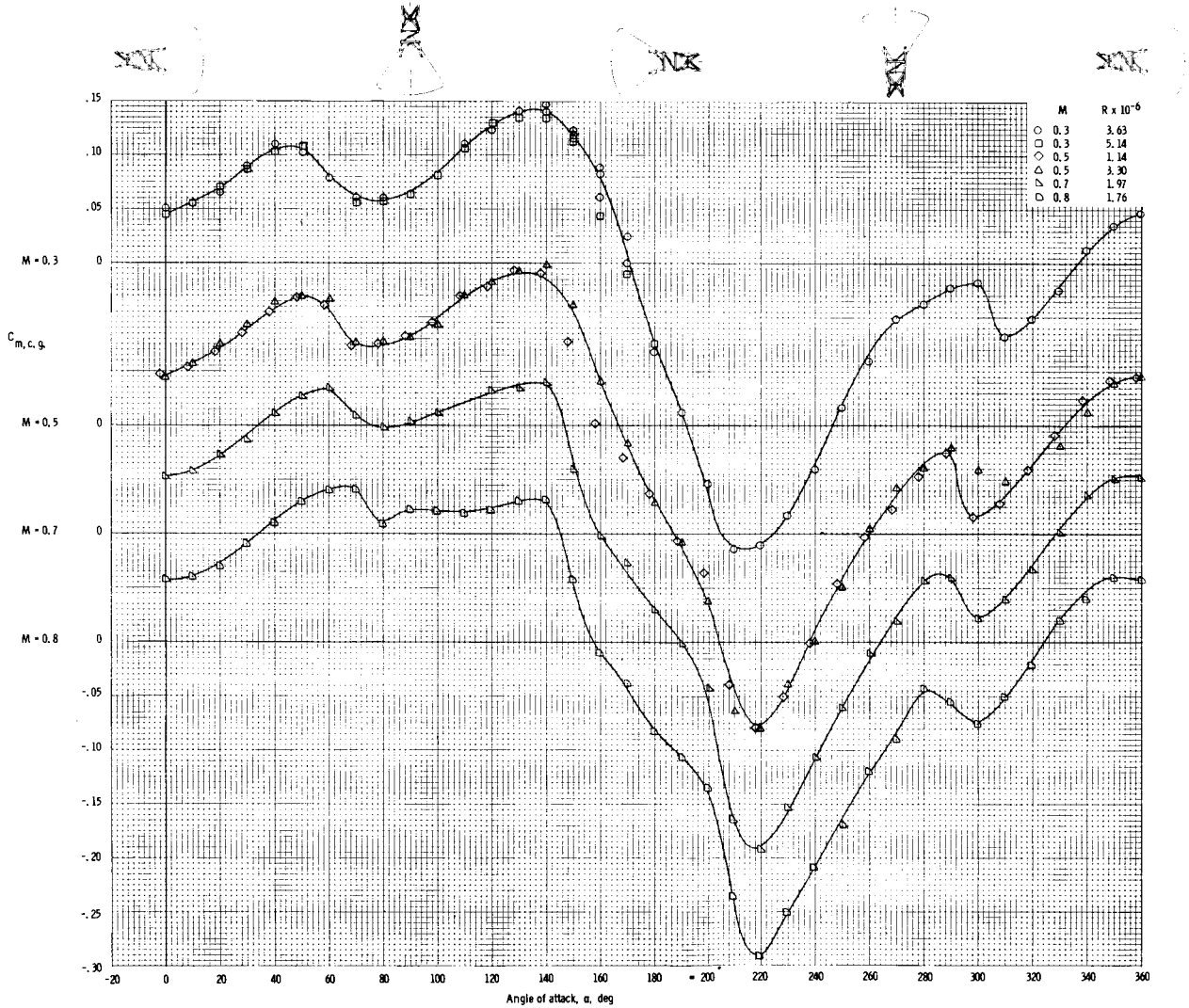

Figure 35. - Aerodynamic characteristics of the Apollo command module (C_{47}) and escape tower with flap (T_{65}) with sting-interference effects obtained at Ames 12-foot facility at M = 0.3 to M = 0.8 (c.g. = x/d = -0.625, z/d = 0.058).

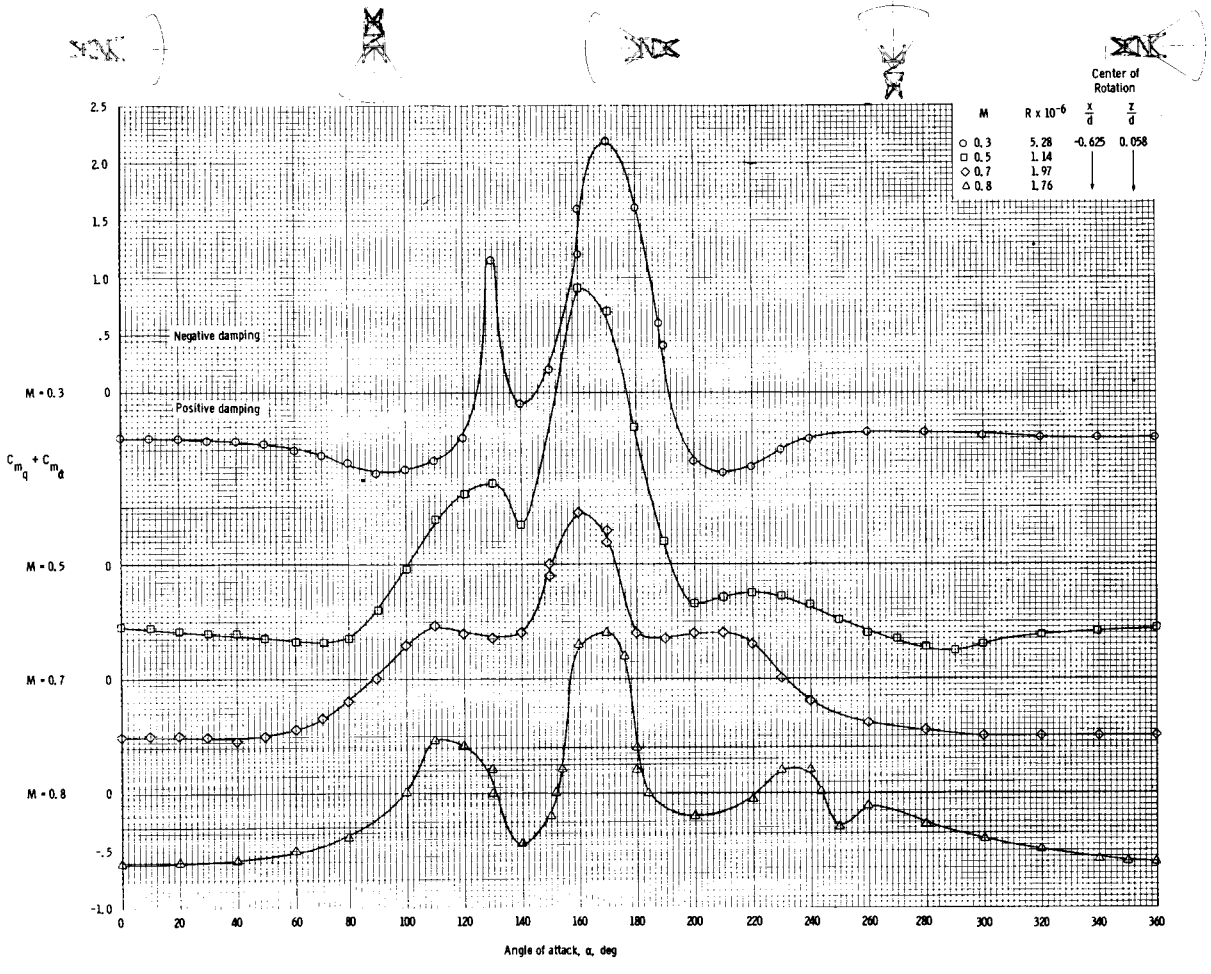

Figure 36. - Longitudinal oscillatory stability characteristics of the Apollo command module (C_{47}) and escape tower with flap (T_{65}) obtained at the Ames 12-foot facility at M = 0.3 to M = 0.8.